University of Southampton

Faculty of Life Sciences

Ocean and Earth Science

Methods for Determining Gas Flux within the Water Column

by

Ben John Roche

Thesis for the degree of Doctor of Philosophy (PhD)

June 2021

University of Southampton

Abstract

Faculty of Life Sciences

Ocean and Earth Science

Doctor of Philosophy

Methods for Determining Gas Flux within the Water Column

by

Ben John Roche

The passage of greenhouse gases, from both natural and anthropogenic sources, through the upper sedimentary succession and into overlying aquatic systems is a poorly understood process. Our understanding of it however conditions our ability to detect potential leaks from Carbon Capture and Storage sites (CCS) as well as our overall knowledge of the global carbon cycle. In this thesis repeated high-resolution seismic reflection surveys are used to image carbon dioxide (CO_2) gas released into shallow sub-surface sediments above a potential CCS storage site in the North Sea. Observations of temporal changes in seismic reflectivity, attenuation, unit thickness and the bulk permeability of sediment were used to develop a four-stage model of the evolution of gas migration in shallow marine sediments: Proto-migration, Immature Migration, Mature Migration, and Pathway Closure. Variations in ebullition rates from natural methane (CH_4) seeps in Lake Constance (central Europe) are observed over a 9-month period using physical and acoustic measurement techniques, demonstrating a significant negative correlation between gas flux and in-situ pressure. The water level (hydrostatic pressure) dictates flux rates on monthly timescales, while atmospheric pressure causes minor fluctuations on daily to weekly periods, the effect of land-lake breeze cycles are observed for the first time. Exploiting this relationship, we find that long-term ebullition rates are best estimated by quantifying the relationship between in-situ pressure and gas flux, and then using this relationship to predict gas flux from more easily measurable in-situ pressure data. Finally, the use of passive acoustic flux inversion techniques is refined by measuring the initial amplitude of a bubble's excitation when released from sediment, a previously poorly constrained parameter, demonstrating a strong correlation with the bubble equilibrium radius. We demonstrate the use of this refined acoustic inversion technique by measuring the flux from a volcanic CO_2 seep in offshore Panarea (Italy), seeing a significant increase in precision with estimates consistent with optical and physical flux measurements. These findings have enhanced our understanding of gas migration in the near surface and improved our ability to measure gas emissions.

Contents

List of Figures

List of Tables

Declaration of Authorship

Print name: Ben Roche

Title of thesis: Methods of determining gas flux within the water column

I declare that this thesis and the work presented in it are my own and has been generated by me as the result of my own original research.

I confirm that:

- This work was done wholly or mainly while in candidature for a research degree at this University;
- Where any part of this thesis has previously been submitted for a degree or any other qualification at this University or any other institution, this has been clearly stated;
- Where I have consulted the published work of others, this is always clearly attributed;
- Where I have quoted from the work of others, the source is always given. With the exception of such quotations, this thesis is entirely my own work;
- I have acknowledged all main sources of help;
- Where the thesis is based on work done by myself jointly with others, I have made clear exactly what was done by others and what I have contributed myself;
- Parts of this work have been published as:

Chapter 2) Roche, B., Leighton, T.G., White, P.R., Bull, J.M., (In Review) **Ambient Bubble Acoustics – Seep, Rain and Wave Noise.** Noisy Oceans: Monitoring Seismic and Acoustic Signals in the Marine Environment AGU Monograph

B.R wrote the first draft with revisions by; T.L., P.W & J.B.

Chapter 3) Roche, B., Bull, J.M., Marin-Moreno, H., Leighton, T.G., Falcon-Suarez, I.H., Tholen, M., White, P.R., Provenzano, G., Lichtschlag, A., Li, J., Faggetter, M., (2021) **Time-lapse imaging of CO2 migration within near-surface sediment during a controlled sub-seabed release experiment**. Int. J. Greenh. Gas Control 10.1016/j.ijggc.2021.103363

B.R wrote the first draft; B.R & J.B conceived the survey; B.R & M.F processed the seismic reflection data; M.T and A.L analysed the gravity core; H.M analysed volume estimates; I.F analysed hydrodynamic data; J.B, P.W & T.L helped revise the paper.

Chapter 4) [Ragg, R.B., Roche, B.], Fone, J., Bull, J.M., Peeters., F., White, P.R., Leighton, T.G., Hofmann, H., (In Review) **Temporal variability of methane ebullition in Lake Constance – Prediction via lakebed pressure**. Biogeosciences

B.R wrote the first draft; B.R & R.R conceived and conducted the survey; B.R & J.F processed optical data; B.R & J.F processed acoustic data; R.R. processed acoustic and pressure data; R.R created time series figures; R.R, J.B, F.P, P.W, T.L & H.H helped revise the paper.

Chapter 5) Roche, B., Christi, C., White, P.R., Leighton, T.G., Bull, J.M., Fone, J., Li, J. (Submission Pending) **Refining methods of acoustic gas flux inversion – investigation into the initial amplitude of bubble excitation**. Geophysical Research letters

B.R wrote the first draft; B.R & P.W conceived the test tank experiment; B.R & J.B conceived field study; B.R, C.C, P.W, J.B., J.F., J.L were involved in data collection; B.R processed acoustic data; B.R & J.F processed optical data; J.B, P.W & T.L helped revise the paper.

Signature: .....*B. Roche* Date: *25/06/21*

Acknowledgements

Firstly, I would like to thank my supervisors for their supervision and guidance throughout my PhD: Jon Bull, Paul White and Tim Leighton. They did an outstanding job of sieving through my misspelt ramblings to find the veritable nuggets seen here.

I would also like to give special thanks to John Davis, for his continuous support and his hard work satisfying all of my bizarre experimental designs. As well as Jianghui Li, for allowing me to collaborate on so many projects with him, and Ramona Ragg for inviting me to be a part of her work in Lake Constance.

I have collaborated with many great researchers throughout my time in Southampton and would like to thank them all (in alphabetical order): Alison Schaap, Anita Flohr, Anna Lichtschlag., Aude Lavayssiere, Ben Callow, Bettina Schramm (GEOMAR), Brett Hosking, Christoph Böttner (GEOMAR), Dirk Koopmans (Max Planck Institute), Diego Cotterle (OGS), Emiliano Gordini (OGS), Gaye Bayrakci, Giuseppe Provenzano, Hilmar Hoffmann (UoK), Hector Marin-Moreno, Ismael Falcon-Suarez, James Strong, Jonas Gross (GEOMAR), Kate Peel, , Mario Esposito (GEOMAR), Marius Dewar (PML), Mark Chapman (UoE), Michael Faggetter, Michele Deponte (OGS), Naima Yilo, Rachel James, Rudolf Hans, Samuel Monk, Veerle Huvenne. Thanks also to the incredible technical staff who made everything possible, namely: Alfred Sulger, Andrea Fogliozzi, Boris Kiefer, Hannah Wright, Josef Halder, Kevin Saw, Martin Mainberger, Martin Wolf, Martina Gaglioti, Rico Schlimper, Robin Brown and the crew of the RRS James Cook. I would also like to recognise Douglas Connelly for his overall leadership during the STEMM-CCS project and Carla Sands & Vikki Gunn for organising numerous early career research events

Thanks, and condolences must also be extended to the poor undergraduate students who worked with me; Colin Christie, Maddie Tholen and Joe Fone.

My research has generously been supported by the EU (as part of the Horizon 2020 research and innovation programme under grant agreement No.654462 STEMM-CCS project) and NERC (as part of the Highlight Topic NE/N016130/1 CHIMNEY).

Contractually I am obligated to thank Mum and Dad, for my general existence and support up to this stage, as well as Blonde, for her failed attempts to end my existence. Alongside the rest of my family (with the exception of Sean & Mathew who did their best to distract me by playing Minecraft).

I would like to thank my friends for their continuously poor judgment sticking around: Callum (who history will surreptitiously describe as my flatmate), Lewis (who encouraged good behaviour through the use of chocolate animals), Aled (who studies snakes or something IDK), Mike (who was supposed to be in the technical staff section but that felt a little harsh on them), Emma (who regularly organised needed distractions), Ben (who always supported my quiplashes), Annie (who doesn't hate me quite as much as she used to), Jess (who provided the TV and life advice), Breah (who took me to meet Zog the dragon) and Lyla (who ensured Jess was up at all hours of the night to respond to me). Rebecca, I'm sorry you didn't get to see me dressed more flamboyantly than you for once. Finally, I would like to thank Benny for making this final year the most interesting "è una possibilità da un milione a uno, ma potrebbe funzionare!"

Abbreviations

AP	Atmospheric Pressure
AUV	Autonomous underwater vehicle
BSL	Below Sea Level
CCS	Carbon Capture and Storage
CH_4	Methane
CO_2	Carbon Dioxide
HP	Hydrostatic Pressure
LEFM	Linear Elastic Fracture Mechanics
mbsf	metres below seafloor
MMV	Measurement, Monitoring and Verification
QICS	Quantifying and Monitoring Potential Ecosystem Impacts of Geological Carbon Storage (Project title)
RMS	Root Mean Square
RMSD	Root Mean Square Difference
ROV	Remotely Operated Vehicle
SI	Supplementary Information
SPL	Sound Pressure Level
STEMM-CCS	Strategies for Environmental Monitoring of Marine Carbon Capture and Storage (Project title)
TP	Total Pressure
TWT	Two Way Travel time
WOTAN	Wind Observations Through Ambient Noise

Publications

1. Roche, B., Leighton, T.G., White, P.R., Bull, J.M., (In Review) **Ambient Bubble Acoustics – Seep, Rain and Wave Noise.** Noisy Oceans: Monitoring Seismic and Acoustic Signals in the Marine Environment AGU Monograph
2. Roche, B., Bull, J.M., Marin-Moreno, H., Leighton, T.G., Falcon-Suarez, I.H., Tholen, M., White, P.R., Provenzano, G., Lichtschlag, A., Li, J., Faggetter, M., (2021) **Time-lapse imaging of CO2 migration within near-surface sediment during a controlled sub-seabed release experiment**. Int. J. Greenh. Gas Control 10.1016/j.ijggc.2021.103363
3. [Ragg, R.B., Roche, B.], Fone, J., Bull, J.M., Peeters., F., White, P.R., Leighton, T.G., Hofmann, H. (In Review) **Temporal variability of methane ebullition in Lake Constance – Prediction via lakebed pressure**. Biogeosciences
4. Roche, B., Christi, C., White, P.R., Leighton, T.G., Bull, J.M., Fone, J., (Submission Pending) **Refining methods of acoustic gas flux inversion – investigation into the initial amplitude of bubble excitation**. Geophysical research letters

Other journal publications arising during the period of my PhD are listed below. I made significant contributions to publications 5, 6 and 7, as detailed after the citation in each case

5. Li, J., **Roche, B**., Bull, J.M., White, P.R., Leighton, T.G., Provenzano, G., Dewar, M., Henstock, T.J., 2020. **Broadband Acoustic Inversion for Gas Flux Quantification—Application to a Methane Plume at Scanner Pockmark, Central North Sea.** J. Geophys. Res. Ocean. 125. https://doi.org/10.1029/2020JC016360

   I was responsible for the original conception and raw data analysis for this project as well as writing the introduction to this paper. It is featured in Chapter 7 "Auxiliary Work."

6. Li, J., **Roche, B**., Bull, J.M., White, P.R., Davis, J.W., Deponte, M., Gordini, E., Cotterle, D., 2020. **Passive acoustic monitoring of a natural CO2 seep site – Implications for carbon capture and storage.** Int. J. Greenh. Gas Control 93, 102899. https://doi.org/10.1016/j.ijggc.2019.102899

   I was responsible for planning and execution this survey as well as writing elements of the introduction.

7. Li, J., White, P.R., **Roche, B**., Bull, J.M., Leighton, T.G., Davis, J.W., Fone, J.W., 2021. **Acoustic and optical determination of bubble size distributions – Quantification of seabed gas emissions.** Int. J. Greenh. Gas Control 108, 103313. https://doi.org/10.1016/j.ijggc.2021.103313

   I was responsible for designing the landers used in data collection as well as overseeing their deployment and the development of the optical inversion code.

8. Marín-Moreno, H., Bull, J.M., Matter, J.M., Sanderson, D.J., **Roche, B**., 2019. **Reactive transport modelling insights into CO2 migration through sub-vertical fluid flow structures.** Int. J. Greenh. Gas Control 86, 82–92. https://doi.org/10.1016/j.ijggc.2019.04.018
9. Li, J., White, P.R., Bull, J.M., Leighton, T.G., **Roche, B**., Davis, J.W., 2021. **Passive acoustic localisation of undersea gas seeps using beamforming.** Int. J. Greenh. Gas Control 108, 103316. https://doi.org/10.1016/j.ijggc.2021.103316
10. Li, J., White, P.R., **Roche, B**., Davis, J.W., Leighton, T.G., 2019. **Underwater radiated noise from hydrofoils in coastal water.** J. Acoust. Soc. Am. 146, 3552–3561. https://doi.org/10.1121/1.5134779
11. Falcon-Suarez, I.H., Lichtschlag, A., Marin-Moreno, H., Papageorgiou, G., Sahoo, S.K., **Roche, B**., Callow, B., Gehrmann, R.A.S., Chapman, M., North, L., 2021. **Core-scale geophysical and hydromechanical analysis of seabed sediments affected by CO2 venting.** Int. J. Greenh. Gas Control 108, 103332. https://doi.org/10.1016/j.ijggc.2021.103332

12. Flohr, A. A., Schaap, A., Achterberg, E.P., Alendal, G., Arundell, M., Berndt, C., Blackford, J., Böttner, C., Borisov, S.M., Brown, R., Bull, J.M., Carter, L., Chen, B., Dale, A.W., de Beer, D., Dean, M., Deusner, C., Dewar, M., Durden, J.M., Elsen, S., Esposito, M., Faggetter, M., Fischer, J.P., Gana, A., Gros, J., Haeckel, M., Hanz, R., Holtappels, M., Hosking, B., Huvenne, V.A.I., James, R.H., Koopmans, D., Kossel, E., Leighton, T.G., Li, J., Lichtschlag, A., Linke, P., Loucaides, S., Martínez-Cabanas, M., Matter, J.M., Mesher, T., Monk, S., Mowlem, M., Oleynik, A., Papadimitriou, S., Paxton, D., Pearce, C.R., Peel, K., **Roche, B.**, Ruhl, H.A., Saleem, U., Sands, C., Saw, K., Schmidt, M., Sommer, S., Strong, J.A., Triest, J., Ungerböck, B., Walk, J., White, P., Widdicombe, S., Wilson, R.E., Wright, H., Wyatt, J., Connelly, D., 2021 **Towards improved monitoring of offshore carbon storage: A real-world field experiment detecting a controlled sub-seafloor CO2 release.** Int. J. Greenh. Gas Control 106, 103237. https://doi.org/10.1016/j.ijggc.2020.103237

13. Robinson, A.H., B. Callow, C. Böttner, N. Yilo, G. Provenzano, I. H. Falcon-Suarez, H. Marín-Moreno, A. Lichtschlag, G. Bayrakci, R. Gehrmann, L. Parkes, **B. Roche**, U. Saleem, B. Schramm, M. Waage, A. Lavayssière, J. Li, F. Jedari-Eyvazi, S. Sahoo, C. Deusner, E. Kossel, T. A. Minshull, C. Berndt, J. M. Bull, M. Dean, R. H. James, M. Chapman, A. I. Best, S. Bünz, B. Chen, D. P. Connelly, J. Elger, M. Haeckel, T. J. Henstock, J. Karstens, C. Macdonald, J. M. Matter, L. North, and B. Reinardy, 2021,. **Multiscale characterisation of chimneys/pipes: Fluid escape structures within sedimentary basins.** Int. J. Greenh. Gas Control 106, 103245. https://doi.org/10.1016/j.ijggc.2020.103245

14. Callow., B., Jonathan B.M., Provenzano, G., Böttner, C., Birinci, H., Robinson A.H., Henstock T.J, Minshull T.A., Bayrakci, G., Lichtschlag, A., **Roche, B.**, Yilo, N., Gehrmann, R., Karstens J., Falcon-Suarez I.H., Berndt, C. (In Press) **Seismic chimney characterisation in the North Sea – Implications for pockmark formation and shallow gas migration** Marine and Petroleum Geology

Chapter 1 Introduction

1.1 General Introduction

Climate change has been identified as the single greatest threat to mankind, being considered more likely and more devastating a risk than war or disease (World Economic Forum, 2020). The increasing emissions of greenhouse gases such as carbon dioxide (CO_2) and methane (CH_4) since the industrial revolution have already permanently damaged life on Earth (Friedlingstein et al., 2019). Global mean surface temperatures have increased 1 °C directly as a result of increasing levels of greenhouse gases in our atmosphere (IPCC, 2018; Fujimori et al., 2021). This small increase in temperature has already led to rising sea levels, increasingly unpredictable and extreme weather events (such as flooding and drought), and rapidly changing ecosystems all around the globe (Seroussi et al., 2020; Brás et al., 2021; Mamalakis et al., 2021; Moffette et al., 2021; Nicholls et al., 2021; Ortiz-Bobea et al., 2021). The speed at which our climate is changing is having a devasting impact on flora and fauna, which struggle to adapt to the changing environment, leading many to go extinct (Amano et al., 2020; Martin and Mouton, 2020; Woolway and Maberly, 2020). What is truly concerning is that climate change shows no sign of slowing down, with the volume of anthropogenic greenhouse gas being released each year continuing to increase (Crippa et al., 2019; Zhou et al., 2021). In order to combat this, the United Nations Framework Convention on Climate Change has agreed on a strategic plan, commonly known as the Paris Agreement, to stop the global mean temperature from rising more than 2 ˚C above the pre-industrial level (UNFCCC, 2015). This strategy primarily revolves around reducing anthropogenic emissions into the atmosphere via (among other things) cleaner energy sources and more energy efficient processes (UNFCCC, 2015; Fujimori et al., 2021; le Quéré et al., 2021).

The large-scale adoption of Carbon dioxide Capture and Storage (CCS) has been identified as a key factor in reducing anthropogenic greenhouse gas emissions to reach climate goals (IPCC, 2014; Hanssen et al., 2020; Fujimori et al., 2021). During CCS activities, CO_2 gas produced during

industrial processes is captured and stored in appropriate geological reservoirs deep beneath the surface to mitigate the potential greenhouse effects. Compared to other strategies, such as enhanced energy efficiency and the use of renewable energy sources, the crucial benefit of CCS lies in its potential to reduce (in a significant, timely, and cost-effective way) the CO_2 emissions, by utilizing existing infrastructure from oil and gas production (IPCC, 2005; Mikunda et al., 2021).

As a result of CCS facilities currently in operation ~40 Mt of CO_2 a year (that would otherwise be released directly into the atmosphere) is being permanently stored underground (GCCSI, 2020). While this is an impressive achievement, annual anthropogenic CO_2 emissions are of the order of ~40 Gt. Indeed, the increase in anthropogenic emissions between 2017 and 2018 alone was equal to 38 Mt (Crippa et al., 2019). Hence if any meaningful progress is to be made offsetting anthropogenic CO_2 emissions, there needs to a hundredfold increase in the number/capacity of CCS sites located around the globe. To date there are 65 commercial CCS facilities (Fig. 1.1), of which 26 are currently operating, two have suspended operations, three are under construction, 13 are in advanced development and 21 are in early development. Notably 17 of these early development projects were launched since 2019, indicating the rapidly growing interest in CCS (GCCSI, 2020).

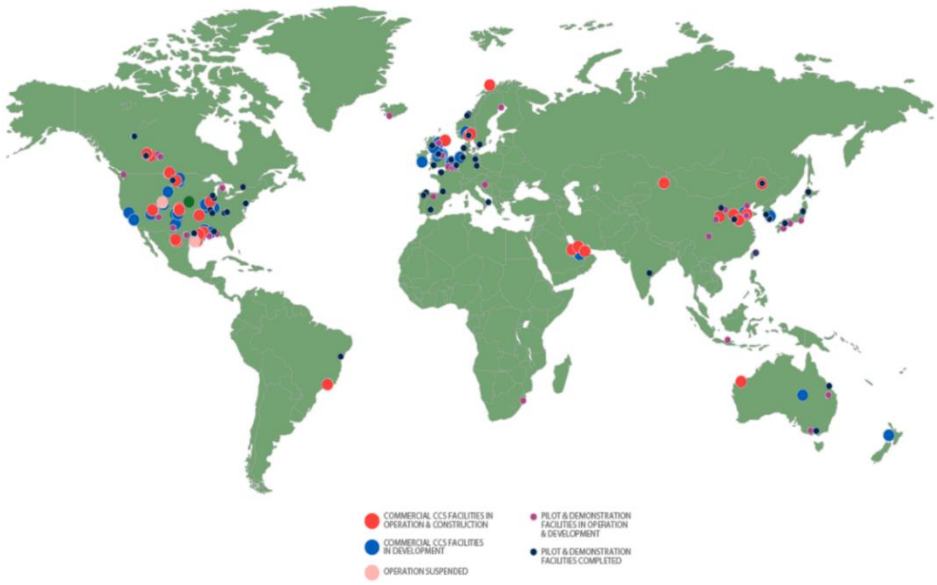

Figure 1.1: Map of CCS facilities at various stages of development around the world. Adapted from GCCSI (2020).

The majority of new commercial CCS sites are located in the United States, primarily motivated by lower regulatory requirements, and enhanced tax credits making them more financially attractive (GCCSI, 2020; IOGP, 2020; Jenkins, 2020). In comparison Europe has fallen behind with only two CCS sites currently in operation. While there have been numerous feasibility and pilot studies performed, a lack of support from government policies has stifled growth (GCCSI, 2020; IOGP, 2020). Norway has been the only prominent proponent of CCS and operates both active European CCS sites, the Sleipner and Snøhvit facilities (Ringrose, 2018). Europe's reluctance to fully embrace CCS can be pinned on the questionable economic value (requiring massive infrastructure investments) and a persistent fear that such storage facilities may one day leak, releasing CO_2 back into the environment (NAO, 2017). Frustratingly, Europe's North Sea is a prime candidate for CCS storage, with the potential to hold 475-570 Mt of CO_2 (Strachan et al., 2011).

Hence if European nations are able to reduce the cost of CCS and improve confidence in their ability to safely inject and store CO_2, they have the potential to lead the world in offshore CCS (Strachan et al., 2011). Indeed, the vast majority of current and future offshore CCS sites are located in the North Sea (Tbl. 1.1).

Location	Project Name	Starting Date	CO_2 Captured / Year	Status
Denmark	Greensand	2025	0.5-1 Mt	Feasibility study
Ireland	ERVIA	2028	2 Mt	Feasibility study
Italy	CCS Ravenna Hub	2025-2028	0.04-5 Mt	Prefeasibility study
Norway	Sleipner CO2 Storage	1997	1 Mt	**Operational**
Norway	Snøhvit CO2 Storage	2008	0.7 Mta	**Operational**
Norway	Longship (including Northern Lights)	2023-2024	0.8 Mt	Final Investment Decision
Sweden	Preem CCS	2025	0.5 Mt	Pilot Phase
Sweden	Stockholm Exergi Bio-CCS	-	0.8 Mt	Pilot Phase
The Netherlands	Porthos	2024	< 5 Mt	Feasibility study
The Netherlands	Althos	2030	< 7.5 Mt	Feasibility study
UK	Acorn	2023	0.2 Mt	Feasibility study
UK	Caledonia Clean Energy	2023	3 Mt	Feasibility study
UK	Net Zero Teesside	2026	5 Mt	Technical Evaluation and business model operation
Belgium	Antwerp@C	Unknown	Unknown	Feasibility Study
France	DMX Demonstration	2025	1 Mt	Pilot Phase
South Korea	Korea-CCS 1 & 2	2021-2030	1 Mt	Early Development
Indonesia	Gundih CCS Pilot	2021-2030	0.01 Mt	Advanced Development
Libya	Mellitah Complex CO2 Management	2023-2025	3 Mt	Final Investment Decision
South Africa	Pilot Carbon Storage Project (PCSP)	2020	0.01-0.05 Mt	Advanced Development

Table 1.1: Overview of active and planned offshore CCS projects around the world as of December 2020. Source GCCSI (2020) and IOGP (2020).

In order to encourage the adoption of offshore CCS in Europe and around the world, considerable effort has been expended in recent years into developing strategies and technologies for the monitoring and verification of CO_2 storage (Jenkins, 2020). Dean & Tucker (2017) presented a risk-based framework for the Measurement, Monitoring and Verification (MMV) of the Goldeneye storage complex, a potential offshore CCS site in the North Sea, in order to ensure the long-term security of injected CO_2. While this project ultimately did not go ahead, due to the uncertain economic case, the project was deemed to conform with regulatory requirements meaning the MMV plan serves as a useful guideline for future projects in Europe. Dean & Tucker (2017) identified the five key leak scenarios (Fig. 1.2) as:

- migration through plugged and abandoned wells
- migration through injection wells
- migration through faults and fractures
- lateral migration away from storage complex
- a combination of wells/faults and lateral migration.

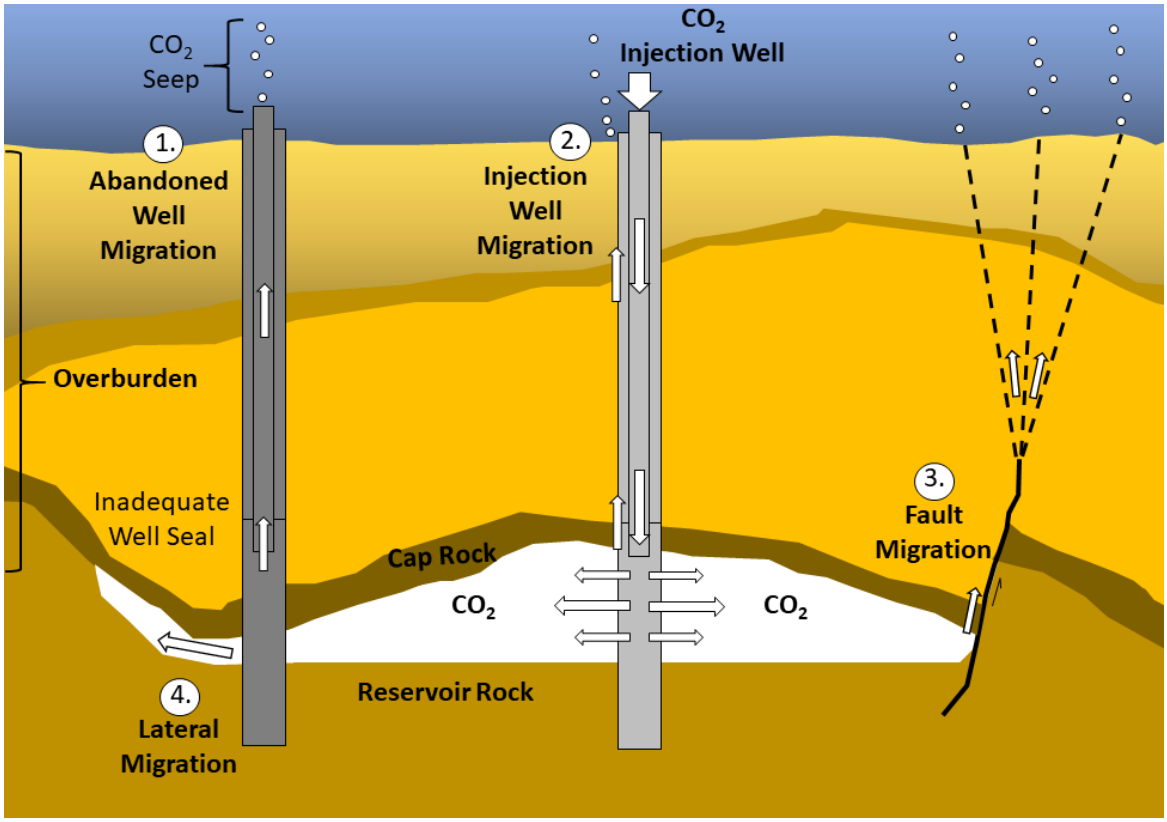

Figure 1.2: Diagram outlining potential CO_2 leakage scenarios associated with Carbon Capture and Storage sites. These being gas migration along (1) inadequately secured abandoned wells (2) migration along the injection well (3) migration along faults and fractures (4) lateral migration outside of storage site. Modified from Damen et al., (2006) using Dean and Tucker (2017).

Based on these leakage scenarios, Dean & Tucker (2017) determined that any MMV must plan to monitor: pressure and CO_2 plume development inside the storage complex; legacy and injection well integrity; geological seal integrity, as well as any potential impacts on the marine biosphere. While numerous technologies would allow for the detailed monitoring of any of the preceding factors, only some were deemed cost-effective and ultimately included in the final MMV, (Tbl. 2.2). The selected technologies place a strong emphasis on the use of active acoustics (primarily seismology) to monitor the migration of CO_2 after injection. They also highlighted a need to understand baseline conditions in the biosphere and natural variations within it, so that artificial deviations can be more easily detected.

Domain	Data acquisition	Technology	Proposed in MMV Plan
Water column, seabed and shallow geosphere	Water column profiling near seabed	Geochemical probes	Yes
	Seabed sampling (seabed sediment, flora and fauna sampling)	Van Veen Grab	Yes
		Vibro Corer	No
		Core Penetrating Testing (CPT) rig fitted with a probe	No
		Hydrostatically sealed corer	No
	Pockmarks	Multi Beam Echo Sounder (MBES) and Side Scan Sonar (SSS)	Yes
	Subsidence and uplift	Global Positioning System (GPS)	Yes
	Shallow overburden seismic	Chirps/Pingers	No (but in contingency plan)
		2D lines/3D swath	
Deeper geosphere	Time-lapse seismic	3D streamer	Yes
		Ocean Bottom Node (OBN)	Yes
		3D swath/2D lines	No
		Geophone Vertical Seismic Profile (VSP)	No
		Distributed Acoustic Sensing (DAS) VSP on tubing	Yes (R&D)
	Microseismic	Geophone Microseismic	No
		DAS Microseismic	Yes (R&D)
	Passive seismic	Seabed geophones	Yes (baseline only)
Wells	Well integrity	Cement bond logging	Yes
		Casing integrity logging	Yes
		Tubing integrity logging	Yes
		Distributed Temperature Sensing (DTS) on tubing	Yes
		DAS on tubing	Yes (R&D)
	CO_2 Detection	U-tube	No
		Downhole sampling	Yes
	CO_2 Conformance	Sigma logging	Yes
		Neutron porosity logging	Yes
	Pressure conformance	Pressure Downhole Gauge	Yes
		Long term gauge	Yes
		Cased-hole pressure and temperature	Yes
	Fingerprint	Inert chemical tracer	Yes (R&D)

Table 1.2: Summary of CCS site monitoring technologies and their status in the MMV, from Dean & Tucker (2017).

The focus on seismic monitoring strategies is understandable given the wealth of experience the oil and gas sector has in mapping lithological gas reservoirs. However, this knowledge base is focused on 'deep earth' observations, typically ~1 to 100 km below the surface, and large volumes of gas. The migration of gas through the uppermost sedimentary succession is still poorly understood (Lumley, 2019; Anyosa et al., 2021). Our understanding of newly self-established fluid flow features (gas conduits to the seabed), and their effect on the surrounding sediment, conditions our ability to detect small-scale CCS leakage and ameliorate any potential environmental impacts (Robinson et al., 2021). Dean & Tucker (2017) noted the need to use high frequency seismic reflection data in their contingency plan to examine possible leaks in the subsurface. There thus exists a need to gain a greater understanding of the fate of injected gas in the uppermost sedimentary succession.

More broadly, a greater understanding of the fate of injected gas in the subsurface will enhance our understanding of processes operating in natural CO_2 and CH_4 seeps that are found

around the globe as a result of decaying organic sediment, hydrocarbon systems and volcanic activity (Fig. 1.3) (Dlugokencky et al., 2011; Ruppel and Kessler, 2017; Oppo et al., 2020; Razaz et al., 2020). Actively quantifying the rate of gas release from natural seep sites, especially over extended periods of time, is notoriously difficult, particularly in marine settings (Li et al., 2018; Flohr et al., 2021). Accurately quantifying ebullition rates from natural systems is difficult because 1) techniques for measuring ebullition rates in the field are still relatively limited in terms of survey area and the length of observation, and 2) we lack a proper understanding of how the release rates vary over time and space (Boles et al., 2001; Greinert et al., 2010; Klaucke et al., 2010; Razaz et al., 2020). As a result, the relative contributions of natural and anthropogenic CO_2 and CH_4 to the global carbon cycle remains uncertain (Houghton, 2014; Bush, 2020; Oppo et al., 2020). In order to properly offset anthropogenic carbon emissions (via CCS and other emerging technologies), a more complete understanding of the natural carbon cycle and how it fluctuates over a variety of timescales is essential (Bush, 2020). Thus, it is important that work is done to refine methods for quantifying gas flux into the water column and better understand the variability of natural seeps sites.

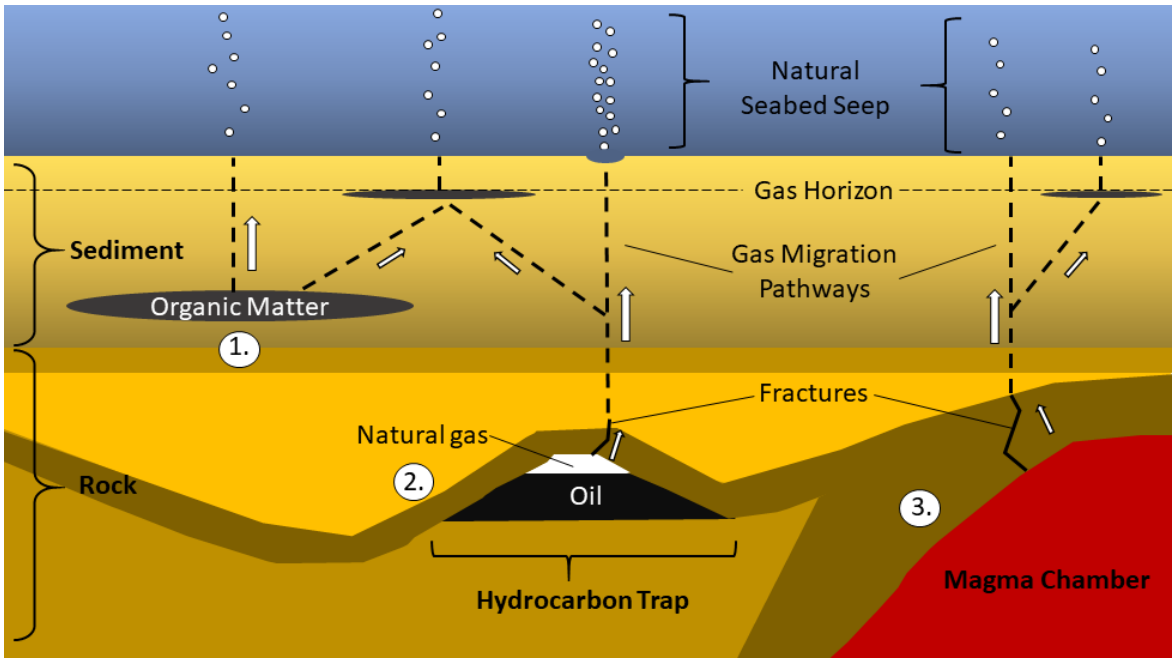

Figure 1.3: Diagram outlining common causes of natural gas seeps (1) biodegrading organic matter in sediment (2) hydrocarbon reservoirs (3) volcanic activity. Regardless of origin, upward migrating gaseous material often forms a natural gas horizon a few meters below the seabed, acting as a secondary reservoir.

In order to address these knowledge gaps, this thesis reports and analyses the results of three experiments, each designed to improve methods of detecting and quantifying gas migration into the water column. The first uses high frequency seismic reflection data to analyse the evolution of gas migration pathways in the seabed. The second observes a number of natural lakebed seeps in order to identify the key driving factors behind varying flux levels and proposes new (more accurate) techniques for estimating annual greenhouse gas emissions. The third refines methods for inverting the gas flux from seeps via passive acoustic data, paving the way for large-scale adoption of the technique.

1.2 Research Questions

The key research questions addressed in this thesis are:

- How do gas migration pathways evolve in the subsurface, from the initial injection of gas to formation of an active seep and beyond?
- How does the ebullition rate from natural seeps vary over time and how may we better predict this?
- How can we improve the passive acoustic inversion technique method for quantifying gas flux?

1.3 STEMM-CCS Project

This PhD was funded by, and run-in collaboration with, the **St**rategies for **E**nvironmental **M**onitoring of **M**arine **C**arbon **C**apture and **S**torage (STEMM-CCS) project. STEMM-CCS was an EU Horizon 2020 initiative that aimed to enable the widespread adoption of CCS sites in the marine environment through developing improved techniques for the safe monitoring of CCS sites. The project involved researchers from 14 different institutions including the University of

Southampton, the National Oceanography Centre and GEOMAR, along with industry partners such as Shell.

The STEMM-CCS project culminated in the 2019 controlled release experiment (Fig. 1.4) in the central North Sea (Fig. 1.5), which was designed to simulate a CCS leak. Over a period of 11 days a total of 675 kg of CO_2 was injected ~3m beneath the seafloor, naturally migrating though the sediment and into the water column. The area immediately surrounding the release point was continuously surveyed with an array of new and traditional techniques in order to test their potential for CCS monitoring strategies (Flohr et al., 2021). Results from this experiment are presented in Chapter 3.

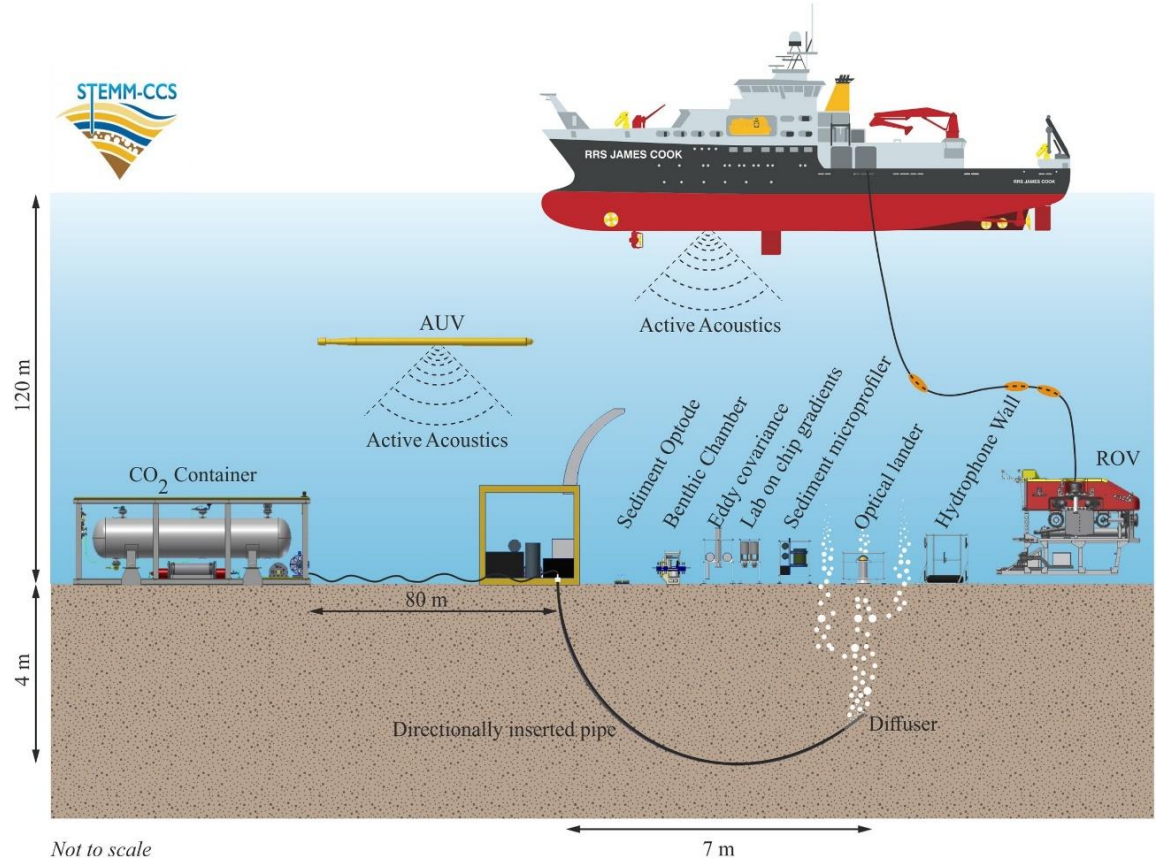

Figure 1.4: Schematic overview of the STEMM-CCS CO_2 release experiment and a selection of deployed detection methods. This experiment, and in particular the autonomous underwater vehicle (AUV) active acoustics, are featured in Chapter 3. From Flohr et al. (2021).

1.4 Bubbles in the Marine Environment

Throughout this thesis we will discuss the release of “bubbles” into the water column. A bubble here being a volumes of gas, surrounded by liquid (here, taken to be water), having surface tension forces (the so-called Laplace pressure) generated by a single wall. This should not be confused with children’s soapy bubbles, where the volume of gas is surrounded by two gas/liquid boundaries. In the marine environment bubbles can produced in all manner of ways, from fish flatulence to volcanic emissions with the entrainment of bubbles from rainfall and breaking waves having a notable effect on the marine soundscape, as is discussed in Chapter 2.

In this thesis, outside of Chapter 2, we will be focusing on the release of bubbles from sediment. The continuous passage of gas (from natural or anthropogenic sources) through the same area leads to the development of open channels (or chimneys) in the sediment which direct the flow of gas to a single localised point on the seabed, forming a seep. Such features can be found all around the world, varying in size from less than a centimetre to large pockmarks 100s of meters across (Judd and Hovland, 2007). The rate of gas release from these seep also various massively, from millilitres to 100s of litres per minute, being a product of the size and number of bubbles released per second (Judd and Hovland, 2007). While a strong emphasise has been placed on measuring the total volume of gas released from seeps, little attention is often applied to the size of the bubble released. This is unfortunate as such measurements provide useful information about how gas will be distributed in the water column via dissolution (Liang et al., 2011). Tbl. 1.3 compiles literature measurements of bubble size from natural seep around the world. In both Chapter 4 and 5 we acquire measurements of both the volume of gas and bubble sizes released from a number of seeps via optical measurements and passive acoustic inversion.

Location	Gas	Source	Bubble Radius (mm)			Measurement Technique			Refrecence
			Minumum	Maximum	Mean	Opitcal	Active Acoustic	Passive Acoustic	
Hikurangi Margin, New Zealand	CH_4	Dewatering of the lower subducting plateau	0.0001	0.001	0.004	✓	-	-	Higgs et al., 2019
Lake Baikal, Russia	CH_4	Methane hydrates in bottom sediment	1	10	3	✓	-	✓	Makarov et al., 2020
Mississippi & Green Canyon, Gulf of Mexico	CH_4	Natural Hydrocarbon seep	0.5	5	1.5	✓	-	-	Wang et al., 2015
"	"	"	0.5	2.5	1	✓	-	-	Johansen et al., 2017
"	"	"	1	4.5	2	✓	-	-	"
"	"	"	1	5	2.5	✓	-	-	"
Panarea, Mediterranean Sea	CO_2	Underlying magma chamber	10	25	16	-	-	✓	Li et al., 2020
"	"	Underlying magma chamber	1	8	4	✓	-	✓	This thesis, Chapter 5
Coal Oil Point Field, California	CH_4	Natural Hydrocarbon seep	0.8	5	1.5	✓	-	-	Leifer et al., 2009
"	"	"	1.4	4	2	✓	-	✓	Leifer and Tang 2006
"	"	"	1.2	4	2.8	✓	-	-	Jordan et al., 2020
"	"	"	0.5	2.5	1.6	✓	-	-	"
"	"	"	1	2.7	1.5	✓	-	-	"
"	"	"	0.5	3.5	1.6	✓	-	-	"
Cascadia continental margin, USA	CH_4	Natural Hydrocarbon seep (pockmark)	4	10	7	-	✓	-	Salmi et al., 2011
"	"	"	1	4.5	1.5	-	✓	-	"
"	"	"	4	10	6	-	✓	-	"
Goldeneye Site, North Sea	CO_2	Controlled Release Experiment	2	10	1.7	✓	-	✓	Li et al., 2021
Utsira High, North Sea	CH_4	Abanonded Hydrocarbon Wells	1.7	3.5	2.6	✓	-	-	Vielstadte et al., 2015
Witch Ground Basin, North Sea	CH_4	Natural Hydrocarbon Seep, Scanner Pockmark	0.01	15	0.03	-	✓	-	Li et al., 2020
Lake Constance, Austria/Germany	CH_4	Natural Biogenic Seeps	2	12	7	✓	-	✓	This thesis, Chapter 4

Table 1.3: Summary of bubble sizes as measured from various seabed seeps around the world (Leifer and Tang, 2007; Leifer et al., 2009; Salmi et al., 2011; Vielstädte et al., 2015; Wang and Socolofsky, 2015; Johansen et al., 2017; Higgs et al., 2019; Jordan et al., 2020; Li et al., 2020a, 2020b, 2021; Makarov et al., 2020).

1.5 Thesis Structure

Chapter 2 – Ambient Bubble Acoustics – Seep, Rain and Wave Noise

This chapter provides an overview of bubbles as sound sources in the water column, as summarised in the literature. It discusses the mechanics behind an individual bubbles' acoustic signature (in particular the Minnaert equation and other relevant properties), before discussing the formation of bubbles from subsurface gas migration, rainfall, and wave action, characterizing the acoustic nature of each process. The primary focus of this chapter is to outline the physical mechanisms behind the sound resulting from bubble generation from each of these sources. This chapter has been submitted for publication as part of an upcoming American Geophysical Union monograph, "Noisy Oceans: Monitoring Seismic and Acoustic Signals in the Marine Environment".

Chapter 3 – Time-lapse imaging of CO_2 migration within near-surface sediment during a controlled sub-seabed release experiment

The first major data analysis component of this thesis uses repeated high-resolution seismic reflection data to image the migration of CO_2 gas during the STEMM-CCS release experiment in the central North Sea (Fig. 1.5).

The chapter details observations of temporal changes in seismic reflectivity, attenuation, unit thickness and the bulk permeability of sediment as well a detailed gravity core analysis. Using these observations, a four-stage model of the evolution of gas migration in shallow marine sediments is developed:

- Proto-migration
- Immature Migration
- Mature Migration
- Pathway Closure

This enhanced understanding of the migration of free gas in near-surface sediments will help improve methods of detecting and quantifying gas in subsurface marine sediments. This work has been accepted for publication in the International Journal of Greenhouse Gas Control.

Chapter 4 – Temporal variability of ebullition in Lake Constance – prediction via lakebed pressure

The second major data analysis component of this thesis involves long term observation of ebullition rates in Lake Constance, central Europe (Fig. 1.5). In this case, physical funnels and acoustic hydrophones were positioned above natural methane seeps for a ~3-month period. This project was a joint venture between myself and Ramona Ragg, a PhD student at Konstance University. Ragg oversaw the field campaign and the collection of physical flux data while I oversaw the collection of acoustic and optical data.

This chapter demonstrates a significant negative correlation between gas flux and in-situ pressure, control predominantly regulated by lake water level (hydrostatic pressure) on monthly timescales, while smaller fluctuations on daily to weekly periods are controlled by atmospheric pressure variations. We also demonstrate that long-term ebullition emissions are best estimated by quantifying the relationship between in-situ pressure and gas flux, predicting subsequent (or past) emissions via this empirical relationship. This approach is more accurate than extrapolating estimates from short-term observations and is easily achievable with commonly available water level and weather station data. This work has been submitted for publication in the Journal of Biogeosciences with myself and Ragg as joint lead-authors. I led the writing, while Ramona created the majority of the figures.

Chapter 5 – Refining methods of acoustic gas flux inversion – investigation into the initial amplitude of bubble excitation

The third and final major data analysis component of this thesis details an experiment conducted in the AB Wood Tank, Southampton (Fig. 1.5) into the relationship between the equilibrium radius of a bubble and the initial amplitude of the oscillation it undergoes when released into the water column. The initial amplitude of oscillation has until this point been an unknown parameter central to the passive acoustic inversion technique. Fitting a first order

polynomial to this data set and substituting it into existing passive acoustic inversion models we observe a significant reduction in the uncertainty of flux estimates.

When using this technique to invert the flux from a natural CO_2 seep in Panarea (Fig. 1.5), the need to account for the effects of bubble merging and fragmenting was identified. This refinement of the inversion technique will facilitate its large-scale adoption as a field technique. This work will be submitted for publication in Geophysical Research Letters.

Chapter 6 – Conclusions

The final portion of this thesis summarises the major findings of the preceding chapters, discusses the thesis research question presented above, and outlines avenues for future work.

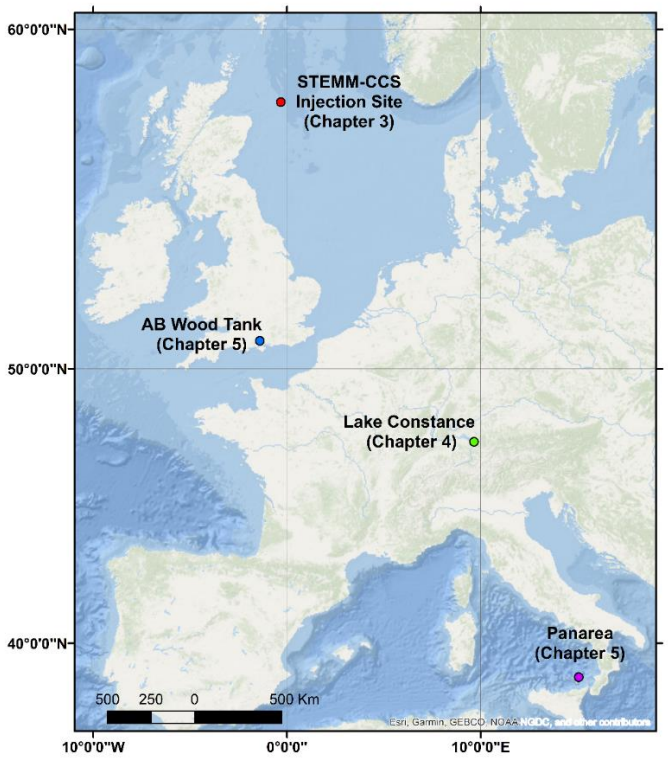

Figure 1.5: Location of each major experiment site discussed in this thesis. From North to South these are: (Red) STEMM-CCs injection site in the central North Sea featured in Chapter 3, (Blue) the AB Woods Tank in Southampton (UK) featured in Chapter 5, (Green) Lake Constance on the German/Austrian/Swiss border featured in Chapter 4, and (Purple) Panarea (Italy) in the southern Tyrrhenian Sea featured in Chapter 5.

Chapter 2 Ambient Bubble Acoustics – Seep, Rain, and Wave Noise

This chapter discusses the sounds emitted by gas bubbles when they are generated underwater. Here we consider bubbles to be volumes of gas, surrounded by liquid (here, taken to be water), having surface tension forces (the so-called Laplace pressure) generated by a single wall, and so are distinguished from the soap bubbles familiar in children's games, where the volume of gas is surrounded by two gas/liquid boundaries (Leighton, 1994). In comparison with other acoustic sources, such as marine mammals, ships and tectonic events, a single bubble may seem insignificant. Indeed, without ideal conditions it can be difficult to observe the sound of a single bubble from a distance of more than a few tens of centimetres. However, natural processes rarely produce single bubbles, and in fact can generate them in their millions at which point the sound generation is significant. With the formation of bubbles as a result of gas seeps, rainfall and breaking waves being a major component of ambient noise in the marine environment and can even alter the propagation of sound waves from other sources. This chapter focuses on the passive emissions of bubbles as they are formed, released, or injected into water, and here the volume pulsations are linear.

In this chapter we will discuss the mechanics behind an individual bubbles' acoustic signature, in particular the Minnaert equation and other relevant properties, before discussing the formation of bubbles from subsurface gas migration, rainfall and wave action, characterizing the acoustic nature of each process. The primary focus will be on the sound resulting from bubble generation from each of these sources. A number of different units are used to define each acoustic source, while this may appear confusing and make direct comparison difficult, this is done to be consistent with the literature. The topics covered here are broad, so the approach taken is to summarise the key principles and state of the field, while providing substantial linkage to the literature.

2.1 Bubbles as Acoustic Sources

While bubbles may be found throughout the water column and produced in all manner of ways, from fish flatulence to volcanic emissions, it is only the initial formation of the bubble near the source that is of interest in passive acoustics. Additionally, only a few sources of bubble production are common and large enough to warrant a full discussion, namely bubbles released from gas seeps on the seabed and those produced by either rainfall or breaking waves at the surface. The following section will discuss the initial release of gas bubbles into a body of water and the resulting acoustic signal. These are the fundamental principles behind bubble acoustics and are directly applicable to all initial sources of bubble production.

2.1.1 The injection of a gas bubble

A bubble does not instantly appear fully formed in the water column. The gas is injected into the body of water over a very short period of time. While there are several processes by which this injection can happen, the core principles remain the same; a small volume of gas from a larger reservoir encroaches into a body of water with the two volumes of gas being connected via a thin neck. As the small volume of gas extends further and further into body of water the neck is stretched thinner and thinner, eventually snapping, and releasing the small volume of gas into the water as a distinct bubble. It is the snapping of the bubble neck that is of most interest to us as it results in a jet of water being momentarily propelled into the bubble, triggering an initial volume oscillation. This volume oscillation is ultimately what results in the acoustic signal of a bubble release (Longuet-Higgins et al., 1991; Leighton, 1994; Czerski and Deane, 2010).

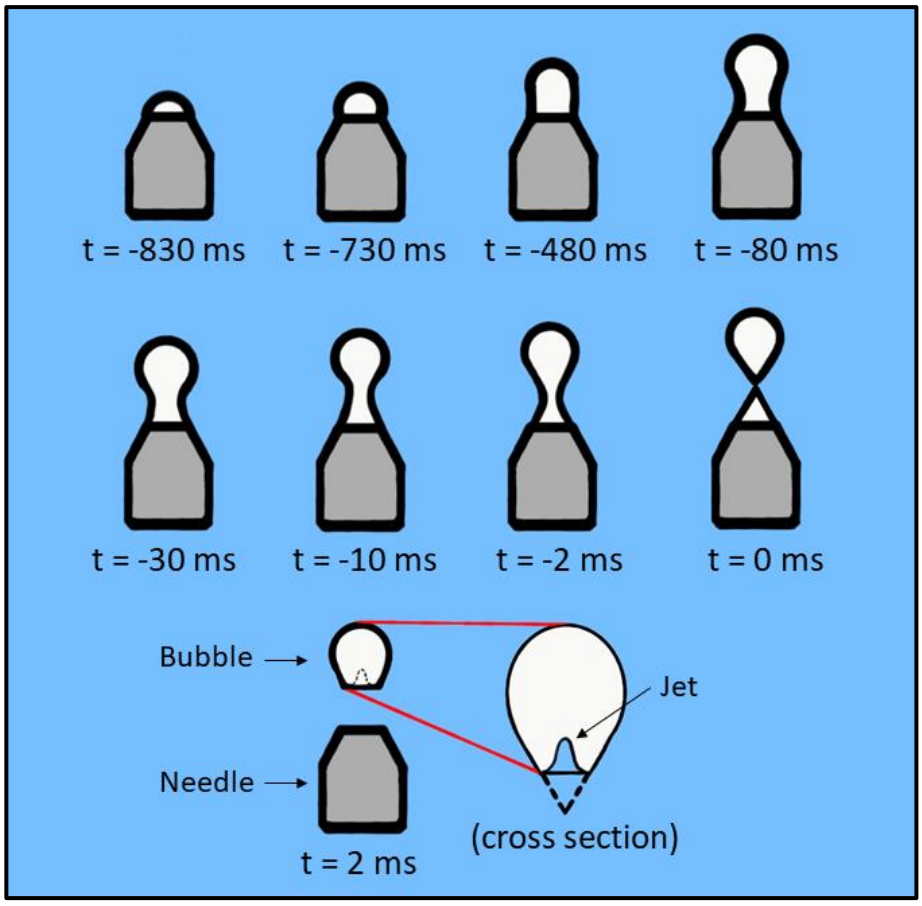

Figure 2.1: A bubble emerging from an underwater nozzle of internal diameter 4.00 mm. As the bubble grows a neck forms between it and the injection nozzle, the neck eventually snaps releasing the bubble and propelling a jet of water into the it. This jet decreases the volume of the bubble and causes it to undergo simple harmonic motion. Times are given in milliseconds relative to the moment the bubble is detached (i.e., the neck snaps), note these timings will change with nozzle size and gas flow rate. Adapted from Longuet-Higgins et al., (1991) and Czerski & Deane et al., (2010).

The easiest way to understand the process of bubble release is to study gas being injected into a body of water via a needle, as seen in Fig. 2.1. Theoretical calculations have been used to deduce the stages of bubble injection via a needle, reinforced by lab observations (Longuet-Higgins et al., 1991). These stages are best described in relation to the radius of curvature (the radius of a circular arc that best approximates the curve) of the meniscus at the top of the bubble, the scales are dimensionless. The bubble initially grows from the surface of the nozzle as gas flows through it, the radius of curvature decreasing from 1 to <0.5 with volume increasing steadily (t = -830 ms in Fig. 2.1). The bubble profile changes from near horizontal to semi-circular in shape. Near the moment *the tangent to the meniscus at the point of attachment to the nozzle* becomes

vertical (t = -730 ms in Fig. 2.1), the volume increases rapidly while the radius of curvature remains roughly constant (t = -480 ms in Fig. 2.1). Subsequently the volume and radius of curvature increase steadily. Here a “neck” begins to form, this is the narrowest part of the bubble profile, located between the nozzle and the main body of the bubble (t = -80 ms in Fig. 2.1). Once the radius of curvature equals ~0.655 the *tangent to the meniscus at the point of attachment* (now the neck of the bubble) becomes near vertical again and there is a second sharp increase in volume. The bubble now has a distinct diapir like shape (t = -2 ms in Fig. 2.1). The volume of gas in the bubble reaches a maximum, beyond this point the bubble in considered unstable. Further air forced into the bubble causes it to detach, a snapping of the neck releases the bubble allowing it to rise upwards (t = 0 ms in Fig. 2.1) (Longuet-Higgins et al., 1991). The upper half of the neck recedes back into the bubble as a jet of water propels itself inwards (t = 2 ms cross section in Fig. 2.1), this decreases the volume of the bubble resulting in a volume oscillation (Longuet-Higgins et al., 1991; Leighton, 1994; Czerski and Deane, 2010).

2.1.2 Bubbles as simple harmonic oscillators

Immediately after its release into the water column, regardless of the means of production, a bubble begins to pulsate. The bubble itself might undergo a wide range of oscillatory changes in shape, but these can be decomposed into a summation of spherical harmonic pulsations, and only one of these (the zeroth order) changes bubble volume to first order, and hence changes the gas pressure to first order (at low Mach numbers), and so couples to acoustic fields (Leighton, 1994). Therefore, despite the fact that the bubble will often depart from sphericity, with a few notable exceptions that will not be discussed further in this chapter (Phelps et al., 1997), it is appropriate when discussing the interaction with sound fields at low Mach numbers to refer to the pulsations of a spherical bubble. This oscillation approximates a simple harmonic oscillator at low amplitudes, occurring at the natural frequency of the bubble (Leighton, 1994). It is possible to derive the relationship between the radius of a bubble and the

frequency of its initial free oscillations by assuming there are no dissipative losses, e.g., through viscosity or thermal conduction, via consideration of the flow between potential and internal energy. The natural frequency of bubble oscillation is known the “Minnaert frequency” (Minnaert, 1933).

As a simple harmonic oscillator, the pulsation of a bubble is analogous to the classic bob on a spring system, of unloaded length l_0 and loaded length l. The walls of the bubble are the bob weight and the gas within the bubble is the spring, as demonstrated in Fig. 2.2a. The displacement ε from the equilibrium position corresponds to displacement of the bubble wall R_ε between its equilibrium radius R_0 (the bob at $l - l_0$) and its present radius R at any given moment (the bob at $l + \varepsilon - l_0$), see Fig. 2.2. The gas pressure following compression or expansion act to restore the bubble to its equilibrium position, so is analogous to the spring stiffness in the spring-bob example. However, it is important to note that the gas in the bubble is less dense than the surrounding medium (unlike the bob in air). So, while in the spring-bob system inertia and momentum are dominated by the bob it is the inertia of the water surrounding a bubble which dominates in the bubble system, the mass of the gas being negligible.

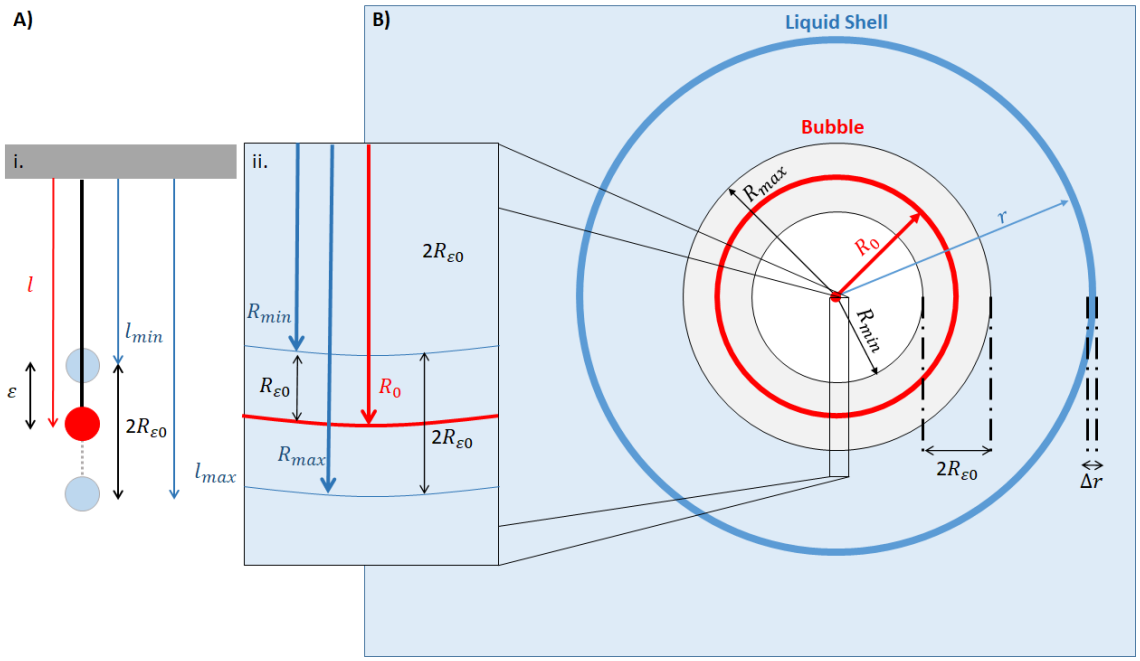

Figure 2.2: A) diagram comparing simple harmonic oscillators i. a spring bob system ii. a bubble wall moving B) diagram of a bubble of radius R_0 the wall of which is undergoing small amplitude oscillations of amplitude $R_{\epsilon 0}$. It is surrounded by spherical shells of liquid, one of which has a radius of r and a thickness of Δr.

It is this final stage of the bubble formation that triggers the simple harmonic motion of a bubble (Leighton, 1994; Czerski and Deane, 2010). The snapping of the neck triggers an initial volume oscillation that acts as an exciting force causing the bubble to emit sound at its natural frequency. We assume this initial driving impulse is of an infinitesimally small duration meaning that while the bubble undergoes subsequent oscillation it effectively experiences no driving force.

With this idea of a bubble as a simple harmonic oscillator we can describe the shape of the bubble over time. Imagine a bubble (Fig. 2.2b) with a mean radius of R_0 that remains spherical at all times while undergoing a volume oscillation at a frequency of ω_0. The maximum displacement of the bubble wall is $R_{\varepsilon 0}$ so that $R_{max} = R_0 + R_{\varepsilon 0}$ and $R_{min} = R_0 - R_{\varepsilon 0}$. Thus, the bubble radius R at any time t can be express as the real part of

$$R = R_0 + R_\varepsilon(t) = R_0 + R_{\varepsilon 0} e^{i\omega_0 t}. \quad (2.1)$$

The displacement of the bubble wall R_ε from equilibrium over time describes a motion

$$R_\varepsilon = -R_{\varepsilon 0} e^{i\omega_0 t}. \tag{2.2}$$

2.1.3 Minnaert frequency

With a description of the motion of the bubble wall over time we can describe the flow between kinetic and potential energy. From here we can apply the concept to conservation of energy in order to derive the Minnaert (or natural) frequency of a bubble (Minnaert, 1933; Leighton, 1994).

$$f_M = \frac{1}{2\pi R_0}\sqrt{\frac{3\kappa p_0}{\rho}}, \tag{2.3}$$

ρ being the density of water, p_0 being the hydrostatic liquid pressure outside the bubble and κ being the polytropic index (which takes a value equal to unity when the gas behaves isothermally and equals the ratio of the specific heat of the gas at constant pressure to that at constant volume, when the gas behaves adiabatically). A full derivation of Minnaert frequency can be found in the SI of this chapter.

The Minnaert equation demonstrates that the frequency of a bubble's oscillation is inversely proportional to its equilibrium radius R_0. As the other factors are fairly consistent or easily predictable (polytropic constant, density of water, water pressure outside of the bubble) it is relatively easy to measure the size of a bubble based on its acoustic signal. As a general rule of thumb for bubbles near the surface the radius in mm multiplied by the frequency in kHz is equal to approximately 3 i.e., a 1 mm radius bubble has a 3 kHz frequency, a 1.5 mm radius bubble has a 2 kHz frequency, and a 3 mm radius bubble has a frequency of 1 kHz

Once a bubble starts oscillating it begins to lose energy in three ways. Firstly (and most importantly for us) energy is radiated from the bubble through acoustic waves (radiation damping). Secondly energy is lost through conduction between the gas and the surrounding liquid (thermal damping). Finally, energy is lost moving the bubble wall itself (viscous damping) (Leighton, 1994). It is because of these factors that the bubble can be considered lightly damped (Ainslie and Leighton, 2011). This damping is typically described by the "quality factor" of the bubble, Q, which is approximately defined as the ratio of the initial energy to the energy lost in one radian cycle of oscillation (Walton et al., 2005). We will avoid a full discussion on the damping constant of a bubble, see Ainslie and Leighton (2011) for this, and will note that the oscillation of millimetre sized bubbles decays exponentially over ~10-30 of milliseconds (Leighton, 1994) and varies with gas content i.e., for air Bubbles $Q = 34$ while for pure methane bubbles and carbon dioxide bubbles $Q = 24$ and 29 respectively (Walton et al., 2005).

The polytropic adaptation of the Minnaert equation was first used in the 1980s to infer the size distribution and number of bubbles formed in the natural world, in waterfalls and streams (Leighton and Walton, 1987), and over subsequent years this method was extended to do the same for bubbles entrained by breaking waves (Medwin and Beaky, 1989) and rainfall (Pumphrey and Crum, 1990). The method works well when the 'signature' passive emission from each bubble is clearly separated in time from others, however this method of counting and sizing bubbles becomes more difficult as the signatures from each bubble get closer in time and overlaps, and while signal processing techniques can alleviate the problem (Leighton et al., 1998), eventually the degree of overlap becomes so great that this technique must be replaced by a spectral approach (discussed later) (Leighton and White, 2012).

A recording of a bubble signature, as seen in Fig. 2.3, shows a sinusoidal wave which decays exponentially indicative of a lightly damped oscillator with a frequency consistent with that predicted by the Minnaert equation (Eq. 2.3). Though it should be noted that as the sound generated by a bubble is an exponentially decaying sinusoid, the sound will contain a range of frequencies and the spectral profile of each bubble will be Lorentzian (Leighton, 1988), centred

around the natural frequency (Leighton, 1994). The bubble seen in Fig. 2.3 was released at a water depth of 2.5 m has a frequency of 0.38 kHz. Using Eq. 2.3 this corresponds to a radius of 9.6 mm.

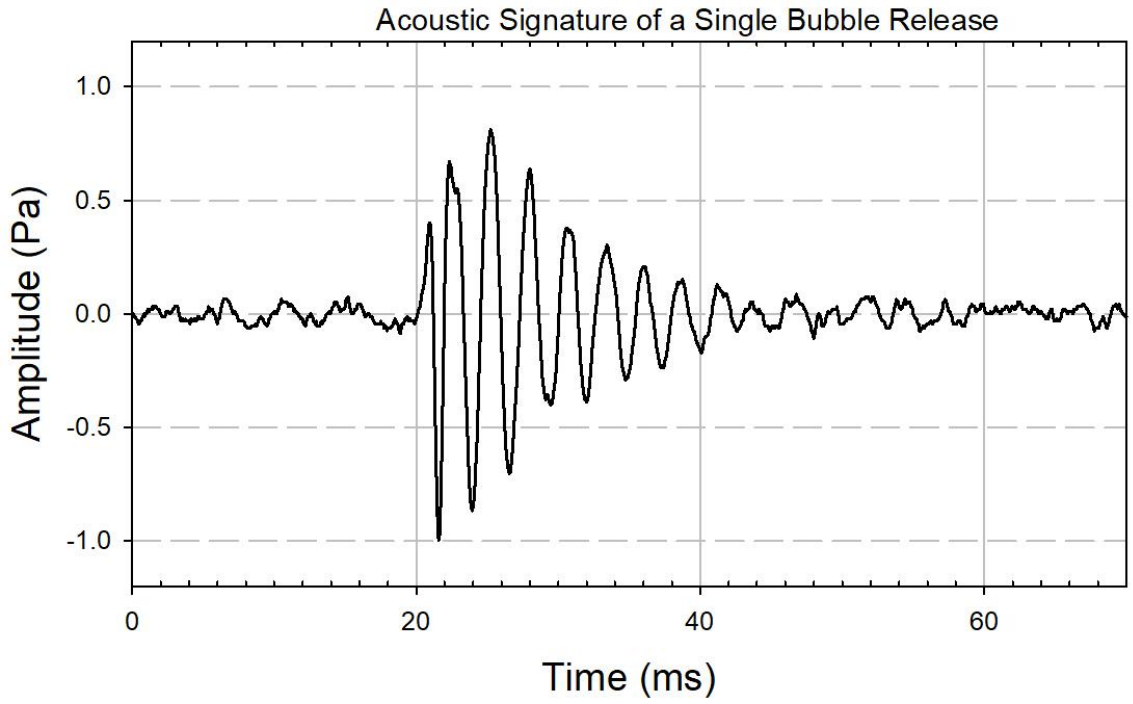

Figure 2.3: Sonogram displaying the typical acoustic emission of a bubble as recorded by a hydrophone. Here the bubble was released from sediment at a water depth of 2.5 m, 25 cm from the hydrophone. The bubble became detached at around 20 ms, triggering simple harmonic oscillation resulting in exponentially decaying sinusoidal wave. The bubble oscillates with a frequency of 0.38 kHz (T = 2.6 ms) which we can inverted via the Minnaert equation (Eq. 2.3) to indicate a radius of 9.6 mm.

The Minnaert equation was later adapted to include the effects of vapour pressure p_v, surface tension σ, and shear viscosity η and so is more correctly presented as (Leighton 1994; Leighton 2004);

$$f_M = \frac{1}{2\pi R_0\sqrt{\rho_0}}\sqrt{3\kappa\left(p_0 - p_v + \frac{2\sigma}{R_0}\right) - \frac{2\sigma}{R_0} + p_v - \frac{4\eta^2}{\rho_0 R_0^2}}. \quad (2.4)$$

Bubbles generated near the ocean surface will actually have a natural frequency f_0, which is slightly higher than that specified by the Minnaert equation as a consequence of the reduced inertia of the fluid near the surface. A similar effect occurs if the water surrounding the bubble also contains bubbles in close proximity. Strasberg calculated the effect on the frequency showing that (Strasberg, 1953).

$$f_0 = \frac{f_M}{\sqrt{1 - \left({R_0}/{2h}\right) - \left({R_0}/{2h}\right)^4}}, \tag{2.5}$$

where h is the distance from the *centre* of the bubble to the surface of the water. As h is always greater than R_0, the denominator is always less than 1 and so, the oscillation of a bubble in the near surface is always slightly greater than that predicted by the Minnaert equation. For example, a bubble at a depth $h = 4R_0$ will have a frequency ~7% higher. Alternatively, one should also be able to see that when $h \gg R_0$, i.e., the bubble is a few tens of centimetres or more beneath the water's surface, the frequency of a bubble is equal to the Minnaert frequency.

$$f_0 = f_M \text{ for } h \gg R_0. \tag{2.6}$$

Another notable deviation from the Minnaert equation occurs when bubbles are generated (nearly) simultaneously in close proximity, as is the case with wave generated bubbles. The bubbles are linked by acoustic and hydrodynamic interactions resulting in coupled oscillator systems that tend to oscillate at much lower frequencies than the natural frequency of any individual bubble within it. In effect, a cloud of small bubbles can emit an acoustic signature similar to that of a much larger bubble. A region of bubbly water containing a total of N_b identical bubbles (each having a radius R_0 and a natural frequency of f_0) composes an air water mixture with a void fraction VF. If this bubbly water was submerged in bubble-free water and the

boundary between the two were assumed to be rigid (a poor assumption but a useful starting point), then the modal frequency f_n of a bubble cloud can be given by (Lu et al., 1990)

$$f_n = f_0 \frac{n}{N_b^{1/3} \cdot \{VF\}^{1/6}},$$

(2.7)

where n is the mode of oscillation. It should be apparent that for any cloud with more than a few hundred bubbles the lower order modal frequencies will be lower than the natural frequency of the individual bubbles. For example, a 10 cm cloud of 1000 bubbles will have a 1st order modal frequency 1/3 that of the bubble oscillations (Leighton, 1994). The greater the number of bubbles in the same space, the lower the modal frequency. Obviously, bubble clouds do not have rigid walls, but the general trend holds true with complexities in cloud geometry and bubble size distribution being a greater source of error. In practice this means that if bubbles exist in clouds, then the emission, and perhaps more prominently the scattering, of sound by the cloud of bubbles, will contain elements at this cloud frequency, in addition to the signals of the individual bubble resonances themselves (Leighton, 1994).

In summary the release of a bubble into the water column causes it to undergo simple harmonic oscillation. The resulting acoustic signal is an exponentially decaying sinusoidal wave at the natural (or Minnaert) frequency of the bubble, which is approximately inversely proportional to its equilibrium radius. Measuring the volume of gas release at slow sources of bubble production (a few Hz) acoustically is relatively trivial. One simply needs appropriate recording equipment and an understanding of the basic field/lab conditions (water depth etc.) to individually count and size each bubbles signal without needing any knowledge of the energy emission from an individual bubble (Leighton and White, 2012). Indeed this 'signature' method of flux measurement can even be used as an undergraduate lab experiment. However, as we will discuss later measuring the volume of gas released becomes increasingly difficult as the rate of bubble production increases.

2.2 Subsurface Gas Release

Gas can be generated below the seabed from a number of different sources namely thermogenic, biogenic, and anthropogenic. When this gas reaches the seabed, it will escape upwards into the water column by the formation of bubbles (Judd, 2003; McGinnis et al., 2006; Knittel and Boetius, 2009). This can have a major impact on ocean chemistry via dissolution and is a poorly understood part of the global carbon cycle (Johnson, B. D., Boudreau, B. P., Gardiner, B. S., and Maass, 2002; Jain and Juanes, 2009; Johnson et al., 2012; Roche et al., 2020). Additionally, the release of each bubble produces an acoustic signal which can affect soundscape in local areas (Leighton, 1994; Leighton and White, 2012; Maksimov et al., 2016). The sound is emitted as soon the bubble detaches from the seafloor and lasts ~20 ms, which given that bubbles tend to rise upwards of a speed of 20-30 cm/s confines the production to within ~5 mm of the seafloor. We will first describe the passage and release of a single bubble before discussing localised seeps, their resultant signal and flux inversion techniques. The following is applicable to bubbles of any gas type, the Minnaert frequency varying only slightly as described by Eq. 2.4.

In a typical near-surface marine sediment, the pores between grains are saturated with water. The introduction of gas, for example from an underlying fault, slowly invades the surrounding pores, displacing the water. This intrusion can occur either by capillary invasion or by fracture opening (Johnson, B. D., Boudreau, B. P., Gardiner, B. S., and Maass, 2002; Jain and Juanes, 2009; Johnson et al., 2012). The difference in density between the gas and the surrounding medium, creates a buoyancy force which typically causes the gas to rise upwards (Boudreau et al., 2005; Algar et al., 2011; Boudreau, 2012). When gas reaches the seabed, it will continue to rise upwards due to the buoyancy forces. The sediment pores act like a kind of “nozzle”, akin to a needle in a test tank, through which the bubble is injected into the water column (Leighton and White, 2012, Roche et al., 2021). The bubble will escape into the overlying water when the buoyancy forces acting on it overcome the adhesive like forces attaching it to the sediment.

The passage of gas through the upper few centimetres of the seabed can cause a weak oscillatory signal, audible in the water column, possibly as the grains rearrange to create an orifice for the bubble beneath the surface (Leighton, 1994). Vazquez et al., (2015) were able to observe this event using synchronous high-speed video and acoustic recordings of gas migrating through granular sediment. The signal appears unpredictable and is expected to vary with grain size, grain type, bubble size, water pressure etc. Indeed, there is some experimental evidence indication that the sound is absent for fine silts and coarse pebbles. As the magnitude of this precursor signal is smaller than that of subsequent bubble oscillation the phenomenon remains largely unexplored. Thus, the acoustic signature of a single bubble being released from sediment can be defined as an exponentially decaying sinusoidal wave resulting from bubble oscillation (Leighton and Walton, 1987) potentially preceded by a weak unpredictable oscillatory signal in certain sediment types (Vazquez et al., 2015), as seen in Fig. 2.4.

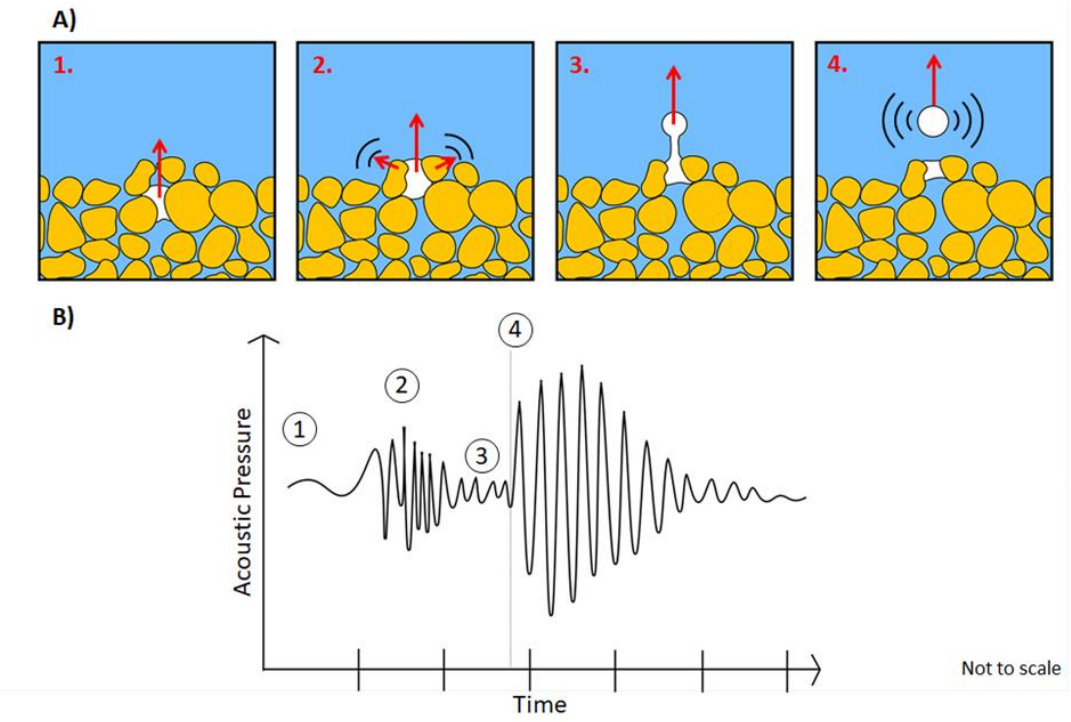

Figure 2.4: A) the release of a bubble from granular sediment and B) the corresponding acoustic signal. Note (2) the chaotic weak signal resulting from the rearrangement of grains as the gas reaches the seabed and (4) the stronger distinct acoustic signature of the bubble being released into the water column. Adapted from Vazquez et al., (2015).

2.2.1 Gas seep acoustics

The continuous passage of gas through the same area may cause the development of open channels (or chimneys) in the sediment which direct the flow of gas to a single localised point on the seabed, forming a seep (Hovland, 2002; Suess, 2014; Coughlan et al., 2021). A subsea gas seep is broadly defined by the continuous release of gas from the seabed into the water column. There is no set magnitude for the flux of gas from a seep (Hovland, 2002; Suess, 2014; Coughlan et al., 2021), meaning the term encompasses seeps that release tens to millions of bubbles per minute. Similarly, there is no strictly defined time scales for being continuous, some seeps are born and die within a few hours, some are only active for certain times of the day or year while others have been active for centuries (Böttner et al., 2019; Li et al., 2020b; Coughlan et al., 2021). It is also worth noting a seep does not have to be in sediment, it may also come from exposed bedrock or even manmade features such as leaking pipes. The term pockmark is often synonymous with gas seeps in sediment, though strictly speaking the term only defines the depressions created in the seabed by the gas release (Böttner et al., 2019; Coughlan et al., 2021).

The size of a bubble released from the seabed is difficult to predict. In a lab the size of a bubble released from a needle is generally considered a factor of the size of the nozzle, the gas injection pressure, and the overlying water pressure, although even these have limited control of bubble size (Leighton et al., 1991; Longuet-Higgins et al., 1991). Even in a controlled setting it is difficult to regularly produce identically sized bubbles, making bubble size highly variable in the field. Assuming the pores between grains act as nozzles then one might anticipate that larger pore spacing, that are generally associated with the larger and more rounded the grains, would generate larger the bubbles. However, when open conduits form in sediment, pore size becomes less important in favour of conduit size which can vary significantly based on numerous factors including the age of the chimney. Consequently, bubble size distributions are unique for each seep, indeed the exact bubble size distribution (and thus gas flux) is likely to change over time as the underlying conduits evolve and the overlying water pressure fluctuates with tidal and seasonal variations (Boles et al., 2001; Klaucke et al., 2010; Bergès et al., 2015; Leifer, 2015;

Wiggins et al., 2015; Römer et al., 2016; Scandella et al., 2016; Riedel et al., 2018; Sultan et al., 2020). Gas flux from underwater seeps can also vary as a result of underlying causes such as seabed temperature, seismic or volcanic activity (Leifer and Patro, 2002; Esposito et al., 2006; Ostrovsky et al., 2008; Muyakshin and Sauter, 2010; Leifer, 2015; Li et al., 2020b). In deep marine settings bubble sizes have commonly been observed between 1 and 6 mm in radius (Bergès et al., 2015; Li et al., 2020a) while shallower waters (<10 m) have been observed to contain larger bubbles greater than 10 mm in radius (Leighton, 1994; Leighton and White, 2012; Li et al., 2020b), though this trend is far from a rule and exceptions are plentiful.

The acoustic signature of a seep is thus defined by its bubble generation rate i.e., the rate at which bubbles of different sizes are released. Unfortunately, as every seep has a unique bubble generation rate it is difficult to define a general rule for the passive acoustic emissions. In the simplest case of a “slow seep” releasing a few bubbles a second, its acoustic emission can be defined by the continuous release of bubbles, i.e., a continuous repetition of signal seen in Fig. 2.2 (Greene and Wilson, 2012; Leighton and White, 2012). Ultimately these signals are weak and have little impact on the marine soundscape due to the flux rates being so low meaning they are of little interest to many researchers.

Larger seeps with higher gas flux rates generate stronger signals which can be observed at greater distances and may have a noticeable impact on ocean chemistry. However, as the frequency of bubble release increases with flux rate, eventually the acoustic signals of each release begin to overlap making it impossible to distinguish individual bubble oscillations (Bergès et al., 2015; Chen et al., 2016; Roche et al., 2019).

By considering the combined signal of multiple bubble releases Leighton and White (2012) derived the power spectral density $S(\omega)$ of the far field acoustic signature of a gas seep at some distance r;

$$S(\omega) = \int_0^\infty B(R_0)|X_b(\omega, R_0)|^2 \, dR_0,$$

(2.8)

where ω is the angular frequency, $B(R_0)$ is the bubble size distribution as a function of R_0 defined such that $\Psi(n) = \int_{R_1}^{R_2} B(R_0)dR_0$ represents the number of bubbles generated per second with a radius between R_1 and R_2 i.e., the bubble generation rate, δ_{tot} is the total damping constant for pulsation at resonance and

$$|X_b(\omega, R_0)|^2 = R_{\epsilon 0i}^2 \frac{\omega_0^4 R_0^4 \rho^2}{r^2} \left(\frac{4[(\omega_0 \delta_{tot})^2 + 4\omega^2]}{[(\omega_0 \delta_{tot})^2 + 4(\omega_0 - \omega)^2][(\omega_0 \delta_{tot})^2 + 4(\omega_0 + \omega)^2]} \right).$$

(2.9)

The important unknown in this equation being the initial amplitude of displacement of the bubble wall at the start of the emission ($R_{\epsilon 0i}$) [not to be confused with $R_{\varepsilon 0}$ the maximum displacement of bubble wall from the equilibrium radius]. There is strong evidence to suggest this is a function of the equilibrium bubble radius (R_0). However, this exact relationship is yet to be defined. Consequently, many studies have elected to treat $R_{\epsilon 0i}/R_0$ as a constant existing somewhere between 1.4×10^{-4} and 5.6×10^{-4}, based on experimental observations(Leighton and White, 2012). Though it should be stressed this is a pragmatic choice with no theoretical foundation. It is important to note that the above formulation excludes the signal from the rearrangement of grains prior to a bubbles release. However, this is reasonable as 1) the signal is very weak (Vazquez et al., 2015) and 2) seeps with a higher flux contain open conduits that do not require grains to be rearranged to facilitate the migration of gas (Roche et al., 2020).

This spectral approach allowed Leighton and White to invert the signal from a given gas seep (at a known distance from a hydrophone) to determine the number of bubbles of various sizes released within a given period, providing them with an estimate of gas flux (Leighton and White, 2012). In replacing the signature method for counting and sizing bubbles in circumstances

where their passive acoustic emissions overlapped, they drew particular attention to the lack of knowledge about the energy of an individual bubbles' emission. While the signature method had managed to bypass this unknown their spectral method could not. Whilst the spectral method had the power to count and size bubbles when the signatures overlapped, they noted that the reliance on literature values for the energy released by a bubble was the greatest source of uncertainty, particularly as the energy associated with the release of a given bubble is likely to vary with the mode by which it is entrained (injected by a needle, or through sediment, via a gas pipe leak or entrained in the upper ocean by rainfall or breaking waves), and the depth at which it is entrained. In simple terms, if the count of bubbles of a certain size is based on the energy detected in a given frequency band, then if the acoustic energy in that band is divided between the bubbles contributing to it, the estimation calculates fewer bubbles were entrained the more acoustic energy is contained in each bubble signature (Leighton and White, 2012). Further complications were identified, in that a given injection process can cause the bubble to fragment after release, or merge with other bubbles, and this can lead to the injection of a single bubble generating multiple signatures (Leighton et al., 1991). Despite all of this, to date the use of the spectral method in the field has proven effective, providing continuous estimates of gas flux over extended periods of time validated by intermittent physical measurements. However, a need to reduce the uncertainty in these measurements is continually noted (Bergès et al., 2015; Roche et al., 2019; Li et al., 2020b).

Given the highly variable nature of seafloor gas seeps, particularly in regard to the size of the bubbles and their rate of release, it is difficult to give a general impression of their contribution to the marine soundscape. In order to do so here we use the above equations to simulate the sound pressure level (SPL) of a seep venting gas at the rate of 10, 100, 1000 and 10,000 L/min assuming a log normal bubble size distribution between 0.5 and 10 mm radius. The results are displayed in Fig 2.5 alongside the SPL of various intensities of wind and rain generated bubble noise. We would emphasise that these graphs are meant to serve only as an approximate guide to the potential effect natural seeps can have on the marine soundscape. Here we see the

signal is confined mainly between 1 to 10 kHz (a result of the selected bubble size distribution) with the magnitude of the signal increasing in line with rate of gas flux. A maximum amplitude of 97 dB re 1µPa^2/Hz is seen at 10,000 L/min, well in excess of wind and rain generated bubble noise.

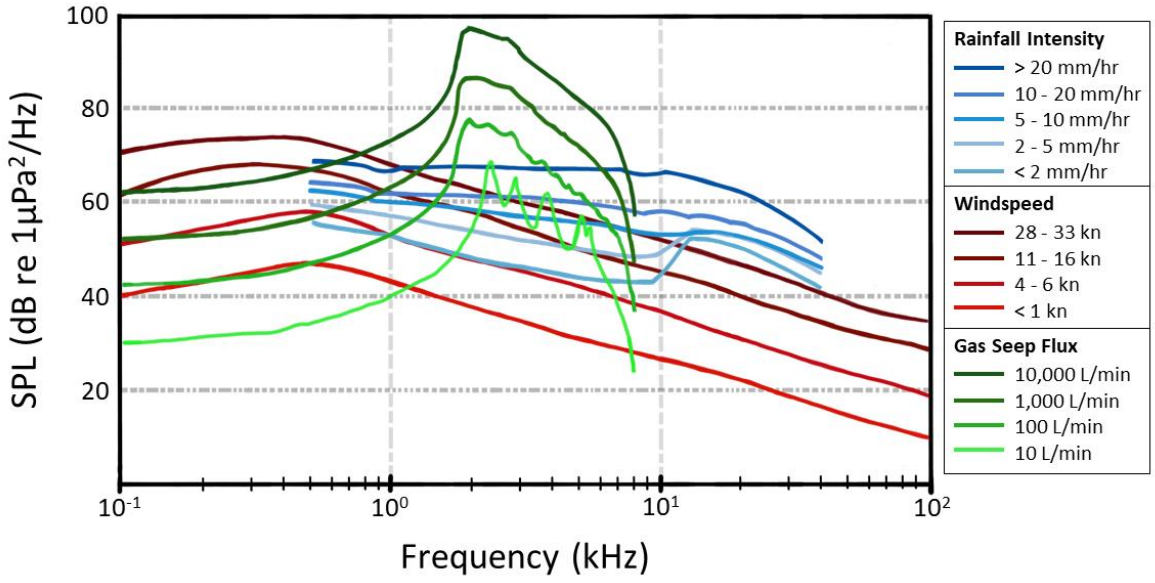

Figure 2.5: Ambient noise spectral density from 0.1 to 100 kHz for common bubble production sources in the marine environment including gas seeps, rainfall, and breaking waves. Gas seepage is simulated at different flux rates in L/min at 100 m water depth assuming a Gaussian bubble size distribution between 0.5 - 10 mm radius. Rainfall data at different intensity levels in mm/hr is from Ma and Nystuen (2004), breaking wave data observations at different wind speeds in knots is from Wenz (1962).

In summary the release of gas from the seabed releases an acoustic signal at the natural frequency of the resulting bubble. As the flow of gas out of a seep increases the acoustic signals of each bubble released begins to overlap making the resultant signal a summation of each individual bubble's natural frequency. Consequently, it is currently impossible to predict the sound resulting from a gas seep (or indeed a field of seeps) without an understanding of its' bubble size distribution. However, by observing the acoustic signature of a known seep, it is possible to quantify the size of bubbles being released and thus estimate the flux, observing tidal and seasonal variations.

2.3 Rainfall Acoustics

When a rain droplet impacts a body of water it forms an impact crater and may entrain a bubble. Consequently, falling rain produces two sounds in the marine environment, firstly the initial impact of the droplet on the body of water which generates a compressional wave (Fig. 2.6b). Secondly the simple harmonic motion of a bubble following its release into the water, once again at the Minnaert frequency (Leighton, 1994). This scenario is directly comparable to a leaky tap dripping water into a sink, producing a distinct "plinking" noise (Pumphrey and Walton, 1988; Pumphrey and Elmore, 1990; Leighton, 1994). While some incorrectly assume this sound is a consequence of the initial collision between drop and water surface, it is in fact the entrainment of bubbles that produces the majority of the acoustic signature. We will first discuss the sound of the initial droplet impact before discussing the processes of entrainment, the resulting acoustic signature of rainfall and methods of rainfall quantification.

The impact of the rain droplet on the water's surface initially produces a sharp acoustic pulse, with a duration of 10-40 μs, as a result of the "water hammer" effect (a pressure surge caused when the motion of a fluid is stopped). The pressure radiated by the impact is given by (Pumphrey and Crum, 1990),

$$p_{impact} = \frac{\rho u_d^3 L_d}{2c} \frac{\cos\theta}{r} \boldsymbol{u}, \tag{2.10}$$

where ρ is the water density, u_d is the impact speed of the droplet, L_d is the diameter of the droplet, c is the speed of sound in water, θ is the angle between the observer and sound source relative to the z axis, and $\boldsymbol{u}$ is the impact Mach number. Raindrops typically have a diameter between 0.5 to 5.0 mm (larger droplets tending to break up) resulting in an impact velocity between ~2.0 and 9.0 m/s (Nystuen, 2001). This means that while for individual droplets it is easy to identify the impact signature, this sound is dwarfed by the later oscillation of a bubble, by a factor as large as 200:1, meaning that during rainfall (where bubbles are continuously oscillating)

the sound of impact has very little effect on the overall acoustic signature, and is responsible only for a weak broadband signal (Pumphrey and Elmore, 1990).

The entrainment of a bubble by a droplet of water is dynamic process, much more complex than the injection of gas through sediment pores. The exact mechanism by which this occurs varies based on a number of factors, mainly impact velocity and droplet diameter. These processes are (Pumphrey and Elmore, 1990).

1) Irregular Entrainment: in which the complex and unpredictable details of a splash somehow entrain a bubble(s)
2) Regular Entrainment: in which a retreating impact crater leaves behind a small volume of gas connect via a narrow neck that is eventually pinched off leaving behind a single bubble (see Fig. 2.6a)
3) Entrainment of large bubbles: in which most of the volume of the crater is trapped as a bubble
4) Mesler Entrainment: in which many tiny bubbles are trapped in the early stages of impact process, possibly between the crest of capillary waves on the droplet and body of water

Bubbles produced by entrainment act identically to examples discussed previously, oscillating to produce an exponentially decaying sinusoidal wave in the near field (Pumphrey and Elmore, 1990). The only notable difference to seabed gas release is that the bubbles are much closer to a free surface (the water surface), meaning the mass of water regulating the oscillations is lower and thus the natural frequency of the bubbles is slightly higher than the Minnaert frequency (see Eq. 2.5).

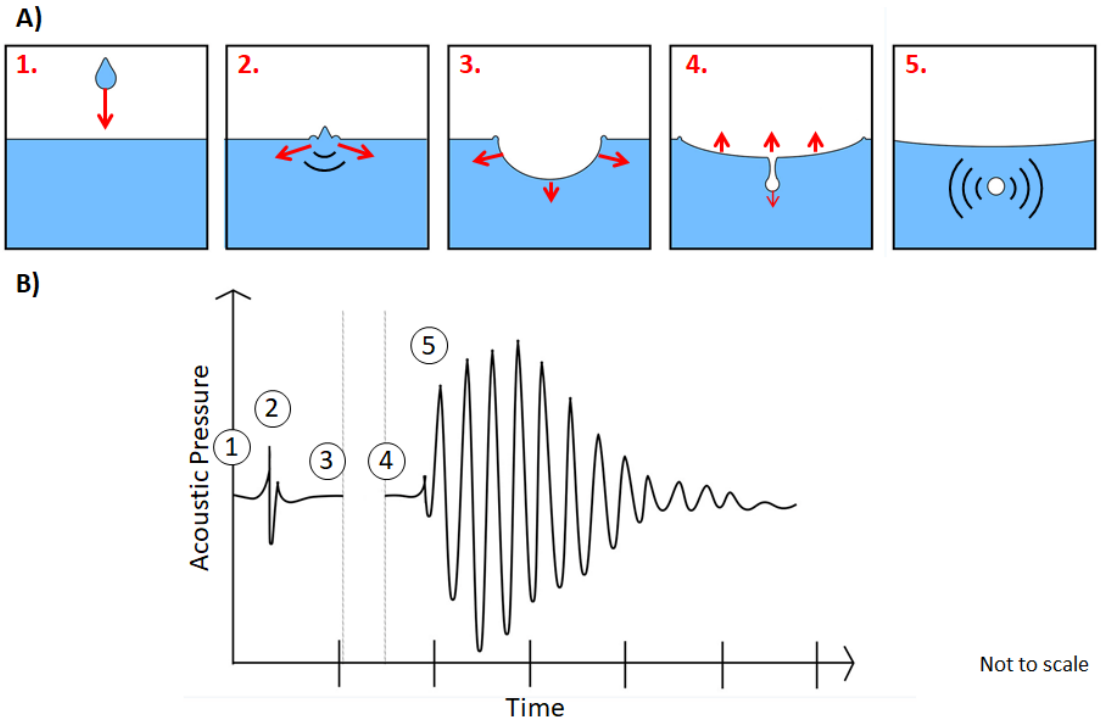

Figure 2.6: A) a diagram of regular entrainment of a bubble following the impact of a water droplet B) the acoustic signature of a raindrop. Note the weak sharp signal from the impact itself (2) followed by the larger oscillation of the bubble (5) once it detaches from the crater. Adapted from Medwin & Nystuen (1990).

Given a large enough area and a large enough number of raindrops (of a consistent size distribution), one can assume a constant number of raindrops are impacting the water and therefore a constant number of bubbles are being entrained. Consequently, rainfall results in a constant "ambient" noise. Using this principle and quantifying the number of bubbles entrained per second $n(f)$ in a 1 Hz frequency band over a 1 m^2 area of water, Pumphrey & Elmore (1990) were able to show that the intensity below the surface of the oscillating bubbles at any given frequency f is.

$$I_{Rain} = \frac{n(f)D^2Q}{4f\rho c}, \tag{2.11}$$

where Q is the quality factor and D is the initial dipole strength of the bubble. From which the intensity spectrum level is given by.

$$ISL_{Rain} = 10\log\frac{I_{Rain} \cdot \rho c}{1\ \mu Pa^2/Hz} = 10\log\frac{n(f)D^2Q/4f}{1\ \mu Pa^2/Hz}.$$

(2.12)

From here it is important to note that while D increases with increasing f, Q decreases. These two effects cancel each other out meaning the spectrum is dominated by the number of bubbles entrained per second (Pumphrey and Elmore, 1990). Additionally, it has been observed that, neglecting refraction and absorption, 90% of the rain signal arrives from a sample area with a radius equal to 3 times the observer's depth (Pumphrey and Elmore, 1990). Thus, using Eq. 2.12 and the size and number of bubbles produced per second by entrainment during a given rainstorm one can calculate the acoustic spectrum of the rainfall or vice versa.

It is difficult to precisely predict the relative occurrence of each entrainment process during a rainstorm. While regular entrainment is by far the most well understood process, its name is more a consequence of being the easiest to comprehend and predict. Indeed, when Pumphrey and Elmore (1990) mapped which processes occurred at which impact velocity (for a range drop diameter) the plot is dominated by Mesler entrainment. Additionally, if one were to assume all impacts occurred at terminal velocity then the entrainment of large bubbles would never occur, and irregular entrainment would occur only during storms with particularly large droplets (Pumphrey and Elmore, 1990; Black et al., 1997; Nystuen, 2001; Ma and Nystuen, 2005; Anagnostou et al., 2008; Nystuen et al., 2008, 2015; Ashokan et al., 2015; Pensieri et al., 2015; Yang et al., 2015; Serra, 2018; Taylor et al., 2020). It is logical to assume that the splashing of water will produce some droplets that impact at below terminal velocity meaning all entrainment processes are likely to occur at some point during a rainstorm. However, it is reasonable for now to assume only regular and Mesler entrainment dominate and justify further consideration.

Mesler entrainment produces multiple very small bubbles ~25 µm in radius regardless of the size and velocity of the droplet. This results in a natural frequency of approximately 1.3 MHz. The high frequency / small size of Mesler bubbles ultimately means they produces very little noise

with high levels of attenuation and consequently have little to no impact on the acoustic signature of rainfall, especially in the far field, meaning regular entrainment is responsible for the majority of bubble oscillation sound during rainfall (Nystuen, 1986, 2001; Scrimger et al., 1987; Pumphrey and Elmore, 1990; Black et al., 1997; Nystuen and Selsor, 1997; Nystuen et al., 2000, 2015; Ma and Nystuen, 2005; Ashokan et al., 2015; Pensieri et al., 2015; Yang et al., 2015; Serra, 2018; Taylor et al., 2020).

Regular entrainment produces different bubble sizes for different droplet sizes and impact velocities. If we consider only the bubbles produced by raindrops traveling at terminal velocity, regular entrainment is the result of droplets 0.40 to 0.55 mm in radius (with larger and smaller droplets resulting in Mesler entrainment) (Nystuen et al., 2000; Ma and Nystuen, 2005; Ashokan et al., 2015). Bubbles produced by regular entrainment of droplets of this size are predicted to be in the range 0.16 to 0.33 mm in radius, resulting in frequencies between 10 and 20 kHz. Laboratory and field data has consistently shown that there is a general increase in the number of bubbles entrained with bubble radius, peaking at ~0.23 mm in radius and dropping off rapidly above ~0.27 mm (Pumphrey and Elmore, 1990; Ma and Nystuen, 2005; Nystuen et al., 2008; Ashokan et al., 2015; Pensieri et al., 2015).

Consequently, the spectral content of rainfall on a body of water is expected to gradually increase in intensity as frequency decreases, leading to a large peak at around 14-15 kHz and followed by a sharp decline below 10-12 kHz, the exact intensity of the signal depending on the number of bubbles entrained per second (a consequence of the number of raindrops impacting per second) (Nystuen, 2001; Ma and Nystuen, 2005; Ashokan et al., 2015). This prediction fits well with field observation, see Fig. 2.7. Data collected from lakes, land-based water tanks, brackish ponds and deep marine environments all show a distinctive peak at 14-15 kHz with a sudden drop off below 10-12 kHz (Nystuen, 2001).

One consistent observation in repeat studies is a decrease in the prominence of the 14-15 kHz peak with increased rates of rainfall, with the peak being almost indistinguishable above 30

mm/hr as seen in Fig. 2.5 and 2.7 (Medwin et al., 1990; Ma and Nystuen, 2007). This is because at higher rainfall rates, more bubbles oscillating between 10 to 20 kHz are generated per second resulting in an increased intensity of the signal. However as can be seen in Eq. 2.12 this is a logarithmic increase with diminishing returns meaning while the surrounding frequencies increase in intensity the 14-15 kHz peak is relatively unmoved, flattening out the spectrum. Additionally, in the field increased rainfall tends to be accompanied by increased windspeed, which as we will discuss next also affects the rain spectrum. For this reason, the rain spectrum is best observed during a drizzle or light rain (Cavaleri and Bertotti, 2018).

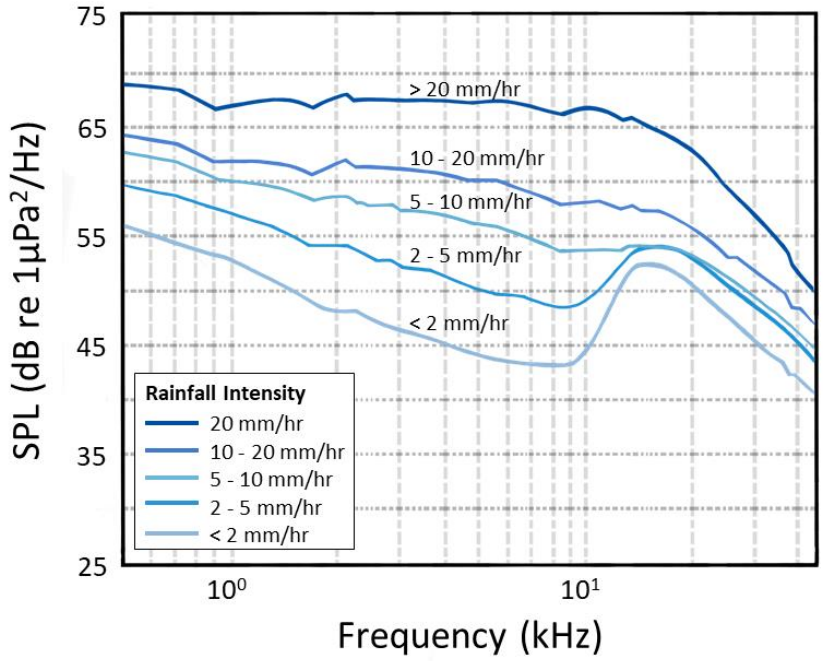

Figure 2.7: The average SPL spectrogram of rainfall acoustic at various rates as record by a number of buoys in lakes and seas around the world over a collective total of 30 months. Note the distinct peak at 14 kHz caused by the regular entertainment of bubbles from rainfall that becomes less prominent as rainfall become more intense. Adapted from Ma and Nystuen (2005).

The rain signature above 10 kHz is known to be affected by wind speed (Pumphrey and Elmore, 1990; Black et al., 1997; Ma and Nystuen, 2005; Anagnostou et al., 2008). Ma and Nystuen (2004) noted that as wind speed increased from 0.6 to 3.3 m/s, the 15 kHz peak became less prominent and broader, shifting up by a few kHz. The increased wind speed drives waves on the surface of the water which has two effects. Firstly, it alters the angle of incidence of raindrops

on the water, this reduces the probability that an individual droplet will produce a bubble from a 100% at normal incidence to 10% at a deviation of 20° (Ma and Nystuen, 2005). Additionally, a deviation of 20° causes a 30% decrease in the energy emitted by the initial impact (Ma and Nystuen, 2005). This means that dominance of the bubble noise over the impact noise reduces by a factor of 10, thus making the peak less prominent. Secondly, as we will discuss later, at high wind speeds breaking waves / white caps can also produce bubbles of similar magnitude which will interfere with the sound of rainfall. However, it has been observed that under certain conditions rainfall can prevent the formation of breaking waves (Wu, 1979; Leighton, 1994; Holthuijsen, 2007; Cavaleri, 2020).

Some studies have noted a secondary rise in the rain spectrum starting at 2-3 kHz and peaking around 5 kHz. This is believed to be a consequence of irregular entrainment of bubbles caused by very large droplets 2.0-3.5 mm in diameter (Anagnostou et al., 2008; Pensieri et al., 2015; Yang et al., 2015; Serra, 2018; Taylor et al., 2020). We had previously dismissed irregular entrainment and the entrainment of large bubbles by assuming the majority of droplets impacted at terminal velocity and that larger droplets were less common than small ones. However, it appears that when a rainstorm is comprised of particularly large droplets (>2.0 mm) the frequency of irregular and large entrainment events is significant enough to cause a recognisable spike in the spectrum. Possibly as a result of accompanying wave action lowering the impact velocity. This secondary 5 kHz peak while less conspicuous than the 14-15 kHz peak may in fact be more useful as it exists in the part of the spectrum less affected by wind and wave noise (2 - 10 kHz) (Ma and Nystuen, 2005). This means that observations of the intensity of the 5 kHz peak can be used for rainfall quantification regardless of windspeeds. Using comparative rain gauge data Ma and Nystuen (2001) proposed the following equation for calculating the rainfall rate S_{rain} in mm/hr based on the sound pressure level at 5 kHz (SPL_{5kHZ}).

$$10\log_{10} S_{rain}/10 = (SPL_{5kHZ} - 42.4)/15.4. \quad (2.13)$$

While the exact relationship varies from location to location based on local conditions and ambient noise levels, acoustic inversion of rainfall (with sufficient calibration) is a highly promising technique for use in meteorological & oceanographic research which is becoming increasingly common (Nystuen et al., 2000; Deane and Stokes, 2002; Ma and Nystuen, 2005, 2007; Anagnostou et al., 2008; Pensieri et al., 2015; Yang et al., 2015; Taylor et al., 2020).

In summary the acoustic signature of rainfall in the marine environment is caused by the entrainment of bubbles, not the impact of the droplets themselves. The rain spectrum is a distinctive peak at 14-15 kHz with a sudden drop off below 10-12 kHz, caused by regular entrainment, and occasionally a secondary smaller peak at 5 k Hz, caused by irregular entrainment when droplet are particularly large. The intensity of these peaks is dictated by the number of raindrops impacting the water per second. As the intensity of the rainfall increases the peaks becomes broader and less well defined. Increasing wind speeds also mutes the 14-15 kHz peak due to altering the impact angle of droplets and interference from wave noise, however the 5 kHz peak is less affected by wind and can be used for rainfall quantification.

2.4 Breaking Wave Acoustics

In the natural marine environment sufficiently high wind speeds can cause surface gravity waves to break as whitecaps (or whitehorses) (Leighton, 1994). Unsurprisingly this process entrains a large number of bubbles which oscillate near the surface, as described by Eq. 2.5 (Farmer and Vagle, 1988; Bass and Hay, 1997; Deane and Stokes, 2002; Manasseh et al., 2006). Not only do these bubbles have a noticeable effect on the ambient noise of the ocean (via oscillation) (Deane and Stokes, 2002) but they may also affect the passage of other acoustic signals by altering the propagation of sound waves near the sea surface (Deane and Stokes, 2002). First, we will discuss waves as acoustic sources before discussing the effect wave generated bubbles have on the speed of sound and finally the ambient noise generated by wave action and how this can be related to wind speed. We will not discuss in detail the hydrodynamic controls behind breaking waves, other than to note in general, strong winds result in larger breaking waves, as this in itself would demand a full chapter (Leighton, 1994; Deane and Stokes, 2002).

The entrainment of bubbles from wave action is a highly dynamic process (even more so than rainfall) with the exact minutia of the bubble generation being poorly understood (Deane and Stokes, 2002). We know, however, from laboratory and field data that distinct bubbles are initially generated during one of two phases: Jet Entrainment and Cavity collapse (Deane and Stokes, 2002).

Jet entrainment begins as soon as the wave starts to break. The crest of the wave overturns and plunges into the wave face, forming a plunging jet, with a cavity of air trapped between the two bodies of water. This chaotic collision of the jet generates bubbles generally between 0.1 and 2.0 mm in radius (2 to 30 kHz) (Leighton, 1994). Additionally, the impact of the jet causes the water to splash and a number of droplets to also entrain bubbles. Towards the end of a breaking wave's life cycle the cavity of air trapped between the wave face and the plunging jet will collapse. This forms a large number of bubbles the majority of which are between 2.0 and 10.0 mm in radius (0.4 to 2 kHz) (Deane and Stokes, 2002). Given the high density of bubbles the

remnants of the cavity act as a “bubble cloud.” As discussed, earlier bubbles in a cloud tend to act as coupled oscillators with normal modes of oscillation much lower than that of individual bubbles (Carey and Bradley, 1985; Deane and Stokes, 2002). The cavity collapse phase is thus responsible for frequencies between 0.1 and 0.5 kHz due to the bubble cloud, and higher frequencies up to ~2 kHz from individual oscillations (Carey and Bradley, 1985; Deane and Stokes, 2002). It is also at this time that the plunging jet forms a shear zone along the wave surface which encircles the cavity remnants. Some bubbles will be pulled through this shear zone which can cause a bubble to fragment into two or more smaller fragments, which once again oscillate though at a higher frequency than their parent bubble (Leighton, 1994; Deane and Stokes, 2002, 2010). For example, a large bubble oscillating at 3.1 kHz may produce two daughters one at 50 kHz and one at 32.3 kHz (Thorpe, 1982; Deane and Stokes, 2002). The intensity of the cavity collapse signature is far greater than that of the Jet period (or later shearing) thus when waves are continuously breaking in the marine environment it is the sound of these bubble clouds which dominates. Therefore, the acoustic signature of a breaking wave near the surface can most easily be recognised by low frequency signal between approximately 0.2-2 kHz (Carey and Bradley, 1985; Deane and Stokes, 2002) distinct from that of rain and gas seeps (Ma and Nystuen, 2005; Bergès et al., 2015).

Deane & Stokes (2002) presented the average acoustic signature of (17) 10 cm tall plunging breakers, Fig 2.8. Here one can clearly see the jet period, which is continuous throughout the breaking of the wave, responsible for the signal above 2 kHz with the majority of the sound generated below 10 kHz. The cavity collapse period can also be clearly identified as a quick (~0.3 s) low frequency burst centred around 0.3 kHz (Thorpe, 1982; Deane and Stokes, 2002). It should be intuitive that the acoustic signature (or rather the resulting bubble cloud) of a wave is a consequence of its size (and the style of breaking), which is typically a function of wind speed. Thus, by observing the breaking of a wave one could infer the acoustic signal or vice versa.

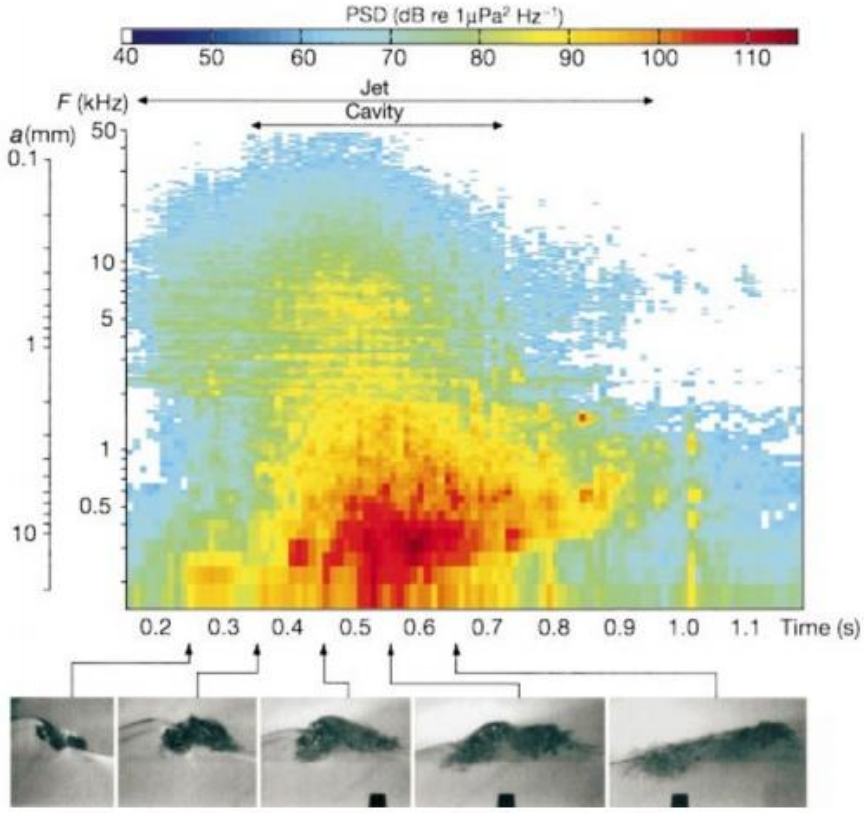

Figure 2.8: Spectrogram of wave noise calculated from an average of 17 breaking events. Note the "Jet" and "cavity" phases. The colour contours represent sound intensity plotted in a decibel scale (the intensity if referenced to 1 $\mu Pa^2 Hz^{-1}$) versus frequency and time. The log scale labelled "a" on the left-hand side indicates the radius of a bubble resonant at the corresponding frequency of the frequency scale (F). The wave noise was measured by a hydrophone mounted in the wave flume beneath the bubble plume. The images plotted below the spectrogram show the sequence of flow features at different times during the acoustic emissions. From Deane and Stokes (2002).

Given the energetic and variable nature of breaking waves it is difficult to predict exactly what happens to the resulting bubbles post-production. The exception to this is during Langmuir circulation, which is the slow shallow counter rotational vortices aligned with wind direction that develop when wind blows steadily over a body of water, which have been extensively analysed. After formation Langmuir circulation, can carry wave generated bubbles up to 10 m below the surface (Monahan and Lu, 1990). In wind speeds >7 m/s this has been known to result in linear bubble clouds orientated parallel to wind direction (Leighton, 1994). These *Langmuir bubble clouds* consist of bubbles produced throughout the lifecycle of a wave (jet and cavity collapse phase) as well as potentially those entrained by rainfall. Individual bubbles in the cloud will naturally shrink due to dissolution and eventually disappear (Liang et al., 2011), however a high

concentration of bubbles may delay this process and a continued supply of freshly generated bubbles can allow the cloud as a whole to persist as long as circulation is active (Clay and Medwin, 1978; Leighton, 1994; Liang et al., 2011). The clouds generally have void fractions between 10^{-4} and 10^{-5} % that is assumed to be uniform in the horizontal plane but falls off exponentially with depth (Farmer and Vagle, 1988; Vagle et al., 1990; Leighton, 1994; Farmer et al., 2001).

As the speed of sound depends on the inertia and stiffness of the material it is passing through the speed of sound in a bubble cloud (or "bubbly liquid") differs from that of pure water. As gas is less dense than water, sound waves travel more slowly through bubble clouds, becoming slower the larger and more numerous the bubbles are, i.e., the larger the void fraction (Garrett et al., 2000; Wang et al., 2016). If there is a distribution of bubble sizes within a cloud, such that $n_n^{gr}(z,R)dR_0$ is the number of bubbles per unit volume at depth z having a radii between R_0 and $R_0 + dR_0$, the speed of sound in a cloud c_c is given by (Clay and Medwin, 1978)

$$c_c(z,\omega) = c\left\{1 - (2\pi c^2)\int_{R_0=0}^{\infty}\frac{R_0}{\omega^2}\left(\frac{(\omega_0/\omega)^2 - 1}{\{(\omega_0/\omega)^2 - 1\}^2 + d^2}\right)n_n^{gr}(z,R)dR_0\right\}, \tag{2.14}$$

where d is the dimensionless damping constant for a single bubble, and ω_0 being the resonant circular frequency of the bubble given by $\omega_0 = 2\pi f_0$.

Given the above, and the fact surface generated bubble clouds tend to decrease in concentration with depth, one can see how the presence of breaking waves can result in an ocean model where sound speed increases noticeably with depth within the upper ~10 m (Knudsen, V.O., Alford R.S and Emling, 1948; Wenz, 1962; Farmer and Vagle, 1989; Buckingham, 1991; Leighton, 1994; Zhao et al., 2014). In such a scenario downward propagating sound waves will tend to turn, due to refraction, bending upwards back towards the surface. Similarly, upward propagating waves will also turn, refracting downwards. Repeating this cycle can result in the horizontal propagation of sound waves, trapping acoustic energy in the near surface (Farmer et al., 2001; Deane and Stokes, 2010). In terms of wave acoustics, Farmer and Vagle (1989) and

Buckingham (1991) both suggested that for a given mode the signal becomes evanescent (unable to propagate further) below certain "extinction" depth. They suggest trapping of sound in such a waveguide might influence the ambient acoustic spectra of wave noise and that by observing certain "drop out frequencies" one could infer the bubble size population generated by breaking waves, though Buckingham argues the loss of signal alone is not sufficient for a full analysis (Farmer and Vagle, 1989; Buckingham, 1991). Unfortunately, the latter appears to be correct as despite numerous attempts in the following years little progress has been made inverting bubble populations from wave acoustics (Garrett et al., 2000; Wang et al., 2016).

Accounting for the bubble cloud effects Deane & Stokes (2010) presented a model for calculating the underwater noise of a single breaking wave at a distance r with good agreement with experimental observations. Here, assuming wave noise is superposition of oscillations from generated bubbles, the creation times of bubbles being uniform and randomly distributed throughout the breaking period, the Power spectrum is given by

$$P(\omega, r) = \int_V \int_{a_{min}}^{a_{max}} \lambda(a, r) |\gamma(\omega, a)\alpha(\omega, a)|^2 \, da dV, \tag{2.15}$$

where a_{min} and a_{max} are the minimum and maximum bubble sizes generated, V is the plume volume, $\lambda(a, r)$ is the rate at which bubbles are generated, $\gamma(\omega, a)$ and $\alpha(\omega, a)$ are the Fourier transforms of the convolution of free-space bubble pulses and Greens function for the medium of propagation respectively (Deane and Stokes, 2010).

With an understanding of the individual acoustic signal of a breaking wave and the manner in which bubble clouds effect the near surface, one might assume calculating the resulting signal of multiple breaking waves would be straightforward. After all, an observer, at a given depth, will record a signal that is the superposition of all the waves breaking above it at any given moment. Given a large enough area and a large enough number of waves, i.e., an ocean, one can assume a constant number of waves are breaking resulting in a constant "ambient" noise,

as was the case with rainfall. Indeed, if all the waves were identical and occurring in some symmetrical pattern around the recorder, we could attempt to estimate the signal via theoretical calculations. However, this is not realistic and would be of little practical use, a range of breaking wave size and styles will always exist distributed erratically along the sea surface (Knudsen et al., 1948; Wenz, 1962; Bass and Hay, 1997; Manasseh et al., 2006). Additionally, a detailed understanding of the size distribution of bubbles generated in a breaking wave $\lambda(a,r)$ in Eq. 2.15 is required, something lacking outside of easily replicable waves (Deane and Stokes, 2010).

For simplicity's sake the seminal work of Knudsen et al., (1948) and Wenz (1962) describing the ambient sound pressure level (SPL) in the ocean at different wind speeds using field observations, seen in Fig. 2.5, is still relevant (Medwin and Beaky, 1989; Vagle et al., 1990; Zhao et al., 2014). Starting at around 0.20 kHz rising 3-5 dB re 1µPa^2/Hz to a peak at approximately 0.5 kHz (consistent with the above discussion) before dropping off slowly, ~25 dB re 1µPa^2/Hz by 10 kHz, with peak sound pressure levels of 60 and 73 dB re 1µPa^2/Hz respectively for wind speeds of 3.4- 5.5 m/s and 17.2- 20.7 m/s (Farmer and Vagle, 1988; Vagle et al., 1990; Felizardo and Melville, 1995; Zhao et al., 2014). This does not generally cover strong gales (wind speed > 20.8 m/s), as during higher wind speeds it becomes difficult to identify periods of pure wind noise (i.e., non-rain contaminated).

Despite the complexity of the task however, many still wish to be able to calculate the ambient noise of breaking waves e.g., for storm monitoring (Anagnostou et al., 2008; Zhao et al., 2014, 2017; Pensieri et al., 2015; Yang et al., 2015) or studying ocean atmospheric mixing (Deane and Stokes, 2002; Vagle et al., 2010). The most widespread approach is via WOTAN (Wind Observations Through Ambient Noise) calculations. Here observations of the ambient noise from breaking waves has been correlated with wind speed through numerous studies to empirically map their relationship (Vagle et al., 1990; Zhao et al., 2014). Originally this work was done with the intent of estimating wind speed based on ambient wave noise, but the reverse should also possible (calculating ambient wave noise based on wind speed).

Using past studies and their own data Vagle et al., (1990) determined that the source sound level at a depth of 1 m from breaking waves was given by

$$SSL_0 = q \log f + G,$$

(2.16)

where q is the slope of the logarithmic spectrum of the wind generated sound which they find to be equal to -19.0 dB/decade (in good agreement with past estimates (Farmer and Vagle, 1988)). G is a variable function of wind speed. Vagle et al., (1990) determined values for G between set wind speeds which we note approximately follows $G = 1.3U_{10}$+56 (U_{10} being the wind speed 10 m above water level). Unfortunately, this sound level equation only holds true for low wind speeds ($U_{10} \leq$ 15 m/s) and below a certain critical frequency, $\log f_c = 1.9 - 0.07U_{10}$ (Vagle et al., 2010).

Zhao et al. (2014) expanded upon this work and by studying the underwater acoustics of typhoons using Lagrangian floats. Fig. 2.9 displays the spectral content they observed at a range of high wind speeds from a number of floats. They noted that low frequency sound (<1 kHz) monotonically increased with wind speed while intermediate and higher frequencies initially increase then decrease with wind speed. They presented the following empirical equation to calculate the sound pressure level of a given frequency in wind speeds up to 50 m/s (Zhao et al., 2014).

$$SPL = S_{noise} + S_{10} \frac{\left(U_{10}/10\right)^{n_{lf}}}{1 + \left(U_{10}/f_{peak}\right)^{n_{hf}}},$$

(2.17)

where S_{noise} is the noise floor, S_{10} is the sound level at 10 ms^{-1} wind, f_{peak} controls the wind speed with the sound level maximum and n_{lf} / n_{hf} are values which control the increasing / decreasing in lower/higher wind conditions. All of these values are a function of the target frequency though the exact relationship is not fully understood nor linear, determined instead via

least square fitting of observations (Zhao et al., 2014). Consequently, real time analysis of wind speed via acoustics is still an emerging field. While highly promising this approach needs to be tested in multiple environments many more times, especially if the underlying variables are to be better understood (Vagle et al., 1990; Zhao et al., 2014; Pensieri et al., 2015; Farrell et al., 2016; Cazau et al., 2017, 2019; Cauchy et al., 2018).

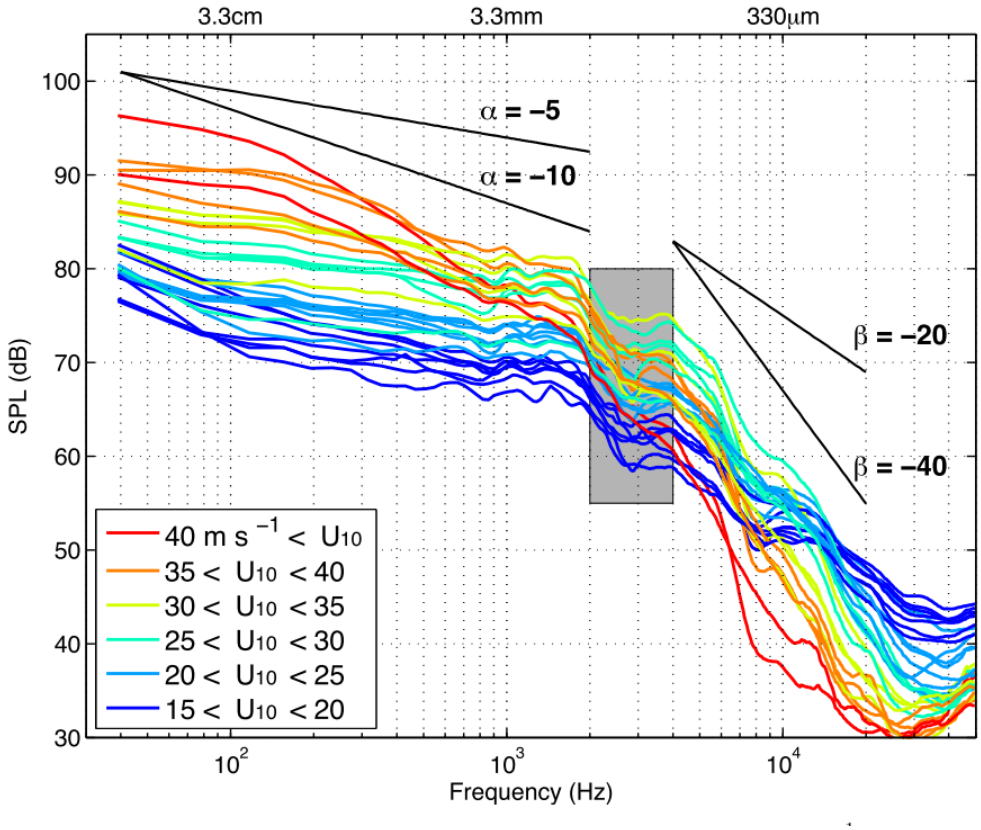

Figure 2.9: Spectrogram of breaking wave noise at various wind speeds recorded at sea during tropical cyclones. Each curve averages all spectra in 5 ms^{-1} wind speed bins from measurements at depth > 2m of a single float, multiple curves of the same colour denote observations from multiple floats. The four black lines show representative spectral slopes at low (α) and high (β) frequencies. Gray box shows the transition frequency (2-4 kHz) between the two slope regions. The dip in sound level near 3 kHz may be an instrumental effect. Taken from Zhao et al. (2014).

It should be apparent from the above that accurately predicting the acoustic signal recorded at a hydrophone as a result of breaking waves, at any given wind speed, is an exceedingly difficult task especially at gale force winds (>17.6 m/s) (Vagle et al., 1990; Zhao et al., 2014), and particularly without some prior observations for calibration. Furthermore, many empirical WOTAN studies themselves are intrinsically flawed for the purpose of noise calculations at depth as their work primarily focuses on studying a handful of select frequencies rather than the broadband signal. Additionally, without a better understanding of the affect bubble clouds have on the downward propagating signals, estimations at depth (>100 m) are highly speculative.

In summary the acoustic signature of a breaking wave is primarily the result of bubble cloud generation during the final cavity collapse phase of a waves life cycle. While individual bubble frequencies range from 0.4 to 2.0 kHz the frequency of the bubble cloud itself is typically lower, at 0.1 to 0.5 kHz. The exact frequency spectrum depends on the properties of the wave itself, which is usually a consequence of wind speed, so can be highly variable even under laboratory conditions. Bubbles generated by breaking waves can be pulled down up to 10m by Langmuir currents where they can create steep sound speed profiles with depth, possibly trapping select acoustic signals. The highly dynamic and unpredictable nature of breaking waves make predicting ambient noise from multiple breaking waves difficult, especially in gale force winds. "Wind Observations Through Ambient Noise" allow for measurements of wind speed via the ambient noise of wave action based on empirical observations but are insufficient for calculating ambient noise at depth. Knudsen curves are still the most commonly used prediction of ambient noise from wave action, with a positively skewed peak at around 0.5 kHz increasing in intensity with wind speed.

2.5 Conclusion

Bubbles have subtle yet far reaching effects on marine acoustics. The initial formation of a bubble triggers simple harmonic motion at a natural frequency, known as the Minnaert frequency, which is approximately inversely proportional to its radius. Thus, by observing the acoustic signature of a bubble one can determine its size. While the sound of a single bubble is low energy, the continuous release of multiple bubbles can have a significant impact on the ambient marine soundscape. In order to accurately predict the ambient noise produced by either a gas seep, rainfall, or breaking waves one must have a detailed understanding of the size distribution of bubbles being generated. Unfortunately, it is all but impossible to predict the size of bubbles released. However, it is possible to use observations of ambient noise to infer the characteristics of these sources; the flux from a gas seep, the intensity of rainfall and the wind speed resulting in breaking waves.

2.6 Further Reading

The following sources are recommended for continuing research in each of the areas introduced in this chapter.

Bubble Physics

- Leighton, T. G. The Freely-oscillating Bubble. in *The Acoustic Bubble* 129–286 (Elsevier, 1994). doi:10.1016/B978-0-12-441920-9.50008-0.

Subsea Gas Seep Acoustics

- Leighton, T. G. & White, P. R. Quantification of undersea gas leaks from carbon capture and storage facilities, from pipelines and from methane seeps, by their acoustic emissions. *Proceedings of the Royal Society A: Mathematical, Physical and Engineering Sciences* **468**, 485–510 (2012).
- Bergès, B. J. P., Leighton, T. G. & White, P. R. Passive acoustic quantification of gas fluxes during controlled gas release experiments. *International Journal of Greenhouse Gas Control* **38**, 64–79 (2015).

Rainfall Acoustics

- Serra, Y. L. Precipitation measurements from the Tropical Moored Array: A review and look ahead. *Quarterly Journal of the Royal Meteorological Society* **144**, 221–234 (2018).
- Ma, B. B. & Nystuen, J. A. Passive Acoustic Detection and Measurement of Rainfall at Sea. *Journal of Atmospheric and Oceanic Technology* **22**, 1225–1248 (2005).
- Pumphrey, H. C. & Crum, L. A. Free oscillations of near-surface bubbles as a source of the underwater noise of rain. *The Journal of the Acoustical Society of America* **87**, 142–148 (1990).
- Pumphrey, H. C. & Elmore, P. A. The entrainment of bubbles by drop impacts. *Journal of Fluid Mechanics* **220**, 539–567 (1990).
- Pumphrey, H.C., Walton, A.J., 1988. Experimental study of the sound emitted by water drops impacting on a water surface. Eur. J. Phys. 9, 225–231. https://doi.org/10.1088/0143-0807/9/3/011

Breaking Wave Acoustic

- Deane, G. B. & Stokes, M. D. Scale dependence of bubble creation mechanisms in breaking waves. *Nature* **418**, 839–844 (2002).
- Deane, G. B. & Stokes, M. D. Model calculations of the underwater noise of breaking waves and comparison with experiment. *The Journal of the Acoustical Society of America* **127**, 3394–3410 (2010).

- Zhao, Z., D'Asaro, E. A. & Nystuen, J. A. The Sound of Tropical Cyclones. *Journal of Physical Oceanography* **44**, 2763–2778 (2014).
- Leighton, T. G. The Freely-oscillating Bubble. in *The Acoustic Bubble* 129–286 (Elsevier, 1994). doi:10.1016/B978-0-12-441920-9.50008-0
- Vagle, S., Large, W. G. & Farmer, D. M. An Evaluation of the WOTAN Technique of Inferring Oceanic Winds from Underwater Ambient Sound. *Journal of Atmospheric and Oceanic Technology* **7**, 576–595 (1990).

2.7 Supplementary Information

2.7.1 Minnaert Frequency Derivation

The following is a derivation of the Minnaert equation following Leighton (1994).

We can find the Kinetic Energy, ϕ_K, of the water surrounding a bubble by integrating over shells of liquid from the bubble wall to infinity. A shell of radius r and a thickness dr has a mass of $4\pi r^2 \rho dr$ (ρ being the density of water), thus the kinetic energy of the surrounding water is.

$$\varphi_K = \int_R^\infty (4\pi r^2 \rho \, dr)\dot{r}^2.$$

(SI 2.1)

The mass of liquid flowing in time dt through any spherical surface around the bubble is $4\pi r^2 \dot{r} \rho dt$. Assuming the liquid is incompressible then by conservation of mass this general flow can be equated to the flow at the bubble surface which can be shown to be $\dot{r}/\dot{R} = R^2/r^2$. Substituting this into the above gives.

$$\varphi_K = 2\pi R^3 \rho \dot{R}^2.$$

(SI 2.2)

Kinetic Energy is a maximum at the equilibrium position (as with any harmonic oscillator) when $R = R_0$ and $\dot{R} = i\omega_0 R_{\varepsilon 0} e^{i\omega_0 t}$ implying that $\left|\dot{R}\right|^2 = (\omega_0 R_{\varepsilon 0})^2$. Thus, the maximum value of the kinetic energy is

$$\varphi_{KMax} = \frac{1}{2} m_{RF}^{rad} (\omega_0 R_{\varepsilon 0})^2 = 2\pi {R_0}^3 \rho (\omega_0 R_{\varepsilon 0})^2,$$

(SI 2.3)

where m_{RF}^{rad} is the radiation mass of the bubble in radius-force frame. This mass is the effective inertia of the liquid component of the oscillating system which the pulsating bubble represents i.e., $m_{RF}^{rad} = 4\pi {R_0}^3 \rho$. It arises from the liquid that is transmitting acoustic waves and is the only inertia considered by the Minnaert derivation.

Through conservation of energy, maximum kinetic energy φ_{KMax} must equal maximum internal energy φ_{PMax} which occurs when $R = R_0 \pm R_{\varepsilon 0}$ and $\dot{R} = 0$. The work done compressing the bubble from equilibrium volume V_0 (at radius R_0) to minimum volume V_{min} (at radius $R_0 - R_{\varepsilon 0}$) is the integral of $-(p_g - p_0)dV$ where p_g is the gas pressure and p_0 is the hydrostatic liquid pressure outside the bubble.

$$\varphi_{PMax} = -\int_{V_{max}}^{V_{min}} (p_g - p_0)\, dV = -\int_{R_0}^{R_0 - R_{\varepsilon 0}} (p_g - p_0) 4\pi r^2\, dr.$$

(SI 2.4)

Minnaert derived his equation assuming that the gas behaved adiabatically, i.e., that there was no heat flow across the bubble wall. This was adapted by the introduction of the polytropic index κ (which takes a value equal to unity when the gas behaves isothermally and equals the ratio of the specific heat of the gas at constant pressure to that at constant volume, when the gas behaves adiabatically) (Leighton and Walton, 1987). Assuming the gas behaves polytropically so that $p_g V^{\kappa} = constant$ then since $R_{\varepsilon} = R - R_0$ by equating the pressure and volume condition at equilibrium to those when the bubble attains minimum volume gives.

$$p_g(R_0 + R_\varepsilon)^{3k} = p_0{R_0}^{3k},$$

(SI 2.5)

for small displacements, the binomial expansion of this is.

$$p_0 - p_g \approx \frac{3\kappa R_\varepsilon p_0}{R_0},$$

(SI 2.6)

substituting this into the maximum internal energy φ_{PMax} with the use to first order $R_\varepsilon = R - R_0$ coordinates gives.

$$\varphi_{PMax} = \int_0^{R_{\varepsilon 0}} \frac{3\kappa R_\varepsilon p_0}{R_0} 4\pi {R_0}^2 \, dR_\varepsilon = 6\pi\kappa p_0 R_0 {R_{\varepsilon 0}}^2,$$

(SI 2.7)

this allows us to equate the maximum kinetic energy and maximum potential energy

$$\varphi_{KMax} = 2\pi {R_0}^3 \rho(\omega_0 R_{\varepsilon 0})^2 = 6\pi\kappa p_0 R_0 {R_{\varepsilon 0}}^2 = \varphi_{PMax},$$

(SI 2.8)

which can be solved for the resonance circular frequency ω_0;

$$\omega_0 = \frac{1}{R_0}\sqrt{\frac{3\kappa p_0}{\rho}},$$

(SI 2.9)

and finally using $\omega_0 = 2\pi f_M$ gives us the Minnaert frequency equation.

$$f_M = \frac{1}{2\pi R_0}\sqrt{\frac{3\kappa p_0}{\rho}}.$$

(SI 2.10)

2.8 Symbology

SYMBOL	DEFINTION
a_{min}	Minimum bubble size generated
a_{max}	Maximum bubble size generated
$B(R_0)$	Bubble size distribution
c	Speed of sound in water
c_c	Speed of sound through a bubble cloud
d	Dimensionless damping constant for a single bubble $= 2\beta/\omega$
D	initial dipole strength of the bubble
f	Frequency
f_{peak}	Peak frequency
f_M	Minnaert frequency – oscillation frequency of a bubble as predicted by Minnaert equation
f_0	Natural frequency of a bubble oscillation
G	A variable function of wind speed
h	Distance from the *centre* of the bubble to the surface of the water
I_{Rain}	Intensity of rainfall beneath the surface at a given frequency
ISL_{Rain}	Intensity spectrum level of rainfall beneath the surface at a given frequency
l	loaded length of spring
l_0	unloaded length of spring
L_d	Diameter of water droplet
m_{RF}^{rad}	Radiation mass of bubble in radius force frame
n	Mode number
$n(f)$	Number of bubbles entrained per second by rainfall
n_{lf}	A quantity controlling the increasing slope of wave noise in lower wind conditions
n_{hf}	A quantity controlling the decreasing slope of wave noise in higher wind conditions
$n_n^{gr}(z, R)dR_0$	Number of bubbles per unit volume at depth z having a radii between R_0 and $R_0 + dR_0$
N_b	Number of identical bubbles in a bubble cloud
p_g	Gas pressure inside bubble
p_0	Hydrostatic liquid pressure outside the bubble
p_v	Vapour pressure
$P(\omega, r)$	Power spectrum of a breaking wave
q	Quality factor
Q_w	Slope of the logarithmic spectrum of the wind generated sound
r	Radial distance
R	Radius of Bubble wall
R_0	Equilibrium radius of bubble

R_ε	Displacement of the bubble wall from equilibrium radius
$R_{\varepsilon 0}$	Maximum displacement of bubble wall from equilibrium radius
$R_{\epsilon 0 i}$	Initial amplitude of displacement of the bubble wall
R_{max}	Maximum radius of bubble
R_{min}	Minimum radius of bubble
S	Column vector containing the measured spectrum $S(\omega_k)$
$S(\omega)$	Power spectral density of a marine gas seep
S_{10}	Sound level at 10 ms^{-1} wind
S_{noise}	Noise floor
S_{rain}	Rainfall rate
SPL	Sound pressure level
SPL_{5kHZ}	Sound pressure level at 5 kHz
SSL_0	Source sound level of breaking waves at a depth of 1m
t	Time
u	Impact mach number
u_d	Impact speed of water droplet
U_{10}	Wind speed 10 m above water level
V	Volume of bubble plume
V_0	Equilibrium bubble volume
V_{min}	Minimum bubble volume
VF	Void Fraction
z	Depth below sea surface
$\alpha(\omega, a)$	Fourier transform of the Greens function for the medium of propagation respectively
$\gamma(\omega, a)$	Fourier transform of the convolution of free-space bubble pulses
δ_{tot}	Total damping constant for bubble pulsation at resonance
ε	Displacement from equilibrium
θ	Polar angle, angle between observer and source relative to the z axis
φ_K	Kinetic energy
φ_{KMax}	Maximum kinetic energy
φ_{PMax}	Maximum internal energy
κ	Polytropic index
σ	Surface tension
η	Shear viscosity
ρ	Density of water
ω	Angular frequency $= 2\pi f$
ω_0	Angular resonate frequency
$\Psi(n)$	Bubble generation rate (for marine gas seep)

Chapter 3 Time-lapse imaging of CO_2 migration within near-surface sediment during a controlled sub-seabed release experiment

The ability to detect and monitor any escape of carbon dioxide (CO_2) from sub-seafloor CO_2 storage reservoirs is essential for public acceptance of carbon capture and storage (CCS) as a climate change mitigation strategy. Here, we use repeated high-resolution seismic reflection surveys acquired using a chirp profiler mounted on an autonomous underwater vehicle (AUV), to image CO_2 gas released into shallow sub-surface sediments above a potential CCS storage site at 120 m water depth in the North Sea. Observations of temporal changes in seismic reflectivity, attenuation, unit thickness and the bulk permeability of sediment were used to develop a four-stage model of the evolution of gas migration in shallow marine sediments: Proto-migration, Immature Migration, Mature Migration, and Pathway Closure. Bubble flow was initially enabled through the propagation of stable fractures but, over time, transitioned to dynamic fractures with an associated step change in permeability. Once the gas injection rate exceeded the rate at which gas could escape the coarser sediments overlying the injection point, gas began to pool along a grain size boundary. This enhanced understanding of the migration of free gas in near-surface sediments will help improve methods of detection and quantification of gas in subsurface marine sediments.

3.1 Introduction

Since the industrial revolution, the concentration of CO_2 in the atmosphere has risen from 277 parts per million (ppm) to a current level of > 410 ppm (Friedlingstein et al., 2019). This rise has been directly linked to anthropogenic sources such as the burning of fossil fuels, the manufacture of cement, and changing land uses (Friedlingstein et al., 2019). The increased level of atmospheric CO_2 has resulted in a rise in the global mean surface temperature of 1 °C (IPCC, 2018). Global warming has already had a severe negative effect on the environment, leading the United Nations Framework Convention on Climate Change (UNFCCC 2015) to agree on a strategic plan to stop the global mean temperature from rising more than 2˚C above the pre-industrial level (IPCC, 2014).

The large-scale adoption of Carbon dioxide Capture and Storage (CCS) has been identified as a key factor for reducing anthropogenic greenhouse gas emissions to reach climate goals (IPCC 2014). During CCS activities, CO_2 gas produced during industrial processes is captured and stored in appropriate geological reservoirs deep beneath the surface to mitigate the potential greenhouse effects. Compared to other strategies, such as enhanced energy efficiency and the use of renewable energy sources, the crucial benefit of CCS lies in its potential to reduce (in a significant, timely, and cost-effective way) the CO_2 emissions, by utilizing existing infrastructure from oil and gas production (IPCC, 2005). Depleted hydrocarbon fields in the North Sea are prime candidates for CCS storage with the potential to hold 475-570 Mt of CO_2 (Strachan et al., 2011). Several successful demonstration projects have already provided confidence in the performance of offshore gas injection and storage; K12-B (North Sea, Netherlands), Sleipner (North Sea, Norway), and Snøhvit (Barents Sea, Norway) (Vandeweijer, et al. 2011, Hansen et al., 2013, Van der Meer, 2013, Furre et al.,2017, Ringrose and Meckel, 2019). However, robust strategies for leak detection and management are still in their infancy despite being a regulatory requirement to comply with international marine legislation (e.g., EU CCS Directive, London Protocol, OSPAR) and must be advanced to make CCS a safe and reliable strategy for the long-term mitigation of atmospheric CO_2 increase.

While CO_2 escape from a CCS site is unlikely (IEAGHG, 2013), risks can broadly be categorised into two types: i) injection facility failure and ii) seal failure. Injection facility failure would occur close to the seabed and include faulty pipelines, wellheads, or injection wells within the subsurface, and can be considered part of the standard operating risk of offshore oil and gas facilities. Seal failure would occur at much greater depth and is most likely caused by either inadequately secured abandoned wells, or previously undetected/newly formed small-scale stress-induced fractures increasing permeability across a cap rock. These create fluid pathways for injected gas to escape back to the surface. While failure at injection facilities would typically be detected very quickly (if not immediately), failure across a seal could take several days or even years to have an effect on the seabed e.g., detection of bubble plumes in the water column, changes in the pH of bottom waters or changes in the distribution of benthic fauna and flora. Monitoring sub-surface integrity using sub-bottom methods would allow anomalies to be determined earlier than seabed observation techniques (Jenkins et al., 2012, Dean et al., 2020).

Therefore, to enable the large-scale implementation of CCS, a greater understanding of the fate of injected CO_2 in the subsurface is crucial, particularly regarding its migration in the uppermost sedimentary succession. Our understanding of newly self-established fluid flow features (gas conduits to the seabed), and their effect on the surrounding sediment conditions our ability to detect CCS leakage and ameliorate any potential environmental impacts. More broadly, such work will enhance our understanding of processes operating in sub-seabed natural CO_2 and CH_4 (methane) seeps that are found around the globe (Dlugokencky et al., 2011, Ruppel and Kessler 2017).

Several international projects such as ECO_2 (Sub-seabed CO_2 Storage: Impact on Marine Ecosystems), QICS (Quantifying and Monitoring Potential Ecosystem Impacts of Geological Carbon Storage), and ETI MMV (Energy Technologies Institute Measurement, Monitoring, and Verification of CO_2 Storage) have contributed to improving our ability to detect potential leaks at the seafloor and the impact of the CO_2 leakage on marine ecosystems (Dean et al., 2020, Blackford et al., 2014, Blackford et al., 2017, Jones et al. 2015, Taylor et al., 2015). The STEMM-CCS (Strategies for

Environmental Monitoring of Marine Carbon Capture and Storage) project was subsequently established with the overall aim of converting this information into quantified knowledge that would enable cost-effective monitoring in the marine environment for realistic CO_2 leak scenarios.

Central to the STEMM-CCS project was a controlled CO_2 release experiment in the North Sea (Fig. 3.1) designed to simulate a CO_2 leak from a sub-seabed CCS site, to demonstrate and evaluate new approaches for detecting or quantifying this release (Flohr et al., 2021). We use AUV-mounted 2D seismic reflection chirp data collected before, during, and after the release, alongside detailed core analysis, in order to create a time-lapse record of the CO_2 migration. This paper describes in detail the evolution of gas migration pathways, culminating in the formation of seismic chimneys, with a particular focus on constraining the primary mechanisms (stable and dynamic fracture propagation) by which gas migrates within the near-surface over time. Using seismic time lapse imaging, we examine the development of enhanced reflectors, shadowing, as well as variations in attenuation, RMS amplitude, and unit thickness.

3.2 Gas Migration in Near-Surface Sediments

The upward migration of gases in the form of bubbles through near-surface, unconsolidated sediment is a rapid process, which allows the gases to bypass oxidation or absorption processes (Knittel & Boetius, 2009). While our study is concerned with CO_2 gas, most of the principles are equally applicable to other gases including methane (CH_4), another greenhouse gas (Landrø et al., 2019).

In order to understand the migration of gas through sediment, we first consider the migration history of a single bubble, from its nucleation to its escape into the water column. A bubble is a pocket of gas, in our case CO_2, surrounded by a liquid host medium. While traditionally this term is applied to pockets of air in the water column it can also be applied to pockets of gas in water saturated sediment. In the interests of clarity, we will refer to pockets of CO_2 gas in the water column as simply "bubbles", and pockets of CO_2 gas in the sediment as "bubble fractures" and "capillary CO_2". In a typical near-surface marine sediment, the pores between grains are saturated with water. The introduction of gas, for example from an underlying fracture, slowly invades the surrounding pores, displacing the water. This intrusion can occur either by capillary invasion or by fracture opening. In capillary invasion, the gas forces its way into a new pore if the capillary pressure (the difference between gas pressure and water pressure) is larger than the capillary entry pressure. This is more common in coarser-grained sediment and occurs without movement of the surrounding grains. The capillary invasion continues in an outward direction from the point of injection (generally upwards) with gas moving from pore to pore, often replaced by the surrounding water, thus dispersing the gas without the creation of a bubble fracture (Jain and Juanes, 2009). Alternatively, intrusion may occur via fracture opening, whereby the gas within a pore naturally exerts a net pressure on the surrounding grains. As the two fluids do not mix, this pressure difference does not dissipate and leads to the rearrangement of surrounding grains, preferentially fracturing the sediment (Boudreau et al., 2005, Jain and Juanes, 2009, Katsman et al., 2013). This fracture opening is the initial nucleation of a bubble in sediment, as the gas forms its own "cavity" within the surrounding medium.

After nucleation, a bubble fracture exists in a heterogeneous pressure field that increases with depth, resulting in a pressure difference between the top and the bottom of the bubble fracture. This gradient, combined with the difference in density between the bubble fracture itself and the surrounding medium, creates a pseudo-buoyancy force (Boudreau et al., 2005, Algar et al., 2011). If the bubble fracture is large enough, this force allows the fracture to rise upwards through the sediment, the weaker (less cohesive) the sediment, the smaller the fracture needs to be. The upwards force exerted by the bubble fracture on the host medium (the surrounding sediment) depends on the volume of the body, not its shape, and does not depend on its vertical extent, provided the above assumptions hold true and that the body moves coherently as a single entity. Real bubble fractures in marine sediment might easily depart from this latter restriction, through deformation, fragmentation, and coalescence. Furthermore, the properties of the sediment can greatly change the resistive forces that oppose this rise (such as sediment cohesion, and the weight of the gas /vapour mixture itself) and affect bubble fragmentation and coalescence, and how these forces change in time.

The nature of bubble fracture propagation in soft sediment is commonly described via linear elastic fracture mechanics (LEFM) where the bubble can be imagined as a very thin oblate spheroid, the long axis orientated vertically, forming what is known as a “penny-shaped” crack in the sediment (Boudreau et al., 2005, Algar et al., 2011, Boudreau 2012). From here the bubble fracture may propagate through either stable or dynamic fracture propagation. We will first describe stable fracture propagation, a fundamental process that is most in need of refinement.

3.2.1 Stable Propagation

The most prominent application of LEFM to stable fracture propagation was first presented by Algar et al., (2011). They describe how the interior gas of the bubble fracture exerts an outward pressure on the crack walls/sediment with the resulting tensile stresses concentrated at the upper crack tip (Algar et al., 2011) and is characterised by the stress intensity factor K_1;

$$K_1 = \frac{2}{\pi}\sigma\sqrt{a\pi}, \tag{3.1}$$

where σ is the internal bubble pressure in excess of the ambient pressure (i.e., the applied stress), and a is the half major axis of the crack/bubble. If the stress intensity factor K_1 is greater than the stress the material can take before tensile failure, the fracture toughness of the sediment K_{ic}, the fracture will propagate (Algar et al., 2011).

As the fracture expands upwards, the length of the crack/bubble increases, and the pressure difference between the tip and the tail of the crack eventually disappears and the internal bubble pressure equals the compressive stresses of the surrounding medium (σ=0) (Algar et al., 2011). This results in a lower stress intensity factor (K_1<K_{ic}) at the top of the crack, halting propagation. As a result of heterogeneous stress field, the compressive forces at the crack tail force it to close, morphing the bubble into an inverted teardrop shape. The sealing up of the crack behind the rising bubble fracture decreases the crack length, raising the internal bubble pressure and reverting it to its original condition, which restarts the fracture propagation process slightly higher up. The cycle repeats, leading to the bubble fracture rising upwards through the sediment in an alternating sequence of elastic expansion and fracturing, which is commonly referred to as "stable fracture propagation" (Boudreau et al., 2005, Algar et al., 2011, Katsman et al., 2013, Katsman 2019). The rise speed of a bubble fracture is regulated by the period of this cycle, i.e. the length of time between a tip opening and the tail closing, which depends upon the elasticity of the sediment (Boudreau et al., 2005, Boudreau 2012, Algar et al., 2011). The minimum critical size at which a bubble fracture will begin to rise a_r is determined by the properties of the surrounding

sediment, and can be calculated as follows (Barry et al., 2012, Johnson et al., 2012, Johnson et al., 2002):

$$a_r = \left(\frac{3K_{ic}\sqrt{\pi}}{10g[\rho_s(1-\varphi) + \rho_w\varphi]} \right)^{2/3}, \tag{3.2}$$

where ρ_s is the density of the solid grains, ρ_w is the density of water, g is the acceleration due to gravity and φ is the porosity of the sediment (Boudreau 2012, Algar et al., 2011).

While Algar et al., (2011) model is the most comprehensive theory on the concept of stable fracture propagation, with good experimental correlation, there are a number of oversimplifications. Perhaps the most important is that the theory is based on the concept that the sediment acts as a single entity. Even for the most cohesive sediment this is not true. Furthermore, to apply a straightforward adaptation of standard analyses (Westergaard 1939, Irwin 1957) for crack propagation in solids, Algar *et al*. (2011) restricted their consideration to cases where they could argue that the solid around the bubble fracture was 'dry'. Anderson et al. (1998) characterised bubbles propagating via fracture mechanics (Type 3 bubbles) as a gas pocket formed by the displacement of both sediment and liquid. If we acknowledge a bubble consists of both a pocket of gas and its surroundings (Leighton 1994), then the characteristic properties of the bubble fracture (the way its wall moves in response to external drivers; mass transfer across its wall etc.) will depend on both the gas and the surrounding medium. If there is a space between sediment grains that contains an area of gas and an area of liquid water (as opposed to vapour), the interface between the water and the gas forms part of the bubble wall. This clarification highlights the need to have precise definitions, for what is meant by 'dry' formation of new space between the grains, the definition of the bubble wall (the interface between a finite, contiguous but enclosed volume of gas and/or vapour, and the surrounding liquid (and optionally solid) medium or mixture). The specification that the volume is enclosed means that gas cannot escape into dry channels between grains if the gas pressure increases marginally.

Such a concept has a wet interface across the bubble fracture wall, providing a Laplace pressure. We are thus able to relax the concept of dry fractures according to Algar et al, (2011) by assuming that the bubble wall will "always" be in contact with water and incorporating the associated capillary pressure into the definition of the stress intensity factor, amending Eq. 3.1 to the form:

$$K_1 = \frac{2}{\pi}\sigma\left(1 - \frac{\tau}{\sigma}\left(\frac{1}{a} + \frac{1}{b}\right)\right)\sqrt{a\pi} = \frac{2\sqrt{a}}{\sqrt{\pi}}\left(\sigma - \tau\left(\frac{1}{a} + \frac{1}{b}\right)\right), \tag{3.3}$$

where σ is the internal bubble pressure in excess of the ambient pressure, b is the half minor axis, and τ is the surface tension characterising the interface between the gas and the liquid. We must assume the fracture has an aspect ratio ${}^{b}/_{a} \ll 1$ as the concept is only valid for non-spherical bubbles. Note that the above revision does not affect the critical crack size in equation 2 as this depends on the fracture toughness of the sediment K_{ic}, and not the stress intensity factor of the crack/bubble tip K_1.

Although we suggest further work is needed to refine this model, particularly to take into account sediment properties and (most importantly) the wetness of a bubble fracture wall, the mechanism proposed by Algar et al. (2011) of stable fracture propagation is still our best working model, showing good agreement with field data.

In the marine environment gas originating deep below the seabed is subject to a large overburden pressure. This high-pressure causes bubble fractures to ascend via stable propagation with minimal absorption into the surrounding water, as previously mentioned. The gas will continue to rise until the net solute supply through its surface drops to zero, creating a so-called “gas horizon” (i.e., a surface across which bubble ascension stops) (Sirhan et al. 2019), which can, in turn, create a secondary gas reservoir. This horizon is commonly related to variations in grain size, which are typically stratified in marine settings. Thereafter, to reach the water column, the gas must be mobilized by either i) decreasing hydrostatic pressure (commonly due to tidal

variations), altering the depth of the gas horizon to some point above the seabed, allowing stable propagation to resume (Sirhan et al. 2019, Katsman 2019); or ii) the formation of fluid conduits connecting the gas horizon to the seabed, allowing gas to rise via dynamic propagation. It should be noted that for the STEMM-CCS release experiment we introduced gas above some naturally-occurring gas horizons.

3.2.2 Dynamic Propagation

Dynamic bubble fracture propagation occurs either when a crack exceeds a certain critical length (e.g., due to the crack propagating into some pre-existing cavity) or due to rapid variation in loading on the surface of the bubble (e.g., due to internal waves in the overlying water column), which is characterized by a continuously increasing stress intensity factor K_1 at the tip of the bubble (Sirhan et al., 2019). The crack propagates rapidly forming a long-elongated fracture towards the seabed. The internal gas quickly rises upwards, potentially into the water column, reducing the internal pressure and allowing the fracture to close (Katsman 2019).

The passage of a bubble fracture through sediment will momentarily weaken the strength of the sediment left in its wake as the grains are temporarily displaced from their originally stable position. As a result, the buoyant forces required for a subsequent bubble fracture to rise do not need to do as much work to displace the grains. This weakening of sediment facilitates the propagation route for subsequent bubbles fractures. Initially, these conduits are narrow and easily blocked off by external pressure changes condensing/strengthening the sediment but as time goes on the longer-lasting of these channels become more permanent. The continuous passage of bubble fractures through the same area extends the sediment weakening to a larger area (centimetre scale), enhancing the fluid (gas) conductivity through the sediment. Eventually, bubble fractures begin to connect together (i.e., extending crack length beyond the critical length a_r) leading to a transition from stable to dynamic propagation (Katsman 2019, Sirhan et al. 2019). Over time, these dynamic pathways slowly become connected forming open conduits through which gas can pass virtually unrestricted for as long as the gas flux is sufficient to maintain the

internal pressure of the fracture, preventing pathway closure. This can be considered the creation of a small-scale chimney structure.

3.2.3 The Acoustics of Gas Bearing Sediments

The use of ultra-high-frequency (UHF; kHz range) marine seismic reflection to create time lapse studies of marine sediment is still relatively rare (Vardy et al., 2017), mainly due to the demanding positional requirements. However, Faggetter et al. (2020) demonstrate that with high-accuracy positioning and careful processing it is possible to image tidally-influenced methane migration on a decimetre-scale between repeat chirp surveys within shallow marine sediments. Time-lapse imaging of CO_2 migration using chirp profilers was completed as part of the QICS project during which CO_2 was injected 10 m below the seabed of a shallow loch in western Scotland (Cevatoglu et al., 2015). The QICS experiment was completed at ~10 m water depth, so its results are of limited use for deeper marine settings that are of greater interest to the CCS community. Landrø et al., (2019) used time-lapse seismic reflection data in a deep marine (>100 m water depth) setting to study the migration of gas resulting from a hydrocarbon exploration well blowout in the North Sea, at 4700 m depth. They found that most of the leaked gas became trapped in shallow sand layers within the first 1000 m of sediment beneath the seabed indicating a possible tendency for gas flow to become static after an extended period (~20 years). However, they were unable to focus on the small-scale alterations in the near-surface given the nature of their survey equipment. The STEMM-CCS study is thus in a unique position to examine the initial migration of gas through the near-surface and the formation of chimney structures in a deep (>100 m water depth) marine environment with the use of pseudo-3D time lapse 2D seismic reflection chirp data.

3.3 STEMM-CCS Controlled Release Experiment

The STEMM-CCS controlled CO_2 release experiment was conducted in the central North Sea near the Goldeneye platform (Fig. 3.1a), approximately 100 km northeast of Peterhead, Scotland, at ~120 m water depth (Shell 2018). The area has been identified as a potential CCS site (Dean and Tucker 2017).

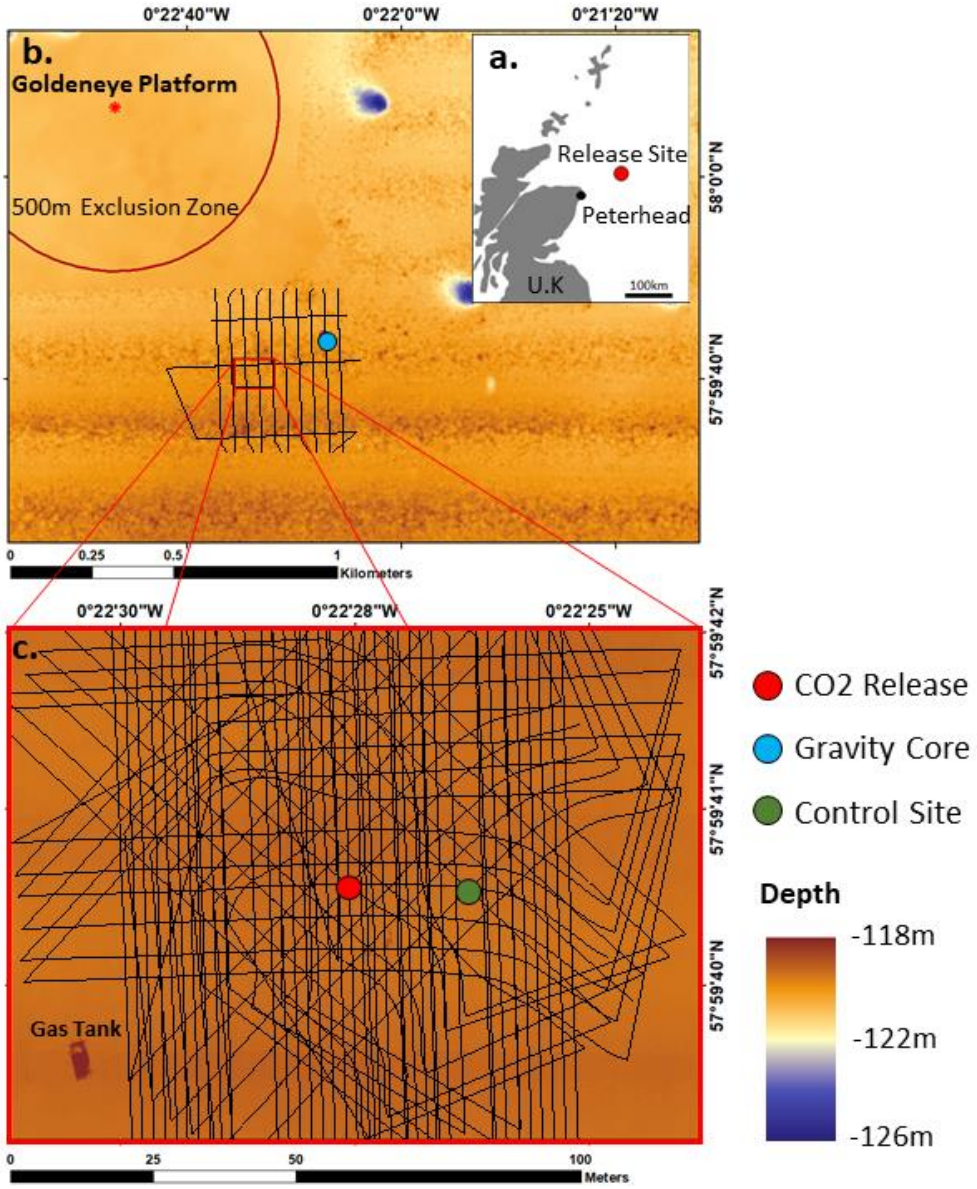

Figure 3.1: Location of the CO_2 controlled-release site and survey configuration a) The Goldeneye complex located 100 km northeast of Peterhead. b) Position of pre-release autonomous underwater vehicle-mounted chirp profiles (black lines) in relation to the Goldeneye platform and gravity core position (in purple). c) Positions of the syn- and post-release AUV chirp profiles. The epicentre of the CO_2 release (red dot), chirp profile is shown in Fig. 3.4, and the location of the control site (green dot) is shown together with bathymetry.

For the experiment, a curved pipe was pushed into the unconsolidated marine sediments with the leading end terminating ~3 m below the seabed (Flohr et al., 2021). The surface end of the pipe was connected to a specially built gas container located 80 m east of the pipe, that contained 3 tonnes of CO_2 gas and additional gas tracers (positions shown in Fig. 3.1c). The subsurface end of the pipe comprised a 460 mm long sintered stainless-steel diffuser, with a pore size of 9 µm, through which the gas was injected into the sediment. The pipe had an upward curve to ensure that the sediment directly above the release point was undisturbed by its emplacement and migration pathways could develop naturally.

During the main phase of the experiment, gas was released into the sediment via the injection pipe. The injection rate was 6 kg/day on day 0 (D 0; Table 3.1) and almost immediately after injection began sporadic gas bubbles were visible along the seabed above the release site and within hours small seeps (the continuous release of gas bubbles from a fixed position) began to form. The injection rate was progressively stepped up (see Fig. 3.2 and Tbl. 3.1) to a maximum of 143 kg/day (D+8) before gas release was stopped on Day + 11.

A large number of techniques were deployed to detect and monitor the escaping CO_2 in the subsurface sediments and the overlying water column, including geochemical, optical, passive acoustic, and seismic reflection profiling. This paper will examine the 2D seismic reflection chirp data collected before (D-13), during (D+3, D+6, D+9), and after (D+16) injection, alongside a gravity core collected prior to release, in order to assess the spatial and temporal propagation mechanism of CO_2 in the subsurface. Full details on the STEMM-CCS experiment are provided in Flohr et al. (2021).

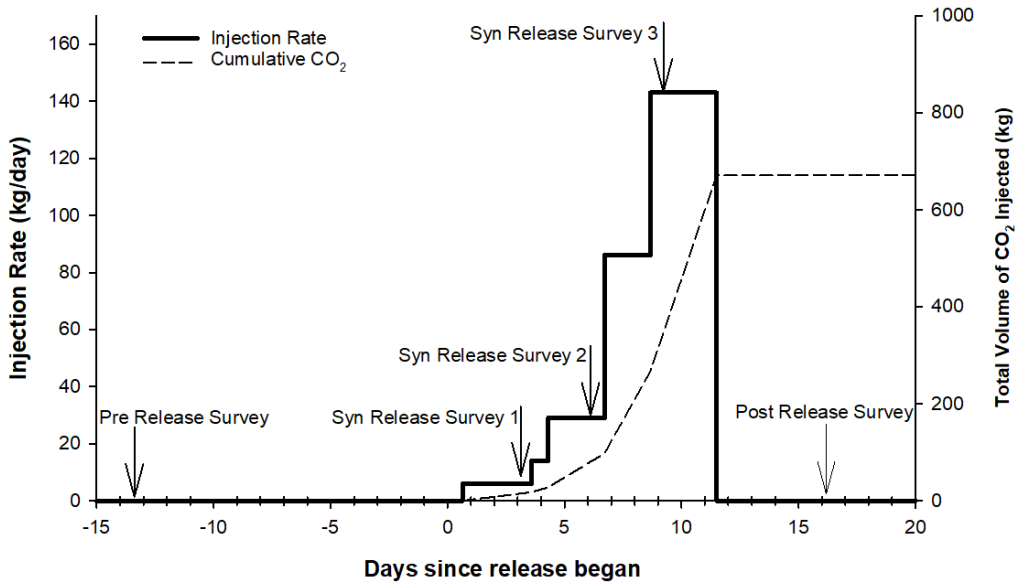

Figure 3.2: Gas injection rate and total volume of CO_2 injected during the STEMM-CCS experiment in the North Sea, and the times at which the AUV chirp seismic reflection profiles were acquired.

Date	Time	Days since release (D)	Event
28/04/19	**~13:00**	**-13**	**Pre-Release Survey (0 kg/day)**
11/05/19	15:27	0	Gas Injection Start 6 kg/day
14/05/19	**~07:00**	**+3**	**Syn-Release Survey 1 (6 kg/day)**
14/05/19	15:27	+3	Gas Injection Increase 14 kg/day
15/05/19	06:48	+4	Gas Injection Increase 29 kg/day
17/05/19	**~07:30**	**+6**	**Syn-Release Survey 2 (29 kg/day)**
17/05/19	16:54	+6	Gas Injection Increase 86 kg/day
19/05/19	15:50	+8	Gas Injection Increase 143 kg/day
20/05/19	**~08:00**	**+9**	**Syn-Release Survey 3 (143 kg/day)**
22/05/19	11:17	+11	Gas Injection stopped
27/05/19	**~07:30**	**+16**	**Post-Release Survey (0 kg/day)**

Table 3.1: Date of acquisition of AUV-mounted chirp seismic reflection surveys with corresponding gas injection rate.

3.3.1 Subsurface Structure of Release Site

Pre-release surveys of the release site identified 6 seismic horizons throughout the study area (Fig. 3.3a). Beneath the high amplitude, continuous, undulating seabed, Unit 1, identified as the Witch member (Stoker, 1985), is a reflection free unit 2-3 ms Two Way Time (TWT) thick unit composed of moderately sorted sandy and silty muds, deposited during Marine Isotope Stages (MIS) 1-2 (Fig. 3.3b; Stoker et al., 2011). It is separated from Unit 2, identified as the Fladen member, a reflection free zone 3-4 ms TWT thick composed of moderately sorted pebbly, sandy, and silty muds deposited in a glaciomarine environment (Böttner et al., 2019) by Horizon 2, a weak continuous subparallel reflector. Horizon 3 indicates the base of the Fladen member and is a sub parallel high amplitude continuous reflector. The underlying Horizons 4-6 are high amplitude reflectors with significant topography, varying in depth 1-4 m throughout the release site. The 2D seismic reflection chirp data were tied with gravity core GC06 (Fig. 3.1b). The majority of the core is composed of homogenous silty/sandy mud and clay with high-water content, but with sparse shell fragments and small pebbles at 3 m below the seafloor (mbsf), and a coarsening in grain size to sand at ~3.4 – 4.4 mbsf. (Fig. 3.3b). This coarsening in grain size is likely to reflect the gradational contact between the Witch and Fladen members. The changing grain size is reflected in the variation in the velocity, density, and impedance plots in Fig. 3.3b. Overall Fig. 3.3b demonstrates evidence for a change from heterogeneous to homogeneous sediment with increasing depth within the Witch member at 1.5 m and a gradational contact between the Witch and Fladen members at 3.4 mbsf (Horizon 2).

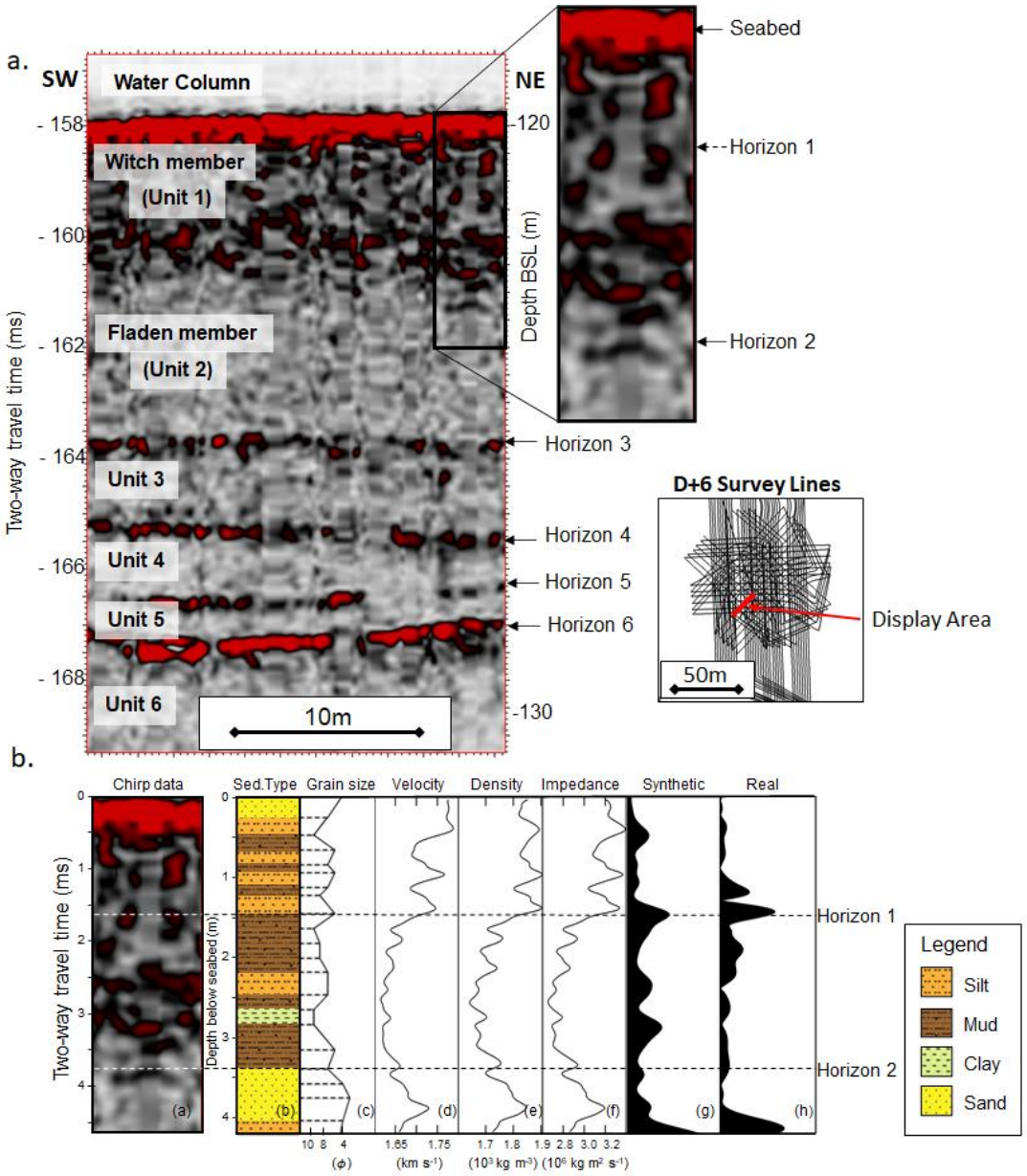

Figure 3.3: Sediment stratigraphy at the CO_2 release site. a) 2D seismic reflection chirp data (instantaneous amplitude) collected on syn-release survey D+6 with units and horizons; enlarged section for comparison with the sediment core data. Data is presented in two-way travel time (TWT) with the equivalent depth below sea level (BSL) provided. b) Seismo-stratigraphic correlation of gravity core GCO6 with chirp profiler data 500 m from the release site (position shown in Fig. 1b). Sediment interpretation with grain size; P wave velocity, density, calculated impedance with a gaussian-weighted moving average filter of window length 20 samples, synthetic trace based on core data, and real trace from corresponding chirp data. Superimposed on the plots are the interpreted positions of two horizons, one at 1.5 mbsf and one at 3.4 mbsf.

3.4 Subsurface Infrastructure

The injection pipe (Fig. 3.4) was clearly visible in multiple seismic reflection profiles throughout the release phase of the experiment, which served as our own method to determine the subsurface position of the pipe. As visible in Fig. 3.4b, the deepest part of the carbon steel pipe approximately two-thirds along its length is located at 4 ms TWT (~4 m) beneath the seabed while the release point is at 3 ms TWT (~3 m) beneath the seabed. This is an important observation as it allows us to pinpoint the exact location of the gas release, within the Fladen member, just below the Witch member lower boundary (Fig. 3.3).

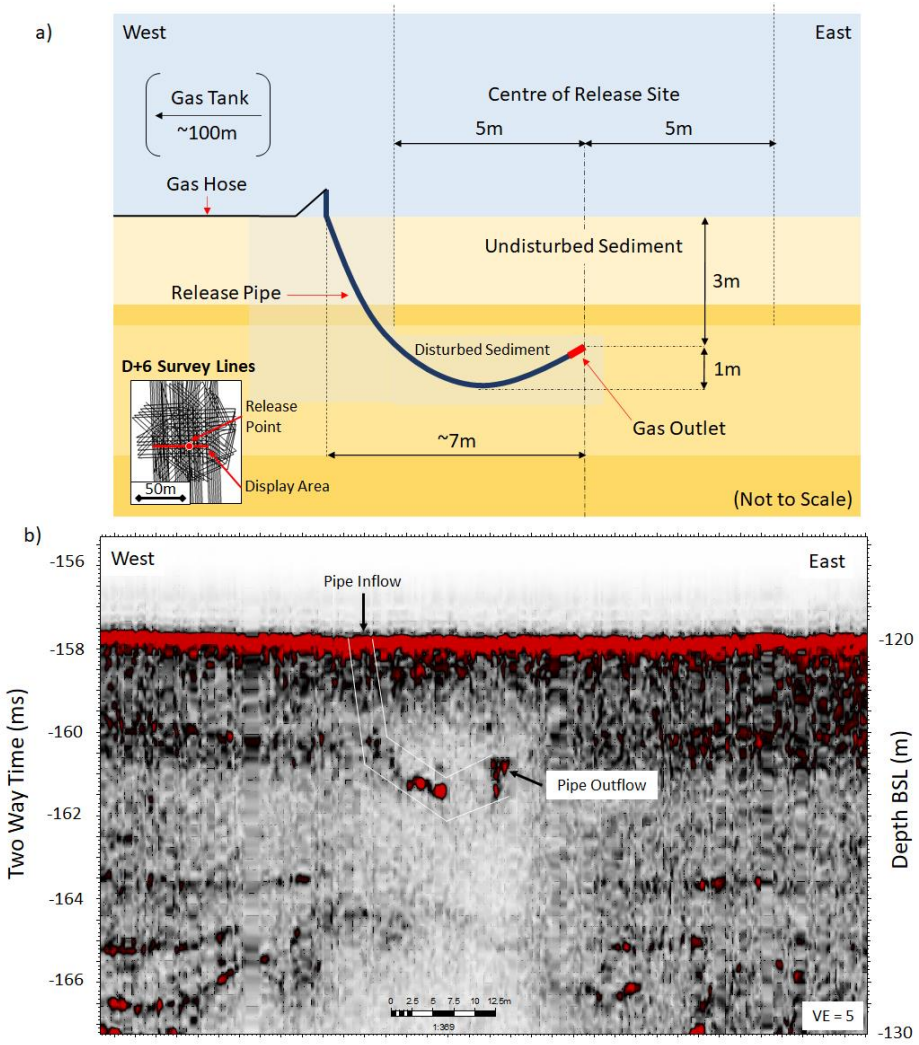

Figure 3.4: Geometry of sub-seabed gas release pipe a) schematic diagram b) projected onto the 2D seismic reflection chirp data (Instantaneous Amplitude), collected during D+3. The approximate position of the release point (outflow) is visible just beneath the Witch/Fladen member boundary (Horizon 2) at 3 ms beneath the seabed (~3 m). The bright spots in the centre and end of the pipe indicate the accumulation of gas within the pipe and immediately around the diffuser.

3.5 Methodology

3.5.1 2D seismic reflection chirp data acquisition

Five high resolution, closely spaced 2D seismic reflection chirp surveys were completed so that gas migration in the sub-surface could be understood: one pre-release, three syn-release, and one post-release (Fig. 3.2; Tbl. 3.1). The chirp system was integrated on a GAVIA Autonomous Underwater Vehicle (AUV) which followed pre-programmed routes at either 7.5 or 2.0 m above the seabed. The single channel sub-bottom profiler produced a chirp sweep with source frequencies between 14 and 21 kHz. The source sweep durations for the 7.5 m elevation surveys was 5 ms at maximum power, while the 2 m elevation survey used a shorter sweep length of 1 ms with reduced power. Surveys were conducted at 15 pings per second which equates to an average ping spacing of ~7 cm. The data were recorded in both correlated waveform and uncorrelated raw SEGY data format.

The correlated data was processed using the following flow: band-pass filter (13.5-14.0-21.0-22.0 kHz), top mute, time varying gain, static correction using the mean Gavia elevation, trace mixing (3-point moving average), Stolt constant velocity migration (Stolt 1978) of 1483ms^{-1} based on average water column measurements and automatic gain control (1.3 ms length), and finally enveloped. Enveloping the data allows us to view its instantaneous amplitude improving data interpretability and enhance imaging of the gas. The Gavia navigation data were corrected using the ship's Ultra-short baseline acoustic positioning system. Time-lapse chirp data were static-corrected so that the two-way-time to the seabed was consistent with bathymetry data collected during the cruise, and lateral drift corrected by using the position of static seabed infrastructure.

The pre-release, pre-installation survey (Fig. 3.1b and Fig. 3.5a) provided a reference data set against which to benchmark changes in physical properties due to gas injection. As this survey was also used to identify an experiment site where the near-surface sediment (the Witch member) was a uniform thickness it needed to cover a much larger area than later surveys resulting in a

sparse survey grid. The on-site grid of lines covered an area of 500 m x 400 m, with a line spacing of 40 m in a north-south direction.

The syn- and post-release surveys were designed to observe the migration of the gas through the sediment while CO_2 was injected at varying rates (Tbl. 3.1) to determine the longevity of gas in the substrate after the experiment had been concluded. The surveys comprised identical dense grids of lines centred above the epicentre of the release experiment (Fig. 3.5b-e). Lines were collected at 7.5 m height in a N/S orientation with a 2 m spacing, in a NW/SE and NE/SW with 5 m spacing and at 2 m height in a E/W orientation with a 5 m spacing (Fig. 3.5b-e).

The data has a vertical resolution of 2 cm, based on a quarter of the dominant chirp wavelength (Kallweit and Wood, 1982). The horizontal resolution (1st Fresnel zone) at a depth of 3 m (i.e., the release point) has a width of 70 cm for the 2 m elevation survey while the 7.5 m elevation survey had an equivalent resolution of 100 cm. Given the close line spacing and interlaced survey pattern, the syn- and post-release surveys are in effect pseudo 3D, making the dataset as a whole a pseudo 4D seismic time-lapse.

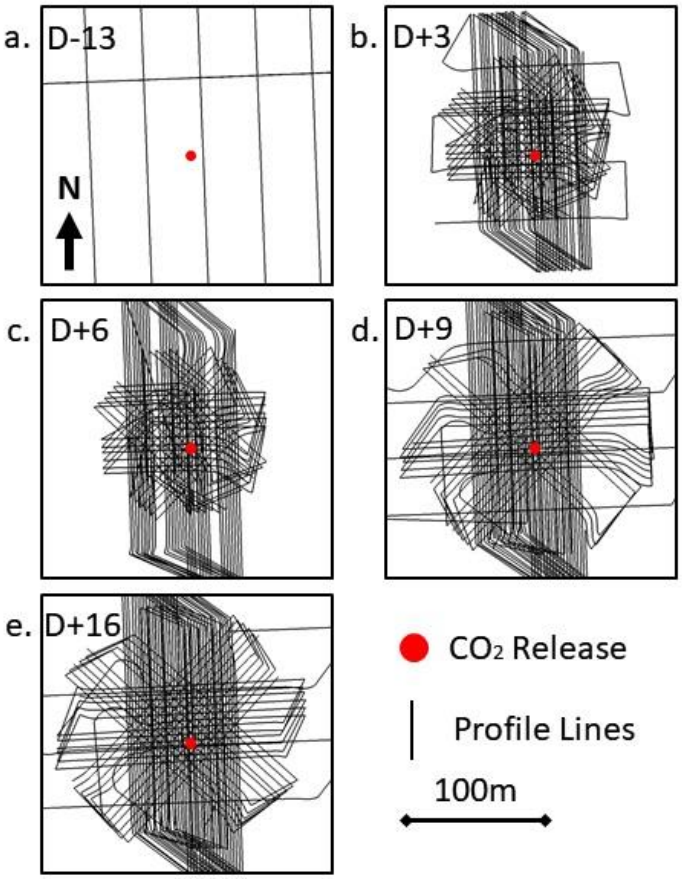

Figure 5: 2D seismic reflection chirp surveys over the release site collected with an Autonomous Underwater Vehicle. a) D-13 CO_2 pre-release profiles; b) D+3 syn-release profiles, c) D+6 syn-release profiles, d) D+9 syn-release profiles, e) D+16 post-release profiles. The end of the subsurface pipe is indicated in red.

3.5.2 Gravity core collection and generation of synthetic seismogram

Gravity cores were collected by the RV Poseidon (POS527), sampling the upper 3-5 m of sediment prior to the CO_2 release. The closest core to the release site, GC06, was analysed for this study (Fig. 3.1b). The sediment interpretation was based on a modified Udden-Wentworth grain-size scale (Blair and McPherson 1999) and observations of colour change, water content, and fossil content. P-wave velocity, density, and resistivity measurements were made using a Geotek Multi-Sensor Core Logger. From the velocity and density data, a synthetic seismic trace was calculated by convolving the gradient of the smoothed impedance (reflectivity) with the chirp sweep (14 – 21 kHz) Klauder wavelet and enveloping the resulting data for later comparison to the acquired chirp seismic traces.

3.6 Results and Analysis

3.6.1 Time lapse imaging of CO_2 induced acoustic anomalies

Day 3) 6 kg/day Release Survey

The seismic reflection data on D+3 (Fig. 3.6b) appears near identical to the pre-release survey on D-13 (Fig. 3.6a) with no changes in reflectivity of the sub-surface. The only visual difference relates to the improved quality of data acquisition following a change in survey pattern. Directly above the release point bubbles are visible in the water column, though no clear escape pathways are imaged in the underlying sediment (Fig. 3.6b).

Day 6) 29 kg/day Release Survey

Seismic reflection data on D+6 (Fig. 3.6c) again appears unchanged compared to the pre-release survey on D-13 (Fig. 3.6a) as well as the previous syn-release survey on D+3 (Fig. 3.6b). The Fladen member appears unchanged. While evidence of bubbles can be seen in the water column in the form of strong reflectors above the seabed there are no clear escape pathways visible in the underlying sediment (Fig. 3.6c).

Day 9) 143 kg/day Release Survey

Seismic reflection data on D+9 shows a strong increase in the reflectivity in the bottom 0.5 ms TWT of the Witch member directly above the release point, extending ~4-5 m in an east west direction and ~7-8 m in a north-south direction, see Fig. 3.6d-f. Additionally, the Witch/Fladen member boundary horizon underlying this appears to bow upwards to a maximum of 0.4 ms TWT. Directly below this zone, a distinct shadowing effect is visible, suggesting minimal penetration of the acoustic signal beyond this point. Below this the Fladen member appears acoustically unchanged.

Also visible in the seismic reflection data is highly reflective linear features connecting the underlying enhanced reflector with the seabed, see Fig. 3.6e and f. These chimney features appear to be only a few 10's of centimetres in diameter, which is close to our minimum detection

threshold. Immediately overlying them gas is clearly visible in the water column, escaping from a shallow depression in the seabed (~5 cm wide by 0.2 ms TWT deep). A 3D interpretation of this data set is given in Fig. 3.7.

Post Release Survey

By D+16 (5 days after gas injection stopped) the seismic reflection data (Fig. 3.6g) appears to be similar to the pre-release data collected on D-13 (Fig. 3.6a). The previously visible enhanced reflectors, bowing horizons, shadowing and chimneys are no longer present, leaving no acoustically visible evidence of the injection experiment.

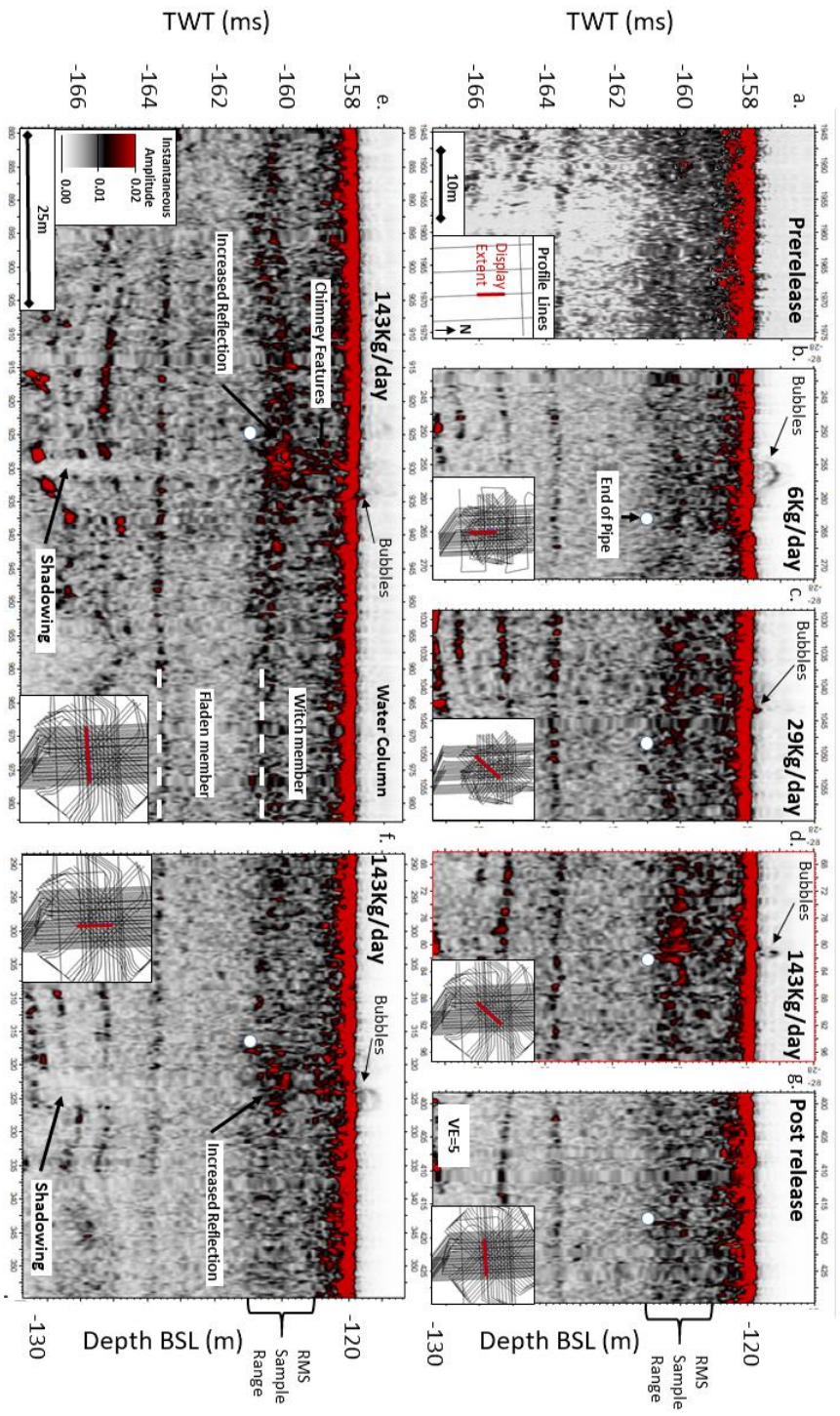

Figure 3.6: Gavia 2D seismic reflection chirp data cross-section of the release site displaying the instantaneous amplitude. a) D-13 before injection b) D+3 at 6 kg/day injection, gas is visible in the water column but there is no evidence for gas in the underlying sediment; c) D+6 at 29 kg/day injection rate there is no evidence of gas within the sediment d-f) D+9 at 143 kg/day injection, evidence of a gas pocket can be seen by the increased level of reflection from the base of the Witch member and the distinct shadow underneath. The column-like strong reflectors extending from the gas pocket to the seabed are likely gas chimneys, large scale fluid escape features. g) D+16 after injection was stopped all evidence of gas has disappeared and the image appears near identical to the pre-release profile shown in a). Data is presented in two-way travel time (TWT) with the equivalent depth below sea level (BSL) provided.

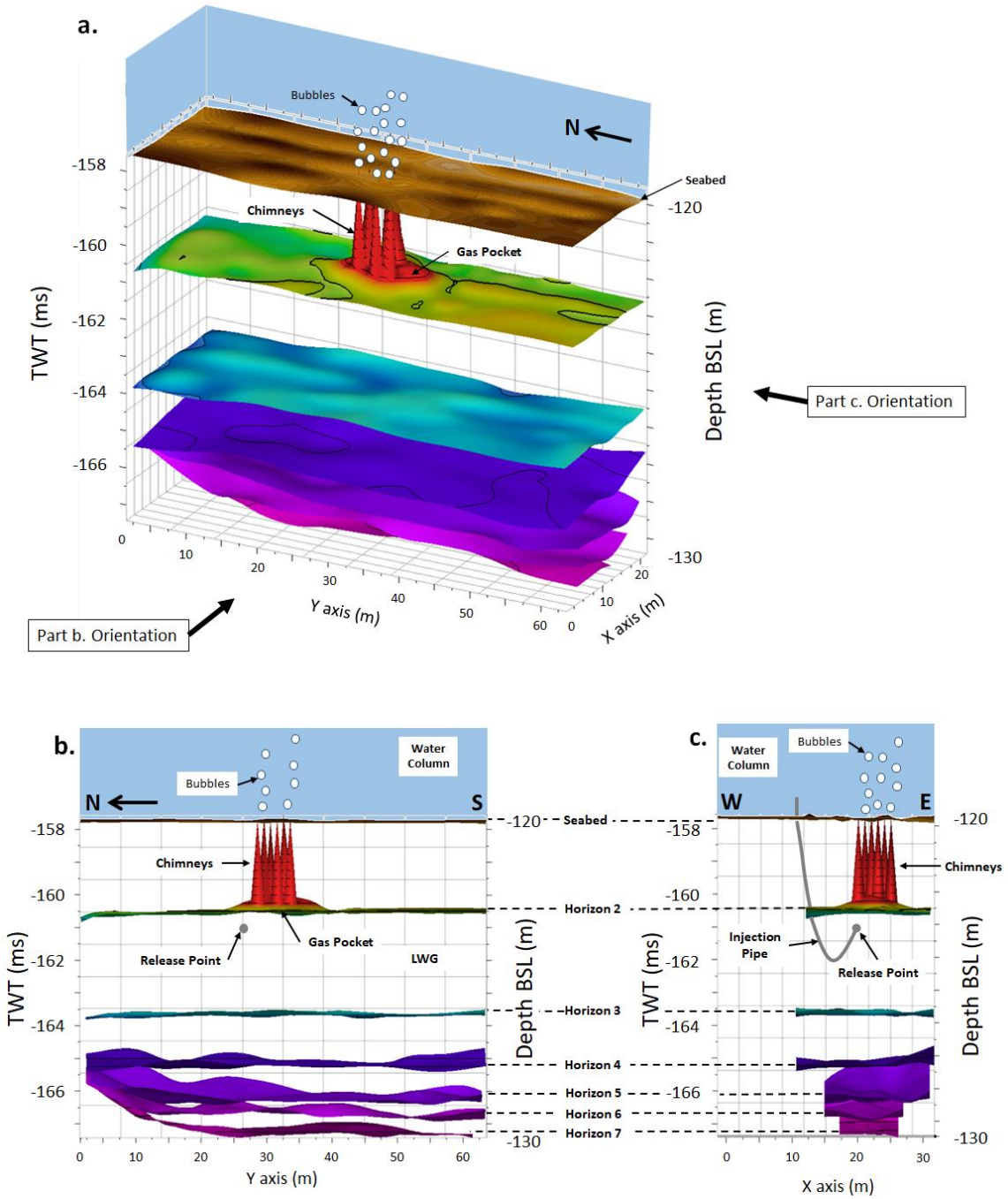

Figure 3.7: 3D interpretation of seismic horizons directly beneath the release site at 143 kg/day injection rate with the resulting gas pocket and fluid escape features (chimneys) shown in red. a) Facing NE; b) facing East, release point indicated in grey, and c) facing north, release point and injection pipe indicated in grey. Data is presented in two-way travel time (TWT) with the equivalent depth below sea level (BSL) provided.

3.6.2 Seismic evidence of CO_2 distribution in the subsurface

Seismic signatures related to increasing CO_2 saturation in the sediment include reflectivity enhancement and energy dissipation (Anderson and Hampton 1980). Energy loss is caused by bubble fractures present in the sediment, which resonate at certain frequencies and scatter the incident sound. We were able to compare the amplitude spectrum of the release site throughout the experimental period with that of a control site ~20 m east (see Fig. 8). The dominant frequency at the control site remained approximately constant (17620 ±100 Hz, at -30 dB) throughout the experiment. By contrast, at the release site the frequency (at -30 dB) decreased by ~2.5 % from the pre- to the first syn-CO_2 release survey, this trend continuing to a total decrease of 3.7 % (relative to the pre- release survey) by D+6, before becoming constant thereafter up to the end of the CO_2 release. These changes could be related to a residual CO_2 fraction in the sediment or an alteration of the sediment properties or a combination of both.

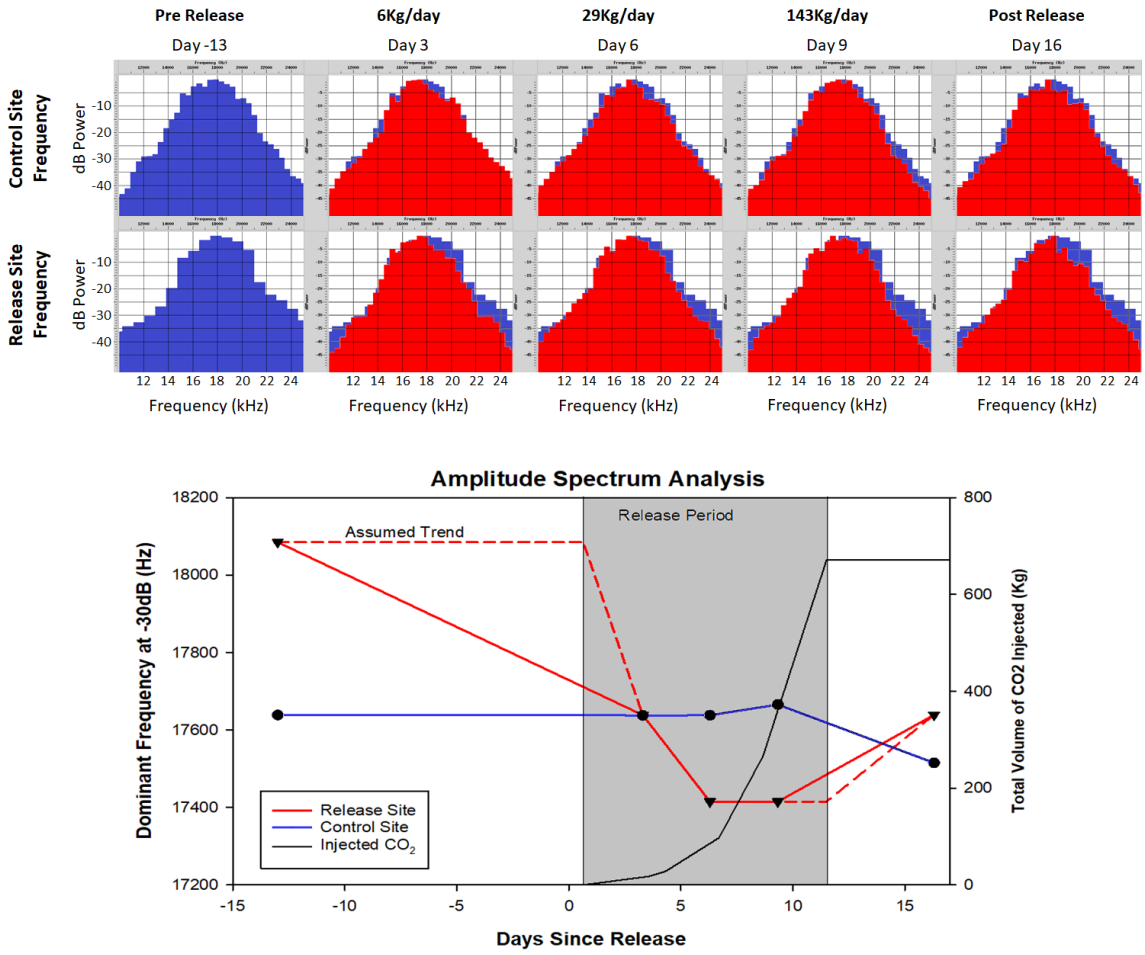

Figure 3.8: Temporal and spatial variation of the seismic amplitude spectrum of 2D seismic reflection chirp data between 1 - 3 ms TWT below the seabed. (a) Amplitude spectrum of the seismic data at a control site and at the release site throughout the experiment (positions shown in Fig. 1c). Shown in blue is the pre-release spectrum for comparison. The release site shows a notable decrease in the presence of high frequency signals as soon as injection begins. (b) Graph of the dominant frequency at −30 dB at the control site (solid blue line) and the release site (solid red line). A decrease in dominant frequency is seen in the release site during the syn-release surveys, followed by an increase in the post-release survey. As we attribute the change in the release rate to the injection of gas, an interpreted trend (dashed red line) is also shown.

Fig. 3.9 shows the root mean square (RMS) amplitude for a TWT time interval 1-3 ms beneath the seabed (~0.9-2.6 mbsf). As the presence of free gas greatly affects the impedance of sediment (Anderson and Hampton 1980) it is often clearly visible in RMS amplitude maps. On D+3 when gas was being injected at 6 kg/day, the RMS amplitude at the release site (12.5 m radius around the injection point) was 0.033 ±0.002 with no obvious hot spots. By D+6 (at 29 kg/day), this average RMS value was unchanged across the release site, although a single “high amplitude” point of 0.040 (>1 m wide) had developed ~3 m north of the injection point. On D+9, at the

maximum flow rate (143 kg/day), a large high amplitude zone ~8 x 5 m wide of 0.045 had developed to the east of the central injection point. Meanwhile, the average RMS value across the release site remained constant. Spatially and geometrically, this zone is consistent with the enhanced bowing reflector seen in cross-section (Fig. 3.6e). The smaller high amplitude point seen on D+6 was still visible, although it had migrated several meters north. The post-release survey on D+16 (5 days after injection was stopped) shows that the high amplitude anomalies completely disappeared, and the whole site still had an RMS value of 0.033 ±0.002, suggesting this is the natural undisturbed value for the sediment. It is thus logical to conclude the RMS changes are associated with the degree of CO_2 saturation within the sediments, with large high amplitude zones corresponding to gas pooling or chimney structures.

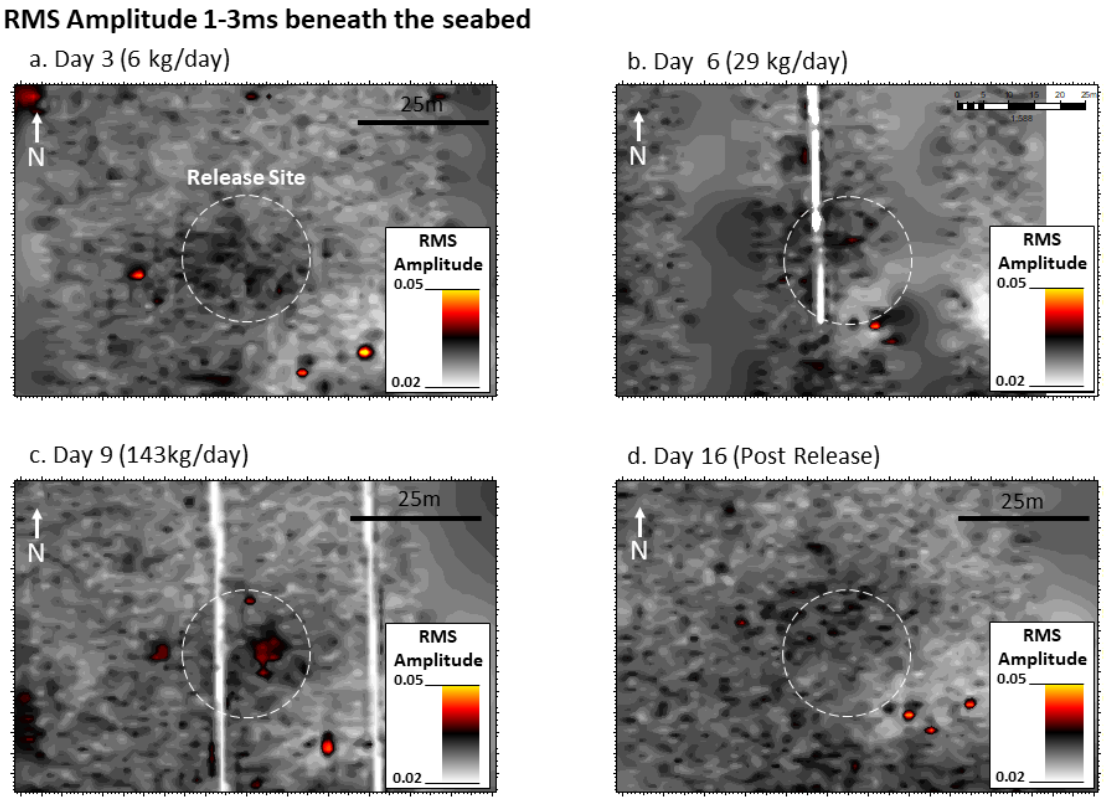

Figure 3.9: Chronological maps of RMS amplitude (1 – 3 ms TWT beneath the seabed) over the experimental site with the release point located in the centre of the white circle. a) D+3 6 kg/day b) D+6 29 kg/day c) D+9 143 kg/day d) D+16 post release. Note the appearance of a high amplitude zone at 143 kg/day that then disappears post injection. Linear white zones during D+6 and D+9 are due to errors in data collection resulting in unusable profile lines. Anomalies outside the release area are deemed to be either noise or the result of reflections from experimental landers on the seabed.

Fig. 3.10 shows the deformation of Horizon 2, the upper boundary of the Fladen member (i.e., top of the sandy layer seen in Fig. 3.3), using its observed depth on D+3 as a baseline. D-13 is not examined as the profile lines collected during this period were too sparse. Horizon 2 was selected as it is believed to lie directly above the potential gas pocket. Horizons beneath a gas pocket are more difficult to accurately position, especially on the decimetre scale, as the presence of gas alters the sound speed. Given the nature of uncertainty related to AUV positioning systems an error of ±0.25 ms TWT can be expected here. On D+6 (29 kg/day injection rate) at the release site the horizon is 0.1 ms TWT closer to the seabed than on D+3, well within positional error. However, on D+9 Horizon 2 appears 0.40-0.50 ms TWT (0.3 ±0.1 m) closer to the seabed than on D+3 in a 10 x 7m wide zone centred just east of the release point. This is a variation in depth too great to be a consequence of positional error. By D+16, 5 days after gas injection was stopped, Horizon 2 appears 0.20-0.25 ms TWT closer to the seabed within the release site than on D+3, again within positional error. Given the correlation with gas injection we suggest the apparent deformation of Horizon 2 is a direct consequence of the presence of gas.

This change could be related to 1) gas pooling in the sandy layer, resulting in sediment swelling and narrowing of the overlying Witch member; or 2) due to the presence of gas in the overlying sediment increasing the seismic velocity via resonance. The latter option can be dismissed because the base of the horizon remains approximately constant (~2.32 ms TWT beneath the seabed) for the frequency range 15-20 kHz (i.e., frequency close to resonance). We are thus confident that the deformation of Horizon 2 is a real physical change caused by the pooling of gas within the upper sandy layer of the Fladen member.

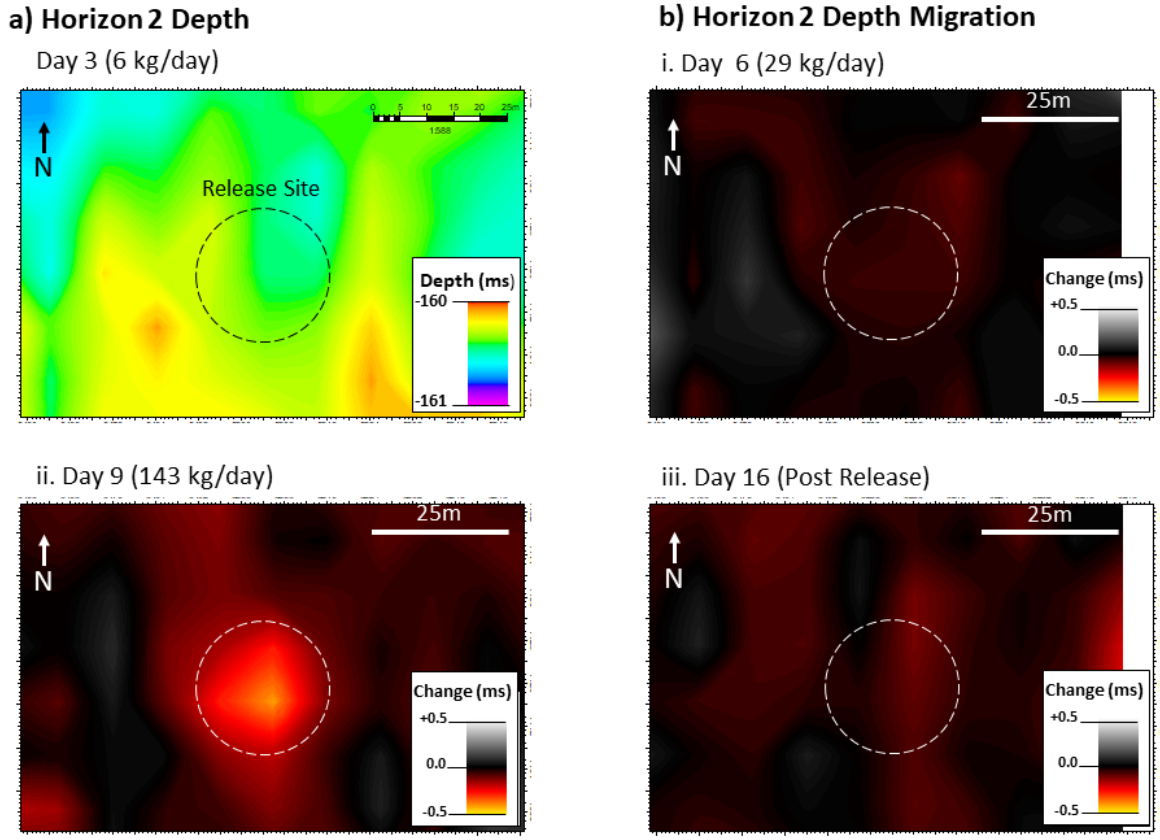

Figure 3.10: Map of the release site with the release point located in the centre of the white circle showing a) the depth of Horizon 2 on D+3 in TWT, b) the change in the depth of Horizon 2 relative to its position on D+3 (i) on D+6 at 29 kg/day injection rate, (ii) on D+9 at 143 kg/day injection rate and (iii) on D+16, 5 days after injection had stopped.

3.6.3 CO_2 volume estimation

To estimate the mass of injected CO_2 that can explain the uplift observed in our time-lapse seismic data for the base of the Witch member (Fig. 3.10), we assume it is caused by CO_2 injection in the pores and steady state conditions of CO_2 gas flow. Then, the change in sediment porosity over time is given by:

$$\frac{D\varphi(V_\varphi,V_s)}{Dt} = \frac{D}{Dt}\left(\frac{V_\varphi}{V_\varphi+V_s}\right) = \left(\frac{\frac{D}{Dt}V_\varphi(V_\varphi+V_s)-V_\varphi\frac{D}{Dt}V_\varphi}{(V_\varphi+V_s)^2}\right) = \frac{D\varepsilon_v}{Dt}(1-\varphi_0), \tag{3.4}$$

where φ_0 is the initial porosity before CO_2 injection, V_φ and V_s are the volume of pores and solid grains, respectively, and ε_v is the volumetric deformation which can be expressed as,

$$\varepsilon_v = \frac{\Delta V}{V_0} = \varepsilon_1 + \varepsilon_2 + \varepsilon_3,$$

(3.5)

where ΔV is the increment in sediment volume, V_0 is the initial sediment volume and $\varepsilon_1, \varepsilon_2, \varepsilon_3$ are the deformations in the three principal directions of strain. Assuming that the three principal directions of strain are orientated with the Cartesian coordinate system (x, y, z) and that deformations occur only in the vertical direction we obtain,

$$\varepsilon_v = \varepsilon_{zz} = \frac{\Delta H}{H_0},$$

(3.6)

where ΔH is the sediment uplift, and H_0 is the initial injection depth (the point at which gas enters the affected layer). Combining Eqs. 3.4 and 3.6 we can estimate the total change in porosity ($\Delta\varphi$) due to CO_2 injection as,

$$\Delta\varphi = \frac{\Delta H}{H_0}(1 - \varphi_0).$$

(3.7)

To facilitate the calculation, we approximate the deformed volume to that of a cylinder with the height given by the uplift, and no CO_2 dissolution. Then, we can estimate the volume and mass of injected CO_2, as:

$$V_g = \Delta\varphi V_t = \Delta\varphi(\Delta H + H_0)\pi r^2,$$

(3.8)

$$M_g = V_g \rho_g.$$

(3.9)

In Eqs. 8 and 9 V_g, M_g and ρ_g are the volume, mass, and density of CO_2 gas, respectively, V_t is the total volume of sediment, and r is the radius of the cylinder. To calculate the density of

CO_2 we use the table for CO_2 thermophysical properties from the National Institute of Standards and Technology (*https://webbook.nist.gov/chemistry/fluid/)* assuming the pressure and temperature conditions at half distance between the CO_2 injection depth and the seabed. Finally, the saturation of CO_2 gas (S_g) that explains the observed uplift can be estimated by,

$$S_g = \frac{V_g}{V_\varphi} = \frac{\Delta\varphi}{(\varphi_0+\Delta\varphi)}. \quad (3.10)$$

The elliptical dome observed in the dataset was 4.5 ±0.5 m east-west, and 7.5 ±0.5 m north-south, with a maximum height of 0.3 ±0.1 m (Fig. 3.10b). A cylinder with the same sediment uplift and an equivalent volume has a radius of 2.4 ±0.2 m. We consider an initial injection depth (the point at which gas enters the sandy layer) of 2.5 m, an initial porosity of 0.51 ±0.05 (from logging; Fig. 3.3), a seabed temperature of 7°C, a geothermal gradient of 0.03°C/m. Using these values, we estimate that 91 ±32 kg of CO_2 was retained in sediment on D+9 (in gaseous form), which corresponds to a CO_2 saturation of 0.10 ±0.03. The total volume of gas injected between raising the injection rate to 143 kg/day and the 3rd syn-release survey (when the pocket was visible) was 242 kg. We, therefore, suggest that 34 ±12% of the injected gas remained within the sediment in the gaseous form during this period.

3.6.4 Hydrodynamic analysis

It is possible to calculate the permeability of the CO_2 pathways beneath the release site on D+9 based on the observations of the gas pocket developing when the injection rate was at a maximum. If we assume one-dimensional poro-elastic expansion of the sediment, then the amount of pore fluid overpressure (u) generating the inferred vertical uplift is given by (Wagen and Halvorsen, 2019).

$$u = \frac{\varepsilon_{zz}}{\alpha}\left(\frac{4}{3}G + K\right),$$

(3.11)

where G is the shear modulus of the sediment and α is the Biot's coefficient.

$$\alpha = 1 - \frac{K}{K_s}.$$

(3.12)

In Eq. 3.12, K is the bulk modulus of the sediment at drained conditions, and K_s is the modulus of the solid grains. For the unconsolidated, soft sediments considered here, α can be assumed equal to 1.

We estimate our pore fluid overpressure for the maximum uplift of 0.3 m is ~0.35 ±0.1 MPa, adopting representative values of the type of sediments within our depth of interest for *K* and *G* (~1 MPa). Our estimate is higher than that measured with a sensor at the end of the CO_2 injection pipe (~0.08 MPa). A better match can be found if the uplift was only ~0.1 m, which is not unrealistic if we imagine the sound speed is depressed by the presence of bubble fractures (Leighton and Robb 2008) causing us to slightly overestimate thickness. Using this value, we can also estimate the effective permeability of a CO_2 pathway connecting the injection depth with the seabed using Darcy's relationship:

$$k = \frac{Q \cdot \mu \cdot (\Delta H + H_0)}{k_{rg} \cdot A \cdot (u - f \cdot u)},$$

(3.13)

where Q is the volumetric CO_2 bubble flow measured at the seabed, μ is the dynamic viscosity of CO_2, k_{rg} is the relative permeability of CO_2 gas, A is the area of the CO_2 pathway (i.e., the area perpendicular to the measured gas flow), and f is a dimensionless parameter between 0 and 1 controlling the fraction of pore fluid overpressure just below the seabed. Here, as observed in gas migration laboratory experiments in unconsolidated, soft, fine-grained, cohesive sediments (e.g.,

Algar et al., 2011), we can assume that the pathways are fully saturated in CO_2 gas (dry pathways), and so k_{rg} is equal to 1. Based on our discussion above, we note this is a simplification as in reality the gas bubble fracture walls are wet.

If we consider the values used and calculated above for the estimation of the CO_2 mass within the uplift area, a Q of 0.05 m^3/s, a CO_2 pathway area A of 20m^2, an f of 0.5, and a CO_2 viscosity with pressure and temperature conditions at half distance between the CO_2 injection depth and the seabed of 1.48×10^{-5} Pa s (CO_2 thermophysical properties from the National Institute of Standards and Technology; https://webbook.nist.gov/chemistry/fluid/), the effective permeability of the CO_2 pathway is ~2×10^{-14} m^2. Falcon-Suarez et al (this issue) used core analysis to estimate the effective permeability of water in the Witch Ground (collective term for Witch and Fladen members), away from the injection site, to be 2×10^{-17} m^2, 1000 times lower than our estimate, emphasizing the effect chimney structures have on the rate of gas flow through the near-surface.

3.6.5 Crack size calculations

Using measured physical sediment properties in conjunction with Eq. 3.2, it is possible to calculate the critical size of bubble fractures/cracks a_r undergoing stable fracture propagation at different depths in the near subsurface (Fig. 3.11). There is broad agreement between sediment type and critical crack size due to the relationship between crack size and solid grain density, water density, porosity, and the sediment fracture toughness. With reference to the observed seismic horizons, low values of crack length (2.2 mm) occur from the seabed to Horizon 1, across which there is an increase to ~ 3.0 mm. These higher values continue down to Horizon 2, where the increase in sand content causes a decrease in crack length to 2.6 mm.

These variations in crack size have important implications for the propagation of a bubble fracture moving upwards through the sediment. Given the coarse nature of sediment immediately

below Horizon 2 gas likely migrates via capillary invasion before transitioning to stable fracture propagation above the Horizon: the size of the fracture changing with sediment type. If a fracture exceeds the critical crack length, it will instead begin to migrate via dynamic fracture propagation (Katsman 2019). The size of a rising bubble fracture does not decrease instantaneously, thus the large and rapid decrease in critical crack size across Horizon 1 will likely result in a transition into dynamic propagation which may control gas migration to the seabed. This may cause an increase in free gas permeability in the sediment above that measured in the pre-release sediment cores.

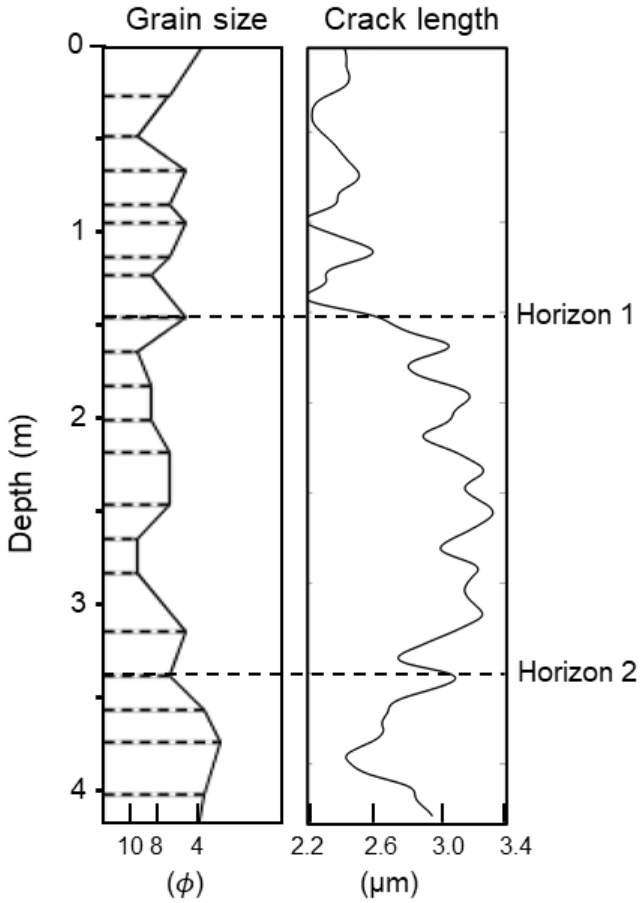

Figure 3.11. The minimum critical size (crack length) for a bubble fracture to rise through the sediment of a specific grain size. Left) grain size variations down core GC06; Right) Crack length calculated using Eq. 3.2. Significant changes in crack length are observed at Horizon 1 and 2.

3.7 Discussion

3.7.1 Migration of CO_2 in sub-seabed sediments at the Release Site

Based on the temporal and spatial development of the acoustic anomalies seen during the CO_2 release experiment along with visual seabed seep observations we propose a four-stage model for the evolution of gas migration pathways in the sub-surface (Fig. 3.12):

Stage 1 – Proto-migration: the initial migration of gas immediately following the start of CO_2 injection where individual bubbles make their own way to the surface via capillary invasion, stable and dynamic fracture propagation with no preferred pathways. Many routes will be highly inefficient, and some gas will fail to reach the seabed.

Stage 2 – Immature migration: the migration of gas occurs along preferred pathways via capillary invasion, stable and dynamic fracture propagation forming small temporary seeps on the seabed. Dynamic fracture propagation becomes more dominant as time goes on.

Stage 3 – Mature migration: the migration of gas has been optimised and occurs via open conduits or chimneys, connecting a gas reservoir to the surface (or a secondary reservoir) forming moderate to large seeps on the seabed.

Stage 4 – Closure: migration pathways have closed completely following the end of the gas injection. The system reverts to its pre migration state.

These stages are universally applicable to any near-surface seep site as general descriptors of the gas migration pathways. However, the exact length of time spent within each stage and transition between stages will vary with stratigraphy, grainsize and injection rates etc. Indeed, many seeps likely do not reach the mature stage and simply skip to the final stage from stage 2 or even stage 1 in the case of sporadic ebullition sites.

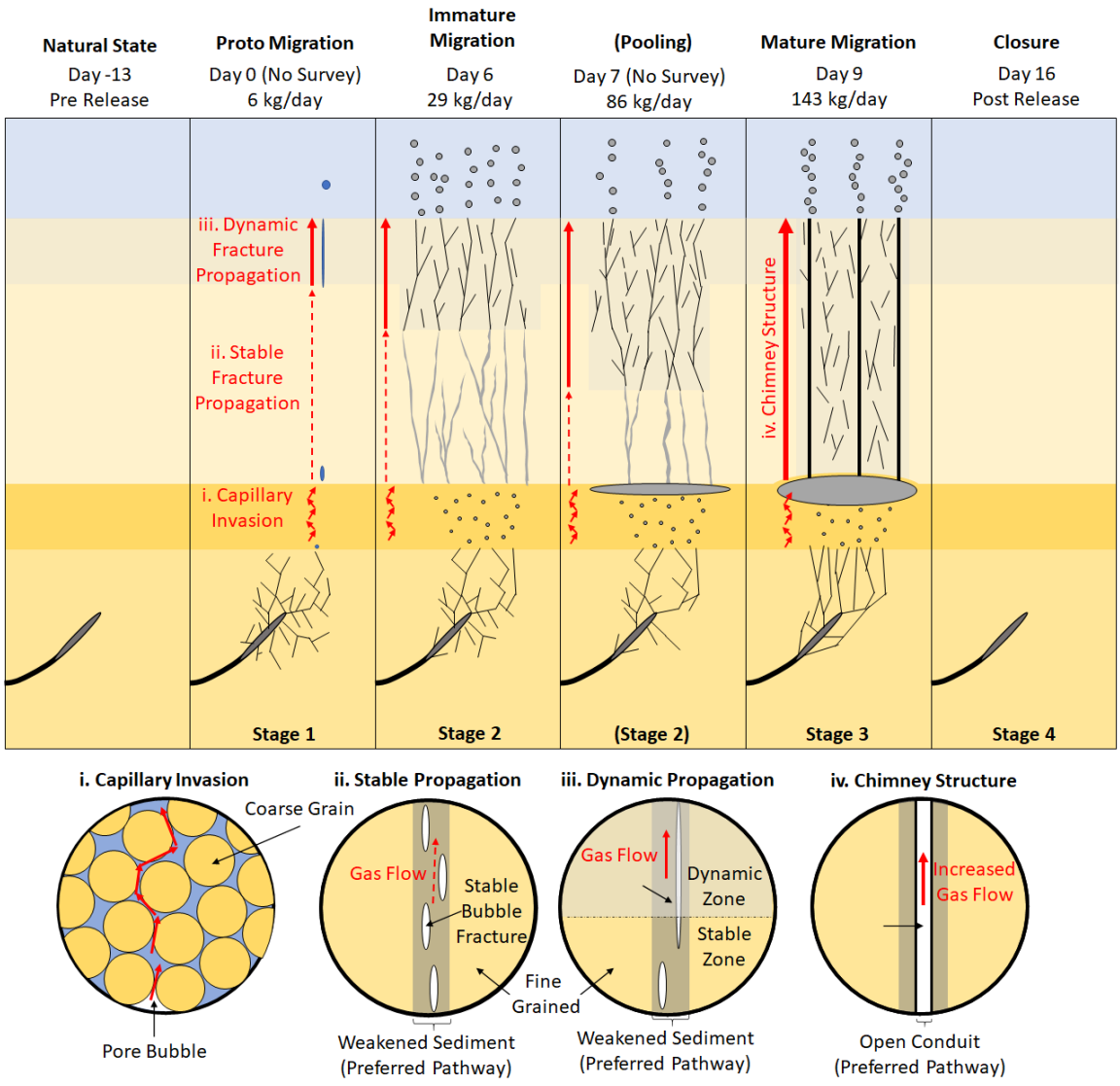

Figure 3.12: Schematic interpretation of gas migration during the release experiment and stages in the evolution of gas migration pathways. Day 0) the "proto migration" stage that occurs immediately after the start of CO_2 injection, where individual gas bubble fractures make their way to the surface with no preferred pathways. Day 6) the "immature migration" phase of the experiment where a number of temporary pathways have developed along which most bubble fractures travel. The depth below the seabed at which dynamic fracture propagation occurs increases over time. Day 7) the rate at which gas was being injected into the sediment (86 kg/day) exceeded the rate at which gas could migrate through the coarse sand layer and pooling of gas begins. Day 9) during the "mature migration" phase the dynamic fracture propagation zone extends to the gas reservoir allowing open conduits to form between the reservoir and the overlying water column. Day 16) the system has experienced the "closure" phase following the end of the CO_2 injection and the sediment has almost reverted to its original state (Day -13).

The following is a hypothesis for the dynamic gas processes within the sediment during each stage consistent with observations made in this paper.

3.7.1.1 Stage 1 - Proto Migration

The Proto-migration stage is the initial chaotic migration of gas with no preferential pathways established immediately following release (within a few hours) and cannot be imaged by acoustic methods.

While we have no direct imaging of gas migration during this phase, based on existing gas propagation theory and gravity core data we speculate the following. During the release experiment CO_2 was injected directly into the Fladen member at a depth of ~3 mbsf. The pressure from the end of the injection pipe likely generated a small fracture network into which the gas escaped. From here the gas would have migrated upwards into an overlying sand layer, ~0.5 m thick. Within the sandy layer gas would have begun migrating via capillary invasion as the larger grain size would have made fracture propagation difficult. After migrating through this layer, the finer-grained sediments within the Witch member favoured migration via stable fracture propagation, the steady rise of single bubble fractures. The gas would rise through the sediment as an upward propagating crack, sealing behind itself in order to maintain a constant pressure. Eventually, at ~1.4 mbsf depth the bubble fractures cross a grain size boundary (Horizon 1) in which the sediment is significantly weaker, and a much smaller crack size is required for stable fracture propagation (Fig. 3.11). As the bubble fractures rising to this depth are much larger than this critical fracture size, they begin to migrate via dynamic fracture propagation. The bubble crack grows rapidly upward until reaching the seabed, at which point the gas is released into the water column and the fracture closes. This interpretation is based on seabed observations and the application of LEFM to gravity core analysis. The first phase lasted less than a few hours as the first seeps were visible on the seabed within 12 hours, indicating the appearance of preferred pathways.

3.7.1.2 Stage 2 – Immature Migration

The immature migration stage is an early step in the evolution of the system, with the establishment of preferred fluid-flow routes. The passage of a bubble fractures weakens the sediment making the subsequent passage of gas more likely, thus creating a positive feedback loop that slowly builds stable fracture propagation pathways over time. These pathways are small (perhaps <1 cm in diameter) and easily destroyed by overlying pressure fluctuations i.e., internal waves in the water column, which compress sediment within the pathway (strengthening it) causing the bubble fractures to find an alternative route. It is at this stage that seeps are first seen on the seabed, though they are generally temporary in nature, becoming extinct as underlying pathways close. This is the stage most subject to change as the system slowly matures overtime, pathways will become less and less mobile before eventually becoming fixed in place and expanding. Acoustically this stage transition may be visible in the water column, but it is very hard to identify in the subsurface, except via comparison with the bulk acoustic properties of the sediment pre-release.

Day 3 (injection rate 6 kg/day) was our first acoustic observation of the system at this stage during the release experiment. Seeps are present and are highly mobile, regularly appearing and disappearing on the seabed as seen by ROV (Remotely Operated Vehicle) observations at the release site (Flohr et al., 2021). A lack of distinct acoustic anomalies in the subsurface suggests no gas was retained in the sediment as shown by clear evidence of gas release in the water column. However, the passage of gas through the sediment caused attenuation of seismic energy, decreasing the dominant frequency. That a quantifiable change can be detected at such an early stage of release, at such a low CO_2 injection rate, suggests spectral analysis of acoustic data could be a useful tool for detection. By day 6 of the release experiment (injection rate 29 kg/day) gas is continuing to flow directly from the release pipe to the surface. Fluid migration pathways are still mainly in the form of weakened stable propagation channels that are small and mobile, though the higher flow rate has resulted in a greater number of pathways (and thus seeps). The continued lack of distinct acoustic anomalies in the subsurface suggests that no gas is retained in

the sediment. The level of attenuation has increased to a maximum at this point, with the dominant frequency plateauing. It is impossible to tell whether this maximum was reached due to the increased flow rate or due to the total volume of gas that had passed through the sediment by this stage.

By day 7 of the release experiment (injection rate of 86 kg/day), we hypothesise that the flow rate out of the sandy layer at the top of the Fladen member had been exceeded by the inflow rate of gas from the injection pipe fracture network, resulting in the pooling of gas within the layer. This causes the unit to slowly expand in a localised area around the release site. While no seismic reflection survey was carried out during this period, later surveys do show clear evidence of pooling and ROV surveys on D+7 showed that no new seeps were formed as a result of increasing the injection rate and the nature of the existing seeps had not significantly changed (Flohr et al., 2021), suggesting the amount of gaseous CO_2 escaping into the water column had remained unchanged despite the rate.

3.7.1.3 Stage 3 – Mature Migration

The mature stage of gas migration is the point at which gas flow through the near-surface has been optimised. Migration is no longer via stable or dynamic fracture propagation but through stable open conduits, named here chimney structures, which allow the gas to pass unrestricted from a reservoir (primary or secondary) to the surface. This stage of gas migration is the most seismically visible as chimney structures leave distinct acoustic anomalies. This stage is also of the greatest interest to environmental studies as the high flow rate of gas through the sediment reduces the residence time of gas in the near-surface and thus increases the volume of gas released into the water column.

We propose that the expansion of the extent of the sub-surface where gas migration occurs by dynamic fracture propagation (and a corresponding decrease in the zone of stable fracture propagation) is fundamental to the formation of mature gas migration systems. The

original position of the stable/dynamic propagation boundary is dictated by local pressure conditions and sediment properties (i.e., a sudden decrease in grain size over the boundary causes a decrease in critical crack size triggering dynamic fracture propagation). Within the stable propagation zone, the continuous passage of gas weakens the sediment allowing for an increased flow rate of gas and eventually, the gas bubble fractures begin to propagate into each other causing them to exceed the critical crack length and transition to dynamic fracture propagation. While such collisions could occur at any point within the stable propagation zone the presence of (momentarily) lingering dynamic fractures across the boundary makes the chances of such events significantly more likely just below the boundary. Hence slowly over time the dynamic fracture propagation zone advances into the stable propagation zone, provided the level of gas flux is sufficient and continuous. This will occur until the dynamic propagation zone covers the full length of the near-surface, from some form of gas reservoir to the seabed. Connecting to a gas reservoir greatly increases the volume of gas supplied to dynamic fractures such that the internal pressure of the gas flowing through the crack is sufficient to keep the crack open for an extended period of time. This allows for the formation of open conduits, chimney structures, connecting gas reservoirs to the seabed. At this point, the gas flow can be thought of as reaching a "mature state" whereby the gas flow is constant, and the pathways are essentially rooted in place. Across a greater depth of unconsolidated sediment (100s of meters) it is easy to imagine this process repeating itself multiple times between a series of small gas pockets until large scale chimney structures are formed as seen in Landrø et al (2019).

By day 9 of the release experiment (injection rate of 143 kg/day) gas has pooled sufficiently in the sandy base of the Witch member to form an elliptical dome-shaped gas pocket ~8 x 5 m wide with a maximum height of ~0.3 m. The gas pocket is evident by the bowing seismic horizon, enhanced reflectors, shadowing, high-frequency attenuation, and increased RMS amplitude within this layer. The gas pocket contains 91 ± 32 kg of CO_2 (see section 3.6.2) which is equal to approximately half the total volume of gas injected since upping the flow rate to 86 kg/day. Fluid pathways are now open channels within the sediment allowing gas/bubble fractures to rise

unrestricted. These pathways are larger and more permanent gas conduits (the overlying seeps being far less mobile) visible in the seismic data as chimneys, connecting the gas pocket (now essentially acting as a secondary reservoir) to the surface. The formation of these open conduits has significantly increased the effective CO_2 permeability of the near-surface to $2x10^{-14}$ m^2. Given the nature of this experiment we cannot say confidently whether these larger open conduits formed as a consequence of the increased injection rate or the length of time the pathways had been active, most probably both contributed. The dynamic propagation zone most likely slowly progressed downwards from an original depth of 1.4 mbsf throughout the "immature migration" stage, the rate of this progression increasing with the injection rate. The dynamic propagation zone reached the newly formed gas reservoir in the sand layer at some point between D+6 and D+9 (when chimney structures were first seen).

Fig. 3.13 is our interpretation of the expansion of the dynamic fracture propagation zone over time during the release experiment. Initially, at lower flux rates the change was minimal, but as the injection rate increased so too did the rate of expansion.

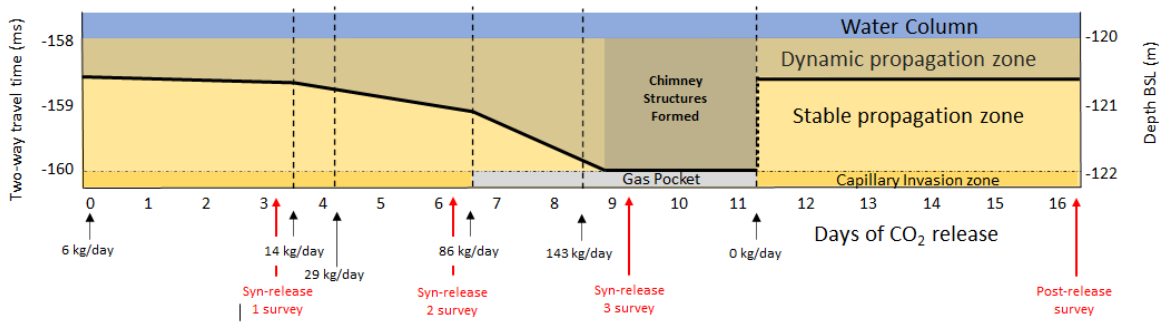

Figure 3.13: Temporal changes in the dominant form of gas migration during the CO_2 release experiment. The depth of sediments where dynamic fracture propagation dominates expands with time and eventually connects the gas pocket with the seabed.

3.7.1.4 Stage 4 – Closure

The closure stage is the final phase of the gas migration lifecycle. Once gas is no longer being injected into the system the inflow of gas through the open pathways stops. Without the outward pressure of the flowing gas, the channels close. Any remaining free gas migrates via stable/dynamic fracture propagation or dissolved into the sediment pore water.

CO_2 injection was stopped on day 11 of the experiment and bubble seeps were no longer observed within an hour. This suggests that the gas pocket had already deflated following the increased flow rate through the open fluid conduits. By day 16 (5 days after the gas release stopped) the subsurface was completely devoid of acoustic anomalies and appeared identical to the pre-release survey. It is likely that the chimney structures closed almost instantly once the passage of gas stopped, leaving only the surface craters which would be slowly infilled with sediment.

These stages of the evolution of gas migration pathways can also be applied to the QICS release experiment. In the QICS experiment, CO_2 gas was injected 11 m below the seabed of a shallow bay in western Scotland, into fine-grained sediment overlaid by coarser sandy sediment (Cevatoglu et al., 2015, Taylor et al., 2015). Proto-migration occurred with dynamic fracture propagation within the muddy sediment immediately surrounding the injection point up to the base of the sandy layer. The weight of the sediment initially prevented fracture propagation, leading to the pooling of gas, though some individual bubbles were able to escape to the surface (Cevatoglu et al., 2015). During the immature migration stage gas migration through the upper sandy layer slowly transitioned from primarily via capillary invasion to primarily via fracture propagation, with a number of seeps forming on the seabed. Once the mature migration stage was reached dynamic propagation pathways extended all the way from the injection point through the overlying sand and to the seabed, forming open conduits over the entire length of the near-surface (Cevatoglu et al., 2015). We note that in QICS, unlike in STEMM-CCS, the

dynamic fracture propagation boundary migrated upwards (not downwards) highlighting that what is important is the extension of the dynamic fracture propagation zone within the sub-surface rather than its depth. Finally, in the closure stage following the end of the gas release experiment the flow of gas into the water column stopped almost instantly and subsequent seismic surveys found no evidence of lasting alteration to the subsurface (Cevatoglu et al., 2015).

3.8 Conclusions

We have used pseudo-3D time-lapse high-resolution chirp seismic reflection imaging of a controlled CO_2 release experiment to map the evolution of gas migration pathways in near-surface sediments. The seismic data, alongside gravity core and hydrodynamic analysis as well as volume estimation modelling, reveals a transition in the primary method of gas migration, from stable fracture propagation to dynamic fracture propagation, and finally the formation of semi-permanent open pathways (chimney structures). These observations have been used to interpret four distinct stages in the evolution of a gas migration system.

During the first stage lasting only a few hours (CO_2 injection rate = 6 kg/day) injected gas made its way to the surface as individual bubble fractures, escaping as discrete ebullition events into the water column. Stage 2 (D+~0.5 to D+8, CO_2 injection rate = 6 - 29 kg/day) began as small unstable gas migration pathways were formed that focused the flow of gas to a number of seeps on the seabed. These gas conduits were easily destroyed (presumably by changing pressure conditions) and regularly reformed in new positions, leading to the continuous termination and creations of new seeps. Once the injection rate of the gas began to exceed the flow rate of the gas through the sediment gas started to pool and an ellipsoid shaped gas pocket became visible in the subsurface. We estimate that 242 kg of gas were trapped in the gas pocket, which is consistent with physical estimates that indicated that ~50% of the injected CO_2 flowed directly into the water column (Flohr et al., 2021).

The major gas migration phase, Stage 3, (D+8 to D+11 CO_2 injection rate = 143 kg/day) began when open conduits, chimneys, formed connecting the gas pocket to the seabed maximising the flow of gas to the near-surface and sharply increasing the effective permeability of the sediments by three orders of magnitude to $2x10^{-14}$ m^2. The seismic chimneys were clear in the seismic reflection data. The final stage 4 (D+11, CO_2 injection rate = 0 kg/day) began when CO_2 injection had stopped. The remaining gas in the sediment escaped into the water column along the chimney features, after which following a loss of internal pressure the conduits closed. Acoustically the system reverted to its pre-release state (within 5 days), except for the subtly increased levels of attenuation, which recovers at a much slower rate, suggesting such observations could be used to detect episodic events.

3.9 Acknowledgements

The STEMM-CCS project has received funding from the European Union's Horizon 2020 research and innovation programme under grant agreement No. 654462. We would like to acknowledge the hard work, enthusiasm, and professionalism of the crews and operators of the RRS *James Cook*, the RV *Poseidon*, the ROV Isis and the AUV Gavia who made the experiment possible. In addition, the authors would like to thank the following who enabled the project and experiment to take place: the staff at Air Liquide UK Ltd., Bronkhorst UK Ltd., Cellula Robotics Ltd., City Gas EOOD, Corsyde International GmbH, DG Pipe Services Ltd., J & J Engineering (Southampton) Ltd., Protea Ltd., and Sourceways Ltd. The British Ocean Sediment Core Research Facility (BOSCORF) is thanked for their expertise and facilities. We are also grateful to Schlumberger Ltd for the donation of Petrel software to the University of Southampton.

Chapter 4 Temporal variability of methane ebullition in Lake Constance – Prediction via lakebed pressure

There is uncertainty in quantifying the contribution of naturally occurring methane seepage from aquatic systems to global methane budgets, and there are few constraints on temporal variability. Ebullition rates of 3 – 18 ml m^{-2} s^{-1} (80 - 95% methane) were estimated from five methane seep sites, at water depths of 4 to 12 m, within Lake Constance (central Europe) with bubble radii ranging between 0.1 and 1.2 cm, using physical, passive acoustic and optical techniques. Analysis of 9-months of data from the seep sites demonstrates a significant negative correlation between gas flux and in-situ pressure. Flux predominantly regulated by lake water level (hydrostatic pressure) on monthly timescales, while smaller fluctuations on daily to weekly periods are controlled by atmospheric pressure variations. Diurnal atmospheric pressure variations generate land-lake breeze cycles and are observed within the ebullition flux data for the first time. No correlation is observed between gas flux and rainfall intensity or wind speed. We demonstrate that long-term ebullition flux variability is best estimated by quantifying the relationship between in-situ pressure and gas flux and then using this relationship to predict gas flux from easily measurable in-situ pressure data. This approach is more accurate than extrapolating average flux rates from short periods of observation.

4.1 Introduction

Carbon dioxide (CO_2) and methane (CH_4) have been identified as two of the most important greenhouse gases (Forster et al., 2007; Friedlingstein et al., 2019). For the decade of 2002-2012, the global methane budget was estimated to be 558 Tg/yr, 35-50% of which is natural in origin (Saunois et al., 2016). Freshwater systems alone, like the one studied here, are estimated to contribute around 103 Tg of CH_4 a year, 53% via gas bubbles (Bastviken et al., 2011). The increasing concentration of CO_2 and CH_4 in the atmosphere has been directly linked to a rise in the global mean surface temperature of 1 °C resulting in climate change across the planet (IPCC et al., 2018). Thus, efforts to combat this global warming have placed a huge emphasis on better understanding the global emissions of greenhouse gases such as CO_2 and CH_4 both anthropogenic and natural (Friedlingstein et al., 2019).

It is relatively straightforward to estimate the emissions from anthropogenic sources. For example, by calculating the amount of pollution released producing one of a given product and extrapolating outward for annual production rates. However, the same is not true for emissions from natural sources, particularly in the marine and lacustrine settings (Li et al., 2018; Flohr et al., 2021). Accurately quantifying ebullition rates from natural systems is difficult because 1) techniques for measuring ebullition rates in the field are still relatively simplistic and 2) we lack a proper understanding of how the release rates vary over time and space (Boles et al., 2001; Greinert et al., 2010; Klaucke et al., 2010; Linkhorst et al., 2020; Ostrovsky, 2003). Thus, it is important that we address the limiting factors preventing the accurate quantification of gas flux from these natural systems.

Natural systems are known to have fluctuating ebullition emission rates, although the scale and causes of such variations are often poorly understood (Boles et al., 2001; Greinert, 2008; IEAGHG, 2015; Ridick et al., 2020). In lakes, greenhouse gases are typically released via ebullition sporadically in the littoral zone. However, in some lacustrine systems, the release of gas is continuous, usually forming distinct gas flares or seeps and pockmarks (Granin et al., 2012). In

Lake Constance, for instance, close to the mouth of the river Rhine more than a thousand gas flares and Pockmarks were discovered (Bussmann et al., 2013; Wessels et al., [In Progress]). Understanding the variability of these seeps is imperative to understanding greenhouse gas emissions from the lake.

An obvious and regularly observed driving factor behind gas flux variations is the in-situ total pressure, a summation of hydrostatic and atmospheric pressure. The rate of gas release being inversely proportional to the pressure on the lake/seabed (Judd & Hovland, 2007; Katsman, 2019; Varadharajan et al., 2012; Encinas et al., 2020). One explanation, most readily used to explain sporadic ebullition, is that changing the pressure conditions alters the position of the "gas horizon", a surface across which bubble ascent through sediment stops (without the existence of fluid flow structure). A decrease in pressure causes this surface to retreat deeper into the sediment, with the previously trapped gas now free to mobilize upwards, resulting in more gas flowing upwards (Katsman, 2019). Other theories more associated with continuously active seeps (as studied here) include the decrease in pressure reopening pre-existing fractures, the so-called "hydraulic pumping" effect, or simply the decrease in pressure allowing pathways to expand facilitating the more rapid ascent of gas through the sediment (Judd & Hovland, 2007; Hovland et al., 2010; Algar et al., 2011; Katsman, 2019). Regardless of which theory is correct, flux levels have been observed varying with daily and monthly tidal cycles (Boles et al., 2001; Pengfei et al., 2015; Römer et al., 2016; Katsman, 2019) as well as seasonally (Römer et al., 2016) and with artificial variations in water depth (Maeck et al., 2014; Encinas et al., 2020), and potentially atmospheric pressure (Casper et al., 2000; Mattson & Likens, 1990; Zhao et al., in review). While most of these observations have been in the marine environment (Boles et al., 2001; Greinert et al., 2006; Judd & Hovland, 2007; Römer et al., 2016; Di et al., 2017), similar results have been found in shallow rivers, lakes, and reservoirs, though many of these studies have been on sporadic ebullition sites (Encinas et al., 2020; Maeck et al., 2014; Pengfei et al., 2015; Casper et al., 2000; Mattson & Likens, 1990; Beaulieu et al., 2018; Linkhorst et al., 2020). However, while commonly observed, this relationship is yet to be formalised in terms of quantification and prediction of the change in

a specific flux rate for a measured change in in-situ pressure and a particular ebullition site. Furthermore, the nature of seeps and therefore the volume of gas released is expected to change with time as the fluid flow plumbing structure changes (Liu et al., 2016; Katsman, 2019).

Most observations of ebullition fluxes represent a snapshot measurement, lasting a few hours or days in shallow aquatic environments (Bastviken et al., 2004; Linkhorst et al., 2020) and even less in a deep marine environment (Bayrakci et al., 2014; Greinert et al., 2006; Li et al., 2020a; Wang et al., 2021). The chance of these single measurements being representative of annual flux rates is small, particularly if ebullition is sporadic (Maeck et al., 2014; Marcon et al., 2019). Demonstrating this, Maeck et al. (2014) compared random observations of varying lengths from natural methane vents to the observed 30 days mean. Finding that an accurate estimate was only consistently found when the observation length was more than 400 hours long. This inability to rely on extrapolated results from small sampling periods is the most likely explanation for errors in the natural greenhouse gas budget (Boles et al., 2001). Obviously the longer a survey is, the more representative its measurements will be, but it is unrealistic to expect natural CO_2 and CH_4 seeps around the globe to be monitored year-round, especially with current techniques, thus a simpler, but more robust method is needed.

The approach of this study is to monitor natural seep sites, that are continuously releasing gas, for an extended time period at a high sampling rate, identifying and characterizing the factors driving flux variations over different temporal periods. The goal is to determine the optimal method for estimating gas flux from natural seeps.

4.2 Material and Methods

4.2.1 Study site

Lake Constance (47°37'N, 9°24'E) is a large, deep (maximum depth 251 m), oligotrophic and monomictic lake, which is located in Western Europe between Germany, Switzerland, and Austria (Fig. 4.1a-b). The main inflow takes place via the alpine river Rhine, which accounts for 60 - 65% of the water inflow (Wessels et al., 2010; Gilfedder et al., 2011).

Schröder (1992) first reported the presence of pockmark-like concave depressions in eastern Lake Constance, and associated ebullition of small millimetre sized bubbles rising to the lake surface. Several hundred pockmarks were found, located mostly atop large sediment waves or ridges, at depths ranging from 4 to 100 m, with sizes ranging from ~10 cm to 16 m in diameter and a maximum seafloor depression of 4 m, seeps generally becoming larger with depth (Wessels et al., 2010). While the majority of pockmarks were found to be inactive over 1000 seeps were found to be actively venting methane gas (Wessels et al., [In Progress]). The isotopic composition of the methane indicates it is biogenic in origin (Bussmann et al., 2011; Bussmann et al., 2013). Here we investigate five small seeps distributed over two sites, A and B (Fig. 4.1c-e), at depths of ~4 and 11 m in the south-east part of the Lake. This part of the lake is mainly exposed to south-easterly and some westerly winds.

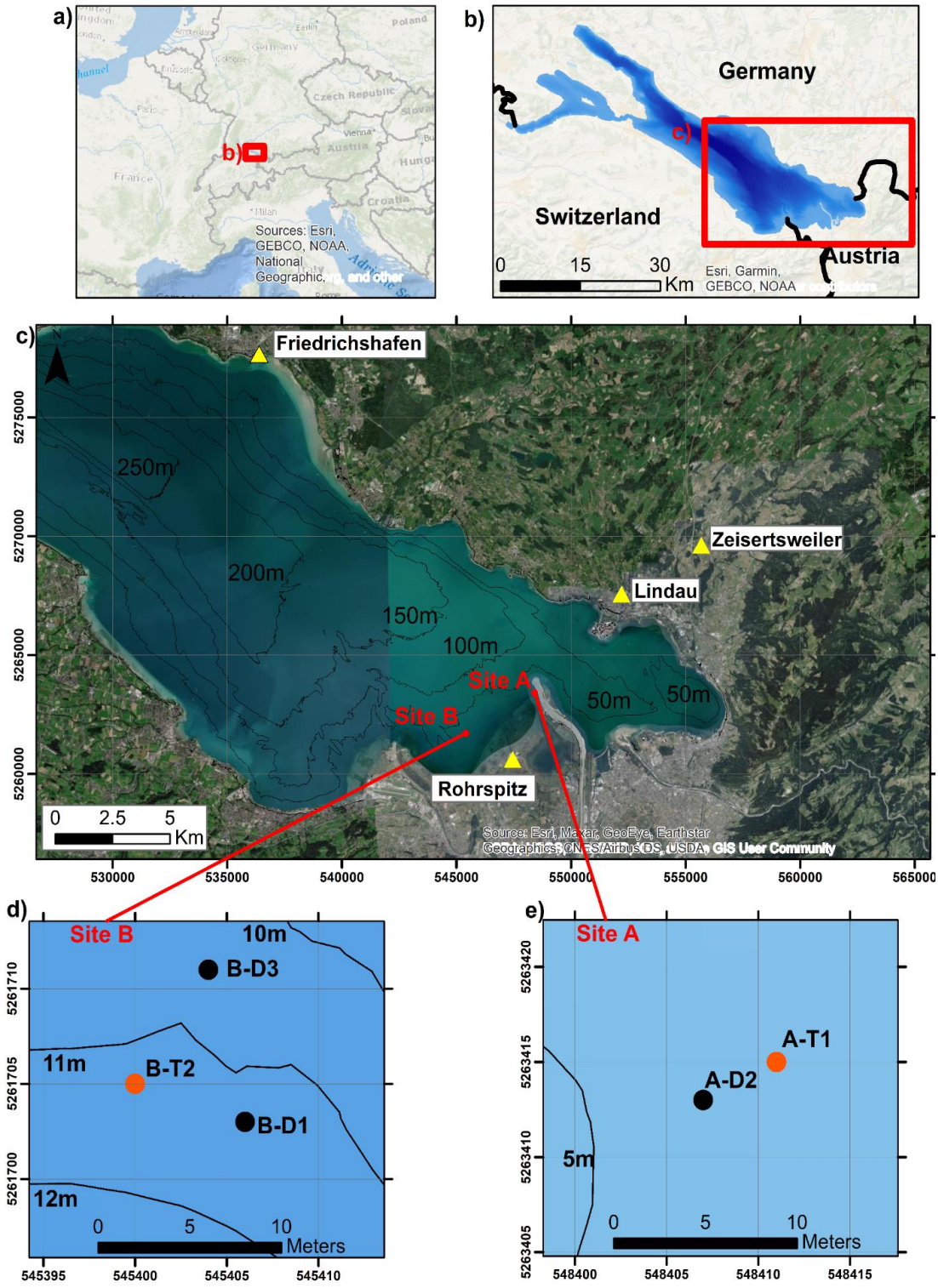

Figure 4.1: Study site projected on a map of a) Europe b) Lake Constance c) Eastern Lake Constance, also indicating the position of Rohrspitz, Lindau, Zeisertsweiler, Friedrichshafen stations from which additional datasets were acquired, d) Site B in deep water indicating the position of deployments D1 and D3 and targeted deployment T2 and e) Site A in shallow water indicating the position of deployment D2 and targeted deployment T1.

4.2.2 Sampling

Time series of the ebullition flux were determined at two seep sites, a shallow-water site A (4 – 5m) and a deeper-water site B (10 - 12 m; Fig. 4.1d-e) for periods of up to three months at each site during 2019 and 2020 (Deployments D1 – D3; Tbl. 4.1). The experimental geometry comprised a funnel positioned directly above the seep and a hydrophone placed below the funnel on the lakebed less than 0.5 m from the seep (Fig. SI 4.1).

In addition to the long-term deployments, two targeted shorter-term deployments (A-T1 and B-T2) were conducted within each site by measuring the ebullition flux with a funnel and subsequently with a lander equipped with video cameras and a hydrophone to record simultaneous acoustic and optical data. The targeted deployments were used to determine the bubble size distribution but also to compare the ebullition flux from the different measurement techniques (Tbl. 4.1).

Deployment	Period	Coordinates (UTM)	Mean water depth (m)	Mean physical flux estimate		Mean acoustic flux estimate (ml s^{-1})	Mean Bubble Radius (cm)
				(ml m^{-2} s^{-1})	(ml s^{-1})		
B-D1	10/04/2019 - 22/06/2019	545406 5261703	11.7	4.53	2.90	-	-
A-D2	14/10/2019 - 13/01/2020	548407 5263413	4.2	2.72	1.74	4.2	0.5 - 0.6 (Acoustic)
B-D3	23/01/2020 - 27/04/2020	545404 5261711	10.6	4.45	2.85	-	-
A-T1	22/01/2020 - 22/01/2020	548411 5263415	4.2	3.25	2.08	2.24	1.0 (Optical)
B-T2	22/01/2020 - 22/01/2020	545400 5261705	10.6	18.25	11.68	12.18	0.7 - 0.8 (Optical - Acoustic)

Table 4.1: Overview of equipment deployments B-D1, A-D2, B-D3, and target deployments A-T1 and B-T2, including survey period, coordinates of the location (UTM), mean water depth during the deployment (m) and mean physical flux estimate (ml m^{-2} s^{-1} and ml s^{-1}), mean acoustic flux estimate (ml s^{-1}), and mean bubble radius measured by the optical and acoustic method (cm).

Throughout each deployment, in-situ pressure and temperature were continuously measured with a pressure sensor (Aquatec AquaLogger 520, or RBR*duet*³ T.D.) at the depth of the funnel. Moreover, at the beginning and the end of the measurement, a gas sample was taken from the funnel for further analysis of the methane concentration.

4.2.3 Measurements of ebullition rate

In order to gain an accurate understanding of natural variations in the rate of gas release from the aquatic system, we used three independent techniques to analyse bubble emissions. The techniques used, physical, optical, and acoustic inversion, are described in detail below. Given that all measurements occur close to the lakebed and methane has a slow dissolution rate all measurements are comparable (see SI for full discussion).

4.2.3.1 Physical flux measurements

Gas flux was physically measured by positioning a custom-built funnel directly above the gas flare. Bubbles released within the footprint of the lander (0.8 x 0.8 m) were trapped within the inverted squared funnel and accumulated in the cylindrical column on top of the funnel. The height H of the accumulated gas in the cylindrical column is proportional to the differential pressure (the difference between the pressure in the trapped gas and the pressure in the water at the same depth) by using a linear calibration (Maeck et al., 2014). Here the differential pressure was continuously measured by a differential pressure sensor at a frequency of 4 Hz and was averaged to a 1-minute resolution for further analysis. The ebullition flux f (ml m^{-2} s^{-1}) was calculated from the ideal gas equation at standard conditions with the standard temperature T_s (273.15 K), and standard pressure P_s (1 atm):

$$f = \frac{\pi r_c}{A} \times \frac{dH}{dt} \times \frac{p}{T} \times \frac{T_s}{P_s}, \quad (4.1)$$

where r_c is the radius of the cylinder (m), T the temperature (K), A the area of the funnel (0.64 m^2), H the height (m) of the trapped gas in the cylinder and p the in-situ pressure (hPa). As soon as the cylindrical column was filled with gas, the top of the system was automatically opened by a solenoid valve, such that the accumulated gas was released, and a new measurement cycle could begin. The measurement uncertainty, calculated via error propagation, is ± 8%.

4.2.3.2 Acoustic flux inversion

Acoustic data for this study were collected using an SM4M acoustic recorder, composed of a single calibrated hydrophone and an internal recording unit. The hydrophone was positioned < 50 cm from the seep directly under the physical gas funnel. Data were recorded every 15 min for a 5 min period (meaning 4 recordings per hour) and was collected at a sample rate of 24 kHz with a gain of 15 dB. From these recordings, a 30 s window with the least total energy was identified for further study to avoid interpreting loud non-seep-related noises (e.g., boats or the gas funnel emptying) as bubbles. Additionally, a median spectrogram for the 5 min period was produced and subtracted from the window period in order to remove background noise.

The passive acoustic inversion technique used in this study was first proposed by Leighton & White (2012) and later validated by Bergès et al. (2015) and Li et al., (2020). It uses the principle that when a bubble larger than a few micrometres escapes from the sediment into the water column, it produces a distinct acoustic signature (Leighton & Walton, 1987; Minnaert, 1933). By considering the magnitude of the energy released within discrete frequency bands we can estimate the number of bubbles with different radii released in a given period. Simultaneous comparisons of acoustic, optical, and physical measurements in the field have shown the accuracy of this technique lies at ± 18 % (Roche et al., 2019).

4.2.3.3 Optical flux measurements

Optical data was acquired by deploying a custom-built lander around the seeps A-T1 and B-T2. The design incorporates two Sony FDR-X3000 cameras in two stereo arrangements, focusing

on a single central point with scale boards positioned directly opposite. The data was then processed using techniques first described in Li et al. (2020b) where the volume of each bubble was calculated using the volume of the revolution equation. This volume of revolution is then used to calculate the radius of a spherical bubble with equivalent volume for comparison to acoustic measurements.

4.2.4 Meteorological data

Wind data and atmospheric pressure were obtained from weather station Rohrspitz (2.3 - 3.0 km from the vent sites). Rain data was acquired from the weather station Lindau (5.6 - 9.0 km from the vent sites) and Zeisertsweiler (9.6 - 13.0 km from the vent sites) with a daily and hourly temporal resolution, respectively (Fig. 4.1c). The water level of Lake Constance was measured at Friedrichshafen (~ 18 km from the vent sites) with a temporal resolution of 15 minutes (Fig. 4.1c).

4.2.5 Analysis

In order to accurately compare the bubble size distributions for each technique, the data were normalised by binning the data and by dividing by the total number of bubbles per second and multiplied by the bin width (in cm). Thus, the probability density is in cm^{-1} and the integral of the bubble population distribution would equal ~1.

For each time series, the gas flux and coinciding pressure data were interpolated at a 1 min resolution, filtered with a second-order low-pass Butterworth filter with a cut off frequency of 6 h (Fig. SI 4.2), to remove noise and improve interpretability. It should be noted that we are assuming the atmospheric pressure above the release site (and Friedrichshafen base station) is the same as that recorded at Rohrspitz weather station, ~3 km from the seep sites. Additionally, hydrostatic pressure was not directly measured at the release sites during this study and was instead calculated by subtracting the atmospheric pressure from the total in-situ pressure

measurements at the seep sites. Lakebed hydrostatic pressure at Friedrichshafen was calculated by the water level measured at the Friedrichshafen station and total lakebed pressure at Friedrichshafen station was calculated by summing the local hydrostatic pressure and the atmospheric pressure from Rohrspitz weather station (located 20 km SE of Friedrichshafen).

During further analysis, gas flux was plotted against total, hydrostatic and atmospheric pressure at the release site for each deployment (B-D1, A-D2, and B-D3) in order to better understand their correlation. We then determined the linear fit between the gas flux (ml m^{-2} s^{-1}) and pressure (hPa) and used this relationship to predict the gas flux throughout each deployment from the measured pressure (via a model fitting approach). To gauge the potential for such a technique to predict gas flux via more commonly available data, i.e., permanent monitoring stations, we also determined the relationship between gas flux and the hydrostatic and total pressure at the base station Friedrichshafen.

An important question in estimating the long-term gas emissions from a seep is how long an observation period needs to be in order to provide a representative measurement. Different temporal observation lengths were examined within a three-month period, with average estimates for subsets from 1 minute to 70 days duration compared to that of the full 70 days period. The subsets were shifted on a time vector with a temporal resolution of 1 min through the 70 days of data. The median flux, the 10^{th} and 90^{th} percentiles and the maximum and minimum of the subsets were then compared with the mean ebullition rate for the entire 70-day period.

4.3 Results

4.3.1 Targeted deployment flux estimates

During the targeted deployments, the seep at A-T1 provided a mean physical flux estimate of 2.08 ± 0.16 ml s^{-1} while the hydrophone recording provided an acoustic flux estimate of 2.24 ± 0.40 ml s^{-1}. Meanwhile, for seep B-T2 the funnel provided a physical flux estimate of 11.68 ± 0.93 ml s^{-1} compared to an acoustic flux estimate of 12.18 ± 2.19 ml s^{-1}. The consistent estimates from these two different measurement techniques serve to validate further estimates from both techniques.

4.3.2 Long-term deployments

The full results from deployments B-D1, A-D2 and B-D3 are shown in Fig 4.2-4.4 respectively. The gas flux measured by the funnel is shown in parts Fig. 4.2a, Fig 4.3b and Fig. 4.4a with deployment A-D2 also displaying the acoustic flux estimate in part Fig. 4.3a. Each figure also shows the in-situ total pressure (alongside the in-situ hydrostatic pressure) as well as the recorded atmospheric pressure, rainfall, and wind data from local weather stations. The negative correlation between gas flux and total pressure will be discussed in detail below, but at a cursory glance one can clearly see a negative correlation between gas flux and total pressure. There is also no apparent correlation between gas flux and rainfall or wind speed, with R^2 values below 0.3 for all periods (Tbl. SI 4.1)

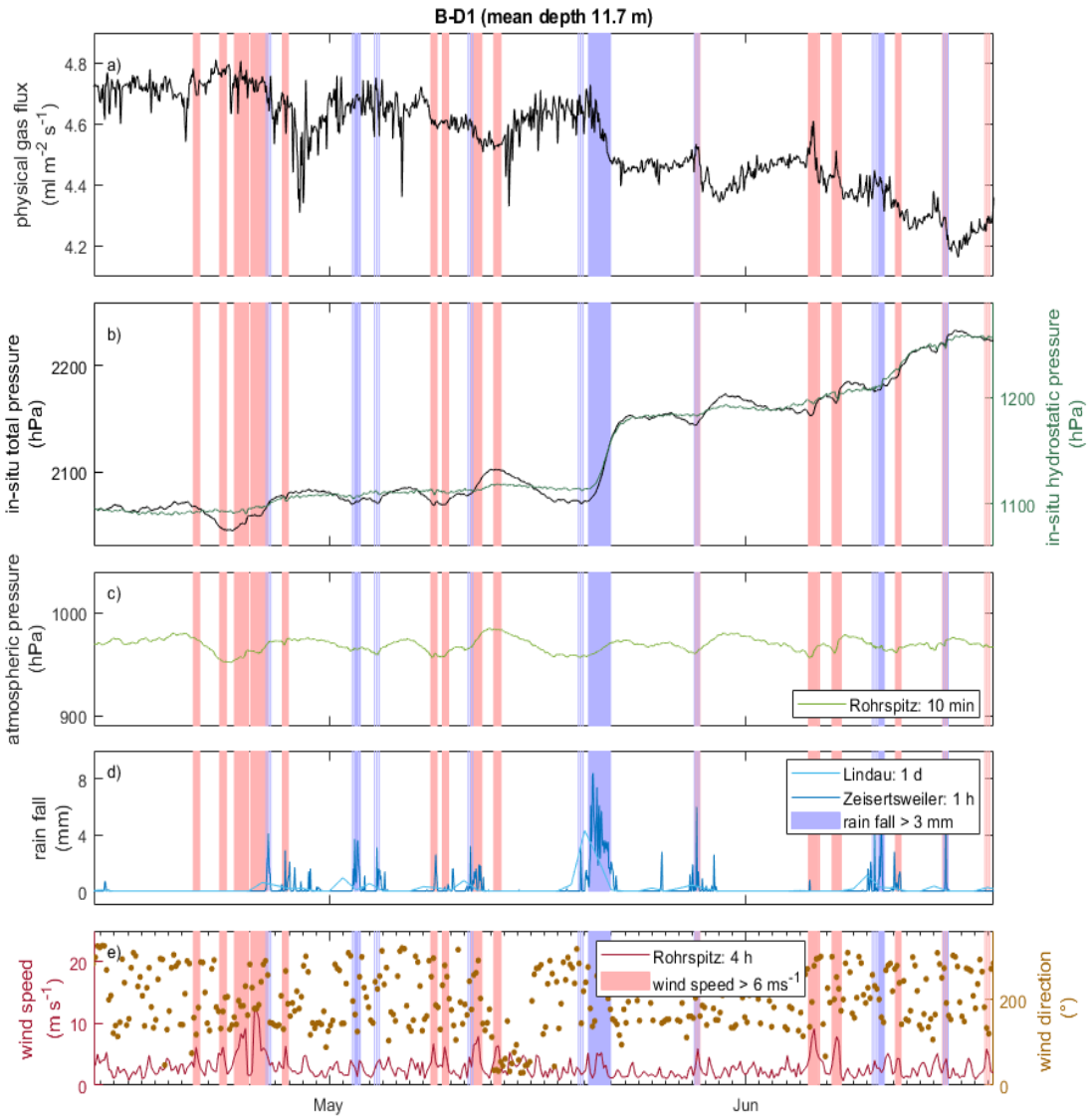

Figure 4.2: Time series of ebullition gas flux and abiotic factors of deployment D1 at site B from 10/04/2019 to 25/06/2019: From top to bottom a) ebullition gas flux (ml m^{-2} s^{-1}) measured by the physical technique at B-D1 (black); b) in-situ pressure (hPa) measured at the depth of the funnel at B-D1 (black) and water level of Lake Constance (cm) measured in Friedrichshafen (dark green); c) air pressure (hPa) measured at the weather station Rohrspitz (light green); rainfall (mm) measured at the weather station Lindau (light blue) and Zeisertsweiler (dark blue); d) wind speed (m s^{-1}) measured at the weather station Rohrspitz at 10 m height (dark red) and e) wind direction (°) measured at the weather station Rohrspitz (brown). Areas with a blue and red background are periods with rainfall > 3 mm and wind speeds > 6 m s^{-1}, respectively.

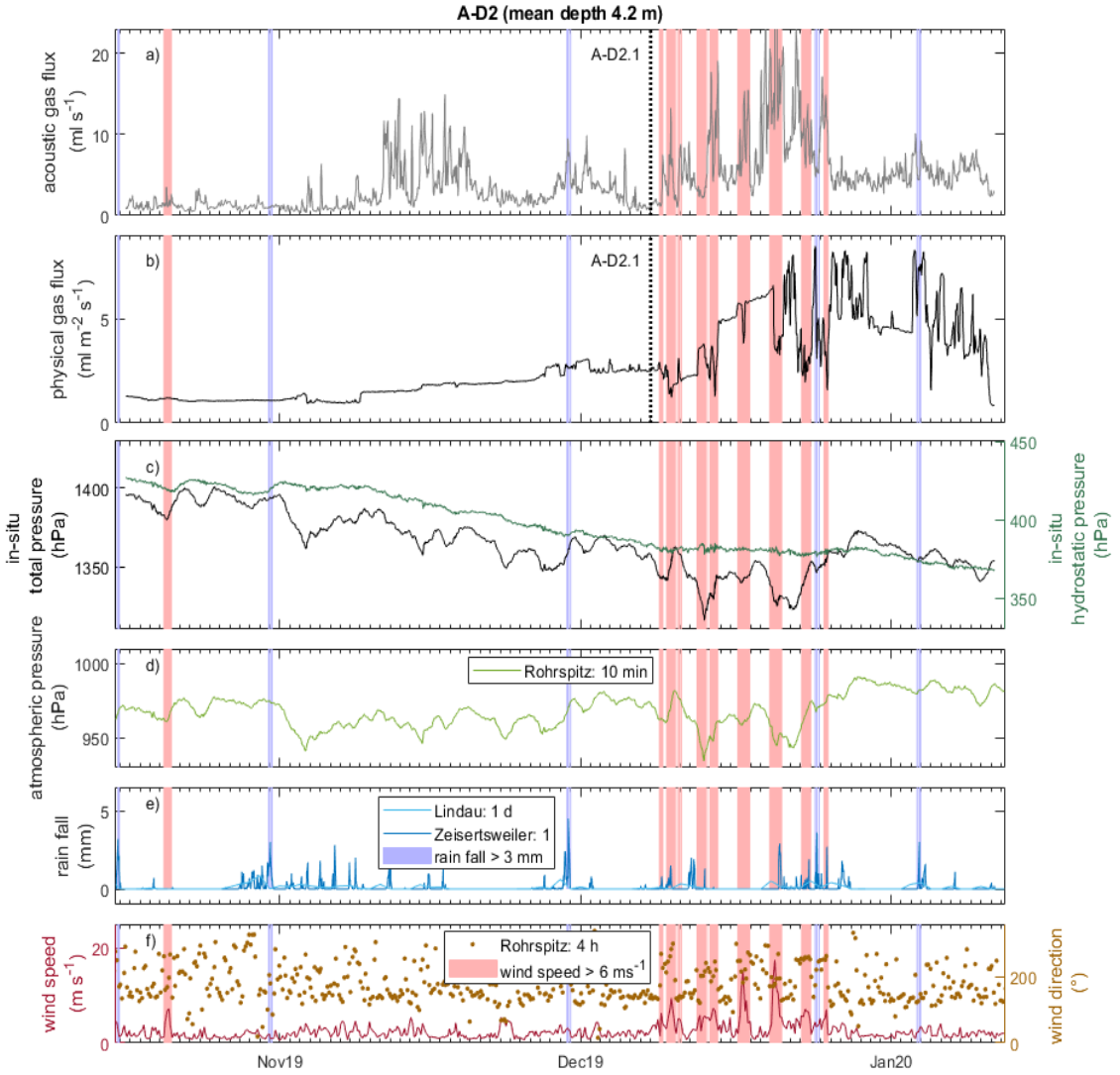

Figure 4.3: Time series of ebullition gas flux and abiotic factors of deployment D2 at site A from 14/10/2019 to 13/01/2020: From top to bottom a) ebullition gas flux (ml m^{-2} s^{-1}) measured by the acoustic technique at A-D2 (black); b) ebullition gas flux (ml m^{-2} s^{-1}) measured by the physical technique at A-D2 (black); c) in-situ pressure (hPa) measured at the depth of the funnel at A-D2 (black) and water level of Lake Constance (cm) measured in Friedrichshafen (dark green); d) air pressure (hPa) measured at the weather station Rohrspitz (light green); rainfall (mm) measured at the weather station Lindau (light blue) and Zeisertsweiler (dark blue); e) wind speed (m s^{-1}) measured at the weather station Rohrspitz at 10 m height (dark red) and f) wind direction (°) measured at the weather station Rohrspitz (brown). Areas with a blue and red background are periods with rainfall > 3 mm and wind speeds > 6 m s^{-1}, respectively.

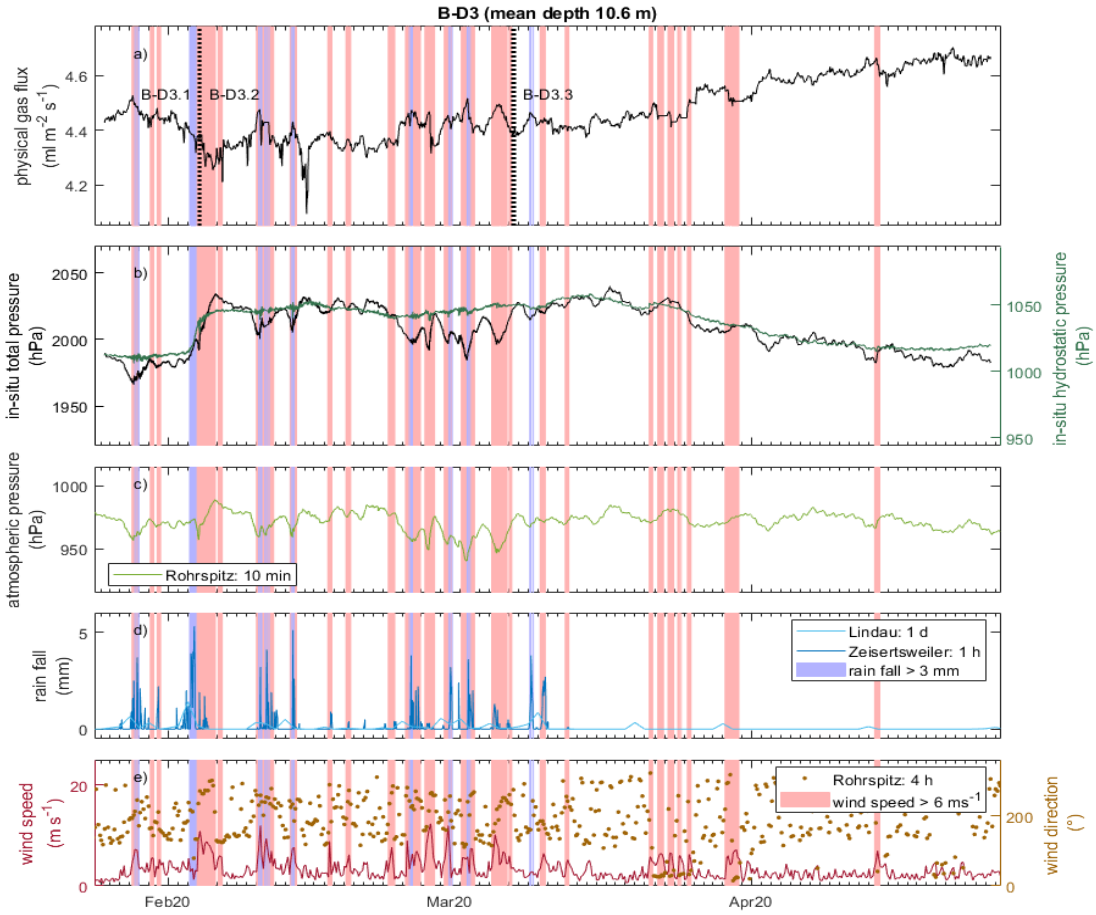

Figure 4.4: Time series of ebullition gas flux and abiotic factors of deployment D3 at site B from 23/01/2020 to 27/04/2020: From top to bottom a) ebullition gas flux (ml m^{-2} s^{-1}) measured by the physical technique at B-D3 (black); b) in-situ pressure (hPa) measured at the depth of the funnel at B-D3 (black) and water level of Lake Constance (cm) measured in Friedrichshafen (dark green); c) air pressure (hPa) measured at the weather station Rohrspitz (light green); rainfall (mm) measured at the weather station Lindau (light blue) and Zeisertsweiler (dark blue); d) wind speed (m s^{-1}) measured at the weather station Rohrspitz at 10 m height (dark red) and e) wind direction (°) measured at the weather station Rohrspitz (brown). Areas with a blue and red background are periods with rainfall > 3 mm and wind speeds > 6 m s^{-1}, respectively.

4.3.3 Diurnal variations

There are no tidal changes in water levels in Lake Constance. However, there are surface seiches with a magnitude of 3 cm which can be seen in the total pressure data with a period of ~54 min. There is also a noticeable day/night atmospheric cycle. During daylight air temperature increases, wind flows in a NWW direction (as observed at Rohrspitz) while total and atmospheric pressure increases a few hPa and gas flux decreases. Whereas during night-time air temperature decreases below the water temperature, wind flows in a SE direction while total and atmospheric pressure decreases a few hPa and gas flux increases (Fig. 4.5). These diurnal variations in pressure (~1 to 5 hPa) and flux are smaller in magnitude than the longer period trends seen above.

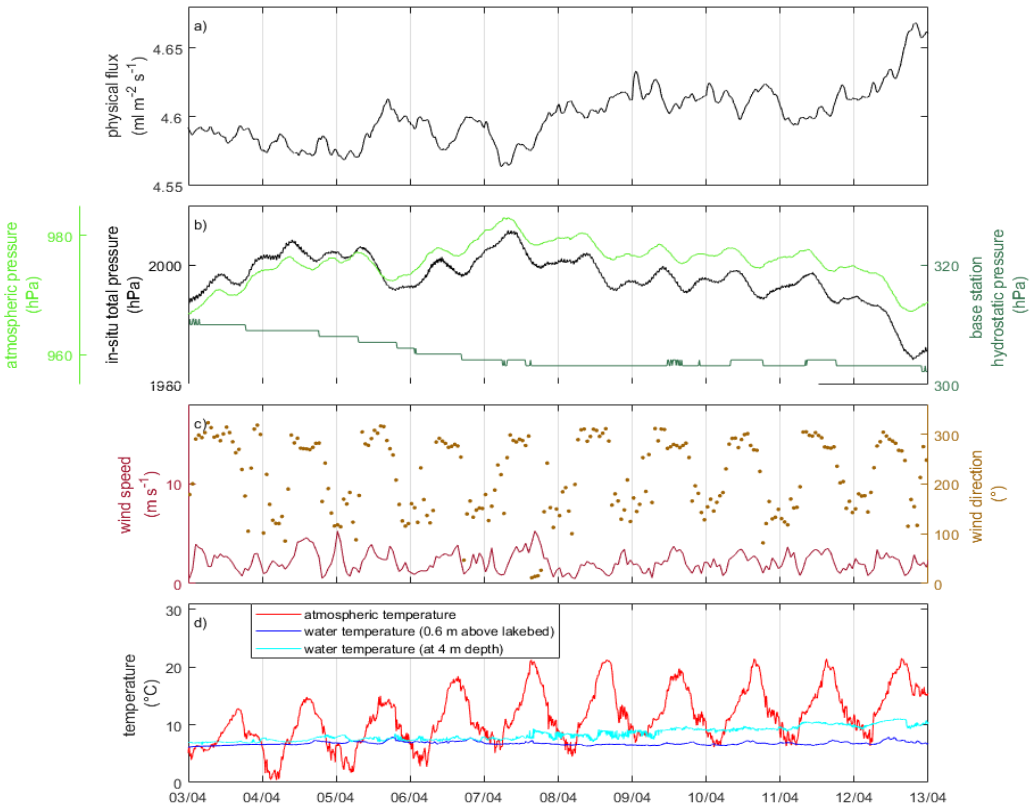

Figure 4.5: Time series of ebullition gas flux and abiotic factors for a short 10 day period during deployment B-D3 from 03/04/2020 to 13/04/2020: From top to bottom a) ebullition gas flux (ml m^{-2} s^{-1}) measured by the physical technique (black); b) in-situ total pressure (black) measured at the depth of the funnel, in-situ hydrostatic pressure (dark green, hPa), and atmospheric pressure (light green, hPa) measured at the weather station Rohrspitz; c) wind speed (dark red, m s^{-1}) and wind direction (brown,°) measured at the weather station Rohrspitz at 10 m height and d) atmospheric temperature (red, °C), water temperature at a depth of 4 m (ceylon, °C), water temperature 0.6 m above the lakebed (blue, °C). Note that the ticks represent midnight, and the weather station Rohrspitz was located southeast east of B-D3.

4.3.4 Bubble characteristics

The acoustic bubble size distribution for target deployment A-T1 shows a bimodal bubble size population between 0.7 and 1.2 cm with a peak at 1.0 cm (Fig. 4.6a). Comparing simultaneous optical and acoustic estimates from seep B-T2 they show a good agreement, both with gaussian distribution ranging between 0.4 and 1.2 cm in radius and peaking at 0.7 cm (Fig. 4.3b).

The acoustic bubble size distribution of A-D2 was split up into 3 selected periods (S1: 20/10/19 – 01/11/19, S2: 15/11/19 – 01/12/19, and S3: 15/12/19-01/01/20; Fig. 4.6c-d). S1 at the beginning of the deployment shows a bimodal distribution with peaks at 0.4 and 0.6 cm while S2 and S3 show Gaussian distributions with a single peak at 0.5 cm and 0.6 cm, respectively. The mean bubble size during A-D2 is increasing over time in a step-like manner from early November onwards, this may be an indication of contamination from other bubble sources (Fig. 4.6d).

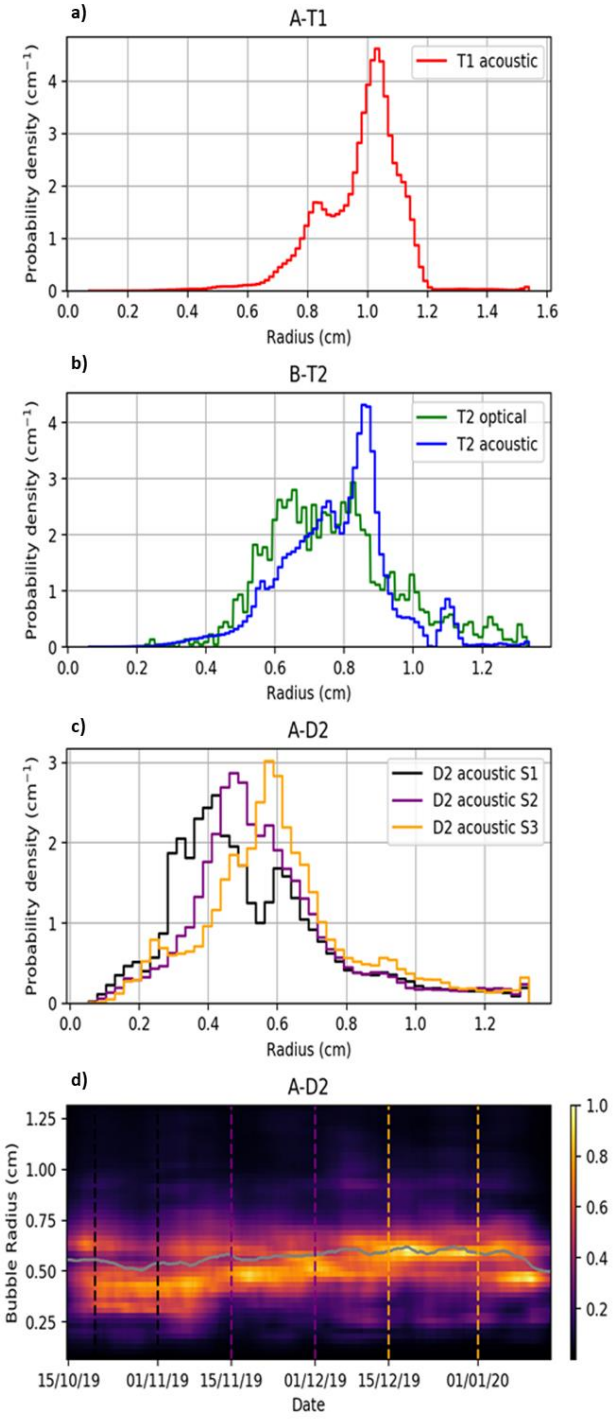

Figure 4.6: Bubble size distribution for a) Targeted deployment A-T1 via acoustic measurements; b) Targeted deployment B-T2 via acoustic (blue) and optical (green) measurements; c) long term deployment A-D2 for the periods S1 20/10/19 – 01/11/19 (black), S2 15/11/19 – 01/12/19 (purple), and S3 15/12/19-01/01/20 (yellow); d) long term deployment A-D2 as a function of time, the mean bubble size is indicated by the grey line and the dashed lines for the periods S1-S3, shown in c).

4.3.5 The effect of pressure on gas flux

Increases in in-situ total pressure correlate instantly with a decrease in gas flux and vice versa, i.e gas flux is negatively correlated with total lakebed pressure (Fig. SI 4.3). The exact empirical relationship between in-situ pressure measurements and physical gas flux is shown in Fig. 4.6 and detailed in Tbl. 4.2 (acoustic measurement detailed in Tbl. SI 42). The deployment B-D1 is strongly negatively correlated (R^2 = 0.84). The deployment A-D2 also shows an inverse relationship between gas flux and pressure but with a much weaker correlation, R^2 = 0.33 for physical and R^2 = 0.55 for acoustic estimates. However, by ignoring the end period of A-D2 (from 08/12/2019 onwards) when emissions increase significantly (most likely due to the formation of new seeps in the area) this correlation is improved for the physical estimate R^2 = 0.42, but not for the acoustic estimate R^2 = 0.47. The deployment B-D3 is of particular interest as the correlation (R^2 = 0.45) improves significantly when splitting the period into 3 distinct sections each correlating to a different period of time from 28/01/20 - 04/02/20 (R^2 = 0.72), 04/02/20 - 09/03/20 (R^2 = 0.73), and 09/03/20 - 22/04/20 (R^2 = 0.95) with a transition period of just a few hours (Fig. SI 4.4).

The total pressure on a lakebed is a sum of the hydrostatic and atmospheric pressure. As the total pressure is known to regulate gas flux it is logical to conclude that variations in these component pressures also regulate the gas flux. Hence, we repeat our prior analysis of in-situ total pressure vs. gas flux, this time for in-situ atmospheric and hydrostatic pressure vs. gas flux (Fig. 4.7d-i) in order to better understand their contribution to total pressure (and thus flux) changes. We also calculate the percentage contribution of hydrostatic and atmospheric pressure change to total pressure variation noting that, except for D3.1 and D3.2, hydrostatic pressure contributes 86 - 97% to the flux fluctuations (Tbl. SI 4.3, Fig. SI 4.5).

We observe strong negative linear correlations between hydrostatic pressure and gas flux particularly for B-D1 (R^2 = 0.84), B-D3.3 (R^2 = 0.95; Tbl. 4.2, Fig. 4.7d-f). No correlation was found between atmospheric pressure and gas flux (R^2 < 0.31) except during periods A-D2 (R^2 = 0.49) and B-D3.2 (R^2 = 0.75; Tbl. 4.2; Fig. 4.7g-i). While both parameters provide gradients in good

agreement with those observed for the same periods using total pressure, hydrostatic gradient values were consistently closer than the atmospheric values. This is unsurprising as the greater magnitude of hydrostatic variations accounts for the majority of total pressure changes. Indeed, the only time atmospheric pressure values were closer to the total pressure values than the hydrostatic pressure values was during B-D3.2 when hydrostatic pressure was comparatively constant (Tbl. 4.2, Fig. 4.7g-i). Performing a multiple linear regression using hydrostatic and atmospheric pressure provides a higher degree of correlation than seen for either individual property directly comparable to total pressure, e.g., $R^2 = 0.95$ for D1, with gradients between both properties being comparable for D1, D3.1 and D3.3 (Tbl. SI 4.4).

From this, we conclude that: 1) hydrostatic pressure (aka water level) variations control the variations in ebullition across the entire length of the deployments; 2) atmospheric pressure variations account for small period (days to weeks) deviations from the longer-term trend (Fig. 4.5a-b).

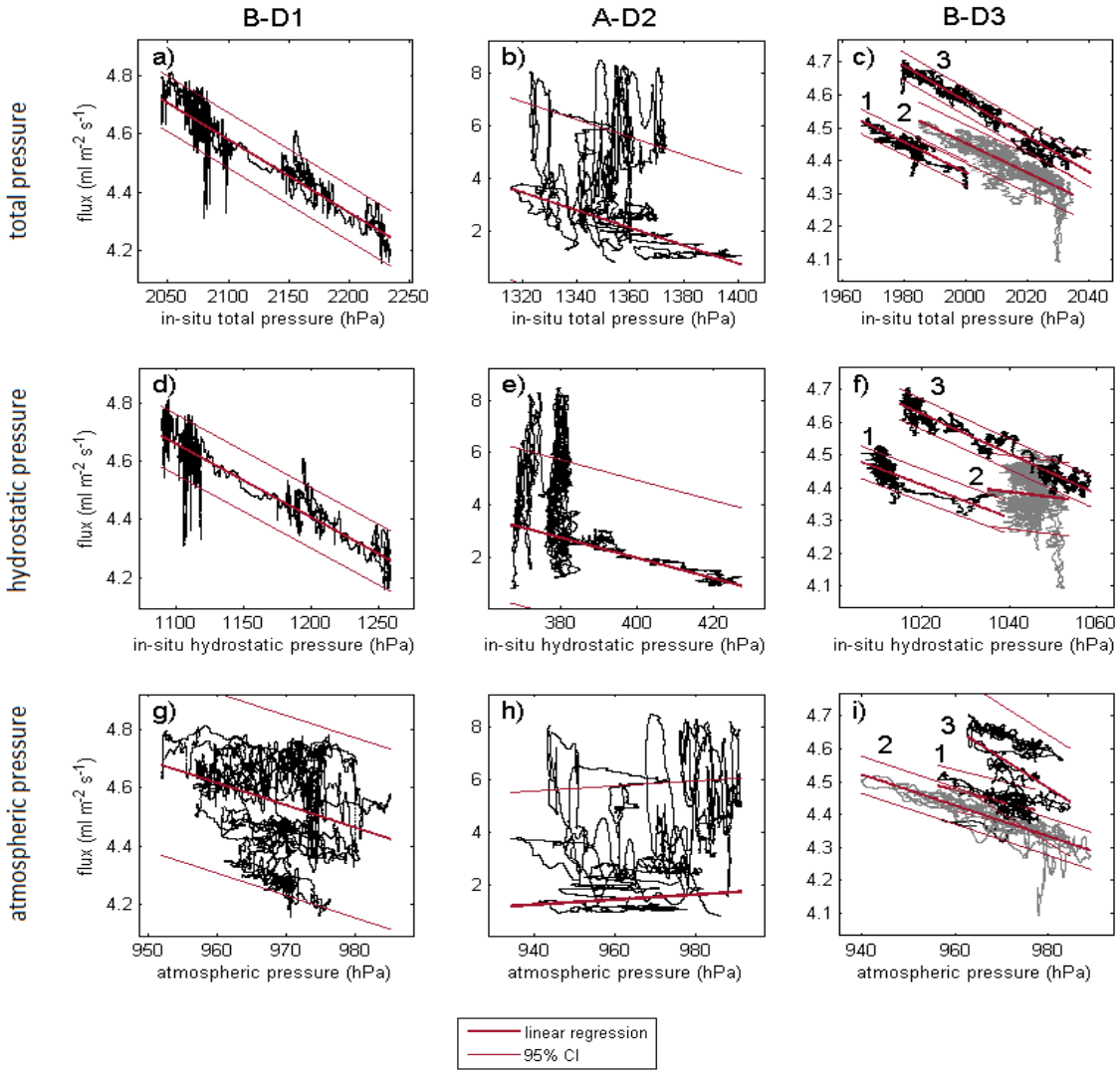

Figure 4.7: Correlation between physical flux and pressure. Physical flux measurement vs. in-situ total lakebed (top), hydrostatic (middle) and atmospheric pressure data (bottom) for the deployments B-D1 (left), A-D2 (middle), and B-D3 (right). For best fit lines see Tbl. 4.2. Note B-D3 is broken into 3 distinct periods: 1) 8/01/20 - 04/02/20, 2) 04/02/20 - 09/03/20, and 3) 09/03/20 - 22/04/20.

Deployment	Gradient m ($x10^{-2}$ ml m^{-2} s^{-1} hPa^{-1}) In-situ			Intercept c (ml m^{-2} s^{-1}) In-situ			R^2 In-situ			RMSD (ml m^{-2} s^{-1})		
	TP	HP	AP	TP	HP	AP	TP	HP	AP	TP	HP	AP
B-D1	-0.25	-0.25	-0.76	9.83	7.43	11.93	0.84	0.83	0.10	0.05	0.05	0.16
A-D2	-3.35	-3.90	0.96	47.73	17.58	-7.81	0.33	0.31	0.49	1.76	1.52	2.20
A-D2.1	-2.44	-4.26	-0.07	35.05	19.05	1.99	0.42	0.87	0.31	0.42	0.19	0.69
B-D3	-0.42	-0.48	-0.37	12.95	9.48	8.05	0.45	0.43	0.06	0.08	0.08	0.11
B-D3.1	-0.46	-0.50	-0.35	13.62	9.54	7.87	0.72	0.50	0.20	0.03	0.03	0.03
B-D3.2	-0.45	-0.16	-0.47	13.42	6.07	8.96	0.73	0.01	0.75	0.06	0.06	0.03
B-D3.3	-0.54	-0.61	-0.90	15.34	10.82	13.35	0.95	0.95	0.20	0.02	0.02	0.08

Table 4.2: Correlation between physical gas flux and in-situ total pressure (TP), hydrostatic pressure (HP) and atmospheric pressure (AP) for each long-term deployment; D1 at site A and D2 and D3 at site B.

4.4 Discussion

4.4.1 Predicting gas flux via pressure

We predict the gas flux throughout each deployment from the measured in-situ total pressure using the relationship presented in Tbl. 4.2 (Fig. 4.8). To the best of our knowledge, this is the first time an attempt has been made to predict gas flux from an underwater seep via pressure conditions, particularly over an extended temporal period. However it has been noted in review our approach here is more akin to model fitting than prediction, future iterations of this work will aim to address this. There is a very good agreement between observed physical flux values and those predicted via in-situ total pressure during periods D1 and D3 with a root mean square deviation (RMSD) between the measured and predicted flux values of 0.05 and 0.08 ml m^{-2} s^{-1}, respectively (Tbl. 4.2; Fig. 4.8). This indicates that in-situ total pressure can be used to

effectively predict gas flux emissions in Lake Constance. The A-D2.1 prediction is less coincident with the observed physical flux values, with an RMSD of 0.42 ml m^{-2} s^{-1}. Most of this divergence is confined to mid-December onwards when we suspect funnel measurements are contaminated by bubbles from other seeps.

Having demonstrated the potential of predicting gas flux via in-situ total pressure, we must consider the fact that most researchers will not have a permanent pressure sensor adjacent to their target seep(s). It is thus intriguing to compare gas flux estimates created using 1) the in-situ hydrostatic pressure above the seep 2) the atmospheric pressure from Rohrspitz weather station (3 km away) 3) the hydrostatic pressure at Friedrichshafen base station (18 km away) and 4) the total lakebed pressure at Friedrichshafen base station (Tbl. SI 4.1 and SI Fig. 4.6).

The base station total pressure predictions are to a first order identical to the predictions based on in-situ pressure predictions (Fig. 4.8), demonstrating it is possible to accurately predict gas flux via offsite data. The base station hydrostatic pressure predictions for periods D1, D2.1 and D3.3 are consistent with measured flux, R^2 = 0.83, R^2 = 0.87 and R^2 = 0.95, respectively. Atmospheric predictions are less consistent with the measured flux, especially when compared to hydrostatic predictions, with R^2 ranging from 0.10 to 0.75, suggesting they are less reliable. The notable exception to this being during D3.2 when the hydrostatic pressure varied very little; consequently, the atmospheric pressure was more closely correlated to the gas flux than the hydrostatic pressure, R^2 = 0.75 vs 0.01.

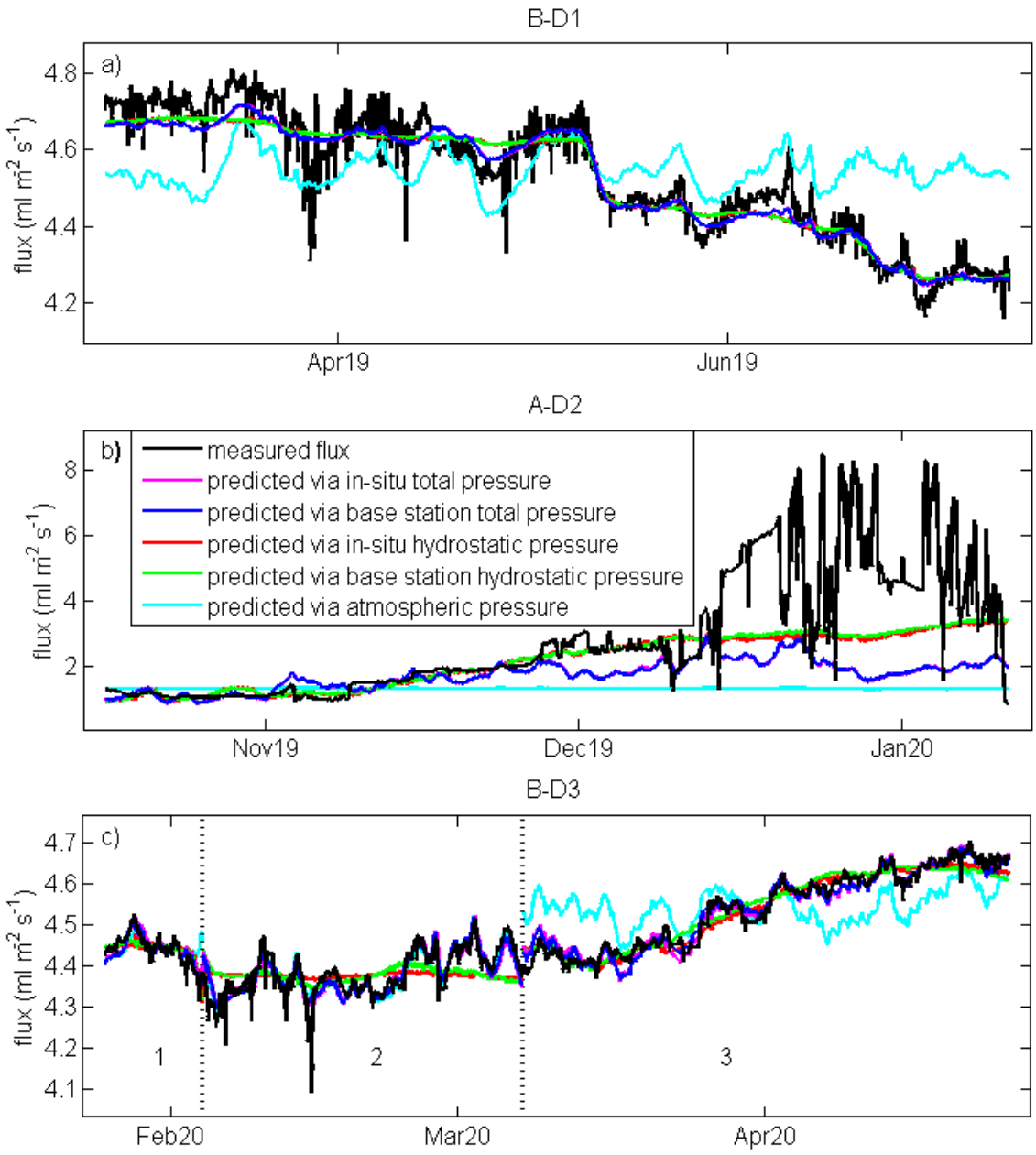

Figure 4.8: Comparison of the measured and predicted/modelled gas flux. Comparison of the gas flux measured by gas funnel with the predicted gas flux determined empirically from in-situ total pressure (pink), total pressure at the base station (blue), in situ hydrostatic pressure (red), hydrostatic pressure at the base station (green), and atmospheric pressure at Rohrspitz weather station (turquoise) for the deployments B-D1, A-D2, and B-D3.

4.4.2 Comparison of acoustic and physical flux estimates

While acoustic and physical measurements from the targeted deployments are consistent (4-8 % difference) a notable divergence is apparent during D2. One possible explanation for simultaneous estimates being inconsistent is that the funnel in some way interfered with acoustic estimates, perhaps via the bubbles colliding with the frame or acoustic reflections from the air-water interface. Further, note at the time of the deployment no other seeps were located in a 4 m radius of the equipment. However, upon recovery 2 newly formed seeps were visible just outside of the funnel's footprint (Fig. SI 4.7). Additionally, several inactive shallow depressions (holes) were visible on the seafloor under and around the funnel. Furthermore, sudden changes in the bubble size distribution as recorded by the acoustic inversion coincided with the flux increases (Fig. 4.6). It is therefore likely that new seeps formed in the vicinity of the funnel, releasing gas that was not captured by the funnel, thus was not recorded in the physical flux estimate, but was recorded by the hydrophone.

Large increases in acoustic gas flux measurements can also be seen to regularly occur alongside periods of high wind and rain (e.g., 16/10/2019 and throughout the mid-December period). Leighton and White (2012) explicitly warned that acoustic inversion of gas flux was susceptible to overestimating flux as a result of increased background noise from bubbles entrained by wind and rain action (Ashokan et al., 2015; Deane & Stokes, 2002; Pumphrey & Crum, 1990; Ma & Nystuen, 2005).

Thus, after early November acoustic and physical estimates begin to rapidly diverge due to 1) the formation of new seeps just outside of the funnel's catchment area and 2) the misattribution of bubbles generated at the surface by rain and breaking waves to the seep.

4.4.3 Flux pressure relationship

A detailed examination of what determines the empirical relationship between gas flux and pressure is beyond the scope of the study. Decreasing pressure conditions in sediment are theorised to allow existing gas pathways to expand and new ones to form, allowing for an increased flow of gas into the water column (Katsman 2019). Thus, a lower m value could suggest chimney structures are less likely to form or expand as a result of pressure decreases making the flow of gas less variable over time. While a larger m value would suggest the opposite. We postulate rapid pressure increase (and potential strong currents) during D3 at least partially destroyed existing gas migration pathways, forcing them to reform with a different m value (Fig. SI 4.4). The influx of gas from deeper sediment ultimately controls the volume of gas released from the seep, this is most likely represented by the intercept value c. We note that despite the changing value of the slope m between -0.45 and -0.54 x 10^{-2} ml m^{-2} s^{-1} hPa^{-1} during D3, the intercept value c only varied from 13.42 to 15.34 ml m^{-2} s^{-1} (Tbl. 4.2).

4.4.4 Atmospheric pressure and gas flux

While the effect of atmospheric pressure on gas release from peat bogs has been investigated, its effect on lacustrine settings has not been definitively determined (Fechner-Levy & Hemond, 1996; Tokida et al., 2007; Kellner et al., 2006). Mattson and Likens (1990) were the first to report a possible correlation between lacustrine gas flux and atmospheric pressure, noting sporadic ebullition from Mirror Lake (New Hampshire) and low-pressure systems, but were unable to discount the effect of possible physical disturbances. Later Casper et al. (2000) were also able to observe a probable correlation between atmospheric pressure and gas flux in Priest Pot Lake (U.K). However, their sampling rates were sparse, once per week, meaning the correlation was tenuous. Similarly, Marcon et al. (2019) noted a correlation between high flux events and decreasing atmospheric pressure from a water reservoir in southern Brazil but they were only able to weakly demonstrate this trend with daily averages for selected periods. We

thus consider this study the first definitive proof of a negative correlation between atmospheric pressure and lacustrine gas flux (Tbl. 4.2, Fig. 4.8).

The effect of atmospheric pressure variation on gas flux can also be observed on the diurnal scale (Fig. 4.5, Fig. SI 4.8). Diurnal atmospheric pressure cycles due to land and sea breeze circulations is a phenomenon that is commonly visible in Lake Constance during good weather periods with strong solar radiation (Werner & Riffler, 2005), i.e., in our data from 03/04/2020 - 09/04/2020 (Fig. 4.5). During the night, a low-pressure cell forms above the lake as it radiates heat, thus the atmospheric (and hence the total) pressure is lower, and the gas flux increases. While during the day a high-pressure cell is centred on the lake as it is cooler than the surrounding area, thus the atmospheric (and hence the in-situ) pressure is higher, and the ebullition rate decreases. This diurnal cycle can also be seen in the autocorrelation of the atmospheric pressure, total pressure, and flux and in the cross correlation of flux and pressure. However, it is not always active, and the phenomenon is only occasionally visible and as the magnitude of this daily atmospheric pressure variation is only a few hPa the effect on flux is small (up to 4 hPa). This study is the first time a correlation between local land-lake wind circulation and ebullition rates has been observed.

4.4.5 Temporal flux variability

From the above discussion, it is clear that the release of gas from a lakebed seep (beyond that controlled by the gas reservoir) is regulated almost entirely by the total pressure at the point of release. This is consistent with observations from other studies (Maeck et al., 2014; Römer et al., 2016). The total pressure being a sum of the atmospheric and hydrostatic pressure means that any variation in meteorological conditions or water level can result in a change in gas flux. An understanding of how these properties change over an extended period is thus key to understanding the variability of gas flux from a lakebed.

Hydrostatic pressure, being a measure of the height of water above a point, typically varies daily, i.e., with tides, surface seiches, or bay oscillations, and annually with the seasonal

changes. The water level in Lake Constance increases in summer, reaching maximum values in June/July due to the snowmelt and increasing precipitation, and declines in winter, reaching its minimum in February (Jöhnk et al., 2004), changing over the season by an average of 1.5 m. It should be noted that water level changes of this magnitude are uncommon in large lakes, Lake Constance being one of the few unregulated large lakes (Jöhnk et al., 2004). The seasonal variation in hydrostatic pressure is clearly visible in our pressure data, peaking in June and reaching its lowest point in January, the overall trend mirrored in the gas flux measurements (Fig. 4.2-4.4). On the other hand, the tidal cycle in Lake Constance is extremely weak and not visible in our dataset, meaning lunar cycles have no measurable effect on gas flux here (but would undoubtedly have one in larger marine settings). Alternatively, though surface seiches, standing waves, are well documented in the lake with a period of ~54 min and a maximum amplitude of some cm, highest at the western part of Upper Lake Constance and less than half that in the eastern part of the lake, east of the River Rhine in Hard (Hamblin & Hollan, 1978; Hollan et al., 1980). Unfortunately, while the effect of surface seiches, with a maximum of 3 cm in magnitude, are visible in the in-situ pressure data (Fig. 4.5b), their effect on gas flux is not verifiable because of the high signal to noise ratio and our subsequent filtering of the data (Fig. 4.5a). It is possible that such variations may be detectable from larger seeps located deeper in the lake due to an increased magnitude in flux.

Atmospheric pressure at fixed geographical positions is known to show diurnal or semidiurnal cycles as a result of global atmospheric tides. However, this effect is only a few hPa in amplitude at the equator and decreases with latitude so can be dismissed here but may be a factor at more equatorial lakes (Oberheide et al., 2015). Weather systems are also known to regularly increase and decrease atmospheric pressure (Spiridonov et al., 2021). The passage of high- and low-pressure systems over the site across several days can be seen throughout the study and account for the deviation of in situ pressure from the overlying seasonal water level changes. Unfortunately, temporally these changes are less predictable, being almost impossible to predict more than a few weeks in advance (Spiridonov et al., 2021). As discussed previously

alternating high- and low-pressure cells tend to form over the lake via a day/night cycle which can be seen to have a minor effect on gas flux. Any apparent correlation between flux and rainfall or wind speed is likely a result of atmospheric pressure systems, so they are not considered driving factors.

4.4.6 Period of observation required to accurately determine long-term ebullition rates

As many studies attempt to extrapolate the long-term ebullition rate from a seep from short-period observations, we calculated the minimum period of observation necessary to accurately estimate the average gas flux from any of the seeps observed during this study. The approach taken here is to compare the raw flux estimates from the funnel across different observation lengths (from 5 min to 70 days) to the average flux calculated for the maximum period of observation (70 days), for each deployment (Fig. 4.9). A single measurement of a given observation length taken randomly during the deployment will lie anywhere in the full range. Repeated observations of the same length spaced out randomly across the period may allow researchers to exclude anomalous data, and thus be expected to lie between the 10 and 90th percentile of estimates.

As expected, the chance of accurately forecasting flux emissions increases with the length of observations. This is best seen during deployment D1 were extrapolating the 3-month flux from a 5 min observation could result in an estimate 0 - 2 times the real value, this error decreases logarithmically up to 1 hour observation with estimates between 0.86 and 1.11 times the real value. A similar trend is seen during deployment D3 with estimates between 0.72 and 1.05 times the real value. However, here while the tendency to overestimate flux flattens off at ~1-hour observations, underestimates are still problematic until ~10-day long observations. Conversely, subset estimates during D2 are not within 50 % of the real values until observations are over 10 days long. This is likely due to flux from D2 being more susceptible to pressure changes than the other seeps as well as potential interference from other bubble sources. This

makes determining how long an observation needs to be to accurately forecast gas flux difficult, as researchers will likely have no prior knowledge of how variable a seep will be.

However, having identified the key driving factor behind variations in gas flux as being variations in in-situ pressure (hydrostatic and atmospheric pressure) we instead speculate that it is not necessarily the duration of an observation that is important for determining the accuracy of its flux estimate, but rather the magnitude of the in-situ pressure variation experienced over its duration. To explore this idea, we determine the empirical relationship between in-situ total pressure and gas flux for deployment D1, this time only using observations made during the storm event on the 20th to the 24th of May (Tbl. SI 4.5). Here we see that the flux relationship produced using an 80 hPa increase in pressure (equivalent to 80 cm of water level change) in just 3.22 days is nearly exactly equal to the full measurement period. This would suggest that in order to accurately estimate the gas flux from a seep over an extended period of time researchers do not need long observation periods but rather observation periods that coincide with large changes in total pressure (e.g. when meltwater is entering the lake). The greater the range of data points for gas flux vs. in-situ total pressure the more accurately one can empirically map their relationship. This gives researchers an insight into how variable a given seep is and would allow them to more accurately predict methane (or carbon dioxide) ebullition fluxes via easily acquired hydrostatic pressure (water level) and atmospheric pressure data.

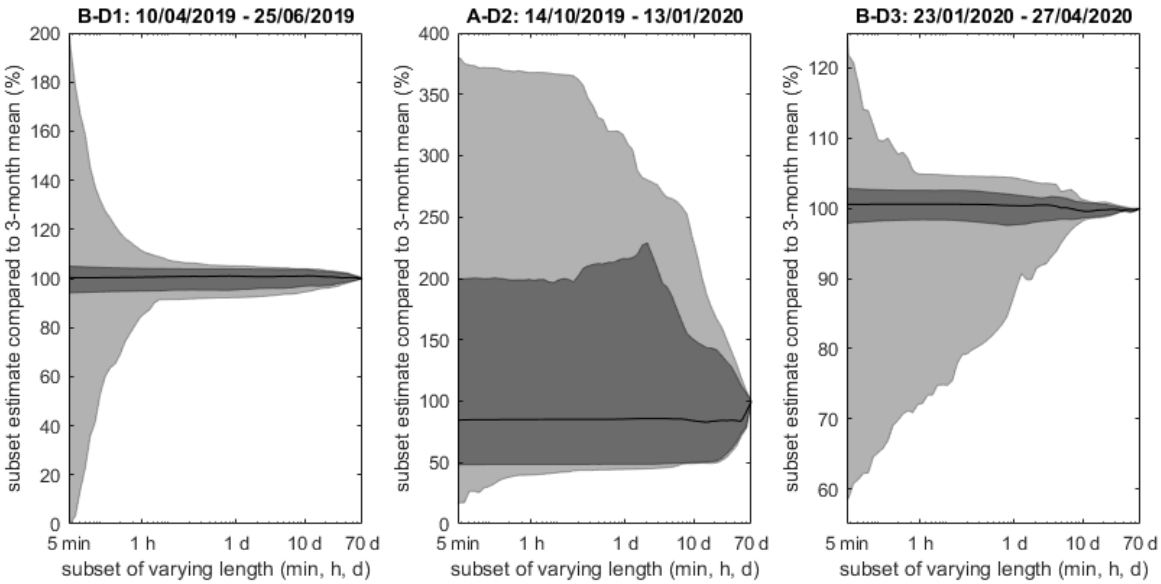

Figure 4.9: Comparison of the mean ebullition flux of subsets of varying length with the mean ebullition flux of 70 days. Observation length vs. possible flux measurement as a percentage of the mean ebullition flux of 70 days for the deployments B-D1, A-D2, and B-D3. The light grey area indicate the total range, the dark grey area the 10th and 90th percentiles and the black line the median of all subsets.

4.5 Conclusions

The rate of methane gas release from seeps in Lake Constance is inversely proportional to the total pressure at the point of release, which is the sum of the overlying hydrostatic and atmospheric pressure. When hydrostatic variation is large, gas flux variation is controlled by water level change. When hydrostatic variation is minimal, gas flux variation is dominated by atmospheric pressure change. A 100 hPa decrease in in-situ pressure, equivalent to a water level decrease of 1 m, results in a 6-12 % increase in gas flux. Wind and rainfall conditions have no direct impact on the rate of gas release. Thus, the variation of gas flux from a seep corresponds to the variation of water level and atmospheric pressure systems in the area.

The overall trend in gas flux variation over several months is driven by annual water level changes. On weekly time scales, weather systems alter the atmospheric pressure conditions above the lake resulting in minor deviations from the overall hydrostatic change. On a smaller scale extremely, weak tidal forces allowed flux rates to occasionally alternate on a day/night cycle

with high/low-pressure cells forming above the lake and decreasing/increasing the flux accordingly. Surface seiches are also suspected to have an effect on flux though we were not able to prove this.

Ebullition from a seep can be predicted from measurements of in-situ pressure, either measured at the site itself or at a base station within the body of water. This approach is more accurate than the extrapolation of average flux rates determined from short periods of observation, as it is commonly seen in the literature. Prediction of flux variations requires a time period of observation coincident with rapid variations in water level, i.e., during a storm event.

4.6 Acknowledgement

We thank J. Davis, J. Halder, A. Sulger, M. Wolf, B. Rosenberg, M. Mainberger and numerous student assistants in particular J. P. Armbruster for their technical assistance and support in the field and the lab. We thank M. Wessels from the Institute of Lake Research (ISF, State Institute for the Environment Baden-Württemberg LUBW) for providing information about the positions of the gas flares. We would also like to thank the State Institute for the Environment Baden-Württemberg (LUBW) for providing water level data. Moreover, we thank S. Hölzl from the Central Institute for Meteorology and Geodynamics (ZAMG), for providing wind and atmospheric pressure data from the weather station Rohrspitz. We also thank the German Weather Service (DWD) for providing rain data from station Lindau and Zeisertsweiler. This work was financially supported by the German Research Foundation (DFG, Grant HO 4536/4-1) and the STEMM-CCS project (European Union's Horizon 2020 research and innovation programme under grant agreement No. 654462).

4.7 Supplementary Information

4.7.1 Tables

Deployment	Gradient m ($x10^{-2}$ ml m^{-2} s^{-1} hPa^{-1}) Base station				Intercept c (ml m^{-2} s^{-1}) Base station				R^2 Base station				RMSD (ml m^{-2} s^{-1}) Base station			
	TP	HP	WS	R	TP	HP	WS	R	TP	HP	WS	R	TP	HP	WS	R
B-D1	-0.25	-0.25	2.24	1.21	7.87	5.45	4.49	4.55	0.84	0.83	0.09	0.02	0.05	0.05	0.16	0.16
A-D2	-3.45	-4.05	9.75	-13.19	46.56	15.34	1.28	1.51	0.33	0.31	0.49	0.50	1.75	1.49	2.20	2.24
A-D2.1	-2.45	-4.42	0.62	-12.43	33.50	16.62	1.31	1.33	0.40	0.87	0.31	0.31	0.43	0.19	0.69	0.68
B-D3	-0.45	-0.52	-1.00	-	10.27	6.13	4.50	-	0.47	0.46	0.04	-	0.08	0.08	0.11	-
B-D3.1	-0.48	-0.53	-0.07	-1.08	10.47	6.03	4.44	4.44	0.76	0.55	0.00	0.05	0.02	0.02	0.04	0.04
B-D3.2	-0.43	-0.59	0.49	3.38	10.00	6.33	4.36	4.37	0.74	0.07	0.05	0.06	0.03	0.06	0.06	0.06
B-D3.3	-0.60	-0.67	-1.02	-	12.28	6.66	4.57	-	0.96	0.92	0.03	-	0.02	0.03	0.09	-

Table SI 4.1: The correlation between the measured flux during each deployment as compared to the total pressure (TP) and hydrostatic pressure (HP) at the Friedrichshafen base station as well as the wind speed (WS) and rainfall (R) as measured at local weather stations.

Deployment (technique)	Gradient m ($*10^{-2}$ ml s^{-1} hPa^{-1})					Intercept c (ml s^{-1})					R^2				
	In-situ			Base station		In-situ			Base station		In-situ			Base station	
	TP	HP	AP	TP	HP	TP	HP	AP	TP	HP	TP	HP	AP	TP	HP
A-D2	-2.15	-2.50	0.62	-2.20	-2.59-	30.55	11.25	-5.00	29.80	9.82	0.33	0.31	0.49	0.33	0.31
A-D2.1 (physical)	-1.56	-2.72	-0.04	-1.57	-2.83	22.43	12.19	1.28	21.44	10.63	0.42	0.87	0.31	0.40	0.87
A-D2	-2.35	-3.82	2.24	-2.46	-4.06	33.59	16.97	-20.50	33.31	15.10	0.55	0.45	0.64	0.54	0.44
A-D2.1 (acoustic)	-0.90	-2.14	1.16	-0.91	-2.29	13.36	9.90	-10.15	12.97	8.93	0.47	0.42	0.49	0.47	0.42

Table. SI 4.2: Correlation between gas flux as measured by the acoustic technique, and in-situ total lakebed, hydrostatic and atmospheric pressure for each long-term deployment.

Deployment	Mean fluctuation of the measured flux compared to the mean measured flux (%)	Mean fluctuation of the modelled flux compared to the mean measured flux (%)	Contribution to the modelled flux fluctuations (%)	
			HP	AP
B-D1	3.07	3.45	87.90	12.10
A-D2	53.08	47.79	93.52	6.48
A-D2.1	18.78	18.86	97.16	2.84
B-D3	2.07	1.78	81.90	18.10
B-D3.1	0.61	0.65	53.12	46.88
B-D3.2	1.02	0.90	1.67	98.33
B-D3.3	1.79	1.97	85.67	14.33

Table. SI 4.3: Percentage mean fluctuations of the measured and modeled flux during the deployments D1-D3 and the percentage contribution of hydrostatic and atmospheric pressure to modeled flux fluctuations. Via physical flux measurements.

Deployment	Gradient m ($x10^{-2}$ ml m^{-2} s^{-1} hPa^{-1})		Intercept c (ml m^{-2} s^{-1})	R^2	RMSE (ml m^{-2} s^{-1})
	HP	AP			
B-D1	-0.26	-0.38	$2.14x10^{-14}$	0.92	0.05
A-D2	-7.17	0.95	$-1.01x10^{-13}$	0.58	1.18
A-D2.1	-4.37	-0.21	$1.37x10^{-13}$	0.91	0.18
B-D3	-0.48	-0.26	$1.22x10^{-14}$	0.48	0.08
B-D3.1	-0.52	-0.38	$-3.87x10^{-14}$	0.74	0.02
B-D3.2	-0.15	-0.47	$-8.11x10^{-15}$	0.75	0.03
B-D3.3	-0.57	-0.32	$-1.57x10^{-13}$	0.96	0.02

Table SI 4.4: Multiple linear regression between the in-situ hydrostatic & atmospheric pressure and the physical gas flux measurement.

Hydrostatic pressure change (hPa)	Observation length (days)	Gradient m ($x10^{-2}$ ml m^{-2} s^{-1} hPa^{-1})	Intercept c (ml m^{-2} s^{-1})	R^2	RMSE (ml m^{-2} s^{-1})
155	65.72 (B-D1 full period)	-0.25	9.83	0.84	0.05
	Storm event				
10	1.01	0.02	4.17	0.07	0.04
20	1.31	-0.22	9.30	0.13	0.04
30	1.53	-0.29	10.63	0.35	0.04
40	1.73	-0.28	10.47	0.45	0.03
50	1.94	-0.29	10.66	0.60	0.03
60	2.17	-0.30	10.77	0.69	0.03
70	2.50	-0.28	10.44	0.77	0.03
80	3.22	-0.25	9.78	0.74	0.03

Table SI 4.5: Correlation between measured physical flux and total in-situ pressure as observed during successive 10 hPa pressure increases during a storm event between 20/05/19 - 24/05/19 as compared to the overall correlation seen during D1.

4.7.2 Figures

a)

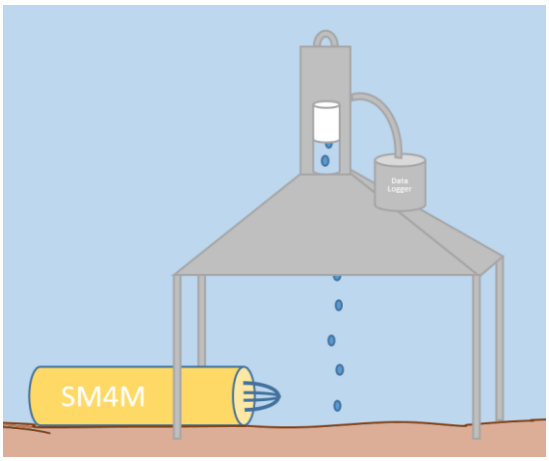

b)

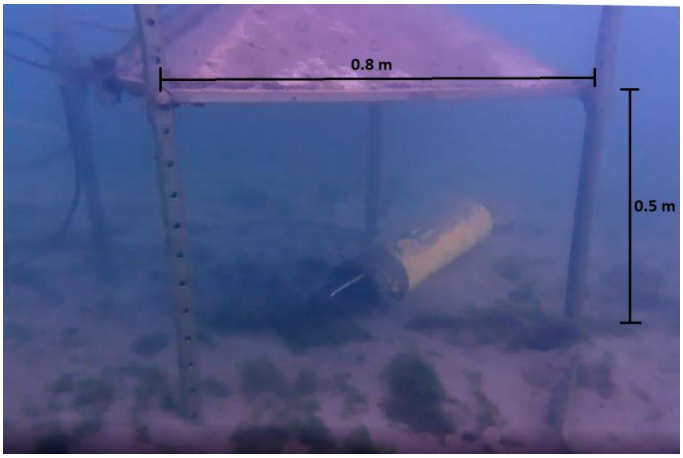

Figure SI 4.1: Deployment of the ebullition flux funnel above the seep and hydrophone under the funnel and close to the seep: a) schematic diagram and b) photo of the deployment, taken during the long-term deployment D3 at 10/11/2019.

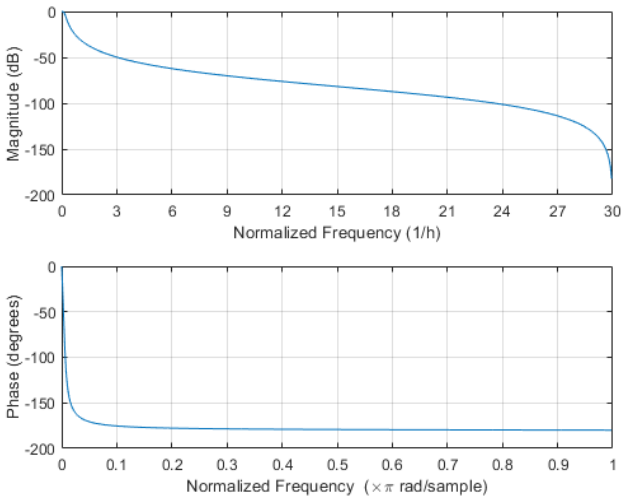

Figure SI 4.2: Cut off frequency used to filter raw data.

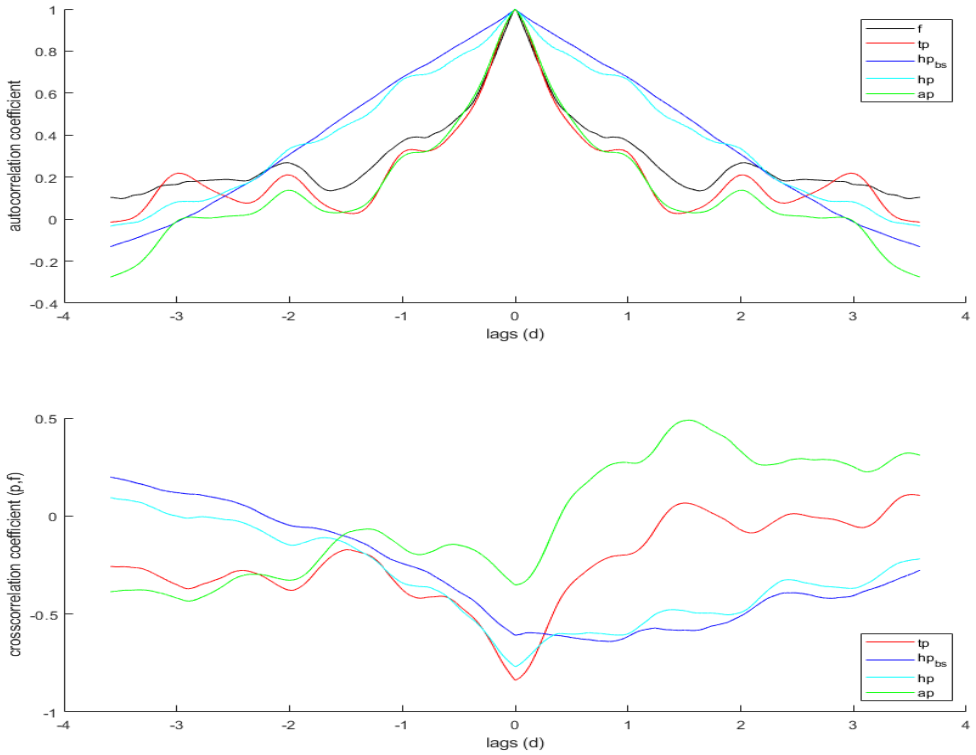

Figure SI 4.3: Auto and cross correlation graphs for a 10-day period during deployment B-D3 from 03/04/2020 to 13/04/2020. f = flux, tp = total pressure, hp_{bs} = hydrostatic pressure at base station, hp = hydrostatic pressure at seep site, ap = acoustic pressure

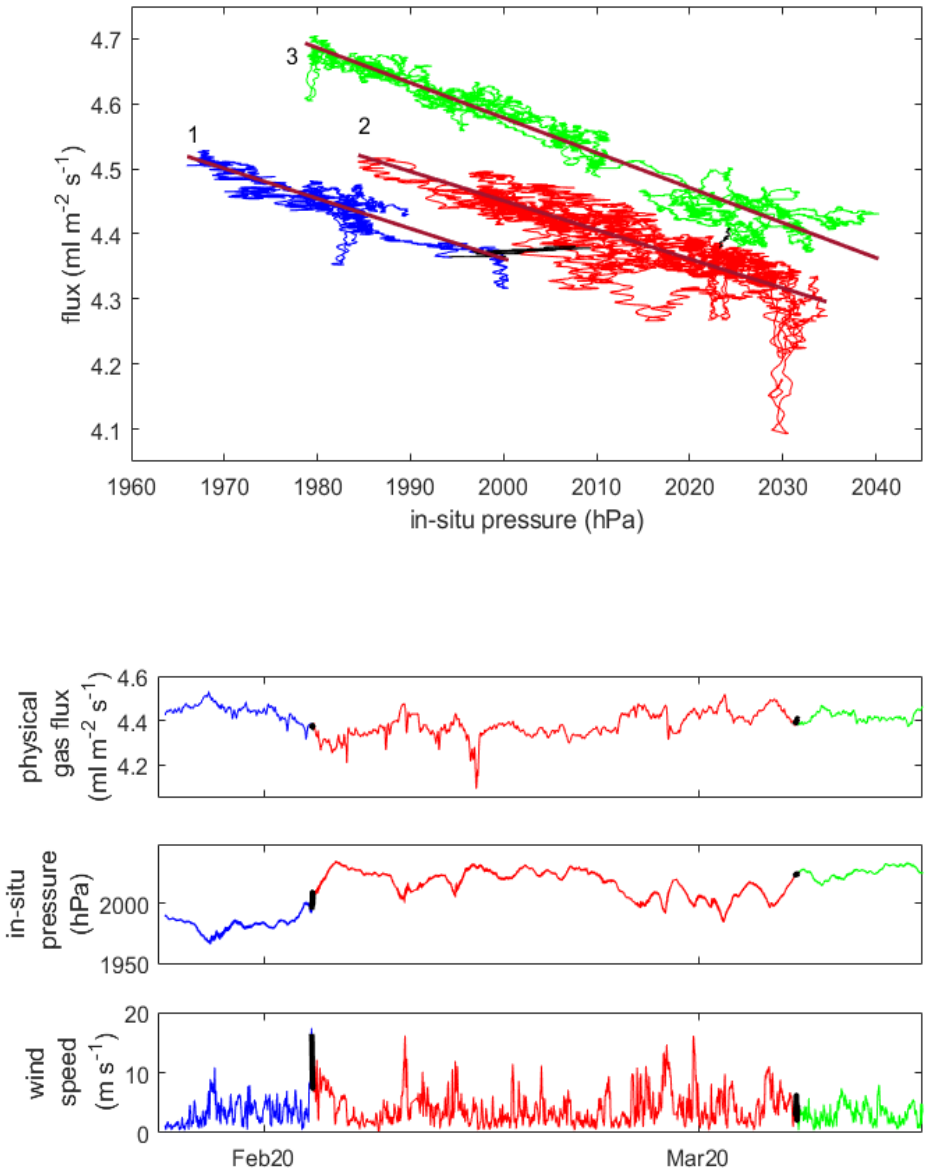

Figure SI 4.4: In-situ pressure vs gas physical gas flux during long term deployment D3 with the transitional periods between D3.1 (blue), D3.2 (red) and D3.3 (green) highlighted alongside top) graph of flux, middle) total in-situ pressure, bottom) windspeed.

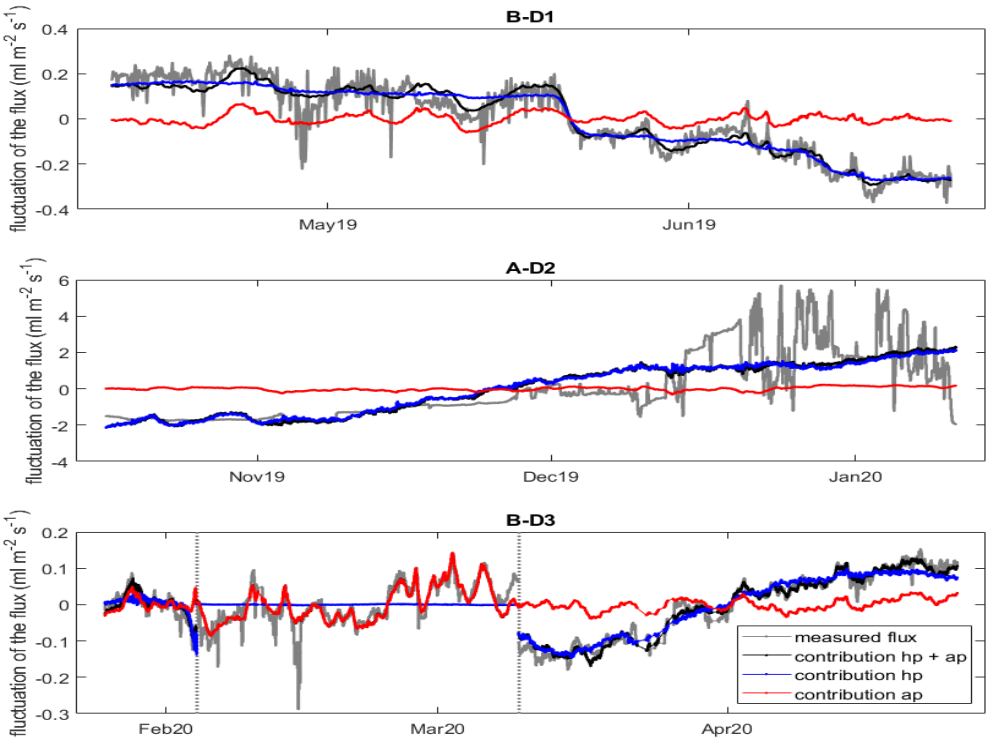

Figure SI 4.5: the normalised fluctuation of the physical flux measurement alongside the contribution from acoustic pressure (red), hydrostatic pressure (blue) and both combined (black).

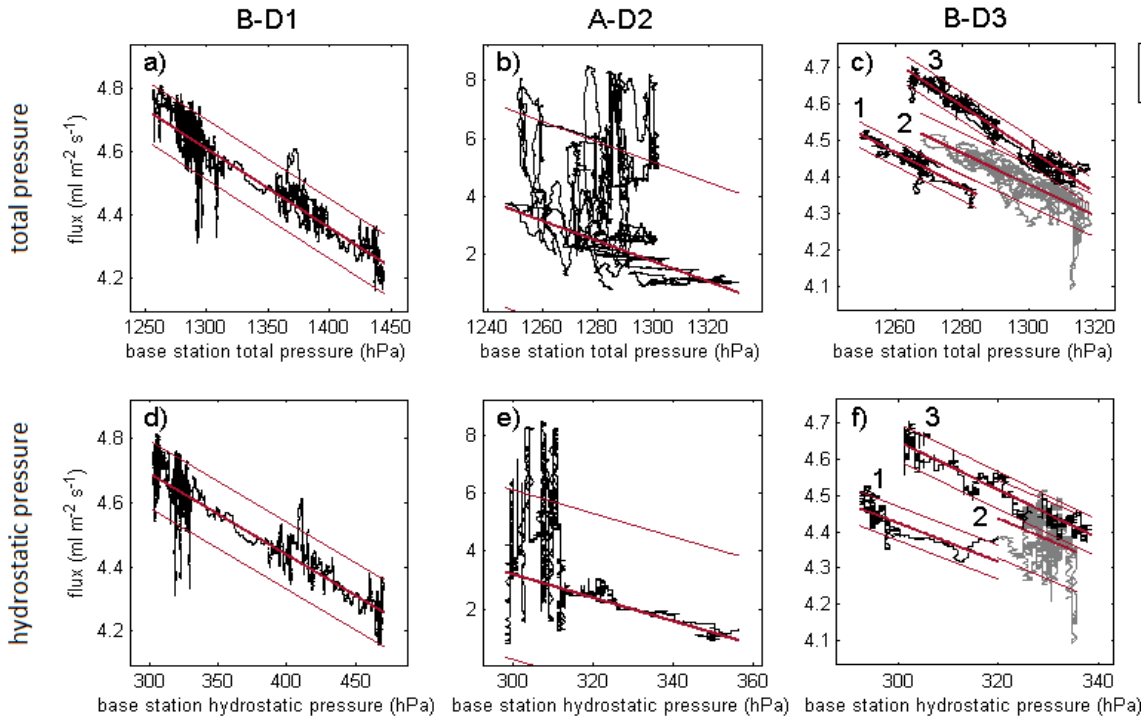

Figure SI 4.6: displaying the correlation between the measured flux during each deployment as compared to the total lakebed and hydrostatic pressure at the Friedrichshafen base station.

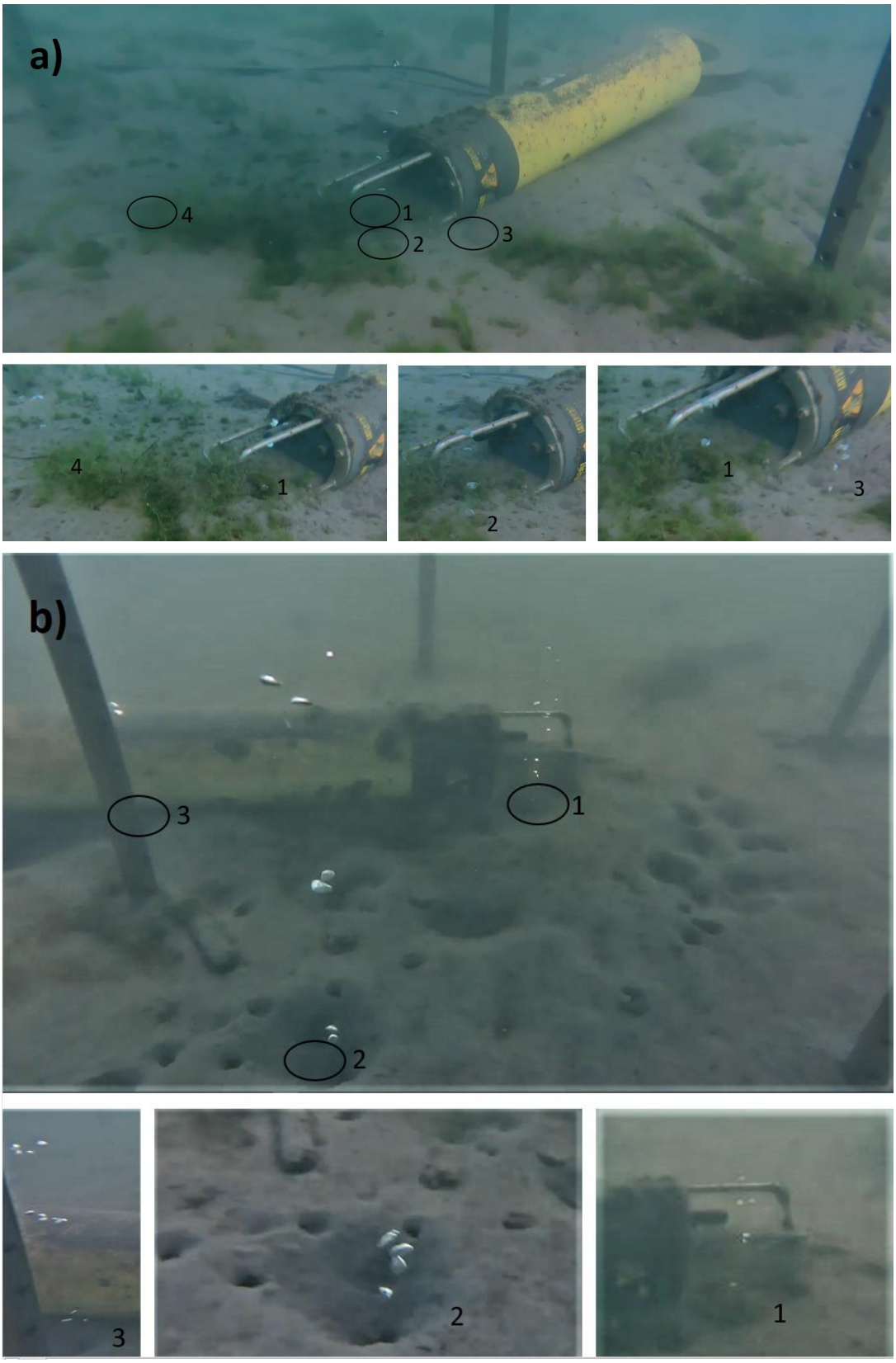

Figure SI 4.7: a) D2 10/11/2019: main flare 1, irregular bubble exits also from 2-4, all inside the funnel. b) *15/01/2020: main bubble stream at 1, additional continuous bubble streams at 2 and 3, that are positioned outside the funnel.*

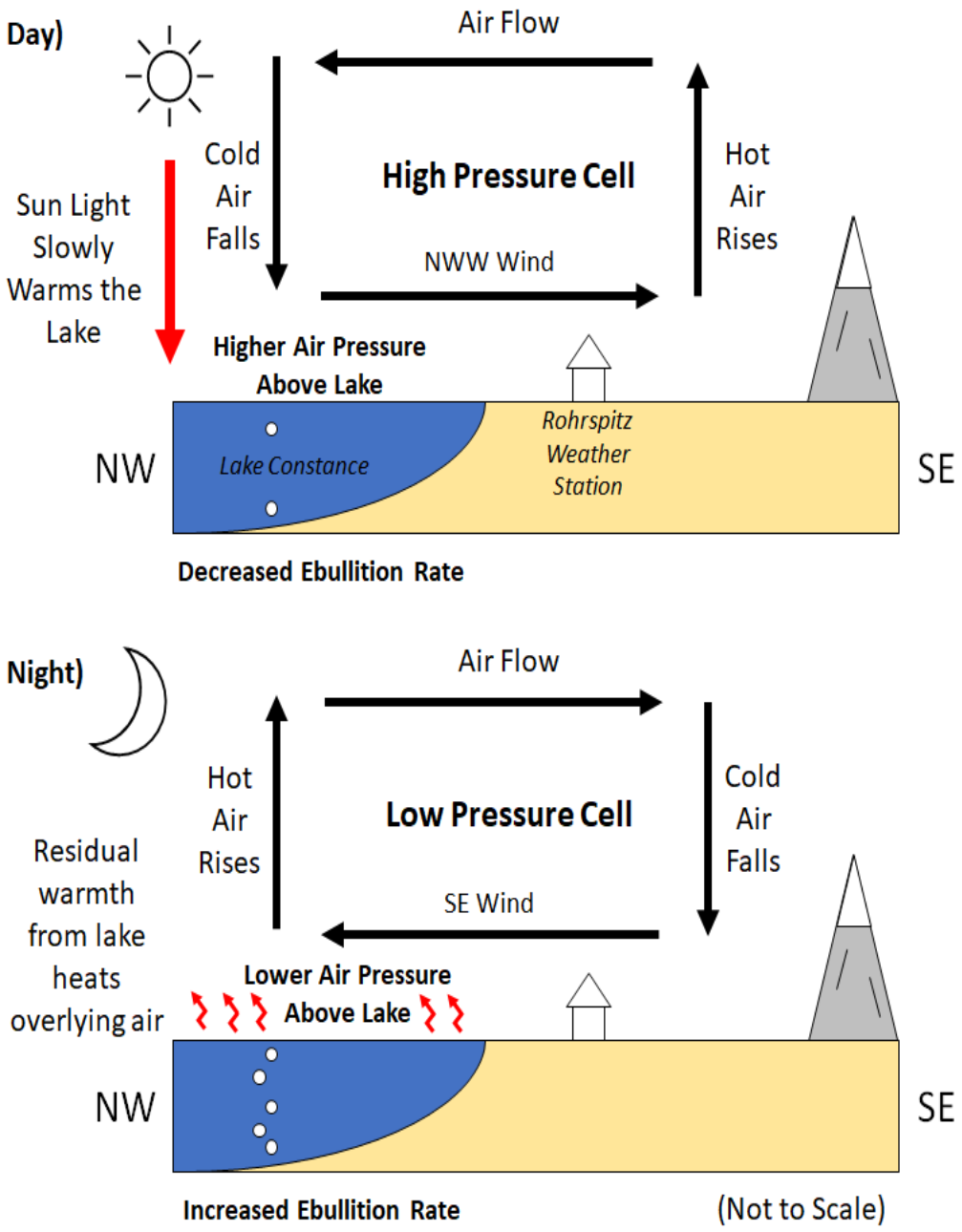

Figure SI 4.8: Diagram of the diurnal pressure cycles above Lake Constance. During the day the water absorbs heat from the sun while the land reflects a large portion of the energy, heating the air above and causing it to rise. The air flows above the lake where it cools and falls, increasing the air pressure on the lake and decreasing gas flux. Meanwhile, during the night the residual heat from the lake warms the air above it, causing it to rise. This leads to a decrease in air pressure above the lake and an increase in gas flux.

4.7.3 Dissolution of Methane Gas

Optical and physical gas flux measurements were made 50 – 60 cm above the lakebed, and consideration is needed for the amount of dissolution when determining the lakebed flux. Methane gas, which is known to be the dominant gas in bubbles in Lake Constance (Bussmann et al., 2013), has a relatively low dissolution rate (Rehder et al., 2002). We calculate that only 10% of the gas would dissolve within the bottom 1 m of the lake and given that larger bubbles contribute the most to the total flux, will rise faster, we determine that the effects of dissolution are negligible to our measurements of gas flux. Therefore, acoustic flux estimates, recorded at the lakebed, may be directly compared to the physical and optical measurements made at 50 - 60 cm above the lakebed.

4.7.4 CH_4 Concentration of bubbles

Samples of the trapped gas from the funnel were transferred with a 1 ml syringe into 122 ml capped gas-tight and evacuated serum bottles. The methane concentration of the gas samples was measured using gas chromatography (GC) with a flame ionization detector (GC-FID; Shimadzu, Kyoto, Japan). The GC data was calibrated using gas standards of 1,000 ppm, and 10,000 ppm (Air Liquide). For each gas sample, four to eight replicates were taken and after every five gas samples, the calibration was repeated and used for the subsequent gas samples.

The released bubbles of the seeps B-D1, A-D2, and B-D3 had average CH_4 volume concentrations of 82.1 %, 95.4 %, and 94.2 %.

4.7.5 Methane emissions into the atmosphere

The observation of many bubbles > 0.5 cm being released from seeps in lake Constance (Fig. 4.3 b-c), has implications on the atmospheric methane budget of the area. Dissolution typically prevents gas from small bubbles being released directly into the atmosphere as gas is quickly absorbed into the surrounding water column. However larger bubbles are more likely to

reach the atmosphere, particularly in shallow water as seen here (Rehder et al 2002; McGinnis et al., 2006). Thus, the large bubble sizes observed during this study imply that a sizable portion of the methane is released directly into the atmosphere.

It is difficult to accurately estimate the percentage of methane that is released directly into the atmosphere from our seeps. Our results show that bubbles rising 7 m through the water column maintained 76% of their original methane concentration. Unfortunately, most work studying the dissolution of methane has been focused on deep marine seeps making a direct comparison to shallow freshwater systems problematic. Regardless, McGinnis et al., (2006) showed in the black sea bubbles larger than 0.5 cm in radius rising from 90 to 80 m water depth (10 m) maintained >70 % of their original methane content. From this one could estimate that ~70 % of the methane released from shallow water seeps in Lake Constance reaches the atmosphere. This implies that a significant portion of the methane from the lakebed is released into the atmosphere.

Chapter 5 Improving methods of acoustic gas flux quantification – investigation into the initial amplitude of bubble excitation

Passive acoustic inversion techniques for measuring gas flux into the water column have the potential to be a powerful tool for the long-term monitoring and quantification of natural marine seeps and anthropogenic emissions. Prior inversion techniques have had limited precision due to lack of constraints on the initial amplitude of a bubble's excitation following its release into the water column ($R_{\varepsilon 0i}$). We determine $R_{\varepsilon 0i}$ by observing the acoustic signal of bubbles released from sediment in a controlled experiment. Strong evidence is found that $R_{\varepsilon 0i}$ is positively correlated with the equilibrium bubble radius, inclusion of this observation within the flux inversion technique improves the precision of the technique by 78%. We demonstrate the refined acoustic inversion technique by quantifying the flux from a volcanic CO_2 seep offshore Panarea (Italy), and finding that the measured flux of 3.2 ± 0.6 L/min is consistent with optical flux measurements, but overestimates physical measurements of 2.3 L/min. We discuss the role of bubbles fragmentation in the water column as a possible cause of this discrepancy as well as the need to compare calibration and field sites.

5.1 Introduction

In recent years there has been a growing need to refine methods of quantifying the volume of gas released into the water column via marine sediments. This demand is fuelled by both a need to better understand the natural carbon cycle and an industry need to monitor offshore industrial activity e.g., Carbon Capture and Storage (CCS) sites (Blackford et al., 2014, 2017; Dean et al., 2020; Oppo et al., 2020; Razaz et al., 2020). While directly capturing the gas may have been sufficient for such investigations in the past, such physical measurements are severely limited in regard to spatial and temporal coverage. Optical techniques are generally accurate for a limited bubble size range (i.e., bubbles large enough to be accurately resolved, but small enough to ensure the closeness to sphericity that many single-camera inversions assume). However, unless multiple cameras are used to reduce parallax errors and discern the volume of aspherical bubbles, they are prone to systematic errors. Furthermore, they are limited in the area they can survey and are dependent on water visibility (Jordt et al., 2015; Wang and Socolofsky, 2015; Li et al., 2021b). Active acoustic techniques, while being able to cover a large area, require time-consuming processing in order to provide accurate quantification data and provide only a snapshot measurement (Greinert et al., 2006; Greinert, 2008; Leighton et al., 2012; Baik et al., 2014; Schneider von Deimling et al., 2015; Li et al., 2020a). Furthermore, the accuracy of the assumptions that underpin the conversion of active acoustic data into gas fluxes is still evolving (Li et al., 2020a). Passive acoustic inversion techniques, on the other hand, are low energy and capable of long-term deployments in any level of visibility and also provide information about the size distribution of bubbles released from the seep (Leighton et al., 1991; Leighton and White, 2012; Bergès et al., 2015; Vazquez et al., 2015; Chen et al., 2016; Li et al., 2021a, 2021b).

Passive acoustic inversion relies on a mathematical model of the sounds emitted by a bubble as it is formed. Originally this principle was restricted to measuring the size of individual bubbles in low flux environments via the so-called “signature method”, to ensure the acoustic signature of bubbles did not overlap (Leighton and Walton, 1987; Pumphrey and Ffowcs Williams, 1990; Longuet-Higgins et al., 1991; Czerski and Deane, 2010). This approach relies on knowing the

frequency emitted by a bubble immediately after release, which is inversely proportional to its equilibrium radius, as defined by the Minnaert equation (Minnaert, 1933; Leighton and Walton, 1987; Leighton, 1994; Bergès et al., 2015).

Signal processing methods were developed to allow this technique to extend to intermediate flux rates, when bubble signatures begin to overlap (Leighton et al., 1998). For high flux rates, when bubble signatures do overlap to a significant degree, an approach based on the spectral density of the acoustic pressure measured in the far field at a known distance from a gas seep is appropriate (Loewen and Melville, 1994; Leighton and White, 2012). Using a model based on the spectrum of bubble release signals, the measured spectrum can be used to infer the bubble size distribution. However, the energy released by individual bubbles remains poorly characterised (Leighton and White, 2012), in particularly how it varies with depth and mode of injection. If, for example, the model assumes the bubble is a stronger sound source that it is, then the inversion will underestimate the gas flux (Leighton and White, 2012). Conversely, if a single bubble emits more energy that predicted by the model, then the passive acoustic inversion will overestimate the gas flux. To date, the use of the spectral method in the field has proven effective, providing continuous estimates of gas flux over extended periods of time validated by intermittent physical and optical measurements. This success is, however, in part because estimates contained large uncertainties (Bergès et al., 2015; Li et al., 2020b, 2021b).

This study examines the acoustic signature of bubbles released from coarse-grained sediment in order to improve the spectral inversion approach by examining the energy released by an individual bubble and the relationship between the initial radius of excitation of a bubble and the equilibrium radius of a bubble. We then use this refined acoustic inversion technique to quantify ebullition from a natural CO_2 seep formed from coarse-grained sediment and compare the estimate to physical and simultaneous optical measurements.

5.2 The Spectral Method – model of acoustic emissions from a bubble

The following is a condensed summary of the mathematical model for the sound from a plume, which forms the basis of the inversion approach, as originally published by Leighton and White (2012). The theory assumes that the acoustic pressure signature from a single bubble is an exponentially decaying sinusoid.

For a spherical bubble, immediately after being entrained into the water column a bubble will undergo damped simple harmonic motion. The radius of a bubble R over time t can be described by

$$R(t) = R_e\left(R_0 - R_{\varepsilon 0 i} e^{j\omega_0 (t-t_\vartheta)} e^{-\omega_0 \delta_{tot}(t-t_\vartheta-t_i)/2} H(t-t_0-t_i)\right), \tag{5.1}$$

where δ_{tot} is the total damping coefficient, H is the Heaviside step function, t_i is the moment when the acoustic signal is first detected, t_0 accounts for the propagation time between perturbations of the bubble and the corresponding pressure signal at the receiver, $t_i - t_0$ is the moment when the bubble begins to oscillate, R_0 is the equilibrium radius of the bubble and $R_{\varepsilon 0 i}$ is the initial amplitude of displacement of the bubble wall (Leighton and White, 2012).

The natural angular frequency ω_0 of the bubble is given by an extended form of Minnaert's equation (Leighton, 1994; Bergès et al., 2015)

$$\omega_0 = \frac{1}{R_0\sqrt{\rho_0}}\sqrt{3\kappa\left(p_0 - p_v + \frac{2\sigma}{R_0}\right) - \frac{2\sigma}{R_0} + p_v - \frac{4\eta^2}{\rho_0 R_0^2}}, \tag{5.2}$$

where κ is the polytropic index of the gas in the bubble, p_0 is the ambient pressure outside of the bubble, p_v is the gas' vapour pressure, ρ_0 is the density of surrounding liquid and η is the liquid's shear viscosity.

The oscillating bubble wall creates an acoustic pressure in the far field at a distance r given by:

$$P(t) \approx R_e\left\{\rho_0 \frac{(\omega_0 R_0)^2}{r} R_{\varepsilon 0 i} e^{j\omega_0(t-t_\vartheta)} e^{-\omega_0 \delta_{tot}(t-t_0-t_i)/2} H(t-t_i)\right\} =$$

$$(\omega_0 R_0)^2 \frac{\rho_0}{r} R_{\varepsilon 0 i} e^{j\omega_0(t-t_\vartheta)} e^{-\omega_0 \delta_{tot}(t-t_0-t_i)/2} H(t-t_i).$$

(5.3)

The squared magnitude of the Fourier transform of the pressure radiated from a single bubble at a distance *r* is:

$$|X(\omega, R_0)|^2 = \left[{\omega_0}^2 {R_0}^3 \frac{\rho_0}{r} \frac{R_{\varepsilon 0 i}}{R_0}\right]^2 \left(\frac{4\left[(\omega_0 \delta_{tot})^2 + 4\omega^2\right]}{\left[(\omega_0 \delta_{tot})^2 + 4(\omega_0 - \omega)^2\right]\left[(\omega_0 \delta_{tot})^2 + 4(\omega_0 + \omega)^2\right]}\right).$$

(5.4)

The spectrum, $S(\omega)$ of the measured acoustic pressure from a population of bubbles with size distribution $D(R_0)$, which is defined such that $\int_{R_1}^{R_2} D(R_0) dR_0$ represents the number of bubbles generated per second with a radius in the range (R_1, R_2) can be expressed as

$$S(\omega) \approx \int_0^\infty D(R_0) |X(\omega, R_0)|^2 dR_0,$$

(5.5)

To estimate the number of bubbles via the far field acoustic signal one needs to determine what value of $D(R_0)$ generates the measured power spectrum, $S(\omega)$, This can be achieved by discretising Eq. 5.5 into N_b finite radii bins, such that the n^{th} radius bin is centred on the radius R_n^c. Assuming the bins are contiguous the power spectrum can be given as:

$$S(\omega) \approx \sum_{n=1}^{N} \Psi(n) |X(\omega, R_0)|^2,$$

(5.6)

where $\Psi(n)$ is the bubble generation rate within a radius bin (i.e., the number of bubbles formed per second within the n^{th} radius bin). This can be expressed in matrix form:

$$\underline{S} = M\underline{\Psi}, \tag{5.7}$$

$\underline{\Psi}$ being a column vector of the values defining the average number of bubbles in a radius bin per second, $\underline{S}$ is a vector containing the estimated spectrum at the frequencies ω_m and *M* is a matrix with elements $\{M\}_{m,n} = |X(\omega, R_0)|^2$.

The matrix equation (Eq. 5.7) can be solved for the number of bubbles generated per second $\underline{\Psi}$ in a radius bin provided $\underline{S}$ and M are known, to yield an estimate of the gas flux. However, while $\underline{S}$ can easily be determined accurately with the use of a calibrated hydrophone, M remains difficult to accurately determine. This is because (4) contains one important unknown value, the initial amplitude of the displacement of the bubble wall when it begins to oscillate, $R_{\varepsilon 0i}$. The earliest estimate $R_{\varepsilon 0i} = 10^{-5} \cdot R_0$ for $R_0 \approx 1$ mm, (Leighton and Walton, 1987) was refined to $R_{\varepsilon 0i} = 10^{-4} \cdot R_0$ by Leighton (1994) when he applied a more sophisticated model to the same data. Medwin and Beaky (1989) estimated $R_{\varepsilon 0i} = 1.5 \times 10^{-2} \cdot R_0$ for $R_0 \approx 0.312$ mm. Deane and Stokes (2008) increased by an order of magnitude the number of bubbles for which $R_{\varepsilon 0i}$ was estimated, by fragmenting over 1000 bubbles in horizontal streams. Analysing bubbles from $R_0 = 0.1$ to 1 mm they found the initial amplitude of the displacement of a bubble as fraction of its equilibrium radius increased with decreasing bubble size; $R_{\varepsilon 0i}/R_0$ decreased with bubble size. However, for a given bubble size $R_{\varepsilon 0i}/R_0$ was seen to vary by up to two orders of magnitude, making accurately defining $R_{\varepsilon 0i}$ for a particular ebullition site impossible. None of these estimates for the initial amplitude are based on bubbles emerging from sediments. Berges et al. (2015) retroactively calculated the $R_{\varepsilon 0i}/R_0$ value needed to correctly invert the flux of bubbles released from needles in a test tank with values generally ranging between 1 and 5 $\times 10^{-4}$.

Drawing attention to the need for further data to provide better estimates of the acoustic source strength of the bubble (for which $R_{\varepsilon 0i}$ stood as proxy), Leighton and White (2012) simplified the analysis by assuming that, over the range of bubble sizes and environmental conditions (e.g. hydrostatic pressure) present in the acoustic dataset that was to be inverted, they would use a first approximation that the ratio of the initial displacement of the bubble wall to the equilibrium radius of the bubble, $R_{\varepsilon 0i}/R_0$ was constant. Bergès et al., (2015) placed the constant between 1.4×10^{-4} and 5.6×10^{-4} based on the 25th and 75th percentile of results from Deane & Stokes (2008), which permitted the successful inversion of gas flux in the laboratory and field, although, the uncertainty in the ratio introduced wide error bars in the final flux measurements (Bergès et al., 2015). Consequently, there is a need for calibrated $R_{\varepsilon 0i}$ values, particularly in conditions replicating those found in the field. This paper undertakes such an exercise.

We note if we consider $R_{\varepsilon 0i}$ to be a function of R_0 in the form, $R_{\varepsilon 0i} = f(R_0)$ we can rewrite (4) without $R_{\varepsilon 0i}/R_0$ as

$$|X(\omega, R_0)|^2 = \left[\frac{R_{\varepsilon 0i}{\omega_0}^2 {R_0}^2 \rho_0}{r}\right]^2 \left(\frac{4[(\omega_0\delta_{tot})^2 + 4\omega^2]}{[(\omega_0\delta_{tot})^2 + 4(\omega_0 - \omega)^2][(\omega_0\delta_{tot})^2 + 4(\omega_0 + \omega)^2]}\right)$$

$$= \left[\frac{f(R_0){\omega_0}^2 {R_0}^2 \rho_0}{r}\right]^2 \left(\frac{4[(\omega_0\delta_{tot})^2 + 4\omega^2]}{[(\omega_0\delta_{tot})^2 + 4(\omega_0 - \omega)^2][(\omega_0\delta_{tot})^2 + 4(\omega_0 + \omega)^2]}\right). \quad (5.8)$$

In this study we analyse the acoustic emissions from 368 bubbles released from sediment into the water column, to determine the $R_{\varepsilon 0i}$, measuring the frequency of each bubble oscillation alongside the maximum radius of excitation and the total energy released.

Methodology

5.2.1 Experimental Design

In order to measure and analyse the acoustic signature of bubbles released from sediment, air was injected into the base of ~30 cm of artificial sediment, with resulting emissions into the water column recorded with a calibrated hydrophone (Reson TC 4032; 30 cm above the sediment surface) (Fig. 5.1a-b). Synthetic sediment (Ballotini, 9mm diameter, pebbly gravel on the Wentworth scale) was used to ensure uniformity between the grains, and to simplify porosity and permeability calculations (Fig. 5.1c). The experiment was designed so that ebullition was in the centre of a large 8 m x 8 m (by 5 m deep) freshwater tank (Fig. 5.1a) to minimise the interference of wall reflections, allowing accurate characterisation of the acoustic signatures (Fig. 5.1d). The gas injection rate at the base of the sediment was adjusted until gas migration through the sediment caused bubbles to enter the water column at less than 1 bubble per second. Bubble radii were determined directly from optical measurements (Sony FDR3000 camera, 50 cm from ebullition site).

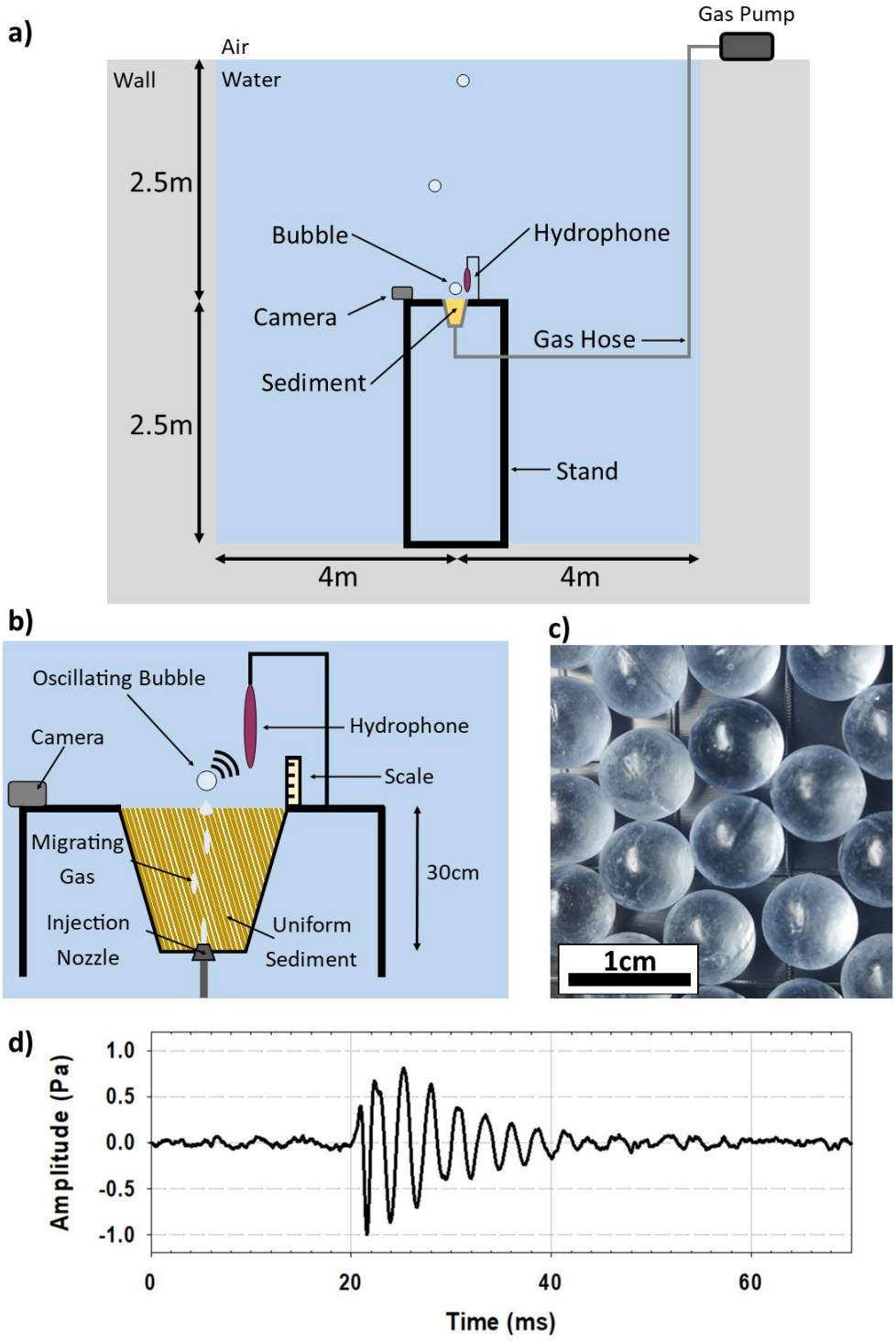

Figure 5.1: Experimental Design. a) schematic showing gas injection at base of sediments and the position of optical and acoustic sensors within the water tank; b) detailed schematic; c) image of the Ballotini sediment used for the experiment; d) sonogram displaying the typical acoustic emission of a bubble as recorded by the hydrophone.

5.2.2 Analysis

The optical footage was used to identify periods where single, discrete bubbles entered the water column, to ensure that the acoustic signal of an individual bubble release was analysed. The acoustic and optical data for each bubble were jointly analysed to determine the start and end time of the bubble oscillation as well as the maximum pressure of the bubble signal (P_{max}). The initial excitation radius of the bubble ($R_{\varepsilon 0i}$) is then calculated using the pressure signals via the following equation (Leighton, 1994; Deane & Stokes, 2009):

$$R_{\varepsilon 0i} = \frac{r}{3\kappa p_0} P_{max}, \tag{5.9}$$

where r is the distance between the release point and the hydrophone and P_{max} is the maximum pressure signal recorded at the hydrophone as a result of the bubble oscillation.

The centre frequency of each bubble signature was determined by iteratively fitting an exponentially decaying sinusoid to the signal in the least squares sense. The frequency of this wave was used to calculate the equilibrium bubble radius R_0 calculated (see Eq. 5.2). The total energy of each bubble oscillation was determined by summing the acoustic pressure as recorded at the hydrophone between the start and end of the event ($t_2 - t_1$) assuming spherical spreading:

$$E = \frac{1}{fs} \frac{4\pi r^2}{2\rho_0 c} \sum_{t_1}^{t_2} |P(t)^2|, \tag{5.10}$$

where c is the speed of sound in water (1500 ms^{-1}). In order to account for background noise, the ambient energy within the tank was calculated using Eq. 5.10, with the average energy released over 1s being equal to 6.2×10^{-9} J. Subsequently $6.2 \times 10^{-9}(t_1 - t_2)$ J were subtracted from each event so that only the energy of the bubble oscillation was observed.

We validate our observations by using them to measure the gas flux from a natural seep in offshore Panarea (Italy) and compare them to optical and physical measurements. Analysis focusses on 10 minutes of simultaneous optical and acoustic data acquired using an open frame lander incorporating a calibrated hydrophone (Geospectrum M36, GTI), and two inward facing cameras (Sony FDR-X3000), focusing on a single central point with scale boards positioned directly opposite. Optical data was processed using techniques described in Li et al. (2021b) where the radius of each bubble was calculated from the assumed volume of revolution. Acoustic data were analysed in 30 s samples while the optical data were analysed in 15 s samples.

5.3 Results

In total 368 single bubble releases were analysed, with the results discussed below. Natural frequencies were observed between 300 and 1000 Hz, corresponding to bubble radii between ~0.003 and 0.012 m (Fig 5.2).

It is useful to examine the energy released by a bubble oscillation as the degree of variation gives us an insight into how consistent the process is. The energy emitted during a bubble's oscillation varies across nearly two orders of magnitude, 10^{-5} to 10^{-3} J, with a mean value of 2.6×10^{-4} J. Plotting the energy released against the equilibrium bubble radius (Fig 5.2a) we see a large degree of scatter for R_0 < 0.6 cm while for R_0 > 0.6 cm a curved trend line appears to be present, peaking at ~0.9 cm, possibly mirrored by a second smaller curve. Statistically the total correlation between E and R_0 seen here has a Pearson's coefficient of -0.29, a p-value of <0.001 and a coefficient of determination value of 0.99 when applying a total least squares regression line (least absolute residuals).

The initial amplitude of excitation of a bubble ranged mainly between 10^{-7} to 10^{-6} m, with a mean value of 6.0×10^{-7} m. Plotting $R_{\varepsilon 0i}$ against the equilibrium bubble radius (Fig 5.2b) we see a strong clustering of the data for larger bubbles (R_0 > 0.6 cm) but once again a larger degree of scatter for smaller bubbles (R_0 < 0.6 cm). Statistically the total correlation between R_0 and $R_{\varepsilon 0i}$ seen here has a Pearson's coefficient of 0.26, a p-value of <0.001 with a trend line, determined using total least squares regression (least absolute residual), of

$$R_{\varepsilon 0i} = f(R_0) = [9.608 \cdot R_0 + 0.447] \times 10^{-6}, \tag{5.11}$$

having a coefficient of determination value of 0.99. While this relationship is highly effective for bubbles R_0 > 0.6 cm with the 10th and 90th percentiles of estimates being with -10 and +15 % of observed values. The trend line is however less effective below R_0 < 0.6 cm with a root mean square error of 2.6x10^{-7} m compared to an average value of 6x10^{-7} m.

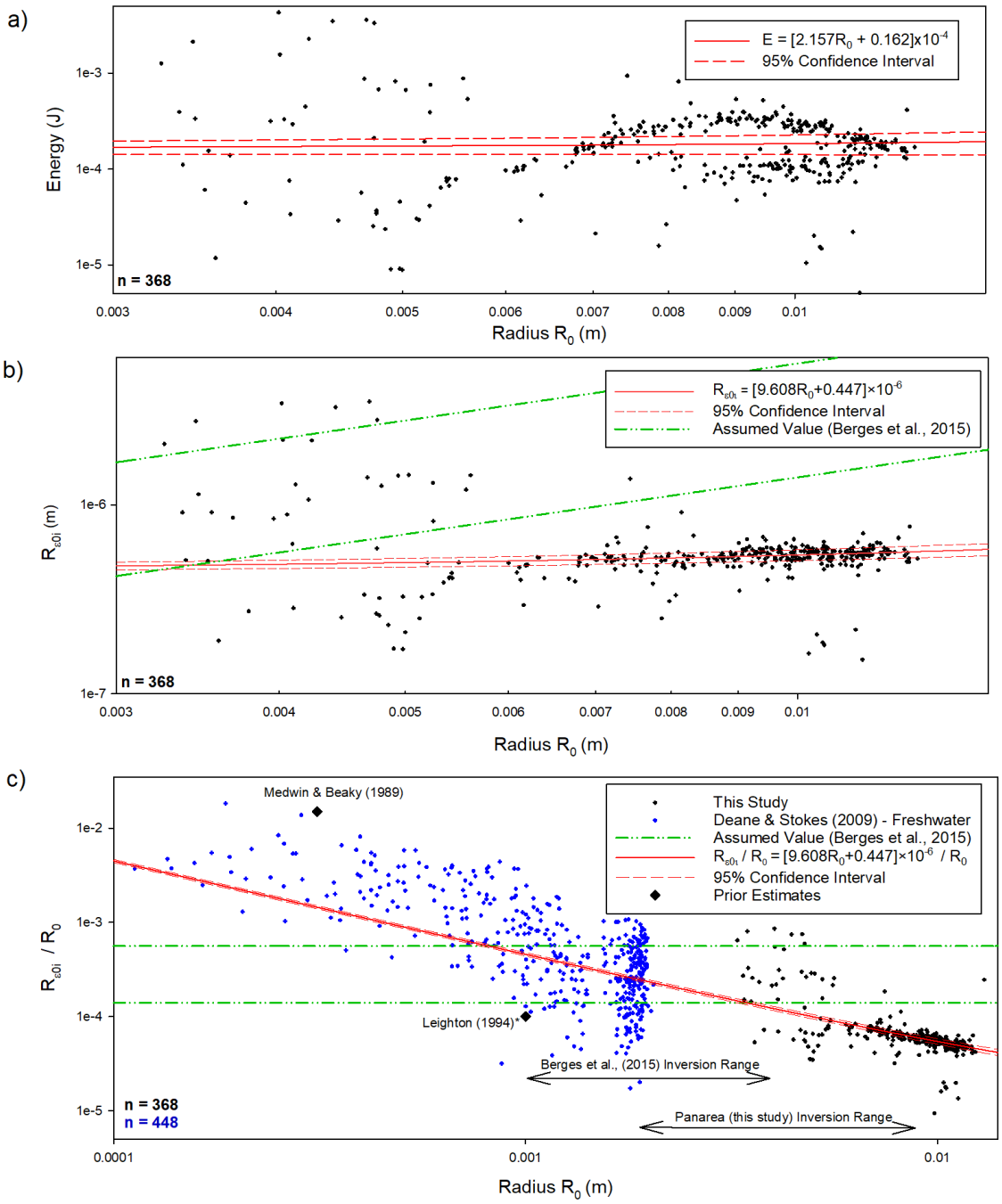

Figure 2: Experimental results from analysis of single bubbles a) energy released by a bubbles oscillation vs its equilibrium radius R_0, b) the initial amplitude of excitation $R_{\varepsilon 0i}$ vs the equilibrium radius. Lines of best fit are shown in red alongside the assumed $R_{\varepsilon 0i}$ values in Bergès et al., (2015) in green, c) the initial amplitude of excitation of bubbles normalised by the equilibrium radius ($^{R_{\varepsilon 0i}}/_{R_0}$) vs the equilibrium radius from this study (black) alongside results from Deane & Stokes (2008) (in blue) and other prior studies (black diamonds), note Leighton (1994)* represents revised data from Leighton & Walton 1987. Also shown is the range of bubble sizes used in Berges et al., (2015) and this study during passive acoustic flux inversion.

5.4 Discussion

We see a weak but definite positive correlation between $R_{\varepsilon 0i}$ and R_0 in our results, particularly at larger bubble sizes, contrasting prior assumptions that $R_{\varepsilon 0i}/R_0$ was constant. In order to see if this trend holds true for bubbles smaller than the ones seen here, we plot our results alongside observations from Deane & Stokes (2008) (Fig 5.2c), who observed bubbles ranging in size from ~0.0001 to 0.001 m. Note this is not a like for like comparison as their experiment sheared bubbles in a hydrodynamic current at 2m water depth (as opposed to as releasing them for sediment here). Despite this we note that our trend line passes through the centre of their data cloud and is in generally good agreement up to smallest bubble sizes, suggesting this trend is applicable for the full range of bubble sizes.

Previous assumption about $R_{\varepsilon 0i}$ were made by Bergès et al., (2015) who used the 25th and 75th percentile of Deane & Stokes (2008) $R_{\varepsilon 0i}$ observations to invert gas flux from needles and porous stones in a test tank. Comparing our estimates of $R_{\varepsilon 0i}$ to those used by Bergès et al., (2015) when inverting gas flux in Fig. 5.2b, we note their assumption is only consistent with our $R_{\varepsilon 0i}$ observation between $R_0 =$ ~0.0001 and 0.003 m, this being below the range of most bubble sizes observed here. This is no way implies their inversion results were incorrect (though their uncertainty estimates may have been overly conservative) however as: (1) bubbles were released via a different mechanism meaning $R_{\varepsilon 0i}$ can be expected to vary slightly; and (2) their bubble sizes ranged between 0.001 and 0.004 m radius, meaning the majority of $R_{\varepsilon 0i}$ calculation were consistent with this study (Fig 5.2c).

This highlights the need for researchers using acoustic flux inversion techniques in the field to compare their natural site to that used to calibrate. How similar the range of bubble sizes, flux rates, release mechanisms (needles, sediment type etc.), depths or even free field conditions are between the two will determine how accurate the $R_{\varepsilon 0i}$ estimates will be. The $R_{\varepsilon 0i} = 6 \times 10^{-7}$ m value established here is not the definitive value, it simply represents the relationship for bubbles released from course sediment in fresh water at 2.5 m depth at a rate of several Hz.

It also worth discussing the dangers that may arise from increasing the precision of the acoustic inversion technique, identifying certain phenomena that are for now hidden in the large uncertainty of the technique. We may expect to overestimate the flux due to 1) the role of seabed and sea surface reflections and 2) secondary bubbles oscillations after release (Leighton and Walton, 1987; Leighton et al., 1991). To address the first possibility, we modelled a bubble signal traveling both directly to the hydrophone and reflecting off the seafloor to a hydrophone 0.75 m away (comparable to the Panarea case study below) and found that the energy of the reflected signal is 4% of the direct path, meaning it can likely be dismissed in many settings. The effect of secondary oscillation (bubbles splitting and merging higher in the water column) is more difficult to quantify . In order to do so researchers will need some gauge of how frequently bubbles from the seep are fragmenting or merging, as compared to the rate of release. This almost certainly varies from seep to seep based on a number of factors such as the bubble size distribution (larger bubbles being more likely to fragment; Tsuchiya et al, (1996)), and the rate of release itself (with bubbles released in rapid succession being more likely to merge together; Leighton et al. (1991)). Further research should attempt to measure the fragmentation and merging rates of bubbles from natural seeps to avoid potential problems in the future.

5.5 Case Study – Panarea

In order to test the effectiveness of the passive acoustic inversion technique, with our newly defined relationship between $R_{\varepsilon 0 i}$ and R_0, we use it to estimate the flux from a natural CO_2 seep offshore Panarea (Bottaro Crater) and compare it to physical diver bottle measurements and simultaneous optical measurements. Panarea is a small Aeolian Island in the southern Tyrrhenian Sea, ~20 km SW of the active volcano Stromboli (Fig. 5.3a). As a result of the underlying magma chamber the waters surrounding the island are host to numerous natural CO_2 seeps (Caliro et al., 2004; Monecke et al., 2012; Bagnato et al., 2017; Inguaggiato et al., 2018). The calm clear shallow waters surrounding Panarea make it an ideal natural laboratory for testing ebullition detection and quantification techniques (Caramanna et al., 2011; Quale and Rohling, 2016; Molari et al., 2019). Bubbles from the target seep were released from coarse grained sediment at a rate ~5 Hz, directly comparable to our tank experiment. Similarly, bubbles released from the seep ranged from in size from 0.001 to 0.008 mm comparable to the 0.003 to 0.012 m seen in the tank (Fig 5.2c). The seep was however located at a depth of 12 m compared to the experiments 2.5m.

Preliminary analysis of the acoustic data revealed a strong continuous signal below ~550 Hz (Fig 5.3e). As optical footage suggested no bubbles larger than 0.8 cm in radius, f_0 = 600 Hz, were released we consider this low frequency noise to likely be the result of moving sediment grains and/or distant seeps (Vazquez et al., 2015). Hence the acoustic inversion is performed between 600 and 2500 Hz (0.0019 to 0.0080 m), to avoid interference from non-bubble related signals. The upper and lower estimates of our refined acoustic inversion were created assuming a 15% error in $R_{\varepsilon 0 i}$ based on the 95% confidence interval.

The refined acoustic inversion technique produces a bubbles size distribution (modal bubble radius 0.47 cm) similar to that produced used by Bergès et al. (2015) (modal radius of 0.44 cm), with slightly more small bubbles reported by the old inversion technique (Fig. 5.3c). Optical inversion measured a single a single peak bubble radius at 0.34 ± 0.06 cm.

The flux results of our refined inversion technique, using $R_{\varepsilon 0i} = [9.608 \cdot R_0 + 0.447] \times 10^{-6}$, are presented in figure 5.3d alongside prior inversion results assuming ${R_{\varepsilon 0i}}/{R_0} =$ 1.4 to 5.6×10^{-4}. Our refined inversion technique estimate is 3.2 ± 0.6 L/min, significantly greater than that predicted by the old acoustic inversion technique (0.8 ± 0.7 L/min), but consistent with the mean flux value derived via optical inversion (3.0 ± 0.8 L/min). Note the reduced uncertainty between the old and refined acoustic inversion from 88 to 19 %, a reduction of 78%. However, the refined acoustic inversion is slightly higher, 5-8 %, than the physical diver measurement taken prior to deploying the lander (2.3 L/min). The failure of the prior inversion technique to match other flux estimates here is due to the larger bubble sizes seen in Panarea, it only strictly being valid up to $R_0 = 0.002$ m (Fig 5.2d).

The overestimate in the acoustic inversion estimates of flux performed using more accurate values of $R_{\varepsilon 0i}$ could be explained by two possible factors: (1) the role of seabed and sea surface reflections and (2) secondary bubbles oscillations after release (Leighton and Walton, 1987; Leighton et al., 1991). To address the first possibility, we modelled a bubble signal traveling both directly to the hydrophone and reflecting off the seafloor to the hydrophone and found that the energy of the reflected signal is 4% of the direct path, meaning its contribution to overestimating flux is too small to explain the discrepancy. This would suggest the most likely explanation for our overestimate is additional bubble oscillation occurring within the water column as bubbles merge or fragment. Wide-area video footage at Panarea shows multiple bubbles fragmenting in the water column, and this evidence is reinforced when consideration is given to the comparison of the bubble size distribution determined by optical and acoustic techniques. Large bubbles are released at the seafloor and are recorded by the hydrophone but not the optics as they are out of view of the camera on the lander. The bubbles then rise ~0.75 m into the view of the camera during which time some fragment into smaller bubbles, these smaller bubbles being measured by the optics for the first time and the acoustics for a second time, resulting in the secondary acoustic peak alongside the optical peak at ~0.35 cm. In summary,

further developments are needed in the acoustic flux inversion code to account for this complex bubble behaviour.

As the precision of acoustic inversion techniques improve it will become increasingly important to quantify the effect of secondary oscillation. In order to do so researchers will need some gauge of how frequently bubbles from the seep are fragmenting or merging, as compared to the rate of release. This almost certainly varies from seep to seep based on number of factors such as the bubble size distribution, larger bubbles being more likely to fragment (Tsuchiya et al., 1996), and the rate of release itself, with bubbles released in rapid succession being more likely to merge together (Leighton et al., 1991). One could attempt to adapt breakup frequency equations for some indication of the rate of secondary oscillation however these typically assume turbulent flows, unlike those seen at the seep here, and does not account for bubbles merging (MARTÍNEZ-BAZÁN et al., 1999). Assuming that secondary oscillation is solely responsible for our overestimate of flux then the resulting scale factor would be between 0.6 and 0.9.

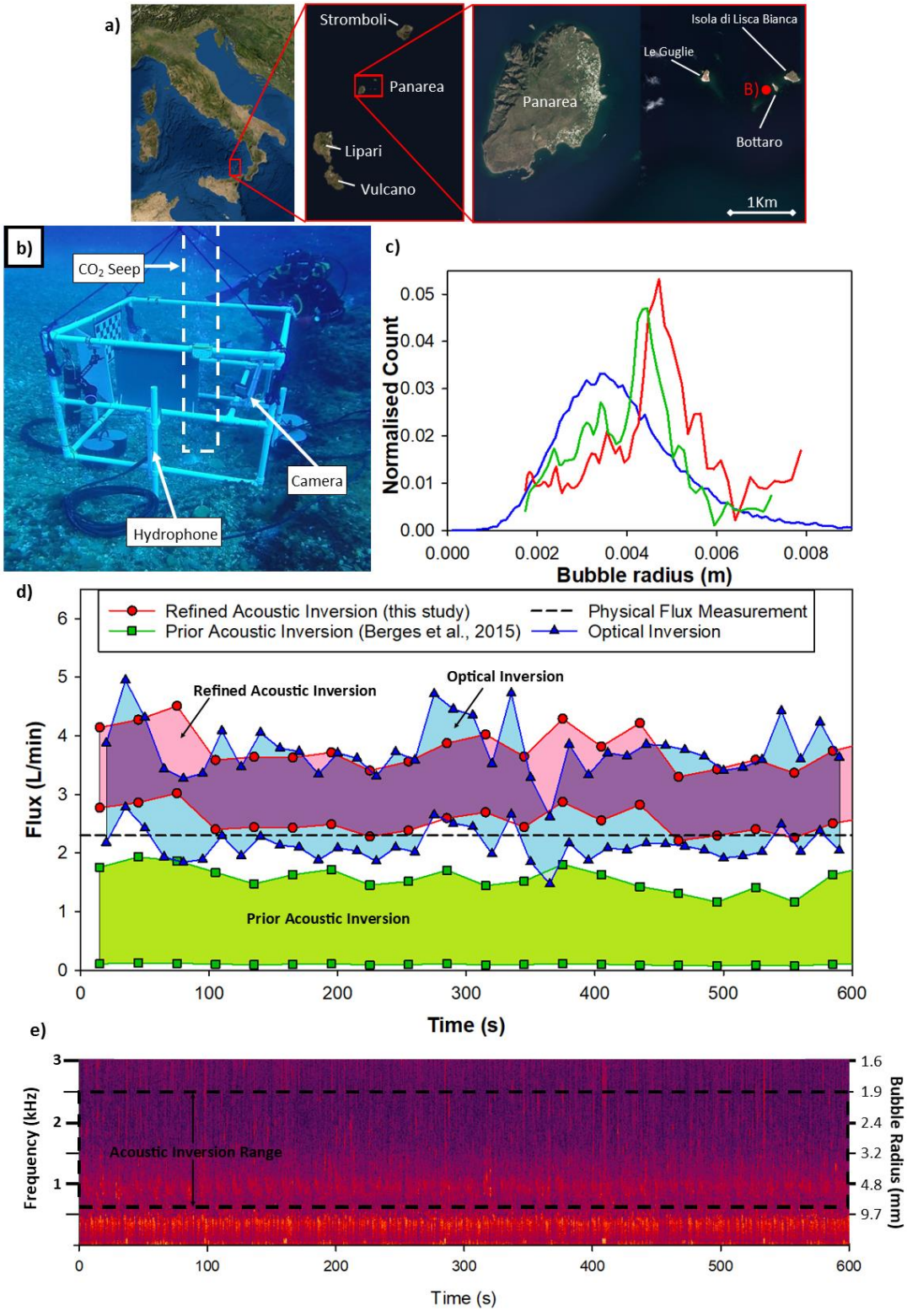

Figure 5.3; Comparison of acoustic inversion schemes and optical and direct physical measurement at a natural CO_2 seep. a) Experimental geometry at the seep site (Bottaro Crater, offshore Panarea, Italy); b) the acoustic optical lander deployed in over the target seep in Bottaro crater; c) the equilibrium bubble radius distribution as estimated by each technique; d) Gas flux estimate via each technique across the 10 min period, the refined acoustic inversion technique developed in this study (red), the previous acoustic inversion technique based assuming $R_{\varepsilon 0i}/R_0 =$ constant (green), optical inversion (blue) alongside the physical diver measurement

taken prior to deployment (dashed black line); e) the acoustic spectrogram as recorded during the observation period with the radius of a bubble that would be responsible for a given frequency displayed on the right axis.

5.6 Conclusion

In order to improve quantification of gas flux from natural seeps and anthropogenic sources by passive acoustic techniques, we have investigated the initial amplitude of excitation of bubbles, $R_{\varepsilon 0i}$, released from coarse sediment at 2.5 m water depth, a previously unknown parameter in the inversion process.

1. We have empirically defined the relationship between $R_{\varepsilon 0i}$ and the equilibrium radius of a bubble, R_0, which prior studies had incorrectly assumed to be a constant. $R_{\varepsilon 0i} = [9.608 \cdot R_0 + 0.447] \times 10^{-6}$

   Our data shows a weak positive correlation, especially at larger bubble sizes, and appears generally consistent with prior investigations of smaller (<1 mm) bubbles.

2. We demonstrate the potential of our refined inversion technique by inverting the flux from a natural CO_2 seep in Panarea (Italy) and comparing the results to simultaneous optical measurements. Here we find that after filtering out low frequency, non-bubble related, noise our acoustic flux estimate is highly consistent with optical measurements and only 5-8 % larger than prior physical measurements. We identify the post release fragmentation of bubbles as a likely explanation of minor overestimation of flux.

The 78% improvement in the precision of the acoustic inversion technique demonstrated here will allow for the more widespread adoption of passive acoustic techniques for the long-term observations of natural seeps and the measuring, monitoring and verification (MMV) of secure Carbon Capture and Storage sites (Dean and Tucker, 2017).

Chapter 6 Thesis Conclusion

In this chapter I will explore the extent to which this thesis has addressed the questions outlined in Chapter 1, discuss the migration of gas through the upper sedimentary succession, and discuss methods of quantifying gas flow into the water column. Finally, I propose future avenues of research leading on from the findings of this thesis.

6.1 Summary

The initial release of a gas bubble into the water column causes them to undergo simple harmonic motion at a natural frequency, known as the Minnaert frequency, which is approximately inversely proportional to its radius (Fig. 6.1). Gas bubbles can be entrained into the water column in a large variety of ways, however only the following methods produce enough bubbles to have a notable impact on the marine soundscape (Fig. 6.2): 1) rainfall impact; 2) breaking waves, and 3) seabed seeps (Nystuen, 1986; Deane and Stokes, 2002). In Chapter 2 I discussed the formation of bubbles from each of these processes and their resulting effect on the marine soundscape.

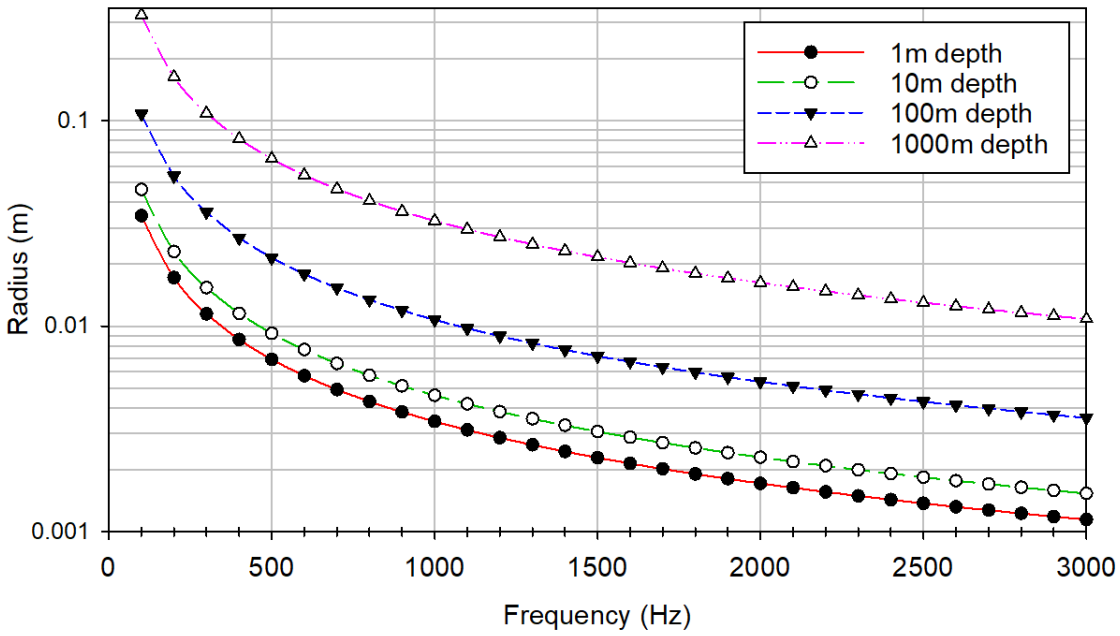

Figure 6.1: The radius of a bubble and its natural frequency as predicted by the Minnaert equation at specific water depths. Note that larger bubbles produce lower frequency signals.

Rain-generated bubbles result in a distinct acoustic spectrum that has a peak at 14-15 kHz with a sudden drop off below 10-12 kHz (Fig. 2.7), caused by regular entrainment, and occasionally a smaller secondary peak at 5 kHz, caused by irregular entrainment when droplets are particularly large (Ma and Nystuen, 2005). The intensity of these peaks is dictated by the number of raindrops impacting the water per second. As the intensity of the rainfall increases, the peaks becomes broader and less well defined.

Breaking wave acoustics is dominated by bubble clouds generated as the wavetop collapses. These cloud properties vary unpredictably with individual wave properties, usually somewhat correlated with wind speed. The complex nature of wave bubble generation has made attempts to model ambient noise ineffective. **W**ind **O**bservations **T**hrough **A**mbient **N**oise (WOTAN) have allowed research to relate the ambient noise levels to wind speeds, but such relationships are site specific (Vagle et al., 1990; Zhao et al. 2014). Consequently, Knudsen curves (Knudsen et al., 1948; Wenz, 1962) are still the most commonly used prediction of ambient noise from wave action, with a positively skewed peak at around 0.5 kHz, increasing in intensity with wind speed (Fig. 6.2) (NRC, 2003).

The acoustic spectrum resulting from seabed gas seeps is a summation of the acoustic signal of each bubble being released. Consequently, it varies from seep to seep, with differing bubble size distributions and generation rates. As a result, it is impossible to predict the acoustic spectrum of a seep without first observing its bubble generation properties. However, it is possible to quantify the size of bubbles being released in a given period by observing the acoustic spectrum of the seep. Such an approach is used in Chapter 4 and refined in Chapter 5.

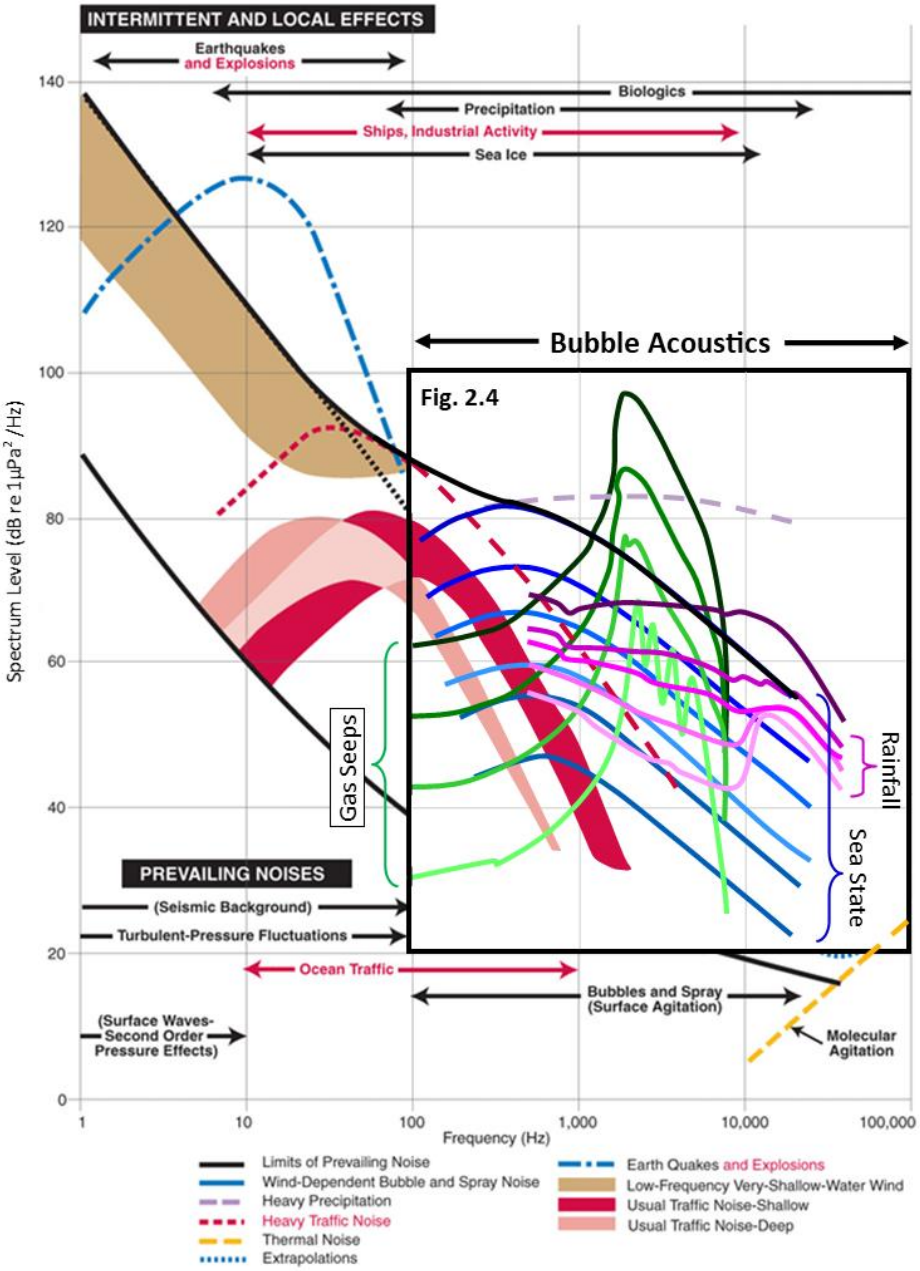

Figure 6.2: The typical sound levels of ocean background noises at different frequencies, as measured by Wenz (1962). Modified from Wenz (1962) and NCR (2003) to indicate the portion of the spectrum occupied by bubble acoustics using Ma and Nystuen (2005), with more detail shown in Fig. 2.5.

The migration of gas through sediment occurs via either open conduits, capillary invasion, the stable upward propagation of bubble fractures or the dynamic fracturing of sediment above the bubble fracture (Katsman, 2019). While the former are well understood, stable and dynamic bubble fracture propagation in sediment are still emerging fields (Algar et al., 2011; Boudreau, 2012). In particular there is a lack of understanding as to how each of these processes contribute to the formation of a marine gas seep. Better understanding the evolution of gas migration pathways in the upper sedimentary succession improves our ability to detect and quantify potential gas seeps, notably those from CCS sites.

The STEMM-CCS release experiment provided a unique opportunity to observe the formation of a marine gas seep. In Chapter 3, based on the temporal and spatial development of the acoustic anomalies seen during the CO_2 release experiment along with visual seabed seep observations and an accompanying gravity core, I propose a four-stage model for the evolution of gas migration pathways in the sub-surface (Fig. 3.3):

The initial “proto-migration” stage is essentially defined by individual gas pockets/bubble fractures making their way to the surface along seemingly random migration pathways, resulting in sporadic surface ebullition. Over time, preferred migration pathways are established, exploiting weaknesses within the sedimentary structure, with this “immature migration” stage resulting in small surface seeps that regularly become extinct and reform in new locations. Eventually the continuous passage of gas along selected pathways leads to the formation of open conduits, or chimneys, connecting the gas reservoir to the surface. At this point the “mature migration” stage has been reached and the release into the water column is focused through semi-permanent seeps. Once the flow of gas from the reservoir ceases, the final “closure” stage is triggered as the migration pathways are forced closed by external pressure, and the site reverts to its near-original state.

These stages are universally applicable to any near-surface seep site as general descriptors of the gas migration pathways. However, the exact length of time spent within each

stage and transition between stages will vary with stratigraphy, grainsize and injection rates etc. Indeed, many seeps likely do not reach the mature stage and simply skip to the final stage from stage 2, or even stage 1 in the case of sporadic ebullition sites. Furthermore, additional new migration pathways may form alongside more mature migration pathways.

Once in the mature migration phase the rate of ebullition from a gas seep is known to vary over time. While this is commonly correlated with the total pressure above the seep the exact degree of this variation is poorly understood. As a result, there is uncertainty in quantifying the contribution of naturally occurring aquatic CO_2 and CH_4 seeps to global carbon budgets, as many annual estimates are based on single short period observations.

In Chapter 4, in order to constrain the temporal variability of lacustrine seeps I analyse nine months of data from natural methane seeps in Lake Constance (central Europe). Ultimately, I found a significant negative correlation between gas flux and pressure, with control predominantly regulated by lake water level (hydrostatic pressure) on monthly timescales, while smaller fluctuations on daily to weekly periods are controlled by atmospheric pressure variations. I further noted that the exact empirical relationship varied between sites and over time. This suggests that decreasing pressure allows migration pathways in the sediment to expand, increasing the flow of gas, while increasing pressure has the opposite effect (Fig. 6.3). Evidence is also seen of large, rapid changes in pressure partially destroying existing pathways. Building on this correlation I demonstrate that long-term ebullition rates are best estimated by quantifying the relationship between in-situ pressure and gas flux and then using this relationship to predict gas flux from easily measurable in-situ pressure data. This approach is more accurate than extrapolating average flux rates from short periods of observation.

Quantifying the gas flux from a marine seep over an extended period of time is difficult. Traditional physical measurements of gas flux, while highly effective for shallow slow seeps (as seen in Chapter 4) become less practical as the size and the depth of the seep increases and

visibility decreases. Alternative techniques such as hydroacoustic imaging, while more effective at depth etc., offer only snapshot estimates of flux and are energy intensive. Passive acoustic inversion techniques have the potential to fill the niche existing between physical and hydroacoustic techniques, being a low energy method for continuously measuring ebullition rates in any environment.

In Chapter 5, in order to refine the passive acoustic inversion technique I report a tank experiment analysing the acoustic signal of bubbles released from artificial sediment. These results allowed us to demonstrate that the initial amplitude of excitation of a bubble released into the water column ($R_{\varepsilon 0i}$) is independent of its equilibrium radius (R_0) and is instead a constant equal to:

$$R_{\varepsilon 0i} = [6.012 \pm 0.902] \times 10^{-7} \text{ m}.$$

While these values are largely inconsistent with prior assumptions (Berges et al., 2015), the relationship is consistent with prior data sets (Deane & Stokes 2008) and should be integrated into future inversions. Using this refined technique to invert the flux from a natural seep in offshore Panarea I note that, after filtering out low frequency, non-bubble related noises, estimates are highly consistent with optical and physical measurements. However, I caution against assuming this is the definitive value of $R_{\varepsilon 0i}$ and emphasise the need to investigate the parameter in an array of settings.

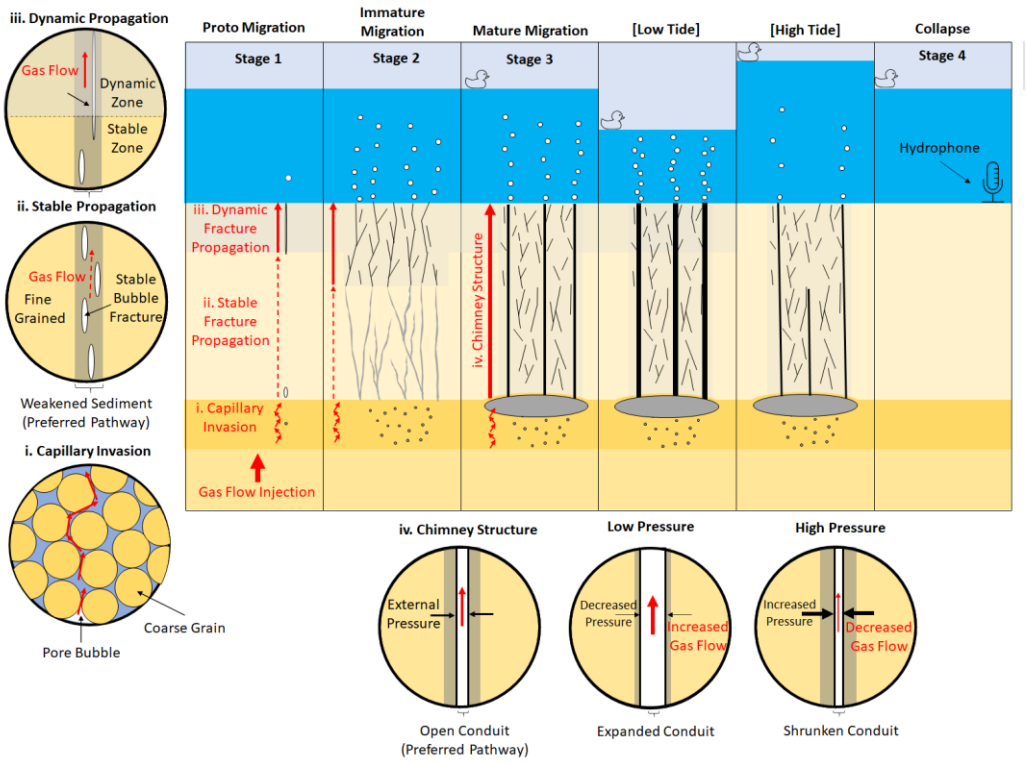

Figure 6.3: Summary of findings from Chapter 3 and 4. The four stages of gas migration pathway evolution, Proto migration, Immature migration, Mature migration, and Collapse. Note the expansion of the dynamic propagation zone to connect the reservoir to the seabed. Also shown is the effect of varying pressure (in this case a result of changing hydrostatic pressure, though atmospheric pressure has also been shown to have an effect) on gas flux as the chimneys expand and contract accordingly.

6.2 Research Questions

- **How do gas migration pathways evolve in the subsurface, from the initial injection of gas to formation of an active seep and beyond?**

Gas naturally rises through sediment via capillary invasion or fracture opening, the latter being more common in finer grained sediment. While capillary gas can simply rise upwards by displacing water in surrounding pores, gas fractures migrate upwards via stable or dynamic propagation (Jain and Juanes, 2009; Algar et al., 2011; Sirhan et al., 2019). Stable propagation is the pulsed ascent of a fracture as buoyancy forces drive the upper crack surface open and external pressure forces seal the lower crack surface, maintaining the overall size (Algar et al., 2011). Dynamic propagation occurs when fractures grow beyond a certain critical length, as defined by the surrounding sediment, resulting in the rapid upwards growth (Sirhan et al., 2019). During the initial formation of a gas migration pathway any of these processes may be active, as dictated by the sedimentary succession, with individual bubbles making their way to the surface for sporadic ebullition (Section 3.5.5). Over time preferred pathways begin to form, exploiting natural weaknesses in the sediment, through which the flow of gas is slowly focused, forming seep sites. The pathways are easily destroyed by changing pressure conditions, meaning new pathways are constantly being established and new seeps formed. Slowly, over time stable fracture propagation zones transition into dynamic fracture zones as stable fractures continuously collide and exceed the critical crack length. Eventually the dynamic fracture zones will extend from the seabed to the gas reservoir facilitating the formation of open conduits (or chimneys) (Section 3.6). At this stage, the migration pathways can be considered mature, with the flow of gas to the near-surface optimised and the position of seabed seep stabilised. Once mature, migration pathways will persist so long as there is a flow of gas through them if this ceases the pathways will close, reverting the sediment to its near natural state. These processes can be directly related to observations at the QICS and STEMM-CCS release experiments (Section 3.5.1).

- **How does the ebullition rate from natural seeps vary over time and how may we better predict this?**

The rate of gas release from seeps is inversely proportional to the total pressure at the point of release (Judd and Hovland, 2007; Scandella et al., 2011; Katsman, 2019), which is the sum of the overlying hydrostatic and atmospheric pressure, with wind and rainfall conditions having no direct impact, as demonstrated in Lake Constance (Section 4.3.2). Thus, variation in ebullition rates are tied to any variation in meteorological conditions or water level. Hydrostatic pressure typically varies daily, i.e., with tides, surface seiches, or bay oscillations, and annually with the seasonal changes (Section 4.5). On the other hand, while atmospheric pressure can vary daily with day-night sea breezes, it is generally less predictable, varying on weekly time scales with weather systems (Section 4.4). The magnitude of the flux change corresponds to the pressure change, as such small pressure variations are not always visible (such as tidal effects in Lake Constance). Furthermore, when hydrostatic variation is large (as compared with atmospheric pressure variation), gas flux variation is controlled by water level change. When hydrostatic variation is minimal, gas flux variation is dominated by atmospheric pressure change (Section 4.5).

It is unclear exactly what defines the empirical relationship between pressure and gas flux. Decreasing pressure conditions in sediment are theorised to allow existing gas pathways to expand and new ones to form, allowing for an increased flow of gas into the water column (Katsman, 2019). This would suggest that less variable seeps have underlying chimney structures that are less likely to expand or reform and vice versa. In Section 4.3 I speculate that this relationship is in some way related to the sediment and age of the seep. In Lake Constance a 100 hPa decrease in the in-situ pressure, equivalent to a water level decrease of 1 m, resulted in a 6-12 % increase in gas flux from seeps in Lake Constance (Section 4.3.4).

If the empirical relationship between flux and pressure is observed then variation in gas flux from a seep can be predicted from measurements of in-situ pressure, either measured at

the site itself or at a base station within the body of water. This approach is more accurate than the extrapolation of average flux rates determined from short periods of observation, a practice commonly followed in the literature (Bastviken et al., 2004; Linkhorst et al., 2020). Prediction of flux variations requires a time period of observation coincident with rapid variations in water level, i.e., during a storm event (Section 4.6).

- **How can we improve the passive acoustic inversion technique method for quantifying gas flux?**

Prior acoustic inversion techniques have been limited in precision due to a lack of constraints on the initial amplitude of a bubble's excitation following its release into the water column ($R_{\varepsilon 0i}$). Prior estimates of this value have been limited to small bubbles (< 2 mm) entrained by needles, breaking waves, and hydrodynamic currents (Leighton and Walton, 1987; Pumphrey and Walton, 1988; Medwin and Beaky, 1989; Deane and Stokes, 2008). Subsequently $R_{\varepsilon 0i}/R_0$ was conservatively estimated to be between $1.4 \text{ and } 5.6 \times 10^{-4}$, R_0 being the equilibrium radius of the bubble. While inversions performed using this assumption were validated by physical flux measurements, estimates were imprecise, with large error bars (Bergès et al., 2015). In order to refine the acoustic inversion process, I observed the relationship between $R_{\varepsilon 0i}$ and R_0 for large bubbles (between 3 and 12 mm) released from coarse sediment. The larger bubble sizes and sediment release mechanism are a better analogue for many natural seabed seeps (Section 5.2).

Ultimately, I found that $R_{\varepsilon 0i}$ is independent of R_0 being instead a constant equal to $[6.012 \pm 0.902] \times 10^{-7}$ m (Section 5.4). Substituting this relationship into the inversion process allowed us to significantly improve the precision of the technique, reducing the error from 86 % to 29 %. The power of this refined inversion technique was demonstrated by inverting the flow of gas from a natural CO_2 seep in offshore Panarea (Italy). After accounting for low frequency, non-bubble related background noise, the refined acoustic flux estimate is highly consistent with optical measurements and physical measurements.

6.3 Potential Future Work

Having separately investigated the evolution of gas migration pathways in the field and the variability of flux rates with pressure, a natural next step would be to investigate the response of gas conduits to changing pressure conditions. I believe such pathways expand and contract in response to exterior pressure conditions moderating the flow of gas, however direct physical evidence for this is minimal. An experiment examining the passage of gas through sediment cores at different external pressures, for example via computerised tomography (CT) scans, could provide definitive proof of this phenomenon. Indeed, given the length of time that has passed since the seminal work of Algar et al. (2010) into stable fracture propagation, there is merit in repeating their experiment with modern tomographic (CT) imaging. Further investigations could also attempt to identify the malleability/susceptibility of different sediment types and migration pathways to changing pressure types so that flux variability in the field can be more easily predicted.

Our extended study of flux variability in Lake Constance, alongside our advancements in passive acoustic inversion, has paved the way for more long-term seep observations. In particular, studying the release of gas from large scale marine pockmarks will be of interest given their higher flow rates and larger tidal range. For example, I estimated using active acoustics that 272-456 L/min of methane gas is being released from Scanner Pockmark in the North Sea, compared with 4-10 L/min from individual seeps in Lake Constance (Li et al., 2020a). Such a large release site will have a more significant impact on the natural carbon cycle, being equivalent to ~100 equivalent seeps in Lake Constance, making understanding their variability even more important. Gaining a single estimate of gas flux from these features in the past has proven extremely difficult and, as demonstrated in Chapter 4, such snapshot measurements may not be representative. The use of passive acoustic landers (as seen in Li et al. 2021) could simplify this task. To maximise a potential long-term deployment (≥ 1 year) a specialist lander could be designed that combines 1) passive acoustic sensors, 2) horizontal active acoustic sensors (as seen in Bayrakci et al. 2014) and

3) optical imaging equipment. Such an experiment, outlined in Fig. 6.4, would likely provide fresh insight into their variability and life cycle of pockmarks.

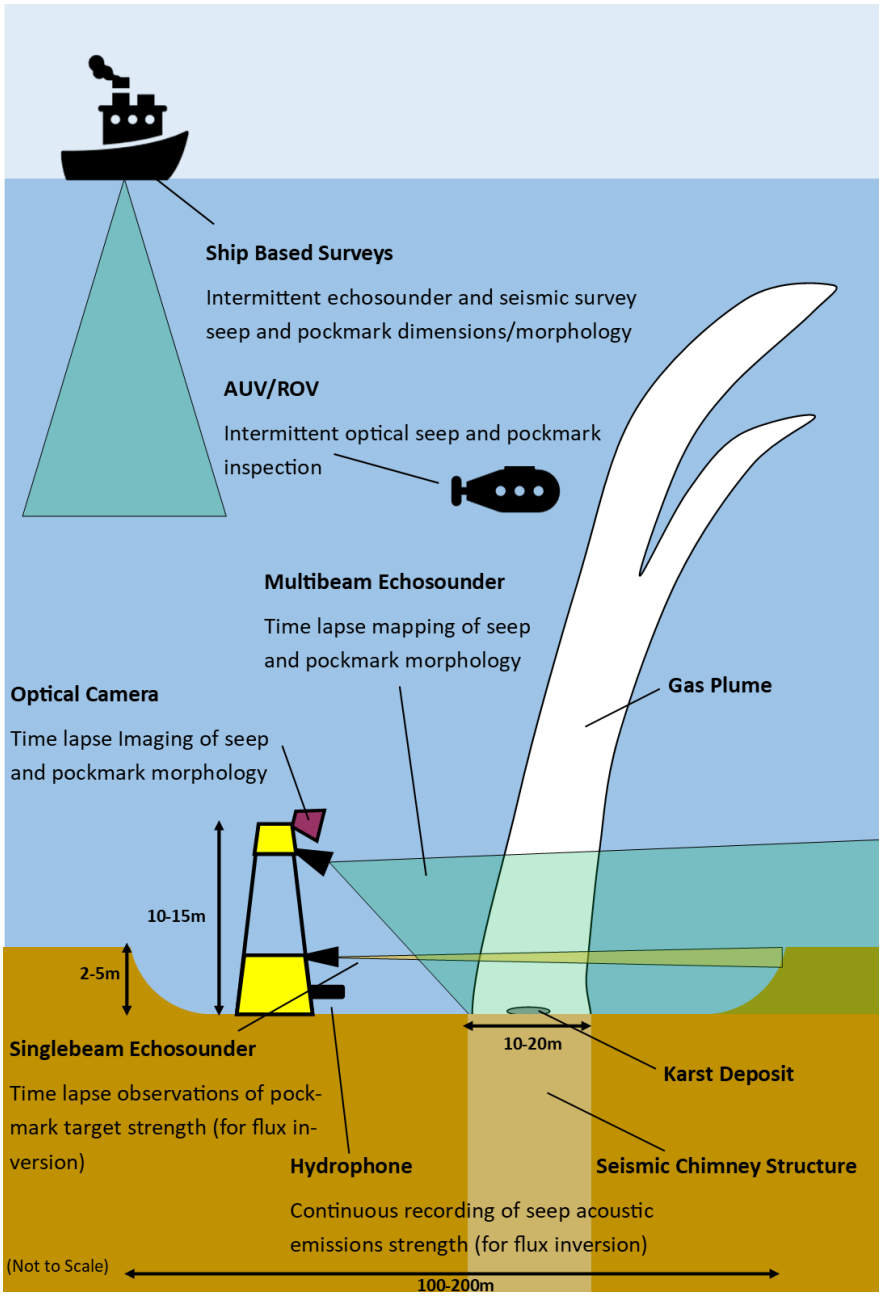

Figure 6.4: Outline of potential experimental investigation into the variability and evolution of active pockmarks. A specialist lander would continuously record active and passive acoustic data for later flux inversion observations and varying seabed morphology for over a year alongside photographic images for later reference. Such a lander may need to be unconventionally tall to provide a full view of the area. Ship-based survey (possibly with the use of underwater vehicles) may provide further information.

Finally, further refinement of passive acoustic flux inversion techniques is possible and desirable. As I noted, a way need to be found to account for the effects of bubbles fragmenting and merging in the water column, potentially via some scale factor. Additionally, while I have successfully measured $R_{\varepsilon 0i}$ at ~2 m depth in fresh water, how this property varies with depth, salinity and even sediment type is unknown. Further attention also needs to be paid to low frequency sediment/grain noise that has been observed preceding bubble releases in some sediment types (Vazquez et al., 2015). As I identified in Panarea, misinterpreting these low frequency sounds as bubble noise can result in large flux overestimations. It is also worth noting that preliminary research undertaken during this PhD suggests the way in which bubbles are released varies with sediment type. Large-grained sediment appears to result in traditional bubble releases with medium-grained sediment, resulting in similarly traditional release but with a preceding low frequency sound as grains are rearranged by the bubble. Fine-grained, non-cohesive sediment appears to result in bubbles being released in clusters propelling sediment into the water column.

In summary, research questions that are still open and prospective for future research include:

- **How do gas conduits mechanically react to changing pressure conditions?**
- **How variable is gas release from large marine pockmarks?**
- **How can we account for secondary bubble oscillation in acoustic inversion results?**
- **How does $R_{\varepsilon 0i}$ vary with depth, salinity, and sediment type?**
- **How does the nature of bubble release vary with sediment type?**

Chapter 7 Auxiliary Research

The following paper demonstrates a new method for measuring gas flux via active acoustic data. Myself and Dr. Li collaborated closely on this paper. I was responsible for the original conception, data analysis and writing the introduction while Li led the modeling and results section.

JGR Oceans

RESEARCH ARTICLE
10.1029/2020JC016360

Key Points:
- A broadband active acoustic method for determining the bubble size distribution and gas flux of gas plumes in the water column is presented
- Imaging of the methane plume in the North Sea showed two distinct arms with larger bubbles and smaller bubbles, respectively
- Total in situ methane flux from the pockmark into the water column is quantified as between 1.6 and 2.7×10^6 kg/year (272 to 456 L/min)

Correspondence to:
J. Li,
J.Li@soton.ac.uk

Citation:
Li, J., Roche, B., Bull, J. M., White, P. R., Leighton, T. G., Provenzano, G., et al. (2020). Broadband acoustic inversion for gas flux quantification—Application to a methane plume at Scanner Pockmark, central North Sea. *Journal of Geophysical Research: Oceans*, *125*, e2020JC016360. https://doi.org/10.1029/2020JC016360

Received 29 APR 2020
Accepted 29 JUL 2020
Accepted article online 3 AUG 2020

Broadband Acoustic Inversion for Gas Flux Quantification—Application to a Methane Plume at Scanner Pockmark, Central North Sea

Jianghui Li[1], Ben Roche[2], Jonathan M. Bull[2], Paul R. White[1], Timothy G. Leighton[1], Giuseppe Provenzano[2], Marius Dewar[3], and Timothy J. Henstock[2]

[1]Institute of Sound and Vibration Research, University of Southampton, Southampton, UK, [2]Ocean and Earth Science, National Oceanography Centre, University of Southampton, Southampton, UK, [3]Plymouth Marine Laboratory, Plymouth, UK

Abstract The release of greenhouse gases from both natural and man-made sites has been identified as a major cause of global climate change. Extensive work has addressed quantifying gas seeps in the terrestrial setting while little has been done to refine accurate methods for determining gas flux emerging through the seabed into the water column. This paper investigates large-scale methane seepage from the Scanner Pockmark in the North Sea with a new methodology that integrates data from both multibeam and single-beam acoustics, with single-beam data covering a bandwidth (3.5 to 200 kHz) far wider than that used in previous studies, to quantify the rate of gas release from the seabed into the water column. The multibeam data imaged a distinct fork-shaped methane plume in the water column, the upper arm of which was consistently visible in the single-beam data, while the lower arm was only intermittently visible. Using a novel acoustic inversion method, we determine the depth-dependent gas bubble size distribution and the gas flux for each plume arm. Our results show that the upper plume arm comprises bubbles with radii ranging from 1 to 15 mm, while the lower arm consists of smaller bubbles with radii ranging from 0.01 to 0.15 mm. We extrapolate from these estimates to calculate the gas flux from the Scanner Pockmark as between 1.6 and 2.7×10^6 kg/year (272 to 456 L/min). This range was calculated by considering uncertainties together with Monte Carlo simulation. Our improved methodology allows more accurate quantification of natural and anthropogenic gas plumes in the water column.

Plain Language Summary Understanding the rate of gas release from natural ebullition sites, such as pockmarks, into the water column is a major factor in understanding the input of greenhouse gases, such as methane and carbon dioxide, into the global ocean system. The detection and quantification of gas flux in the marine environment have relied upon acoustics. However, current active acoustic methods are mainly based on single-frequency quantification, which can never unambiguously quantify the gas flux due to the bubble size distribution and the scattering across a range of frequencies, and lead to an ill-conditioned inversion problem. This paper proposes a solution to this dilemma using two elements. First, we employ a wider range of frequencies than previously used, so that more of the bubble resonances are encompassed. Second, it assumes a form for the bubble size distribution, further constraining the solution and effectively regularizing the inversion. The broadband methodology enables us to quantify gas flux with frequencies spanning the resonances of all the bubbles in the plume, allowing more accurate quantification of natural and anthropogenic gas plumes in the water column.

1. Introduction

Understanding the rate of gas release from natural ebullition sites, such as pockmarks, into the water column is a major factor in understanding the input of greenhouse gases, such as methane (CH_4) and carbon dioxide (CO_2), into the global ocean system (Greinert, McGinnis, et al., 2010; Kennett et al., 2003; Leifer & Boles, 2005; Ligtenberg & Connolly, 2003; McGinnis et al., 2006; Shakhova et al., 2010). The detection and quantification of gas flux in the marine environment have relied upon methods of passive (Berges et al., 2015; Blackford et al., 2014; Leighton & White, 2011; Li, White, Roche, et al., 2019; Li et al., 2020) and active (Greinert, Lewis, et al., 2010; Greinert et al., 2006; Greinert & Nützel, 2004; Leblond et al., 2014; Li, White, Bull, Leighton, & Roche 2019; Nikolovska & Schanze, 2007; Ostrovsky, 2003; Riedel et al., 2018; Rona &

Journal of Geophysical Research: Oceans 10.1029/2020JC016360

Light, 2011; Shakhova et al., 2014; Veloso et al., 2015; von Deimling et al., 2011; Westbrook et al., 2009; Xu et al., 2014) acoustics. These two methods are largely complementary with passive acoustics well suited to long-term and local monitoring of small sites allowing quantification, whereas active acoustics survey equipment is widely available and able to detect gas over a large spatial area but is less well adapted to quantification.

Active acoustics, specifically the use of multibeam echo sounders, has been commonly used for seep detection in the last decades (Greinert, Lewis, et al., 2010; Xu et al., 2020) and has been used to map both natural and anthropogenic ebullition sites worldwide (Greinert, Lewis, et al., 2010; Greinert et al., 2006; Leblond et al., 2014; Nikolovska et al., 2008; Ostrovsky, 2003; Ostrovsky et al., 2008; Urban et al., 2017; von Deimling et al., 2015; Westbrook et al., 2009). Echo sounders also have the advantage of being able to work in any body of water regardless of visibility unlike optical techniques. Gas seeps in sonar data commonly appear as readily identifiable medium/strong reflectors—within the water column, sometimes referred to as "gas flares". Using multibeam echo sounders, the position and shape of these flares can be mapped (Greinert, Lewis, et al., 2010; Urban et al., 2017). By mapping the shape of these flares, observing the angle they make with the seabed, and knowing the tidal velocity, one can predict the vertical velocity of the bubble cloud. There is a simple relationship between ascent velocity and bubble size, and hence, the dominant bubble size can be estimated (Toramaru, 1989).

In order to gain an estimate of gas flux via active acoustics, single-beam (single frequency) echo sounder data has been used (Bayrakci et al., 2014; Greinert, McGinnis, et al., 2010; Römer et al., 2014; Shakhova et al., 2015; Veloso et al., 2015; von Deimling et al., 2010). This is done by first modeling the theoretical return pulse strength from bubbles of different sizes based on the frequency of the acoustic source and the depth of water in the area. Then by observing the mean signal strength from within the plume, an estimate of bubble size distribution can be made. Crucially, this can only be done if the ambiguity is ignored, since when a given scattering strength is attributed to a bubble, there is always more than one bubble size that can scatter that frequency strongly (Leighton et al., 2004). Consequently there is an inherent ambiguity in the gas flux estimated by a technique that only uses data containing a single frequency. This ambiguity exists even when only a single bubble is being measured in free field (Leighton et al., 1996) and becomes much greater if there are many bubbles (as here) or the bubbles are contained within a structure (Baik et al., 2014; Leighton et al., 2012). From this distribution the flux of the plume can be estimated (carrying forward any inherent ambiguity) using the calculated rise speeds of bubbles (Greinert & Nützel, 2004; Greinert et al., 2006; Greinert, Lewis, et al., 2010; Leblond et al., 2014; Nikolovska & Schanze, 2007). Greinert et al. (2006) used both single-beam and multibeam data to estimate the dominant bubble size at different depths in the water column. This method has also been used to make observations of the temporal variations of plumes and their interaction with the thermocline (von Deimling et al., 2015). However, the modeling used in this method requires very accurate measurement of water column physical properties as well as bubble rise velocity.

In an attempt to establish a technique to directly quantify gas flux from active acoustic data, Greinert and Nützel (2004) demonstrated that (within the confines of a specific seep, constrained to remove the inherent ambiguity in the acoustic inversion) there is a direct relationship between the volume backscattering strength of a single-beam pulse and the flux rate of a seep, using a controlled release site and a horizontal acoustic array. However, this relationship varies with the dominant bubble size meaning it is site specific and must be re-established at every new seep via empirical measurements (Greinert & Nützel, 2004; Leblond et al., 2014). This approach was used by Nikolovska et al. (2008) in the Black Sea, using a Remotely Operated Underwater Vehicle (ROV) to collect physical flux measurements alongside a horizontally mounted sonar system, and by Bayrakci et al. (2014) in the Marmara Sea, using a rotating bubble detector (BOB) to reveal temporal variations in the gas flux of surrounding seeps. While this technique is appropriate for long-term measurements of single seep sites, it is intrinsically flawed for widespread quantification of multiple seeps as an empirical measurement of flux is required to make such an estimate. Furthermore, it assumes that conditions do not change (e.g., significantly larger bubbles are introduced through a new fracture in the sediment or infrastructure casing) in such a way as to make the gas flux quantification erroneous through the above-mentioned ambiguity.

The existence of the inherent ambiguity is therefore probably the most significant shortcoming of the existing acoustic techniques, that is, ebullition sites contain a bubble population with a wide range of radii

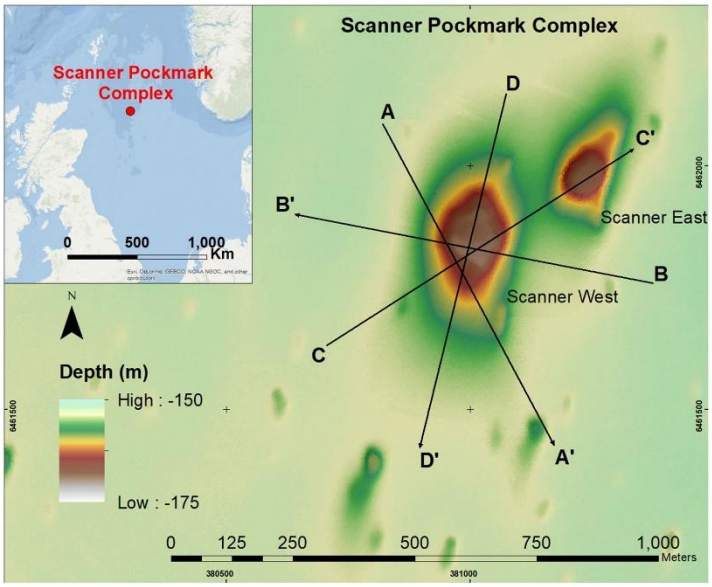

Figure 1. Bathymetric map of the Scanner Pockmark complex with inset showing the position within the central North Sea. The position of four ship profiles (A–D) that acoustically image the methane gas plume within the western pockmark are shown.

(Veloso et al., 2015). Crucially, passive acoustic techniques do not contain inherent ambiguities in the acoustic inversion: They only contain acoustic uncertainties, which are less troublesome. To be specific, each bubble emits energy in a known frequency band relating to its size, depth, etc. The uncertainty in the amount of energy emitted by a given bubble being only a result of the paucity of data, which will be reduced as more data is taken (Leighton & White, 2011). In contrast, quantification of the gas flux by active sonar contains an inherent ambiguity, in that a given bubble can scatter strongly at resonance, and when it is also much larger than resonance (Leighton et al., 2004). As such, a single-frequency echo sounder can never unambiguously quantify the gas flux without additional measurements, for example, passive acoustics, optical methods, or gas collection using bottles, to remove the ambiguity. Measuring scattering across a range of frequencies, which does not cover the resonant frequencies of the bubbles present, leads to an ill-conditioned inversion problem; that is, the errors in the measurements are vastly magnified, leading to solutions that are unreliable. Physically relevant regularization of the solution is needed in order to provide usable solutions (Leighton et al., 1996).

Furthermore, the above-mentioned active methods tend to rely upon scattering models for bubbles, which assume the bubble is small relative to the insonifying wavelength. For the size of bubble that we are looking at and the frequencies of most imaging sonars, this condition is not true. This leads to errors in two ways: First, the calculation of the damping associated with each bubble can be erroneous (Ainslie & Leighton, 2011, 2009); second, the assumed increase of scattering cross section with increasing bubble size (a trend that is only valid for bubbles larger than resonance only do as long as the bubble radius remains much smaller than an acoustic wavelength) breaks down (Salomatin & Yusupov, 2005; Thuraisingham, 1997). Accurate determination of the bubble population, and hence gas flux, can only be determined if the backscatter response is determined for all significant bubble sizes, and this requires the use of a broad range of acoustic frequencies. Typical radii of bubbles emitted from the seabed tend to be in the range of 1 to 15 mm

Journal of Geophysical Research: Oceans 10.1029/2020JC016360

(Veloso et al., 2015) whose resonant frequencies are from 800 Hz to 12 kHz. While there is merit in using single-frequency imaging (at, e.g., 18 kHz; Xu et al., 2014) to identify the location of seep sites, single-frequency systems cannot determine the bubble population or the gas flux accurately. Even a multi-frequency system that did not cover the range of bubble resonances (from below the resonant frequency of the largest bubble present, to above the frequency of the smallest bubble present) will contain inherent ambiguities, and if all the frequencies in a multibeam system are higher than the resonance of the larger bubble present (the convenient option given the frequencies in off-the-shelf multibeam sonars), then the equations in the simultaneous set mentioned above are not independent and cannot be solved to determine the variables (the number of the bubbles in each size bin) unambiguously (Berges et al., 2015; Leighton & White, 2011). Currently, researchers have been using optical methods for quantification of small plumes such as a single bubble stream (Veloso et al., 2015), but this is impractical for analyzing larger emission sites. Little work has been completed on quantifying the emissions from large methane plumes from active pockmarks, which may extend over a diameter of 200 m in the water column, or understanding the gas bubble upwelling process.

This paper proposes a solution to this dilemma using two elements. First, we employ a wider range of frequencies than previously used, so that more of the bubble resonances are encompassed. Second, it assumes a form for the bubble size distribution, further constraining the solution and effectively regularizing the inversion. We combine data from three sonar systems, spanning a wide frequency range, 2.5 to 200 kHz, to calculate methane flux at an actively venting pockmark in the North Sea. Scanner Pockmark complex comprises two large pockmarks (~200–300 m in diameter, Figure 1), which are 15–20 m deep depressions in a relatively flat seabed in water depth of 150 m. Pockmarks are submarine gas escape structures commonly found in basins globally and often associated with active hydrocarbon systems. Despite first being observed in the 1960s, the variability and controls on gas emissions are poorly understood. The evolution of the resulting gas plumes in the water column is closely linked to the overall mechanism of gas leakage from pockmarks, making a greater understanding of plumes essential for better understanding natural seep sites. In order to determine the bubble size distribution of the gas plume and quantify the gas flux within it, we first use multibeam imaging to detect the plume structure and dimensions, then we present a volume scattering strength matching model utilizing iterations of bubble mean radii and standard deviation to match observed strength of single-beam data in the function of frequency ranging from 3.5 to 200 kHz for each depth. Next, a sea current modulation function is applied to integrate the instantaneous bubble rise velocity, estimated at the time of observation. Finally, we apply a depth-dependent number of bubbles and size distribution for methane gas to convert these volume flow rates to mass flow rates.

2. Data

The data in this survey were collected from the RRS James Cook during September 2017. Three hull-mounted sonar systems were employed: a Kongsberg EM710 multibeam echo sounder, a Kongsberg SBP120 sub-bottom profiler, and a Simrad EK60 single-beam echo sounder. The transceivers were orientated vertically downwards for the entire study. The EM710 multibeam echo sounder worked on frequency range 70 to 100 kHz with beam width of 1°. The SBP120 worked on a single-beam of wideband frequency (2.5–6.5 kHz) centered at ~3.5 kHz with a beam width of 3°. The EK60 echo sounder transmits a single-beam of five different monochromatic frequencies: 18, 38, 70, 120, and 200 kHz, with beam widths of 11°, 7°, 7°, 7°, and 7°, respectively. The pulse length of the SBP120 was set to 40 ms, and the pulse length of the EK60 at frequencies 18, 38, 70, 120, and 200 kHz were set to 2048, 1024, 512, 256, and 256 μs, respectively. The multibeam data is used to observe the structure and dimensions of the plume, while the sub-bottom profiler and single-beam data are used to measure the acoustic scattering properties of the plume. The sampling rate of the SBP120 and the EK60 were set to 20.48 and 25 kHz, respectively, which makes it possible for the target strength calculation in a reverberating volume V (m^3) with 1 m vertical resolution.

2.1. EM710 Multibeam Data

The EK710 multibeam system imaged the methane plume from the western Scanner Pockmark. Figure 1shows the transects across the plume. By filtering out background water column noise, it was possible to extract the gas flare and recreate it as a 3-D model, recording its positional data, height, lateral extent, and width; example results of this process are shown in Figure 2. The plume orientations are generally in

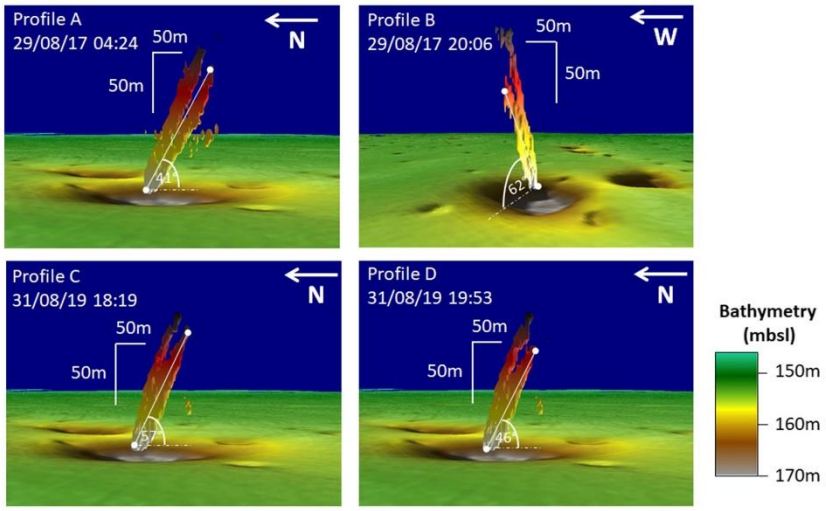

Figure 2. The methane plume at the Western Scanner Pockmark imaged by the EM710 multibeam echo sounder (70–100 kHz) on four multibeam profiles (A–D; position shown in Figure 1). The plume is orientated in the same direction as the tidal flow (i.e., in a north-south direction). The distinct forked shape of the plume can be observed. Plume lateral extent is colored from white at the base to black at the upper surface.

good agreement with tidal direction, the axis of which runs roughly north to south, as predicted by Cazenave's FVCOM model (Cazenave et al., 2016). The plume height varied between 39–145 m above the seabed while the lateral spread varied between 5 and 210 m.

Over the recent decades, numerous methane plumes in different ocean regions have been investigated and the occurrence of multiple arms has been noted on several occasions (Dissanayake et al., 2018; Gentz et al., 2014; Leifer et al., 2017; McGinnis et al., 2006; Ruppel, 2011; Sommer et al., 2015; von Deimling et al., 2015). Examination of Figure 2 reveals that the plume selected here exhibits a clear forked structure with two distinct arms. This is presumed to be a result of two dominant bubble sizes escaping from the pockmark, with the larger bubbles rise faster, creating the upper arm while the smaller bubbles rise more slowly creating the lower arm.

The multibeam data also allow us to map the surrounding seafloor topography, revealing the Scanner Pockmark as being 10–20 m deeper than the surrounding seabed, which is at a depth of roughly 150 m (Figure 1). It was not possible to clearly map the plume within the crater due to the increased reverberation, likely caused by internal reflections and active gas venting.

2.2. SBP120 and EK60 Single-Beam Data

Calibrated, single-beam data from the SBP120 and EK60 were collected along the transects A–D illustrated in Figure 1. Single-beam data at 18, 38, 70, 120, and 200 kHz was collected along the four profiles A–D across the Scanner Pockmark plume using an EK60 system with built-in calibration. This was augmented by data collected from a 3.5 kHz (2.5–6.5 kHz) chirp sub-bottom profiler. An example of the plume imaged on one single-beam system is shown in Figure 3.

Plume data were extracted by filtering out background water column noise data, based on the simultaneously collected multibeam data, leaving only the acoustic signal associated with the gas venting from the pockmark. Individual acoustic anomalies were removed if they were connected to the seafloor, or single, isolated, and vertically elongated stack of high acoustic energy above noise level. Additionally, the

Journal of Geophysical Research: Oceans 10.1029/2020JC016360

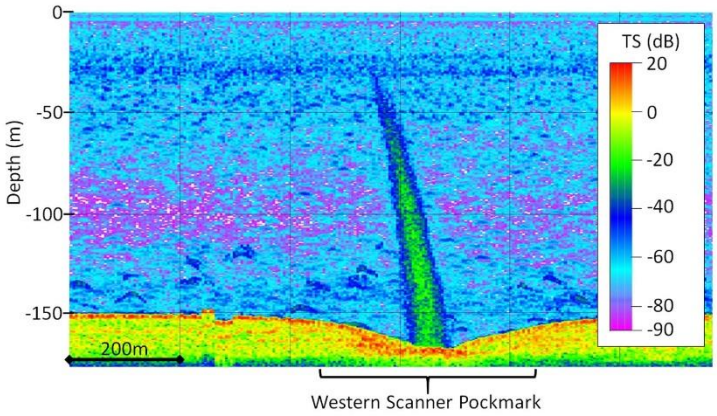

Figure 3. Direct 18 kHz single-beam observation from snap shots of plume for Profile C. With the single-beam data we are unable to observe the forking in the multibeam data shown in Figure 2 due to the 2-D profile orientation.

multibeam data allowed us to cross validate the position of plumes and ensure that the relevant target was being examined.

Figure 4 shows examples of the target strength collected by the single-beam systems. Each sonar data set consists of the target strength of the plume at a range of depth in response to frequencies from 3.5 to 200 kHz.

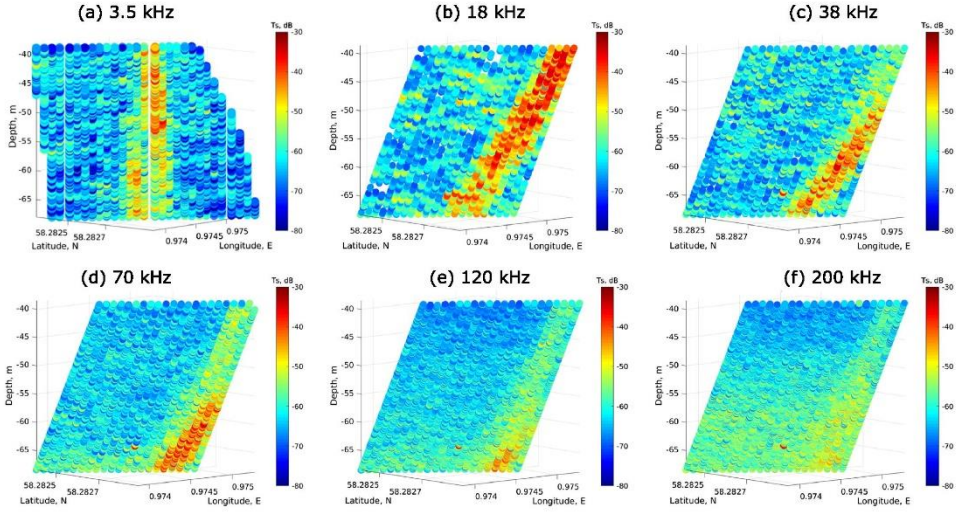

Figure 4. Target strength (Ts) of plume imaged on Profile A extracted from single-beam data at each frequency. The target strengths of received signal are between −80 and −30 dB; (a) 3.5, (b) 18, (c) 38, (d) 70, (e) 120, and (f) 200 kHz.

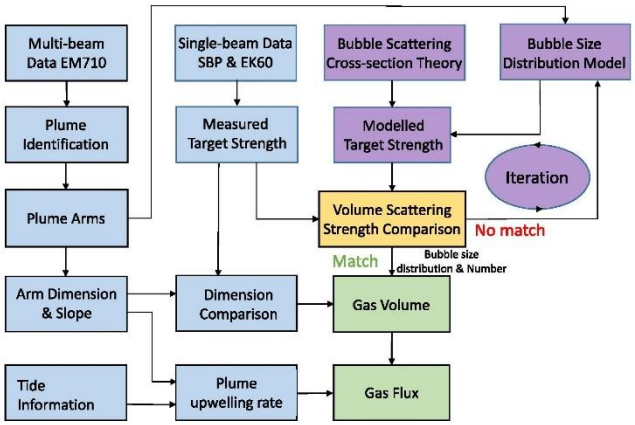

Figure 5. Flow chart describing the processing steps used to determine bubble size and gas flux from the input acoustic data. Blue blocks describe the processing of observed multibeam data, single-beam data, and tidal information; purple blocks describe the iterative volume scattering strength matching model; and green blocks describe the quantification stage.

3. Data Processing, Modeling, and Flow Rate Estimation

This section describes how the observed target strength data is used to determine the depth-dependent bubble size distribution and gas flux of a plume (Figure 5). Acoustic detection and identification of gas plumes can be used to quantify the bubble flow rate if a number of acquisition parameters and assumptions about the physics of methane gas seepage at the seafloor and the surrounding environments are made (Veloso et al., 2015). The multibeam data are used to determine structure of plume arms and the corresponding dimension in depth. The single-beam target strength data are used to derive the observed volume scattering strength in depth. To quantify the bubble size distribution and gas flux, we develop an inversion algorithm, which iteratively matches the modeled and measured volume scattering data. For each depth of interest, the shape of the bubble size distribution is parametrized by a log-normal probability density function (PDF), with a further parameter defining the total number of bubbles. As mentioned in section 2, the Scanner Pockmark produces two dominant bubble sizes, and we incorporate this into our model.

3.1. Beam Data Processing

The intermediate frequencies of each data set are smoothed to create an observation of volume scattering strength as a function of depth and frequency. We denote the received target strength at frequency f of backscattering ping n as $\mathrm{Ts}_n(f)$ (dB), then the volume scattering strength $\mathrm{Vss}_r(f)$ (dB/m^3) can be expressed as (Johanneson & Mitson, 1983)

$$\mathrm{Vss}_r(f) = 10\log_{10}\left(\frac{1}{V}\sum_{n=1}^{N_p} 10^{\mathrm{Ts}_n(f)/10}\right), \tag{1}$$

where N_p is the total number of scatterers in a fragment of volume, and the reverberating volume V is computed as

$$V = h_i \times S_i, \tag{2}$$

where h_i is the vertical height and S_i is the scanning area of interest in the horizontal plane. Considering the propagation loss ($\mathrm{PL}(f)$) in the acoustic channel, the volume scattering strength of gas bubbles $\mathrm{Vss}(f)$ can be expressed as (Smailes, 1976)

$$\mathrm{Vss}(f) = \mathrm{Vss}_r(f) + \mathrm{PL}(f). \tag{3}$$

Journal of Geophysical Research: Oceans 10.1029/2020JC016360

Essentially, the PL(f) is the sum of two terms: the geometrical loss ($PL_g(f)$) and the absorption loss ($PL_\alpha(f)$) (Li, White, Bull, & Leighton, 2019):

$$PL(f) = PL_g(f) + PL_\alpha(f). \tag{4}$$

Here we assume a spherical spreading model for the geometrical losses, and the absorption loss is calculated from Thorp's formula (Harris & Zorzi, 2007; Li, White, Bull, & Leighton, 2019; Ochi et al., 2008; Urick, 2013). Taking into account the propagation loss, the volume scattering strength of gas bubbles as a function of frequency can be extracted.

3.2. Modeling

The model of the acoustic scattering from the bubble plume combines three basic components: (1) the model of the backscattering cross section of a single bubble, (2) an assumed shape of the bubble size distribution, and (3) a method to compute the volume scattering strength. Each of these three elements is detailed in a subsequent subsection.

3.2.1. The Acoustic Backscattering Cross Section of a Single Bubble

The backscattering cross section of a single bubble is relatively well established when wavelength of the ensonifying sound field is significantly greater than the bubble radius, that is, $kr \ll 1$ (sometimes referred to as the "long-wavelength" condition) where k is the wave number equal to $2\pi f/c_w$ with f representing the frequency of the acoustic wave. When using many commercial imaging sonars to examine bubbles from seeps, this condition is frequently violated. For example, for the highest frequency used in this study, 200 kHz, then k is approximately 800 m^{-1}. To keep kr less than 5%, say, in order to make the "long-wavelength" formulations valid, the seeps should emit no bubbles larger than radius 60 μm for a 200 kHz beam. This maximum allowable bubble size, to keep the "long-wavelength" formulation valid, decreases with increasing frequency, for example, $kr = 0.05$ for bubbles of 20 μm radius when $f = 600$ kHz, by no means the highest frequency used to quantify gas from seeps. Given most measurements of seeps show bubble radii that are at least two orders of magnitude larger than this limit then the "long-wavelength limit" is not justifiable. The gas flux from a seep is dominated by the gas carried in the largest bubbles, so to estimate such fluxes it is most important to accurately model the scattering from these large bubbles. As discussed in Ainslie and Leighton (2009, 2011), when the condition $kr \ll 1$ cannot be relied upon then one needs to take considerable care. In particular, it is necessary to ensure that expressions for the damping terms, arising through three mechanisms: acoustic radiation, viscous, and thermal damping, also do not rely upon assuming $kr \ll 1$. Further, the expressions for the cross sections need to be corrected from the prediction of the formulation of the long-wavelength limit (which erroneously predicts that the scattering cross section increases quadratically with increasing radius). They in fact approximately plateau (onto which resonances are superimposed), which is the prediction from detailed modeling (Thuraisingham, 1997).

The expression we shall consider for the backscattering cross section, σ_{bs}, is

$$\sigma_{bs}(r, f) = \frac{r^2}{\left(\frac{\omega_0^2}{\omega^2} - 1 - 2\frac{\beta_a}{\omega}kr\right)^2 + \left(2\frac{\beta_a}{\omega} + \frac{\omega_0^2}{\omega^2}kr\right)^2} \frac{\left(\frac{\sin kr}{kr}\right)^2}{1 + (kr)^2}, \tag{5}$$

This is adapted from Ainslie and Leighton (2009, 2011) to include the final factor, which was proposed by Thuraisingham (1997). This expression implicitly includes radiation damping, with the effect of the other two damping mechanisms (viscous and thermal damping) being combined into a single damping factor, β_0. This formulation provides a consistent approach to incorporating radiation damping into the backscattering model, something which, as Ainslie and Leighton (2011) showed, cannot be achieved using dimensionless damping coefficient, which is the prevailing approach (Veloso et al., 2015). In Equation 5, the frequency ω_0 is defined through the solution of the equation

$$\omega_0 = \sqrt{\Re\{\Omega^2(r, \omega)\}}, \tag{6}$$

where $\Re\{\cdot\}$ denotes the real part of a complex number. Under specific circumstances (when the process is

Table 1
Parameters Used in the Cross Section Computation

Term	Notation	Value/unit
d	water depth	(m)
r	bubble radius	(m)
f	ensonifying frequency	3.5–200 (kHz)
T	measured temperature	8.14 (°C) or 281.29 (kelvin)
τ	surface tension	0.0745 (N/m)
p_v	vapor pressure	872 (Pa) at 10°C
η_S	shear viscosity	1.5×10^{-3} (P·s)
K_{gas}	thermal conductivity of the gas CH_4	8×10^{-2} (W/(m*k))
C_p	specific heat capacity at constant pressure	2.191 (kJ/(kg K))
g	gravity	9.81 (m/s^2)
ρ_{liq}	seawater density	1,025 (kg/m^3)
P_{atm}	atmospheric pressure	101×10^3 (Pa)
c_w	measured sound speed in water	1,485 (m/s)
γ	specific heat ratio of the gas CH_4	1.299
M_m	molar mass of the gas CH_4	0.016 (kg/mol)
R	gas constant	8.31 (m^2 kg s^{-2} K^{-1} mol^{-1})

isothermal or adiabatic), this frequency corresponds to the resonance frequency of the bubble; however, in general, this is not the case. The complex parameter Ω, seen in Equation 6, is defined through

$$\Omega^2 = \frac{3}{\rho_{liq} r^2}\left(\Gamma P_{gas} - \frac{2\tau}{3r}\right), \tag{7}$$

where ρ_{liq} is the density of the liquid surrounding the bubble (kg/m^3), τ is the surface tension (N/m), and P_{gas} is the pressure of the gas inside the bubble (Pa), which can be expressed as follows:

$$P_{gas} = P_{atm} + \rho_w g d + \frac{2\tau}{r} - p_v, \tag{8}$$

where P_{atm} is the atmospheric pressure (Pa), g is the acceleration due to gravity (m/s^2), p_v is the vapor pressure for water, and d is the depth of the bubble. In Equation 7, Γ represents the complex polytropic index (Ainslie & Leighton, 2011)

$$\Gamma = \frac{\gamma}{1 - \left\{\frac{(1+i)X/2}{\tanh((1+i)X/2)} - 1\right\}\left(\frac{6i(\gamma-1)}{X^2}\right)}, \tag{9}$$

with γ representing the specific heat ratio, and the parameter X being defined as

$$X = \sqrt{\frac{2\omega}{D_p}} r, \tag{10}$$

and the thermal diffusivity, D_p, of the gas in the bubble can be expressed as

$$D_p = \frac{K_{gas}}{\rho_{gas} C_p}, \tag{11}$$

in which the K_{gas} is the thermal conductivity of the gas within the bubble and C_p is the specific heat capacity of the gas at constant pressure. The density of the gas ρ_{gas} can be computed using (Leighton, 1994)

$$\rho_{gas} = \frac{M_m}{RT} R_{gas}, \tag{12}$$

where R is the gas constant and T is the temperature (K) and M_m is the molar mass of the gas.

The two remaining damped effects (thermal and viscous) are included in the model (7) through the combined damping coefficient β_0 defined as

$$\beta_0 = \beta_{th} + \beta_{vis}, \tag{13}$$

where β_{th} and β_{vis} are the thermal and viscous damping coefficient (s^{-1}). Further, expressions for these two quantities can be obtained as follows (Ainslie & Leighton, 2009, 2011):

$$\beta_{th} = \frac{\Im\{\Omega^2\}}{2\omega}, \tag{14a}$$

$$\beta_{vis} = \frac{2\eta_S}{\rho_{liq} r^2}, \tag{14b}$$

where $\Im\{\cdot\}$ denotes the imaginary part of a complex number and η_S is the shear viscosity of the liquid (Pa·s). The form for the viscous damping has been a matter of some discussion, with some

authors favoring the inclusion of the effects of bulk viscosity (Love, 1978; Veloso et al., 2015); however, the later analysis of Baik (2013) highlighted flaws in the previous work and recommended the use of Equation 14b.

While this model captures much of the physics of acoustic scattering from bubbles in the large wavelength limit, it should not be regarded as complete. It still relies on the assumption that the bubbles are spherical, which for large bubbles will not hold true and can affect the backscattering cross section (Ostrovsky et al., 2008; Salomatin & Yusupov, 2005). Parameters used in the bubble backscattering cross section computation are summarized in Table 1.

3.2.2. Bubble Size Distribution Assumption

To estimate the bubble size distribution for each plume arm, a log-normal distribution (Johnson et al., 1994) is used as an appropriate bubble size distribution to match the plume bubbles (Veloso et al., 2015):

$$p_b(r) = \frac{1}{rS\sqrt{2\pi}} e^{-(\log(r)-\mu)^2/(2S^2)}, \tag{15}$$

where

$$\mu = \log(r_b) - S^2/2, \tag{16}$$

and

$$S = \sqrt{\log(1 + (\varsigma_b)^2)}. \tag{17}$$

Thus, for each point at which the inversion is applied, we have three parameters to match: the mean radius r_b in Equation 16, the standard deviation ς_b in Equation 17, and the number of bubbles per unit volume N_b. The mean radius r_b is related to the frequency f_{peak} corresponding to the peak value of the volume scattering strength $\mathrm{Vss}_{peak}(f)$ for each depth; the deviation ς_b is related to the curvature **C** of volume target strength curve as a function of frequency f; and the number of bubbles N_b is related to the amplitude of the volume scattering strength $\mathbf{Vss}(f)$. The three parameters are initialized at the beginning of the iteration process.

3.2.3. Modeled Volume Scattering Strength

Assuming the backscattering of all bubbles at depth d are uncorrected, the modeled volume scattering strength $\widehat{\mathrm{Vss}}(f)$ (dB) is the sum of the backscattering strength of the individual bubbles in radius bins centered on $[r_1, \ldots, r_{end}]$, given by

$$\widehat{\mathrm{Vss}}(f) = \frac{1}{V}\sum_{r_n=r_1}^{r_{end}} N_b(r_n)\sigma_{bs}(r_n, f), \tag{18}$$

$$\widehat{\mathrm{Vss}}(f) = 10\log_{10}\left(\widehat{\mathrm{Vss}}(f)\right), \tag{19}$$

where $N_b(r_n)$ is the number of bubbles with radius r_n per unit volume, following the bubble radius PDF $p_b(r)$ in Equation 15. For a series of frequencies $f = \{f_1, \ldots, f_{end}\}$, we obtain a vector of $\widehat{\mathbf{Vss}}(f)$.

3.2.4. Linear Inversion

One existing approach to quantifying gas from backscattered acoustic signals is based on linear inversion techniques. Such methods have been considered in cases when no bubbles are assumed to be resonant (Nikolovska et al., 2008) and without that restriction (Berges, 2015; Muyakshin & Sauter, 2010; Veloso et al., 2015). These methods are based on Equation 19, which can be expressed in matrix form:

$$\mathbf{Ax} = \mathbf{b}, \tag{20}$$

where the elements of the matrix **A** are the backscattering strengths, the column vector **x** contains the number of bubbles per unit volume within a size bin, and **b** contains the linear volume scattering strengths. Assuming the matrix **A** is of full rank and the number of radius bins is equal to the number of ensonifying frequencies, then this is a square system of equations with a unique solution, which can, in principle, be solved through matrix inversion. If the number of radius bins is less than the number of frequencies, a least square solution can be obtained, while if the number of radius bins exceeds the number of frequencies the problem is ill posed and an infinite number of solutions exist.

One problem is that since only a small number of frequencies are typically used to ensonify a cloud, one can only estimate bubbles in a small number of radius bins. Further, the matrix **A** can become ill conditioned as the off-diagonal terms can become large compared to the diagonal elements. This is because both resonant bubbles and large bubbles generate high levels of scattering, so while the diagonal elements in **A** may be large, so too are the regions corresponding to large bubbles ensonified by high frequencies. This ill conditioning in **A** means that during the inversion process small errors are greatly magnified. This can be mitigated by imposing prior constraints on the problem, in the form of regularization and by ensuring that the solution is always nonnegative.

In this work we eschew the use of linear inversion and at the outset impose constraints on the assumed bubble size distribution, which leads to a nonlinear optimization problem for which cannot be solved within a linear framework.

3.2.5. Matching Procedure

Rather than adopting a least squares approach to minimize the difference between the observed and modeled volume scattering strengths we shall use a curve matching strategy. Such an approach allows one to match a curve across the frequency interval at a large number of points, rather than solving the problem at isolated points. There are several curve matching techniques that have been proposed, including the Smith-Waterman algorithm for sequence alignment (Gribskov & Robinson, 1996), the B-spline fusion technique (Xia & Liu, 2004), the Discrete Curve Evolution (Bai et al., 2007), and the optimal alignment method (Sebastian et al., 2003). Here we adopt a method based at the optimal alignment curve matching.

The iteration procedure for each plume arm is shown in Equation A1. We first identify the plume arm structure, measure the dimension for each identified arm in depth, compute the observed volume scattering strength Vss(f) in depth, and prepare coefficients and environmental parameters collected in the experiment as shown in Table 1. For the matching process, we must initialize the bubble radius $r_b(0)$, the standard deviation $\varsigma_b(0)$, and the total number of bubbles $N_b(0)$. The bubble radius $r_b(0)$ is initialized from the plume upwelling velocity v_v as described in Equation 21; the standard deviation $\varsigma_b(0)$ is initialized as 1 mm; and the total number of bubbles per unit volume is initialized as a positive integer (here we use 100 for the upper arm possessing big bubbles, and 10,000 for the lower arm possessing small bubbles). The initial radii, $r_b(0)$, is selected to be 0.05 and 5 mm, for the lower and upper arms respectively. To accelerate the matching, one may need to adapt these initial values according to the observed target strength as a function of depth and frequency.

For each iteration n of the curve matching method, we calculate the volume scattering strength $\mathbf{Vss}(f)$ as a function of frequency f through Equation 19. From the calculated $\mathbf{Vss}(f)$ curve, we find frequency of the peak of the curve, $\hat{f}_{\text{peak}}(n)$, the maximum absolute curvature, $|\hat{C}_{\max}(n)|$, and the value of the peak volume scattering strength at that point, $\widehat{\mathbf{Vss}}_{\text{peak}}(f, n)$. The magnitude of the difference between the modeled and observed volume scattering strength can be computed, that is, $\Delta\widehat{\mathbf{Vss}}(f, n) = |\widehat{\mathbf{Vss}}(f, n) - \mathbf{Vss}(f)|$. If the size of this difference is minimized (e.g., on average less than a threshold $\text{Th}_1 = 1$ dB and the largest difference is less than a threshold $\text{Th}_2 = 3$ dB) in a number of iteration steps (e.g., 50), then the iteration is stopped; otherwise, the parameters (r_b, ς_b, and N_b) are updated according to the recursions shown in Appendix A1.

After the iterative matching process, we obtain estimates of the mean radius r_b, standard deviation ς_b, and the number of bubbles N_b as a function of depth in each of the plume arms. These three parameters define the PDF of the bubble size distribution as a function of depth, so that at any depth one can compute the gas volume and the gas flux.

3.3. Measurement

3.3.1. Measuring Plume Upwelling Velocity

In order to compute the gas flux, one needs to know the amount of gas at a given depth and the velocity of the gas. Individual bubbles rise through a liquid as a result of buoyancy, at a rate called the bubble rise velocity. A plume of bubbles also create motion of the surrounding water, creating a circulation (upwelling), this is the plume upwelling velocity and represents the velocity of bubbles in the plume, which is required in the flux calculation.

To estimate the plume upwelling velocity, we use the plume slope angle and modeled sea current speed. The average slope l_p (highlighted in Figure 2) is obtained by measuring the height and extent of the plume. The

Journal of Geophysical Research: Oceans 10.1029/2020JC016360

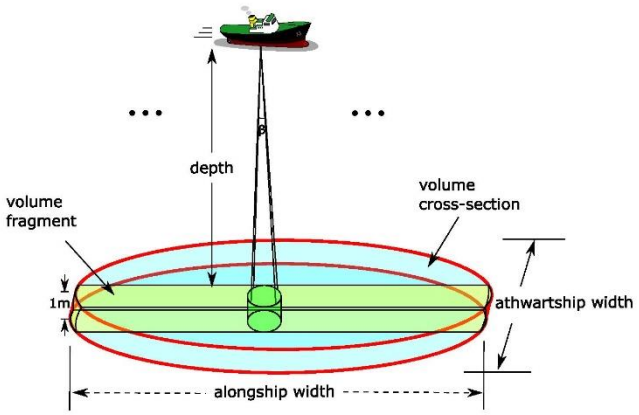

Figure 6. Geometry for converting gas volume from reverberating volume area to plume volume in depth. The single-beam scanned area is a fragment of the plume cross section. The plume horizontal cross section is considered to ellipse as observed from the multibeam data shown in Figure 2. Note that the alongship width and athwartship width are function of the longest diameter and shortest diameter of the ellipse relying on the ship direction.

slope of the plume varies with depth, tide, and current (Sündermann & Pohlmann, 2011). However, our multibeam data (Figure 2) suggests that the plumes observed here rise at an approximately constant angle and we use that angle to estimate a constant plume upwelling velocity.

We assume that the horizontal displacement of plume is entirely controlled by the current. Thus, we assume the relationship/slope angle θ between the horizontal displacement X_h and vertical displacement X_v of the plume is equal relationship between the horizontal velocity v_h (the current) and the plume upwelling velocity v_v. The plume slope is then given by

$$l_p = \frac{X_v}{X_h} = \tan\theta = \frac{v_v}{v_h}. \tag{21}$$

Using Equation 21, the average plume upwelling velocity near the pockmark values ranging from 10 to 15 cm/s. These values correspond to the bubble rise velocities for bubbles with radii in the range 1–6 mm (Park et al., 2017). This is consistent with our choice of an initial mean bubble radius in the upper arm.

3.3.2. Gas Volume Estimation

The plume is assumed to have an ellipsoidal cross section in the horizontal plane as observed from the multibeam data (Figure 2). The major and minor axes of the ellipse are denoted D_l and D_s, which can be measured from the 3-D multibeam data. We consider the gas in the plume in terms of horizontal slices of constant height (here we use 1 m). The scattered signal measured at the single-beam echo sounder consists of contributions from a volume, which is approximately cylindrically shaped oriented along the axis of the beam shown. The length of the cylinder being $c_w\tau/2$ (where τ is the pulse duration) and the diameter of the cylinder is $2h\tan(\beta/2)$, where h is the depth and β is the beam width (Figure 6). Assuming a horizontal cross section of the plume is homogeneous, having the same properties as the observed beam fragment, we can apply our findings appropriately to represent the entire horizontal cross section of the plume.

Based on the estimated bubble size distribution, the gas volume $\widehat{V}_p$ (L) within 1 m thick section through the plume can be approximated using

$$\hat{V}_p = \sum_{bin=1}^{Bin} \frac{4}{3}\pi N(r_{bin}) r_{bin}^3. \tag{22}$$

Figure 6 shows the geometry for converting gas volume from reverberating volume area to plume volume in depth. The calculated gas volumes are only a fragment of the gas volume in the whole gas plume arm at their corresponding depth (or horizontal cross section). We measure the size of the horizontal area in the reverberating volume fragment V according to the beam width. With the measured plume dimension S_h, and the gas volumes for each fragment $\widehat{V}_p$, we calculate the gas volume $\widehat{V}_h$ for each horizontal cross section at each depth with $h_v = 1$ m thickness:

$$\widehat{V}_h = \frac{S_h}{S_p}\widehat{V}_p, \tag{23}$$

where S_p is the horizontal dimension of the volume fragment.

3.3.3. Gas Flux Determination

Because of the interaction between the plume arms and the sea current, the rise velocity of the small bubbles in the lower plume arm is forced to be similar to that of upper plume arm containing larger bubbles. The mean rise velocity of the bubbles in the upper subplume are calculated using Equation 21. The estimated plume gas volumes V_g and the bubble rise velocity, we obtain the gas fluxes $\widehat{f}_g$ (L/min) of the upper plume arm and the lower plume arm in depth:

$$\widehat{f}_g = \widehat{V}_h v_v / h_v, \tag{24}$$

where h_v is the volume thickness, which here is equal to 1 m, considering the pulse length and resolution.

4. Results

Primary observations of this data set (Figure 7) show strong volume scattering strength at 3.5–18 and 70–120 kHz. For larger bubbles that rise faster than smaller bubbles (due to increased buoyancy), the movement direction of bubbles is closer to vertical. The target strength of the plume is integrated as volume scattering strength in depth for 1 m thickness and smoothed as shown in Figure 7. Two bubble clouds are visible, one in 3.5–18 kHz and the other in 38–200 kHz, and with a somewhat blurred border between them. At the low frequencies (f< 18 kHz), the clouds are connected to each other without big gaps, while at high frequencies (f> 38 kHz), the clouds are more separated from each other compared to those at low frequencies. This is consistent with arm structures observed from the multibeam observations, with small bubbles (radii < 0.2 mm) producing the peak at around 120 kHz and large bubbles (radii > 0.2 mm) producing the peak at much lower frequencies (Figure 7, left column).

Using the model matching approach, section 3.2.5, we obtained the scattering profiles shown in Figure 7middle column. This process also yields estimates of the parameters defining the bubble size distribution as a function of depth. The difference between the modeled and observed volume scattering strength is shown in Figure 7 right column. For all these cases, we successfully matched the scattering strength with only small difference remaining. This process also yields estimates of the parameters defining the bubble size distribution as a function of depth. To verify the gas flux change in depth, we compare the results to the predictions from a numerical model, specifically the Methane Individual Bubble Impact (MIBI) model (Dewar, 2016).

4.1. Plume Structure Identification

The two-arm structure that we observe for the plume is consistent with that presented in the literature (Dissanayake et al., 2018; Gentz et al., 2014; Greinert et al., 2006; Leifer et al., 2017; McGinnis et al., 2006; Ruppel, 2011; Sommer et al., 2015; von Deimling et al., 2015). It is proposed that the observed plume structure is a consequence of two dominant peaks in the bubble size distribution. The plume was observed multiple times from different directions, and the two-arm structure is consistently observed (see Figure 2). Acoustic data available for volume scattering strength analysis are at water depths 39–73 and 86–145 m (Figure 7).

4.2. Bubble Size Distribution

Identifying the structure of plume is one of the important elements in quantifying gas flow rate. Another important issue is related to bubble size distribution of each plume arm. Here, we determine the bubble

Journal of Geophysical Research: Oceans 10.1029/2020JC016360

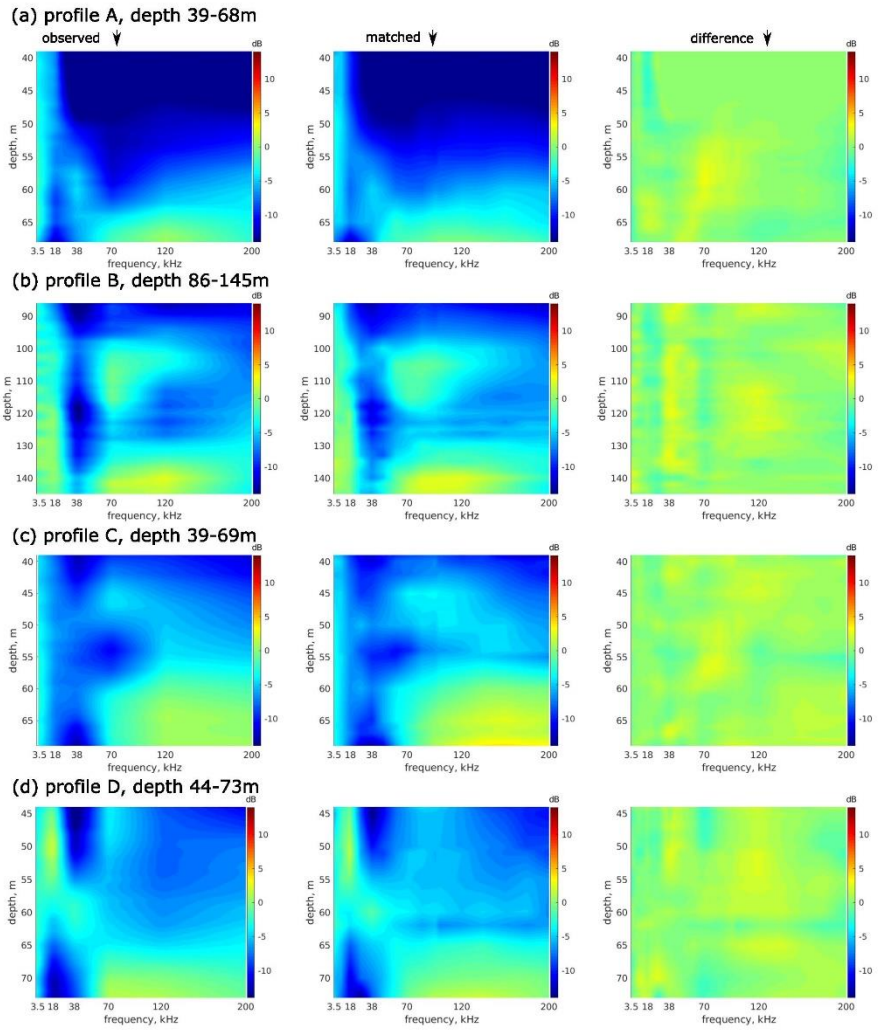

Figure 7. Left column: observed volume scattering strength of gas bubbles as a function of depth and frequency for the four profiles across the Scanner Pockmark methane. Data input was the volume scattering strengths observed at frequencies of 3.5, 18, 38, 70, 120 and 200 kHz; intermediate values are smoothed from the available data. Middle column: matched volume scattering strength as a function of depth and frequency for the four profiles. Right column: difference between the matched and the observed volume scattering strength as a function of depth and frequency for the four profiles. After sufficient iterations, the mean and maximum differences between the matched and observed volume scattering strength for most of these profiles are limited to 1 and 3 dB, respectively.

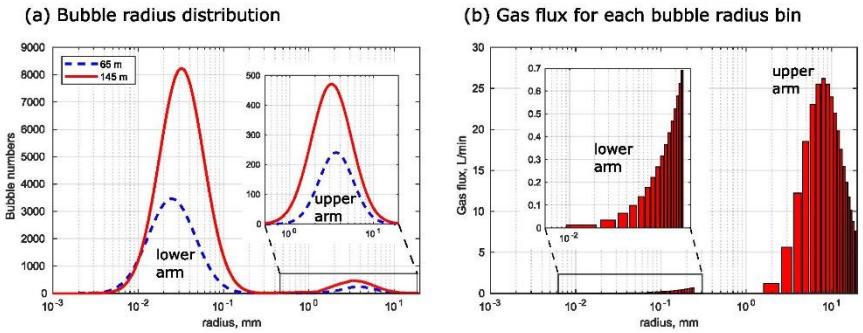

Figure 8. (a) Bubble radius distribution estimated from volume scattering strength matching at depths of 65 and 145 m, respectively. In the upper arm, bubble radii are predominantly in the interval (1 mm, 15 mm); in the lower arm, bubble radii are predominantly in the interval (0.01 mm, 0.15 mm). (b) Relative gas flux comparison for each bubble radius bin at depth 145 m. The highest gas flux is contributed by bubbles with radii of about 8 mm.

size distribution using the iterative volume scattering strength matching model. Applying the model yields two different bubble size distributions for the two plume arms. The acoustic measurements at two bathymetric depths result in similar bubble size distributions.

Figure 8a shows the PDF of the upper and lower plume arms at depth 65 and 145 m, respectively. From the estimation, bubbles in the upper arm possess radii mainly between 1 and 15 mm, while bubbles in the lower arm possess radii mainly between 0.01 and 0.15 mm. In the upper arm, there are more bubbles at 145 m than that at 65 m at all radii. In the lower arm, there are more relatively large bubbles (0.025–0.15 mm) at 145 m than that at 65 m, while there are fewer relatively small bubbles (<0.025 mm) at 145 m than that at 65 m. In the upper arm, the mean radius of the bubbles is $r_b = 5$ mm, and the bubble size distributions are comparable with those estimated elsewhere in the literature (1 to 6 mm) (Greinert, McGinnis, et al., 2010; Leifer & Patro, 2002; Muyakshin & Sauter, 2010; Ostrovsky et al., 2008; Römer et al., 2011; Sahling et al., 2009; Veloso et al., 2015).

4.3. Gas Flow Rate Quantification

The Scanner Pockmark plume was imaged on multiple profiles in different directions and the volume extent of methane bubbles in the water column is well constrained by multibeam data. Using the water column volume mapped from the multibeam data, we could extrapolate the volume scattering strength-derived measurements from single-beam data from the four profiles. We accept that our transect-derived estimates of bubble density and distribution may be a simplification of the 3-D plume.

With the measured sizes and the maximum gas volumes for each fragment, we calculate the gas volumes $\widehat{V}_h$ for each horizontal cross section at 1 m intervals in depth. With the estimated plume gas volumes, we obtain the dominant gas fluxes of both the upper and lower plume arms (Figure 9). From the calculation of gas flux for each size interval of bubbles, we obtain the relative gas flux contribution for each bubble size interval. It shows that the highest contribution of gas flux is from bubbles at radii of about 8 mm, and the contribution of gas flux from the lower plume arm can be omitted as shown in Figure 8b.

The results described in Figure 9 allow the estimation of in situ instantaneous flow rates in the water column, and for the upper plume this is 1.56×10^6 kg/year (294 L/min) at 145 m water depth, while for the same depth, the lower arm flow rate is 2.6×10^4 kg/year (4.9 L/min). In this form of depth-based estimation, the upper arm contributes 98% to the gas emission, whereas 2% are from the bubbles in the lower plume. The gas flux determination results suggest that the upper arm with large bubbles dominates the gas flux of the seabed released methane from the Scanner Pockmark. In addition to the flow rate estimates close to the pockmark, we also estimate gas flow rate in the water column associated with four different tidal heights. While at different tidal heights, comparing that of Profiles A (0.4 m) and C (0.2 m), for example, the variation of gas flux

Journal of Geophysical Research: Oceans 10.1029/2020JC016360

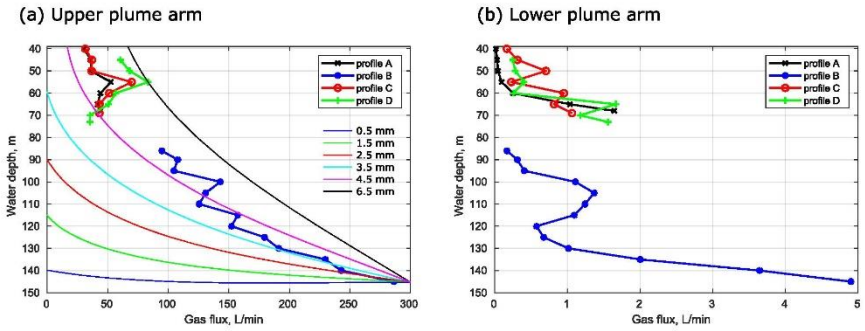

Figure 9. Estimated gas flux for each plume arm. (a) Upper plume arm; lines with markers on are measured gas flux for each profile; lines without markers on are from the MIBI modeling (Dewar, 2016) of the methane bubbles, which match the measured gas flux quite well in depth; 0.5–6.5 mm are bubble radius. (b) lower plume arm.

can be up to 40 L/min (2.4×10^5 kg/year at depth 165 m in the upper arm (Figure 9a) and can be up to 1.0 L/min (6.0×10^3 kg/year at depth 165 m in the lower arm, Figure 9b).

The gas flux gradually decreases from 1.56×10^6 kg/year (294 L/min) at depth 145 m to 6.9×10^4 kg/year (40 L/min) in the upper arm at depth 40 m as a consequence of bubble dissolution. In the lower arm, no obvious trend in gas flow rate is visible due to the intermittent emission of smaller bubbles. Overall, for the western Scanner Pockmark plume, the instantaneous flow rate is estimated to 1.59×10^6 kg/year (299 L/min) at depth 145 m, and 2.4×10^6 kg/year (400 L/min) at depth 165 m extrapolating the results in Figure 9 downward to the base of the pockmark. This instantaneous value may not be wholly representative of average flow rate, as in this study we have not considered tidal or seasonal variability.

4.4. Gas Flux Verification of Upwelling Methane Plume Using Modeling

To verify the gas flux evolution along the plume, we apply modeling of the methane bubbles known as the MIBI model (Dewar, 2016). This is a modified version of a CO_2 bubble model developed by Chen et al. (2009), recreated in a study to compare impacts of CO_2 and methane in the water column (Dewar et al., 2013). To simulate methane, the dominant gas properties on the bubble dynamics and dissolution have been used.

The results obtained from the MIBI model are shown as lines in Figure 9a. The model suggests that the dominant bubble radii is somewhere around 4.5 mm (between 3.5 and 6.5 mm), as superimposed for comparison in Figure 9a. This size best matches the measurements made from Profile B. The dominant bubble radius in the plume appears to be around the 4.5–5 mm mark; this is slightly larger than the measured peak bubble radius of 3.5 mm. However, this is to be expected given that bubbles of radii up to 20 mm are measured in the plume. The MIBI model also predicts that the reduction in plume volume from dissolution and the bubble expansion from reduced pressure. The results at bubble radius between 4.5 and 6.5 mm match well with the acoustic measurements at Profiles A–D, validating the effectiveness of our approach.

Table 2
Measured and Applied Parameters in the Estimation Approach

Term	Unit	Applied	Minimum	Maximum
Temperature	°C	8.1	7.6	10.1
Salinity	g/kg	35.1	35.0	35.2
Sound speed in water	m/s	1,485	1,483	1,489
Density	kg/L	1,028.0	1,027.5	1,028.5
Damping coefficient	clean/dirty bubbles	clean	clean	dirty
Plume slope (e.g.)	degree (°)	44.5	41.0	48.0

5. Uncertainty Estimation and Discussion

To remove ambiguities, one must use frequencies both above and below those of the bubble resonances present. Most multibeam echo sounders have frequencies, which, unless one is looking at very deep seeps, are mostly higher than the bubble resonances present. To remove all ambiguities, the lowest frequency used must be lower than the resonance of the largest bubble present (calculated above to be around 1 kHz). With the

Table 3
Uncertainty Estimation of Gas Flux $\dot{F}_g$ (L/min) Using Monte Carlo Approach

Term	Minimum $\dot{F}_g$	Maximum $\dot{F}_g$	Uncertainty
Temperature	383	393	[−2.0%, 0.4%]
Sound speed in water	389	392	[−0.4%, 0.3%]
Damping coefficient	309	391	[−21.0%, 0.0%]
Plume slope	346	441	[−11.5%, 13.0%]
Total	272	456	[−32%, 14%]

smallest bubbles presented calculated to have a resonance of 12 kHz, then with the energy available in this experiment from 2.5–6.5 kHz from the chirp, and 18 kHz from the echo sounder, we have obtained energy that is at frequencies that are less than the resonances of most of the bubbles present, but not below that of the largest bubbles present. This is an improvement, but does not reach the ideal of achieving a stiffness-controlled scattering from the largest bubbles present (Leighton, 1994).

When considering uncertainty in our calculation of total gas flux, we need to consider two components: the errors due to uncertainty in individual parameters, which are inputs into our calculation; and the propagation of this uncertainty in the model. We initially describe errors in individual parameters, before utilizing a Monte Carlo simulation approach to understand the uncertainty in the calculation of total gas flux. The Monte Carlo simulations are based on 1,000 repetitions, we define measures of uncertainty in the flow rate empirically for the pockmark by varying only one input parameter at a time, holding all others at constant values.

Table 2 describes the uncertainty in physical model parameters in the model. While the uncertainty in some physical parameters are small (e.g., temperature, sound speed in water, and salinity) and not significant, others are much larger. We focus here on discussion of those parameters that have significant uncertainty. The overall uncertainty of the flow rate estimation based on the applied physics is defined as a simple superposition (multiplication) of individual factors of uncertainty as follows. The temperature that we are using in the model is an averaged one of 8.1°C (or 281.25 K) in a range of measured temperature [7.6°C, 10.1°C] (or [280.75 K, 283.25 K]). The sound speed in the seawater was measured as between 1,483 and 1,489 m/s with an average of 1,485 m/s. For the shallow water scenario, we choose to calculate clean bubbles as we assume that gas hydrates are stable (Leifer et al., 2000). However, this clean bubble assumption in shallow water may not hold in all cases; thus, we include the dirty bubbles in the uncertainty estimation. Application of sea current and plume slope to determine plume upwelling velocity (then bubble rise velocity) remains a variation factor of 8% relative to the seabed. The matching difference between the modeled and observed volume scattering strength is limited within a threshold of 1 dB.

After the Monte Carlo simulation, we obtain the uncertainty of gas flow rate as follows. The temperature affects the viscosity and results in −2% to 0.4% uncertainty of the cross-section computation, with lower temperatures generally reducing the flow rate. The sound speed affects the wave number k and reradiation damping coefficient δ_{rad} and can result in −0.4% to 0.3% uncertainty. Such uncertainty resulted from seafloor temperature, near seafloor salinity, sound speed, and seawater density in the shallow water shelf environments and impact on flow rate estimation was found to be nearly indiscernible. While the dirty bubble assumption reduces the flow rate and results in −21% lower gas flux estimation than that of the clean bubble assumption. The plume slope makes −11.5% to 12% uncertainty of plume upwelling velocity values, then the flow rate. A measurement of the overall uncertainty in the calculations can be defined by combining statistics of the range in estimated flow rate values and uncertainty from the theory of flow rate estimation. Totally, the cumulative uncertainty bounds on the average reported flow rates are −32% to 14%. We outline in the following our approach to define an overall uncertainty in the reported values of flow rates, summarized in Table 3.

Our estimated total instantaneous flow rates of 2.4×10^6 kg/year is a representative first-order value for the gas flow at the Scanner Pockmark in the central North Sea, and we propose a total uncertainty in the flow rate estimation of [−32%, 14%]. However, if one assumes in the scattering model that $kr \ll 1$ (Thuraisingham, 1997; Veloso et al., 2015) then one estimates the flux as 1.3×10^6 kg/year and using the new model described here (section 3.2.1) that estimate becomes 2.4×10^6 kg/year.

6. Conclusions

In this paper, we developed a new methodology for calculating gas flux from a seabed seep using multibeam imaging, and quantification from single-beam echo sounders covering a broad bandwidth (3.5–200 kHz). We investigate a methane seep from the Scanner Pockmark in the North Sea and find that the plume in the

Journal of Geophysical Research: Oceans 10.1029/2020JC016360

water column is forked with two arms. The broadband methodology enables us to quantify gas flux with frequencies spanning the resonances of all the bubbles in the plume. It applies an iterative model to match the volume scattering strength from the water column for each of the plume arm. The matching results show that the upper arm comprises larger bubbles (1–15 mm in radius) and the lower arm comprises smaller bubbles (0.01–0.15 mm in radius). The total seabed methane gas flux is quantified to be between 1.6 and 2.7 × 10^6 kg/year (272 to 456 L/min) at the Scanner Pockmark.

Appendix A: Volume Scattering Strength Matching Algorithm

The iterative matching algorithm of volume scattering strength described in section 3.2.5 is shown in Figure A1, with notation shown in Table A1.

Algorithm 1 Volume Scattering Strength Matching Model for each depth of a single plume arm

Require: plume arm structure, arm dimensions in depth, Volume scattering strength $\mathbf{Vss}(f)$ in the function of frequency f for each depth, coefficients and environmental parameters shown in Table 1

Ensure: $\bar{r}_b(0)$, $\varsigma_b(0)$, $N_b(0)$; **pre-decision:** $\bar{r}_b(1)=\bar{r}_b(0)/2$, $\bar{r}_b(2)=2\bar{r}_b(0)$; $\varsigma_b(1)=\varsigma_b(0)/2$, $\varsigma_b(2)=2\varsigma_b(0)$; $N_b(1)=N_b(0)/2$, $N_b(2)=2N_b(0)$

procedure
  for n = 3, ... **do**
    if $\hat{f}_{\text{peak}}(n) \geq f_{\text{peak}}$ **then**
      update $\bar{r}_b(n) \leftarrow (\bar{r}_b(n-1) + \max(\bar{r}_b(n-2), \bar{r}_b(n-3)))/2$
    else
      update $\bar{r}_b(n) \leftarrow (\bar{r}_b(n-1) + \min(\bar{r}_b(n-2), \bar{r}_b(n-3)))/2$
    end if
    if $|\widehat{C}_{\max}(n)| \geq |C_{\max}|$ **then**
      update $\varsigma_b(n) \leftarrow (\varsigma_b(n-1) + \max(\varsigma_b(n-2), \varsigma_b(n-3)))/2$
    else
      update $\varsigma_b(n) \leftarrow (\varsigma_b(n-1) + \min(\varsigma_b(n-2), \varsigma_b(n-3)))/2$
    end if
    if $\widehat{\mathbf{Vss}}_{\text{peak}}(f,n) \geq \mathbf{Vss}_{\text{peak}}(f)$ **then**
      update $N_b(n) \leftarrow N_b(n-1)/\max\left(\mathbf{vss}_{\text{peak}}(f)/\widehat{\mathbf{vss}}_{\text{peak}}(f,n)\right)$
    else
      updatc $N_b(n) \leftarrow N_b(n-1) * \max\left(\mathbf{vss}_{\text{peak}}(f)/\widehat{\mathbf{vss}}_{\text{peak}}(f,n)\right)$
    end if
  end for
end procedure
update the modelled volume scattering strength $\widehat{\mathbf{Vss}}(n)$ in Eq.(19)
calculate $\Delta\widehat{\mathbf{Vss}}(f,n) = \widehat{\mathbf{Vss}}(f,n) - \mathbf{Vss}(f)$
if $\Delta\widehat{\mathbf{Vss}}_{\text{mean}}(f,n) < \text{Th}_1$ (e.g. 1 dB) & $\Delta\widehat{\mathbf{Vss}}_{\max}(f,n) < \text{Th}_2$ (e.g. 3 dB) **then**
  save $\bar{r}_b(n)$, $\varsigma_b(n)$, $N_b(n)$.
end if
Output : $\widehat{\text{V}}_p$, $\widehat{\text{V}}_h$, $\widehat{\text{F}}_g$ calculation in Eqs.(22),(23),(24).

Table A1
Notation Used in the Text

Variable	Description
n	number of iterations
r_b	bubble mean radius
ςb	standard deviation of the bubble radius
N_b	total number of bubbles
$\mathbf{Vss}(f)$	observed volume scattering strength in the function of frequency f
$\mathbf{Vss}_{\text{peak}}(f)$	peak value of observed volume scattering strength
$\lvert\mathbf{C}_{\text{peak}}\rvert$	maximum absolute value of curvature of observed volume scattering strength curve
f_{peak}	frequency corresponding to peak value of observed volume scattering strength
$\hat{\mathbf{Vss}}$	modeled target strength in the function of frequency f
$\hat{\mathbf{Vss}}_{\text{peak}}$	peak value of modeled volume scattering strength
$\lvert\hat{\mathbf{C}}_{\text{peak}}\rvert$	maximum absolute value of curvature of modeled volume scattering strength curve
$\hat{f}_{\text{peak}}$	frequency corresponding to peak value of modeled volume scattering strength
$\Delta\hat{\mathbf{Vss}}$	difference between observed and modeled volume scattering strength
$\Delta\hat{\mathbf{Vss}}_{\text{mean}}$	mean value of the volume scattering strength difference
$\Delta\hat{\mathbf{Vss}}_{\text{max}}$	maximum value of the volume scattering strength difference
$\hat{V}_p$	estimated gas volume of observed fragment
$\hat{V}_h$	estimated gas volume of an entire horizontal cross section with 1 m thickness
$\hat{F}_g$	estimated gas flux

Data Availability Statement

Data supporting this study (https://doi.org/10.5258/SOTON/D1357) are openly available from the University of Southampton repository.

Acknowledgments
Funding for this work was provided by NERC Grant NE/N01610/1 and the European Unions Horizon 2020 research and innovation program under Grant Agreement 654462 (STEMM-CCS). We are grateful to the Captain of the RRS James Cook and crew for enabling the scientific measurements at sea during JC152.

References

Ainslie, M. A., & Leighton, T. G. (2009). Near resonant bubble acoustic cross-section corrections, including examples from oceanography, volcanology, and biomedical ultrasound. *The Journal of the Acoustical Society of America*, *126*(5), 2163–2175. https://doi.org/10.1121/1.3180130

Ainslie, M. A., & Leighton, T. G. (2011). Review of scattering and extinction cross-sections, damping factors, and resonance frequencies of a spherical gas bubble. *The Journal of the Acoustical Society of America*, *130*(5), 3184–3208. https://doi.org/10.1121/1.3628321

Bai, X., Latecki, L. J., & Liu, W.-Y. (2007). Skeleton pruning by contour partitioning with discrete curve evolution. *IEEE Transactions on Pattern Analysis and Machine Intelligence*, *29*(3), 449–462. https://doi.org/10.1109/TPAMI.2007.59

Baik, K. (2013). Comment on "Resonant acoustic scattering by swimbladder-bearing fish"[J. Acoust. Soc. Am. 64, 571–580 (1978)](L). *The Journal of the Acoustical Society of America*, *133*(1), 5–8. https://doi.org/10.1121/1.4770261

Baik, K., Leighton, T. G., & Jiang, J. (2014). Investigation of a method for real time quantification of gas bubbles in pipelines. *The Journal of the Acoustical Society of America*, *136*(2), 502–513. https://doi.org/10.1121/1.4881922

Bayrakci, G., Scalabrin, C., Dupré, S., Leblond, I., Tary, J.-B., Lanteri, N., et al. (2014). Acoustic monitoring of gas emissions from the seafloor. Part II: A case study from the Sea of Marmara. *Marine Geophysical Research*, *35*(3), 211–229. https://doi.org/10.1007/s11001-014-9227-7

Berges, B. (2015). *Acoustic detection of seabed gas leaks, with application to Carbon Capture and Storage (CCS), and leak prevention for the oil and gas industry* (PhD dissertation). Southampton, UK: University of Southampton.

Berges, B. J. P., Leighton, T. G., & White, P. R. (2015). Passive acoustic quantification of gas fluxes during controlled gas release experiments. *International Journal of Greenhouse Gas Control*, *38*, 64–79.

Blackford, J., Stahl, H., Bull, J. M., Berges, B. J. P., Cevatoglu, M., Lichtschlag, A., et al. (2014). Detection and impacts of leakage from sub-seafloor deep geological carbon dioxide storage. *Nature Climate Change*, *4*(11), 1011. https://doi.org/10.1038/nclimate2381

Cazenave, P. W., Torres, R., & Allen, J. I. (2016). Unstructured grid modelling of offshore wind farm impacts on seasonally stratified shelf seas. *Progress in Oceanography*, *145*, 25–41. https://doi.org/10.1016/j.pocean.2016.04.004

Chen, B., Nishio, M., Song, Y., & Akai, M. (2009). The fate of CO_2 bubble leaked from seabed. *Energy Procedia*, *1*(1), 4969–4976. https://doi.org/10.1016/j.egypro.2009.02.329

Dewar, M. (2016). *Modelling the two-phase plume dynamics of CO_2 leakage into open shallow waters* (PhD dissertation). Edinburgh, UK: Heriot-Watt University.

Dewar, M., Wei, W., Khajepor, S., McNeil, D., & Chen, B. (2013). Comparison of the impact and fate of leaked CO_2 and CH_4 bubbles from the seabed on the near field waters within the North Sea. In *EGU General Assembly Conference Abstracts*, *15*. Vienna, Austria.

Dissanayake, A. L., Gros, J., & Socolofsky, S. A. (2018). Integral models for bubble, droplet, and multiphase plume dynamics in stratification and crossflow. *Environmental Fluid Mechanics*, *18*(5), 1167–1202. https://doi.org/10.1007/s10652-018-9591-y

Gentz, T., Damm, E., von Deimling, J. S., Mau, S., McGinnis, D. F., & Schlüter, M. (2014). A water column study of methane around gas flares located at the West Spitsbergen continental margin. *Continental Shelf Research*, *72*, 107–118. https://doi.org/10.1016/j.csr.2013.07.013

Greinert, J., Artemov, Y., Egorov, V., De Batist, M., & McGinnis, D. (2006). 1300-m-high rising bubbles from mud volcanoes at 2080 m in the Black Sea: Hydroacoustic characteristics and temporal variability. *Earth and Planetary Science Letters*, *244*(1-2), 1–15. https://doi.org/10.1016/j.epsl.2006.02.011

Greinert, J., Lewis, K. B., Bialas, J., Pecher, I. A., Rowden, A., Bowden, D. A., et al. (2010). Methane seepage along the Hikurangi Margin, New Zealand: Overview of studies in 2006 and 2007 and new evidence from visual, bathymetric and hydroacoustic investigations. *Marine Geology*, *272*(1-4), 6–25. https://doi.org/10.1016/j.margeo.2010.01.017

Greinert, J., McGinnis, D. F., Naudts, L., Linke, P., & De Batist, M. (2010). Atmospheric methane flux from bubbling seeps: Spatially extrapolated quantification from a Black Sea shelf area. *Journal of Geophysical Research*, *115*, C01002. https://doi.org/10.1029/2009JC005381

Greinert, J., & Nützel, B. (2004). Hydroacoustic experiments to establish a method for the determination of methane bubble fluxes at cold seeps. *Geo-Marine Letters*, *24*(2), 75–85. https://doi.org/10.1007/s00367-003-0165-7

Gribskov, M., & Robinson, N. L. (1996). Use of receiver operating characteristic (ROC) analysis to evaluate sequence matching. *Computers & chemistry*, *20*(1), 25–33. https://doi.org/10.1016/S0097-8485(96)80004-0

Harris, A. F. III, & Zorzi, M. (2007). Modeling the underwater acoustic channel in ns2. In *Proceedings of the 2nd international conference on Performance evaluation methodologies and tools* (pp. 18). Nantes, France: ICST (Institute for Computer Sciences, Social-Informatics and Telecommunications Engineering). https://doi.org/10.1145/1345263.1345286

Johanneson, K. A., & Mitson, R. B. (1983). Fisheries acoustics. A practical manual for aquatic biomass estimation. *FAO Fisheries Technical Papers*, *240*, 99–101.

Johnson, N. L., Kotz, S., & Balakrishnan, N. (1994). Continuous univariate distributions (Vol. *1*). New York: John Wiley & Sons.

Kennett, J. P., Cannariato, K. G., Hendy, I. L., & Behl, R. J. (2003). Methane hydrates in quaternary climate change: The clathrate gun hypothesi. *Methane Hydrates in Quaternary Climate Change: The Clathrate Gun Hypothesis*, *54*, 1–9. https://doi.org/10.1002/9781118665138.ch0

Leblond, I., Scalabrin, C., & Berger, L. (2014). Acoustic monitoring of gas emissions from the seafloor. Part I: Quantifying the volumetric flow of bubbles. *Marine Geophysical Research*, *35*(3), 191–210. https://doi.org/10.1007/s11001-014-9223-y

Leifer, I., & Boles, J. (2005). Measurement of marine hydrocarbon seep flow through fractured rock and unconsolidated sediment. *Marine and Petroleum Geology*, *22*(4), 551–568. https://doi.org/10.1016/j.marpetgeo.2004.10.026

Leifer, I., Chernykh, D., Shakhova, N., & Semiletov, I. (2017). Sonar gas flux estimation by bubble insonification: Application to methane bubble flux from seep areas in the outer Laptev Sea. *The Cryosphere*, *11*(3), 1333–1350. https://doi.org/10.5194/tc-11-1333-2017

Leifer, I., & Patro, R. K. (2002). The bubble mechanism for methane transport from the shallow sea bed to the surface: A review and sensitivity study. *Continental Shelf Research*, *22*(16), 2409–2428. https://doi.org/10.1016/S0278-4343(02)00065-1

Leifer, I., Patro, R. K., & Bowyer, P. (2000). A study on the temperature variation of rise velocity for large clean bubbles. *Journal of Atmospheric and Oceanic Technology*, *17*(10), 1392–1402. https://doi.org/10.1175/1520-0426(2000)017<1392:ASOTTV>2.0.CO;2

Leighton, T. G. (1994). *The acoustic bubble*. London: Academic Press.

Leighton, T. G., Baik, K., & Jiang, J. (2012). The use of acoustic inversion to estimate the bubble size distribution in pipelines. *Proceedings of the Royal Society A: Mathematical, Physical and Engineering Sciences*, *468*(2145), 2461–2484. https://doi.org/10.1098/rspa.2012.0053

Leighton, T. G., Meers, S. D., & White, P. R. (2004). Propagation through nonlinear time-dependent bubble clouds and the estimation of bubble populations from measured acoustic characteristics. *Proceedings of the Royal Society of London. Series A: Mathematical, Physical and Engineering Sciences*, *460*(2049), 2521–2550. https://doi.org/10.1098/rspa.2004.1298

Leighton, T. G., Phelps, A. D., Ramble, D. G., & Sharpe, D. A. (1996). Comparison of the abilities of eight acoustic techniques to detect and size a single bubble. *Ultrasonics*, *34*(6), 661–667. https://doi.org/10.1016/0041-624X(96)00053-4

Leighton, T. G., & White, P. R. (2011). Quantification of undersea gas leaks from carbon capture and storage facilities, from pipelines and from methane seeps, by their acoustic emissions. *Proceedings of the Royal Society A: Mathematical, Physical and Engineering Sciences*, *468*(2138), 485–510. https://doi.org/10.1098/rspa.2011.0221

Li, J., Roche, B., Bull, J. M., White, P. R., Davis, J. W., Deponte, M., et al. (2020). Passive acoustic monitoring of a natural CO_2 seep site—Implications for carbon capture and storage. *International Journal of Greenhouse Gas Control*, *93*(1), 102,899–102,908. https://doi.org/10.1016/j.ijggc.2019.102899

Li, J., White, P. R., Bull, J. M., & Leighton, T. G. (2019). A noise impact assessment model for passive acoustic measurements of seabed gas fluxes. *Ocean Engineering*, *183*(1), 294–304. https://doi.org/10.1016/j.oceaneng.2019.03.046

Li, J., White, P. R., Bull, J. M., Leighton, T. G., & Roche, B. (2019). A model for variations of sound speed and attenuation from seabed gas emissions. In *MTS/IEEE OCEANS 2019-Seattle, U.S.* (pp. 1–9). Seattle, WA, USA: IEEE. https://doi.org/10.23919/OCEANS40490.2019.8962861

Li, J., White, P. R., Roche, B., Bull, J. M., Davis, J. W., Leighton, T. G., et al. (2019). Natural seabed gas leakage—Variability imposed by tidal cycles. In *MTS/IEEE OCEANS 2019-Seattle* (pp. 1–6). Seattle, WA, USA: IEEE. https://doi.org/10.23919/OCEANS40490.2019.8962746

Ligtenberg, H., & Connolly, D. (2003). Chimney detection and interpretation, revealing sealing qualityof faults, geohazards, charge of and leakage from reservoirs. *Journal of Geochemical Exploration*, *78*, 385–387. https://doi.org/10.1016/S0375-6742(03)00095-5

Love, R. H. (1978). Resonant acoustic scattering by swimbladder-bearing fish[a]. *The Journal of the Acoustical Society of America*, *64*(2), 571–580. https://doi.org/10.1121/1.382009

McGinnis, D. F., Greinert, J., Artemov, Y., Beaubien, S. E., & Wüest, A. N. D. A. (2006). Fate of rising methane bubbles in stratified waters: How much methane reaches the atmosphere? *Journal of Geophysical Research*, *111*, C09007. https://doi.org/10.1029/2005JC003183

Muyakshin, S. I., & Sauter, E. (2010). The hydroacoustic method for the quantification of the gas flux from a submersed bubble plume. *Oceanology*, *50*(6), 995–1001. https://doi.org/10.1134/S0001437010060202

Nikolovska, A., Sahling, H., & Bohrmann, G. (2008). Hydroacoustic methodology for detection, localization, and quantification of gas bubbles rising from the seafloor at gas seeps from the eastern Black Sea. *Geochemistry, Geophysics, Geosystems*, 9, Q10010. https://doi.org/10.1029/2008GC002118

Nikolovska, A., & Schanze, J. J. (2007). Acoustic methane seepage quantification model design, experiments and deep-sea application. In *IEEE OCEANS 2007-Europe* (pp. 1–6). Aberdeen, UK: IEEE. https://doi.org/10.1109/OCEANSE.2007.4302285

Ochi, H., Watanabe, Y., & Shimura, T. (2008). Measurement of absorption loss at 80 kHz band for wideband underwater acoustic communication. *Japanese Journal of Applied Physics*, *47*(5S), 4366. https://doi.org/10.1143/JJAP.47.4366

Ostrovsky, I. (2003). Methane bubbles in Lake Kinneret: Quantification and temporal and spatial heterogeneity. *Limnology and Oceanography*, *48*(3), 1030–1036. https://doi.org/10.4319/lo.2003.48.3.1030

Ostrovsky, I., McGinnis, D. F., Lapidus, L., & Eckert, W. (2008). Quantifying gas ebullition with echosounder: The role of methane transport by bubbles in a medium-sized lake. *Limnology and Oceanography: Methods*, *6*(2), 105–118. https://doi.org/10.4319/lom.2008.6.105

Park, S. H., Park, C., Lee, J., & Lee, B. (2017). A simple parameterization for the rising velocity of bubbles in a liquid pool. *Nuclear Engineering and Technology*, *49*(4), 692–699. https://doi.org/10.1016/j.net.2016.12.006

Römer, M., Sahling, H., Pape, T., dos Santos Ferreira, C., Wenzhöfer, F., Boetius, A., & Bohrmann, G. (2014). Methane fluxes and carbonate deposits at a cold seep area of the Central Nile Deep Sea Fan, Eastern Mediterranean Sea. *Marine Geology*, *347*, 27–42. https://doi.org/10.1016/j.margeo.2013.10.011

Römer, M., Sahling, H., Spieß, V., & Bohrmann, G. (2011). The role of gas bubble emissions at deep-water cold seep systems: An example from the Makran continental margin, offshore Pakistan. In *Proceedings of the 7th International Conference on Gas Hydrates (ICGH 2011)*, Edinburgh, Scotland, United Kingdom.

Riedel, M., Scherwath, M., Römer, M., Veloso, M., Heesemann, M., & Spence, G. D. (2018). Distributed natural gas venting offshore along the Cascadia margin. *Nature Communications*, *9*(1), 3264. https://doi.org/10.1038/s41467-018-05736-x

Rona, P., & Light, R. (2011). Sonar images hydrothermal vents in seafloor observatory. *Eos, Transactions American Geophysical Union*, *92*(20), 169–170. https://doi.org/10.1029/2011EO200002

Ruppel, C. D. (2011). Methane hydrates and contemporary climate change. *Nature Eduction Knowledge*, *2*(12), 12.

Sündermann, J., & Pohlmann, T. (2011). A brief analysis of North Sea physics. *Oceanologia*, *53*(3), 663–689. https://doi.org/10.5697/oc.53-3.663

Sahling, H., Bohrmann, G., Artemov, Y. G., Bahr, A., Brüning, M., Klapp, S. A., et al. (2009). Vodyanitskii mud volcano, Sorokin trough, Black Sea: Geological characterization and quantification of gas bubble streams. *Marine and Petroleum Geology*, *26*(9), 1799–1811. https://doi.org/10.1016/j.marpetgeo.2009.01.010

Salomatin, A. S., & Yusupov, V. I. (2005). Quantitative estimation of gas plume parameters by echo-sounder. In *Proceedings of the XVI Session of the Russian Acoustical Society* (pp. 455–458). Moscow: Russian Acoustical Society.

Sebastian, T. B., Klein, P. N., & Kimia, B. B. (2003). On aligning curves. *IEEE Transactions on Pattern Analysis and Machine Intelligence*, *25*(1), 116–125. https://doi.org/10.1109/TPAMI.2003.1159951

Shakhova, N., Semiletov, I., Leifer, I., Sergienko, V., Salyuk, A., Kosmach, D., et al. (2014). Ebullition and storm-induced methane release from the East Siberian Arctic Shelf. *Nature Geoscience*, *7*(1), 64. https://doi.org/10.1038/ngeo2007

Shakhova, N., Semiletov, I., Salyuk, A., Yusupov, V., Kosmach, D., & Gustafsson, O. (2010). Extensive methane venting to the atmosphere from sediments of the East Siberian Arctic Shelf. *Science*, *327*(5970), 1246–1250. https://doi.org/10.1126/science.1182221

Shakhova, N., Semiletov, I., Sergienko, V., Lobkovsky, L., Yusupov, V., Salyuk, A., et al. (2015). The East Siberian Arctic Shelf: Towards further assessment of permafrost-related methane fluxes and role of sea ice. *Philosophical Transactions of the Royal Society A: Mathematical, Physical and Engineering Sciences*, *373*(2052), 20140451. https://doi.org/10.1098/rsta.2014.0451

Smailes, I. C. (1976). Observations of volume scattering strength in the northeast atlantic. *The Journal of the Acoustical Society of America*, *60*(5), 1056–1060. https://doi.org/10.1121/1.381196

Sommer, S., Schmidt, M., & Linke, P. (2015). Continuous inline mapping of a dissolved methane plume at a blowout site in the Central North Sea UK using a membrane inlet mass spectrometer–Water column stratification impedes immediate methane release into the atmosphere. *Marine and Petroleum Geology*, *68*, 766–775. https://doi.org/10.1016/j.marpetgeo.2015.08.020

Thuraisingham, R. A. (1997). New expressions of acoustic cross-sections of a single bubble in the monopole bubble theory. *Ultrasonics*, *35*(5), 407–409. https://doi.org/10.1016/S0041-624X(97)00021-8

Toramaru, A. (1989). Vesiculation process and bubble size distributions in ascending magmas with constant velocities. *Journal of Geophysical Research*, *94*(B12), 17,523–17,542. https://doi.org/10.1029/JB094iB12p17523

Urban, P., Köser, K., & Greinert, J. (2017). Processing of multibeam water column image data for automated bubble/seep detection and repeated mapping. *Limnology and Oceanography: Methods*, *15*(1), 1–21. https://doi.org/10.1002/lom3.10138

Urick, R. J. (2013). *Principles of underwater sound* (3rd ed.). Los Atlos, California: Peninsula Publishing.

Veloso, M., Greinert, J., Mienert, J., & De Batist, M. (2015). A new methodology for quantifying bubble flow rates in deep water using splitbeam echosounders: Examples from the Arctic offshore NW-Svalbard. *Limnology and Oceanography: Methods*, *13*(6), 267–287. https://doi.org/10.1002/lom3.10024

von Deimling, J. S., Greinert, J., Chapman, N. R., Rabbel, W., & Linke, P. (2010). Acoustic imaging of natural gas seepage in the North Sea: Sensing bubbles controlled by variable currents. *Limnology and Oceanography: Methods*, *8*(5), 155–171. https://doi.org/10.4319/lom.2010.8.155

von Deimling, J. S., Linke, P., Schmidt, M., & Rehder, G. (2015). Ongoing methane discharge at well site 22/4b (North Sea) and discovery of a spiral vortex bubble plume motion. *Marine and Petroleum Geology*, *68*, 718–730. https://doi.org/10.1016/j.marpetgeo.2015.07.026

von Deimling, J. S., Rehder, G., Greinert, J., McGinnnis, D. F., Boetius, A., & Linke, P. (2011). Quantification of seep-related methane gas emissions at Tommeliten, North Sea. *Continental Shelf Research*, *31*(7-8), 867–878. https://doi.org/10.1016/j.csr.2011.02.012

Westbrook, G. K., Thatcher, K. E., Rohling, E. J., Piotrowski, A. M., Pälike, H., Osborne, A. H., et al. (2009). Escape of methane gas from the seabed along the West Spitsbergen continental margin. *Geophysical Research Letters*, *36*, L15608. https://doi.org/10.1029/2009GL039191

Xia, M., & Liu, B. (2004). Image registration by "Super-curves". *IEEE Transactions on Image Processing*, *13*(5), 720–732. https://doi.org/10.1109/TIP.2003.822611

Xu, G., Jackson, D. R., Bemis, K. G., & Rona, P. A. (2014). Time-series measurement of hydrothermal heat flux at the Grotto mound, Endeavour Segment, Juan de Fuca Ridge. *Earth and Planetary Science Letters*, *404*, 220–231. https://doi.org/10.1016/j.epsl.2014.07.040

Xu, C., Wu, M., Zhou, T., Li, J., Du, W., Zhang, W., & White, P. R. (2020). Optical flow-based detection of gas leaks from pipelines using multibeam water column images. *Remote Sensing*, *12*(1), 119–139. https://doi.org/10.3390/rs12010119

Bibliography

Ainslie, M. A., and T. G. Leighton, 2011, Review of scattering and extinction cross-sections, damping factors, and resonance frequencies of a spherical gas bubble: The Journal of the Acoustical Society of America, **130**, 3184–3208.

Algar, C.K., Boudreau, B.P., Barry, M.A., 2011. Initial rise of bubbles in cohesive sediments by a process of viscoelastic fracture. J. Geophys. Res. 116, B04207. https://doi.org/10.1029/2010JB008133

Amano, T., Székely, T., Wauchope, H. S., Sandel, B., Nagy, S., Mundkur, T., Langendoen, T., Blanco, D., Michel, N.L., and Sutherland, W. J., 2020, Responses of global waterbird populations to climate change vary with latitude: Nature Climate Change, **10**, 959–964.

Anagnostou, M. N., Nystuen J. A., Anagnostou, E. N., Nikolopoulos, E. I., and Amitai E., 2008, Evaluation of Underwater Rainfall Measurements During the Ionian Sea Rainfall Experiment: IEEE Transactions on Geoscience and Remote Sensing, **46**, 2936–2946.

Anderson, A. L., Abegg, F., Hawkins, J. A., Duncan, M. E., and Lyons A. P. (1998), Bubble populations and acoustic interaction with the gassy floor of Eckernforde Bay, Cont. Shelf Res., 18(14-15), 1807-1838.

Anderson, A. L., and Hampton L. D. (1980), Acoustics of gas-bearing sediments I. Background, J. Acoust. Soc. Am., 67(6), 1865–1889.

Anyosa, S., Bunting, S., Eidsvik, J., Romdhane, A., and Bergmo, P., 2021, Assessing the value of seismic monitoring of CO2 storage using simulations and statistical analysis: International Journal of Greenhouse Gas Control, **105**, 103219.

Ashokan, M., Latha, G., Ramesh, R., 2015. Analysis of shallow water ambient noise due to rain and derivation of rain parameters. Appl. Acoust. 88, 114–122. https://doi.org/10.1016/j.apacoust.2014.08.010

Bagnato, E., Oliveri, E., Acquavita, A., Covelli, S., Petranich, E., Barra, M., Italiano, F., Parello, F., Sprovieri, M., 2017, Hydrochemical mercury distribution and air-sea exchange over the submarine hydrothermal vents off-shore Panarea Island (Aeolian arc, Tyrrhenian Sea): Marine Chemistry, 194, 63–78.

Baik, K., Leighton, T.G., Jiang, J., 2014, Investigation of a method for real time quantification of gas bubbles in pipelines: The Journal of the Acoustical Society of America, 136, 502–513.

Barry, M.A., Johnson, B.D., Boudreau, B.P., 2012. A new instrument for high-resolution in situ assessment of Young's modulus in shallow cohesive sediments. Geo-Marine Lett. 32, 349–357. https://doi.org/10.1007/s00367-012-0277-z

Bass, S. J., and Hay, A. E., 1997, Ambient noise in the natural surf zone: wave-breaking frequencies: IEEE Journal of Oceanic Engineering, **22**, 411–424.

Bastviken, D., Cole, J., Pace, M., & Tranvik, L. (2004). Methane emissions from lakes: Dependence of lake characteristics, two regional assessments, and a global estimate. *Global Biogeochemical Cycles*, *18*(4), 1–12. https://doi.org/10.1029/2004GB002238

Bastviken, D., Tranvik, L.J., Downing, J.A., Crill, P.M., Enrich-Prast, A., 2011. Freshwater Methane Emissions Offset the Continental Carbon Sink. Science (80-.). 331, 50–50. https://doi.org/10.1126/science.1196808

Bayrakci, G., Scalabrin, C., Dupré, S., Leblond, I., Tary, J.-B., Lanteri, N., Augustin, J.-M., Berger, L., Cros, E., Ogor, A., Tsabaris, C., Lescanne, M., Géli, L., 2014. Acoustic monitoring of gas emissions from the seafloor. Part II: a case study from the Sea of Marmara. Mar. Geophys. Res. 35, 211–229. https://doi.org/10.1007/s11001-014-9227-7

Beaulieu, J. J., Balz, D. A., Birchfield, M. K., Harrison, J. A., Nietch, C. T., Platz, M. C., Squier, W. C., Waldo, S., Walker, J. T., White, K. M., & Young, J. L. (2018). Effects of an Experimental Water-level Drawdown on Methane Emissions from a Eutrophic Reservoir. *Ecosystems*, *21*(4), 657–674. https://doi.org/10.1007/s10021-017-0176-2

Bergès, B.J.P., Leighton, T.G., White, P.R., 2015. Passive acoustic quantification of gas fluxes during controlled gas release experiments. Int. J. Greenh. Gas Control 38, 64–79. https://doi.org/10.1016/j.ijggc.2015.02.008

Black, P. G., J. R. Proni, J. C. Wilkerson, and C. E. Samsury, 1997, Oceanic Rainfall Detection and Classification in Tropical and Subtropical Mesoscale Convective Systems Using Underwater Acoustic Methods: Monthly Weather Review, **125**, 2014–2042.

Blackford, J., Artioli, Y., Clark, J., de Mora, L., 2017. Monitoring of offshore geological carbon storage integrity: Implications of natural variability in the marine system and the assessment of anomaly detection criteria. Int. J. Greenh. Gas Control 64, 99–112. https://doi.org/10.1016/j.ijggc.2017.06.020

Blackford, J., Stahl, H., Bull, J.M., Bergès, B.J.P., Cevatoglu, M., Lichtschlag, A., Connelly, D., James, R.H., Kita, J., Long, D., Naylor, M., Shitashima, K., Smith, D., Taylor, P., Wright, I.,

Akhurst, M., Chen, B., Gernon, T.M., Hauton, C., Hayashi, M., Kaieda, H., Leighton, T.G., Sato, T., Sayer, M.D.J., Suzumura, M., Tait, K., Vardy, M.E., White, P.R., Widdicombe, S., 2014. Detection and impacts of leakage from sub-seafloor deep geological carbon dioxide storage. Nat. Clim. Chang. 4, 1011–1016. https://doi.org/10.1038/nclimate2381

Blackford, J., Stahl, H., Bull, J.M., Bergès, B.J.P., Cevatoglu, M., Lichtschlag, A., Connelly, D., James, R.H., Kita, J., Long, D., Naylor, M., Shitashima, K., Smith, D., Taylor, P., Wright, I., Akhurst, M., Chen, B., Gernon, T.M., Hauton, C., Hayashi, M., Kaieda, H., Leighton, T.G., Sato, T., Sayer, M.D.J., Suzumura, M., Tait, K., Vardy, M.E., White, P.R., Widdicombe, S., 2014. Detection and impacts of leakage from sub-seafloor deep geological carbon dioxide storage. Nat. Clim. Chang. 4, 1011–1016. https://doi.org/10.1038/nclimate2381

Blair, T.C., McPherson, J.G., 1999. Grain-size and textural classification of coarse sedimentary particles. J. Sediment. Res. 69, 6–19. https://doi.org/10.2110/jsr.69.6

Boles, J. R., J. F. Clark, I. Leifer, and L. Washburn, 2001, Temporal variation in natural methane seep rate due to tides, Coal Oil Point area, California: Journal of Geophysical Research: Oceans, **106**, 27077–27086.

Boles, J.R., Clark, J.F., Leifer, I., Washburn, L., 2001. Temporal variation in natural methane seep rate due to tides, Coal Oil Point area, California. J. Geophys. Res. Ocean. 106, 27077–27086. https://doi.org/10.1029/2000JC000774

Böttner, C., Berndt, C., Reinardy, B.T.I., Geersen, J., Karstens, J., Bull, J.M., Callow, B.J., Lichtschlag, A., Schmidt, M., Elger, J., Schramm, B., Haeckel, M., 2019. Pockmarks in the Witch Ground Basin, Central North Sea. Geochemistry, Geophys. Geosystems 20, 1698–1719. https://doi.org/10.1029/2018GC008068

Boudreau, B.P., 2012. The physics of bubbles in surficial, soft, cohesive sediments. Mar. Pet. Geol. 38, 1–18. https://doi.org/10.1016/j.marpetgeo.2012.07.002

Boudreau, B.P., Algar, C., Johnson, B.D., Croudace, I., Reed, A., Furukawa, Y., Dorgan, K.M., Jumars, P.A., Grader, A.S., Gardiner, B.S., 2005. Bubble growth and rise in soft sediments. Geology 33, 517. https://doi.org/10.1130/G21259.1

Brás, T. A., Seixas J., Carvalhais N., and Jägermeyr J., 2021, Severity of drought and heatwave crop losses tripled over the last five decades in Europe: Environmental Research Letters.

Buckingham, M. J., 1991, On Acoustic Transmission in Ocean-Surface Waveguides: Philosophical Transactions: Physical Sciences and Engineering, **335**, 513–555.

Bush, M. J., 2020, The Carbon Cycle, *in* Climate Change and Renewable Energy, Springer International Publishing, 109–141.

Bussmann, I., Damm, E., Schlüter, M., & Wessels, M. (2013). Fate of methane bubbles released by pockmarks in Lake Constance. *Biogeochemistry*, *112*(1–3), 613–623. https://doi.org/10.1007/s10533-012-9752-x

Bussmann, I., Schlömer, S., Schlüter, M., Wessels, M., 2011. Active pockmarks in a large lake (Lake Constance, Germany): Effects on methane distribution and turnover in the sediment. Limnol. Oceanogr. 56, 379–393. https://doi.org/10.4319/lo.2011.56.1.0379

Caliro, S., Caracausi, A., Chiodini, G., Ditta, M., Italiano, F., Longo, M., Minopoli, C., Nuccio, P. M., Paonita, A., Rizzo, A., 2004, Evidence of a recent input of magmatic gases into the quiescent volcanic edifice of Panarea, Aeolian Islands, Italy: Geophysical Research Letters, 31,

Caramanna, G., Voltattorni, N., Maroto-Valer, M.M., 2011, Is Panarea Island (Italy) a valid and cost-effective natural laboratory for the development of detection and monitoring techniques for submarine CO 2 seepage? Greenhouse Gases: Science and Technology, 1, 200–210.

Carey, W. M., and M. P. Bradley, 1985, Low-frequency ocean surface noise sources: The Journal of the Acoustical Society of America, **78**, S1–S2.

Casper, P., Maberly, S.C., Hall, G.H., Finlay, B.J., 2000. Fluxes of methane and carbon dioxide from a small productive lake to the atmosphere. Biogeochemistry 49, 1–19. https://doi.org/10.1023/A:1006269900174

Cauchy, P., Heywood, K. J., Merchant, N. D., Queste, B. Y., and Testor, P., 2018, Wind Speed Measured from Underwater Gliders Using Passive Acoustics: Journal of Atmospheric and Oceanic Technology, **35**, 2305–2321.

Cavaleri, L., 2020, Rain, Wave Breaking and Spray, *in* Recent Advances in the Study of Oceanic Whitecaps, Springer International Publishing, 65–75.

Cavaleri, L., and Bertotti, L., 2018, Rain on Generative Seas: Geophysical Research Letters, **45**, 7049–7056.

Cazau, D., Bonnel, J., and Baumgartner, M., 2019, Wind Speed Estimation Using Acoustic Underwater Glider in a Near-Shore Marine Environment: IEEE Transactions on Geoscience and Remote Sensing, **57**, 2097–2106.

Cazau, D., Bonnel, J., Jouma'a, J., le Bras, Y., and Guinet, C., 2017, Measuring the Marine Soundscape of the Indian Ocean with Southern Elephant Seals Used as Acoustic Gliders of Opportunity: Journal of Atmospheric and Oceanic Technology, **34**, 207–223.

Cevatoglu, M., Bull, J.M., Vardy, M.E., Gernon, T.M., Wright, I.C., Long, D., 2015. Gas migration pathways, controlling mechanisms and changes in sediment acoustic properties observed in a controlled sub-seabed CO 2 release experiment. Int. J. Greenh. Gas Control 38, 26–43. https://doi.org/10.1016/j.ijggc.2015.03.005

Chen, L., Trinh, V., Yang, W., and Mohanangam, K., 2016, Prediction of Bubble Generation Based on Acoustic Emission: Acoustics Australia, **44**, 325–331.

Clay, C. S., and Medwin, H. (1978) Acoustical Oceanography: Principles and Applications. New York: John Wiley & Sons, 1977. xviii, 544 pp. (Ocean Engineering: A Wiley Series.) Price £20·65/$34·95.: Journal of the Marine Biological Association of the United Kingdom, **58**, 543–543

Coughlan, M., Roy S., O'Sullivan, C., Clements, A., O'Toole, R., and Plets, R., 2021, Geological settings and controls of fluid migration and associated seafloor seepage features in the north Irish Sea: Marine and Petroleum Geology, **123**, 104762.

Crippa, M., Oreggioni, G., Guizzardi, D., Muntean, M., Schaaf, E., lo Vullo, E., Solazzo, E., Monforti-Ferrario, F., Olivier, J. G. J., and Vignati, E., 2019, Fossil CO2 and GHG Emissions of All World Countries - 2019 Report:

Czerski, H., and Deane G. B., 2010, Contributions to the acoustic excitation of bubbles released from a nozzle: The Journal of the Acoustical Society of America, **128**, 2625–2634.

Damen, K., Faaij A., and Turkenburg W., 2006, Health, Safety and Environmental Risks of Underground Co2 Storage – Overview of Mechanisms and Current Knowledge: Climatic Change, **74**, 289–318.

Dean, M., Blackford, J., Connelly, D. and Hines, R., 2020. Insights and guidance for offshore CO2 storage monitoring based on the QICS, ETI MMV, and STEMM-CCS projects. Int. J. Greenh. Gas Control.

Dean, M., Tucker, O., 2017. A risk-based framework for Measurement, Monitoring and Verification (MMV) of the Goldeneye storage complex for the Peterhead CCS project, UK. Int. J. Greenh. Gas Control 61, 1–15. https://doi.org/10.1016/j.ijggc.2017.03.014

Deane, G. B., and Stokes, M. D., 2010, Model calculations of the underwater noise of breaking waves and comparison with experiment: The Journal of the Acoustical Society of America, **127**, 3394–3410.

Deane, G.B., and Stokes, M.D., 2002. Scale dependence of bubble creation mechanisms in breaking waves. Nature 418, 839–844. https://doi.org/10.1038/nature00967

Deane, G.B., Stokes, M.D., 2008. The acoustic excitation of air bubbles fragmenting in sheared flow. J. Acoust. Soc. Am. 124, 3450–3463. https://doi.org/10.1121/1.3003076

Di, P., Chen, Q., Chen, D., 2017. Quantification of methane fluxes from hydrocarbon seeps to the ocean and atmosphere: Development of an in situ and online gas flux measuring system. J. Ocean Univ. China 16, 447–454. https://doi.org/10.1007/s11802-017-3061-x

Dlugokencky, E.J., Nisbet, E.G., Fisher, R., Lowry, D., 2011. Global atmospheric methane: budget, changes and dangers. Philos. Trans. R. Soc. A Math. Phys. Eng. Sci. 369, 2058–2072. https://doi.org/10.1098/rsta.2010.0341

Encinas Fernández, J., Hofmann, H., & Peeters, F. (2020). Diurnal pumped-storage operation minimizes methane ebullition fluxes from hydropower reservoirs. *Water Resources Research*. https://doi.org/10.1029/2020wr027221

Esposito, A., Giordano, G., and Anzidei, M., 2006, The 2002–2003 submarine gas eruption at Panarea volcano (Aeolian Islands, Italy): Volcanology of the seafloor and implications for the hazard scenario: Marine Geology, **227**, 119–134.

Faggetter, M.J., Vardy, M.E., Dix, J.K., Bull, J.M., Henstock, T.J., 2020. Time-lapse imaging using 3D ultra-high-frequency marine seismic reflection data. GEOPHYSICS 85, P13–P25. https://doi.org/10.1190/geo2019-0258.1

Falcon-Suarez, I.H., Lichtschlag, A., Marin-Moreno, H., Papageorgiou, G., Sahoo, S.K., Roche, B., Callow, B., Gehrmann, R.A.S., Chapman, M., North, L., 2021. Core-scale geophysical and hydromechanical analysis of seabed sediments affected by CO2 venting. Int. J. Greenh. Gas Control 108, 103332. https://doi.org/10.1016/j.ijggc.2021.103332

Farmer, D. M., and Vagle S., 1988, On the determination of breaking surface wave distributions using ambient sound: Journal of Geophysical Research, **93**, 3591.

Farmer, D. M., and Vagle, S., 1989, Waveguide propagation of ambient sound in the ocean-surface bubble layer: The Journal of the Acoustical Society of America, **86**, 1897–1908.

Farmer, D. M., Deane, G. B., and Vagle, S., 2001, The influence of bubble clouds on acoustic propagation in the surf zone: IEEE Journal of Oceanic Engineering, **26**, 113–124.

Farrell, W. E., Berger, J., Bidlot, J.R., Dzieciuch, M., Munk, W., Stephen, R. A., and Worcester, P. F., 2016, Wind Sea behind a Cold Front and Deep Ocean Acoustics: Journal of Physical Oceanography, **46**, 1705–1716.

Fechner-Levy, E.J., Hemond, H.F., (1996), Trapped methane volume and potential effects on methane ebullition in a northern peatland, *Limnology and Oceanography*, 41, doi: 10.4319/lo.1996.41.7.1375.

Felizardo, F. C., and Melville, W. K., 1995, Correlations between Ambient Noise and the Ocean Surface Wave Field: Journal of Physical Oceanography, **25**, 513–532.

Flohr, A., Schaap, A., Achterberg, E.P., Alendal, G., Arundell, M., Berndt, C., Blackford, J., Böttner, C., Borisov, S.M., Brown, R., Bull, J.M., Carter, L., Chen, B., Dale, A.W., de Beer, D., Dean, M., Deusner, C., Dewar, M., Durden, J.M., Elsen, S., Esposito, M., Faggetter, M., Fischer, J.P., Gana, A., Gros, J., Haeckel, M., Hanz, R., Holtappels, M., Hosking, B., Huvenne, V.A.I., James, R.H., Koopmans, D., Kossel, E., Leighton, T.G., Li, J., Lichtschlag, A., Linke, P., Loucaides, S., Martínez-Cabanas, M., Matter, J.M., Mesher, T., Monk, S., Mowlem, M., Oleynik, A., Papadimitriou, S., Paxton, D., Pearce, C.R., Peel, K., Roche, B., Ruhl, H.A., Saleem, U., Sands, C., Saw, K., Schmidt, M., Sommer, S., Strong, J.A., Triest, J., Ungerböck, B., Walk, J., White, P., Widdicombe, S., Wilson, R.E., Wright, H., Wyatt, J., Connelly, D., 2021. Towards improved monitoring of offshore carbon storage: A real-world field experiment detecting a controlled sub-seafloor CO2 release. Int. J. Greenh. Gas Control 106, 103237. https://doi.org/10.1016/j.ijggc.2020.103237

Friedlingstein, P., Jones, M.W., O'Sullivan, M., Andrew, R.M., Hauck, J., Peters, G.P., Peters, W., Pongratz, J., Sitch, S., Le Quéré, C., Bakker, D.C.E., Canadell, J.G., Ciais, P., Jackson, R.B., Anthoni, P., Barbero, L., Bastos, A., Bastrikov, V., Becke, S., 2019. Global Carbon Budget 2019 ETH Library. Earth Syst. Sci. Data. https://doi.org/10.3929/ethz-b-000385668

Fujimori, S., Krey, V., van Vuuren, D., Oshiro, K., Sugiyama, M., Chunark, P., Limmeechokchai, B., S. Mittal, Nishiura, O., Park, C., Rajbhandari S., Silva Herran, D., Tu, T. T., Zhao, S., Ochi, Y., Shukla, P. R., Masui, T.,. Nguyen, P.V.H, Cabardos, A.M., and Riahi, K., 2021, A framework for national scenarios with varying emission reductions: Nature Climate Change.

Furre, A.K., Eiken, O., Alnes, H., Vevatne, J.N., Kiær, A.F., 2017. 20 Years of Monitoring CO2-injection at Sleipner. Energy Procedia 114, 3916–3926. https://doi.org/10.1016/j.egypro.2017.03.1523

Garrett, C., Li, M., and Farmer, D., 2000, The Connection between Bubble Size Spectra and Energy Dissipation Rates in the Upper Ocean: Journal of Physical Oceanography, **30**, 2163–2171.

GCCSI, 2020, Global Status of CCS 2020: www.globalccsinstitute.com/resources/global-status-report

Gilfedder, B. S., Petri, M., Wessels, M., & Biester, H. (2011). Bromine species fluxes from Lake Constance's catchment, and a preliminary lake mass balance. *Geochimica et Cosmochimica Acta*, *75*(12), 3385–3401. https://doi.org/10.1016/j.gca.2011.03.021

Granin, N., Muyakshin, S., Makarov, M., & Kucher, K., Aslamov, I., Granina, L., & Mizandrontsev, I., (2012). Estimation of methane fluxes from bottom sediments of Lake Baikal. Geo-Marine Letters. 32. 10.1007/s00367-012-0299-6.

Greene, C. A., and Wilson, P. S., 2012, Laboratory investigation of a passive acoustic method for measurement of underwater gas seep ebullition: The Journal of the Acoustical Society of America, **131**, EL61–EL66.

Greinert, J., 2008. Monitoring temporal variability of bubble release at seeps: The hydroacoustic swath system GasQuant. J. Geophys. Res. 113, C07048. https://doi.org/10.1029/2007JC004704

Greinert, J., Artemov, Y., Egorov, V., Debatist, M., McGinnis, D., 2006. 1300-m-high rising bubbles from mud volcanoes at 2080m in the Black Sea: Hydroacoustic characteristics and temporal variability. Earth Planet. Sci. Lett. 244, 1–15. https://doi.org/10.1016/j.epsl.2006.02.011

Greinert, J., Lewis, K.B., Bialas, J., Pecher, I.A., Rowden, A., Bowden, D.A., De Batist, M., Linke, P., 2010. Methane seepage along the Hikurangi Margin, New Zealand: Overview of studies in 2006 and 2007 and new evidence from visual, bathymetric and hydroacoustic investigations. Mar. Geol. 272, 6–25. https://doi.org/10.1016/j.margeo.2010.01.017

Greinert, J., Nitzel, B., 2004. Hydroacoustic experiments to establish a method for the determination of methane bubble fluxes at cold seeps. Geo-Marine Lett. 24, 75–85. https://doi.org/10.1007/s00367-003-0165-7

Hamblin, B. F., & Hollan, E. (1978). *On the gravitational seiches of Lake Constance and their generation*. Birkhttnser Verlag Basel 119.

Hansen, O., Gilding, D., Nazarian, B., Osdal, B., Ringrose, P., Kristoffersen, J.-B., Eiken, O., Hansen, H., 2013. Snøhvit: The History of Injecting and Storing 1 Mt CO2 in the Fluvial Tubåen Fm. Energy Procedia 37, 3565–3573. https://doi.org/10.1016/j.egypro.2013.06.249

Hanssen, S.v., Daioglou, V., Steinmann, Z.J.N., Doelman, J.C., van Vuuren D.P., and Huijbregts, M.A.J., 2020, The climate change mitigation potential of bioenergy with carbon capture and storage: Nature Climate Change, **10**, 1023–1029.

Higgs, B., Mountjoy, J. J., Crutchley, Townend, G. J., J., Ladroit, Y., Greinert J., and McGovern C., 2019, Seep-bubble characteristics and gas flow rates from a shallow-water, high-density seep field on the shelf-to-slope transition of the Hikurangi subduction margin: Marine Geology, **417**, 105985.

Hollan, E., Rao, D. B., & Bäuerle, E. (1980). Free surface oscillations in Lake Constance with an interpretation of the “Wonder of the Rising Water” at Konstanz in 1549. Die freien Schwingungen des Bodensees mit einer Interpretation des „Wasserwunders” von Konstanz im Jahre 1549. *Archiv Für Meteorologie, Geophysik Und Bioklimatologie Serie A*, *29*(3), 301–325. https://doi.org/10.1007/bf02247768

Holthuijsen, L. H., 2007, Waves in Oceanic and Coastal Waters: Cambridge University Press.

Houghton, R. A., 2014, The Contemporary Carbon Cycle, *in* Treatise on Geochemistry, Elsevier, 399–435.

Hovland, M., 2002, On the self-sealing nature of marine seeps: Continental Shelf Research, **22**, 2387–2394.

Hovland, M., Heggland, R., De Vries, M.H., Tjelta, T.I., 2010. Unit-pockmarks and their potential significance for predicting fluid flow. Mar. Pet. Geol. 27, 1190–1199. https://doi.org/10.1016/j.marpetgeo.2010.02.005

IEAGHG, 2013. Information Sheets for CCS. https://ieaghg.org/docs/General_Docs/Reports/201316_Information_Sheets_for_CCS_All_sheets.pdf

IEAGHG, 2015. Review of Offshore Monitoring for CCS Projects, 2015/02, July 2015.

Inguaggiato, S., Diliberto, I.S., Federico, C., Paonita, A., and Vita, F., 2018, Review of the evolution of geochemical monitoring, networks and methodologies applied to the volcanoes of the Aeolian Arc (Italy): Earth-Science Reviews, 176, 241–276.

IOGP, 2020, Global CCUS Projects: www.iogp.org/bookstore/product/map-of-global-ccs-projects/

IPCC - Masson-Delmotte, V., Zhai P., Pörtner, H.O., Roberts, D., Skea, J., Shukla, P.R., Pirani, A., Moufouma-Okia, W., Péan, C., Pidcock, R., Connors, S., Matthews, J.B.R., Chen, Y., Zhou, X., Gomis, M.I., Lonnoy, E., Maycock, T., Tignor, M., 2018. Summary for Policymakers. In: Global Warming of 1.5°C. An IPCC Special Report on the impacts of global warming of 1.5°C above pre-industrial levels and related global greenhouse gas emission pathways, in the context of strengthening the global response to. IPCC 177.

IPCC - Pachauri, R.K.M., Ypersele L.v., Brinkman J.P, Kesteren S.v, Leprince-Ringuet L., Boxmeer N.v., F., 2014. Climate Change 2014: Synthesis Report. Contribution of Working Groups I, II and III to the Fifth Assessment Report of the Intergovernmental Panel on Climate Change. IPCC 151.

IPCC, 2005. IPCC special report on carbon dioxide capture and storage. Intergovernmental Panel on Climate Change, Working Group III, Geneva, Switzerland, p. 431.

Irwin, G.R., "Analysis of Stresses and Strains Near the End of a Crack Traversing a Plate," Journal of Applied Mechanics, Vol. 24, pp. 361-364, 1957.

Jain, A.K., Juanes, R., 2009. Preferential Mode of gas invasion in sediments: Grain-scale mechanistic model of coupled multiphase fluid flow and sediment mechanics. J. Geophys. Res. 114, B08101. https://doi.org/10.1029/2008JB006002

Jenkins, C. R., Cook, P.J., Ennis-King, J., Undershultz, J., Boreham, C., Dance, T., de Caritat, P., Etheridge, D.M., Freifeld, B.M., Hortle, A., Kirste, D., Paterson, L., Pevzner, R., Schacht, U., Sharma, S., Stalker, L., Urosevic, M. 2012. Safe storage and effective monitoring of CO2 in depleted gas fields. Proceedings of the National Academy of Sciences 109(2): E35-E41.

Jenkins, C., 2020, The State of the Art in Monitoring and Verification: an update five years on: International Journal of Greenhouse Gas Control, **100**, 103118.

Johansen, C., Todd, A.C., MacDonald, I.R., 2017. Time series video analysis of bubble release processes at natural hydrocarbon seeps in the Northern Gulf of Mexico. Mar. Pet. Geol. 82, 21–34. https://doi.org/10.1016/j.marpetgeo.2017.01.014

Jöhnk, K. D., Straile, D., & Ostendorp, W. (2004). Water level variability and trends in lake constance in the light of the 1999 centennial flood. *Limnologica*, *34*(1–2), 15–21. https://doi.org/10.1016/S0075-9511(04)80017-3

Johnson, B. D., Boudreau, B. P., Gardiner, B. S., and Maass, R., 2002. Mechanical response of sediments to bubble growth. Mar. Geol. 187, 247–363.

Johnson, B.D., Barry, M.A., Boudreau, B.P., Jumars, P.A., Dorgan, K.M., 2012. In situ tensile fracture toughness of surficial cohesive marine sediments. Geo-Marine Lett. 32, 39–48. https://doi.org/10.1007/s00367-011-0243-1

Jones, D.G., Beaubien, S.E., Blackford, J.C., Foekema, E.M., Lions, J., De Vittor, C., West, J.M., Widdicombe, S., Hauton, C., Queirós, A.M., 2015. Developments since 2005 in understanding potential environmental impacts of CO2 leakage from geological storage. Int. J. Greenh. Gas Control 40, 350–377. https://doi.org/10.1016/j.ijggc.2015.05.032

Jordan, S. F. A., Treude, T., Leifer, I., Janßen, R., Werner, J., Schulz-Vogt, H., and Schmale, O., 2020, Bubble-mediated transport of benthic microorganisms into the water column: Identification of methanotrophs and implication of seepage intensity on transport efficiency: Scientific Reports, **10**, 4682.

Jordt, A., Zelenka, C., von Deimling, J.S., Koch, R., and Köser, K., 2015, The Bubble Box: Towards an Automated Visual Sensor for 3D Analysis and Characterization of Marine Gas Release Sites: Sensors, 15, 30716–30735.

Judd, A. G., 2003, The global importance and context of methane escape from the seabed: Geo-Marine Letters, **23**, 147–154.

Judd, A., and Hovland, M., 2007, Seabed Fluid Flow: The Impact on Geology, Biology and the Marine Environment:

Kai Zhao, Tedford, E.W., Zare, M., and Lawrence, G.A., (2021, submitted). Impact of atmospheric pressure variations on methane ebullition and lake turbidity during ice-cover.

Kallweit, R.S., and Wood, L.C., 1982. The limits of resolution of zero-phase wavelets. GEOPHYSICS 47, 1035–1046.

Katsman, R., 2019. Methane Bubble Escape From Gas Horizon in Muddy Aquatic Sediment Under Periodic Wave Loading. Geophys. Res. Lett. 46, 6507–6515. https://doi.org/10.1029/2019GL083100

Katsman, R., Ostrovsky, I., Makovsky, Y., 2013. Methane bubble growth in fine-grained muddy aquatic sediment: Insight from modelling. Earth Planet. Sci. Lett. 377–378, 336–346. https://doi.org/10.1016/j.epsl.2013.07.011

Kellner, E., Baird, A. J., Oosterwoud, M., Harrison, K., and Waddington, J. M. (2006), Effect of temperature and atmospheric pressure on methane (CH_4) ebullition from near-surface peats, *Geophys. Res. Lett.*, 33, L18405, doi:10.1029/2006GL027509.

Klaucke, I., Weinrebe, W., Petersen, C.J., Bowden, D., 2010. Temporal variability of gas seeps offshore New Zealand: Multi-frequency geoacoustic imaging of the Wairarapa area, Hikurangi margin. Mar. Geol. 272, 49–58. https://doi.org/10.1016/j.margeo.2009.02.009

Knittel, K., Boetius, A., 2009. Anaerobic Oxidation of Methane: Progress with an Unknown Process. Annu. Rev. Microbiol. 63, 311–334. https://doi.org/10.1146/annurev.micro.61.080706.093130

Knudsen, V.O., Alford R.S and Emling, L. W., 1948, Underwater Ambient Noise: Marine Research, **7**.

Landrø, M., Wehner, D., Vedvik, N., Ringrose, P., Løhre, N.L., Berteussen, K., 2019. Gas flow through shallow sediments—A case study using passive and active seismic field data. Int. J. Greenh. Gas Control 87, 121–133. https://doi.org/10.1016/j.ijggc.2019.05.001

le Quéré, C., G. P. Peters, P. Friedlingstein, R. M. Andrew, J. G. Canadell, S. J. Davis, R. B. Jackson, and M. W. Jones, 2021, Fossil CO2 emissions in the post-COVID-19 era: Nature Climate Change, **11**, 197–199.

Leifer, I., 2015, Seabed bubble flux estimation by calibrated video survey for a large blowout seep in the North Sea: Marine and Petroleum Geology, **68**, 743–752.

Leifer, I., and Patro, R.K., 2002, The bubble mechanism for methane transport from the shallow seabed to the surface: A review and sensitivity study: Continental Shelf Research, **22**, 2409–2428.

Leifer, I., and Tang, D., 2007, The acoustic signature of marine seep bubbles: The Journal of the Acoustical Society of America, **121**, EL35–EL40.

Leifer, I., Jeuthe, H., Gjøsund, S.H., and Johansen, V., 2009, Engineered and Natural Marine Seep, Bubble-Driven Buoyancy Flows: Journal of Physical Oceanography, **39**, 3071–3090.

Leighton, T. G., 1988, The frequency analysis of transients: European Journal of Physics, **9**, 69–70.

Leighton, T.G. and Robb, G.B.N. (2008) Preliminary mapping of void fractions and sound speeds in gassy marine sediments from subbottom profiles, *Journal of the Acoustical Society of America*, **124**(5), EL313-EL320 (*JASA Express Letters*) (doi: 10.1121/1.2993744).

Leighton, T.G., 1994, The Freely-oscillating Bubble, *in* The Acoustic Bubble, Elsevier, 129–286.

Leighton, T.G., 2004, From seas to surgeries, from babbling brooks to baby scans: the acoustics of gas bubbles in liquids: International Journal of Modern Physics B, **18**, 3267–3314.

Leighton, T.G., and Walton, A. J., 1987, An experimental study of the sound emitted from gas bubbles in a liquid: European Journal of Physics, **8**, 98–104.

Leighton, T.G., Fagan, K.J. and Field, J.E., 1991. Acoustic and photographic studies of injected bubbles. Eur. J. Phys. 12, 77–85.

Leighton, T.G., K. Baik, and J. Jiang, 2012, The use of acoustic inversion to estimate the bubble size distribution in pipelines: Proceedings of the Royal Society A: Mathematical, Physical and Engineering Sciences, 468, 2461–2484.

Leighton, T.G., White, P.R., 2012. Quantification of undersea gas leaks from carbon capture and storage facilities, from pipelines and from methane seeps, by their acoustic emissions. Proc. R. Soc. A Math. Phys. Eng. Sci. 468, 485–510. https://doi.org/10.1098/rspa.2011.0221

Leighton, T.G., White, P.R., and Schneider, M.F., 1998, The detection and dimension of bubble entrainment and comminution: The Journal of the Acoustical Society of America, **103**, 1825–1835.

Li, J., B. Roche, J. M. Bull, P. R. White, T. G. Leighton, G. Provenzano, M. Dewar, and T. J. Henstock, 2020a, Broadband Acoustic Inversion for Gas Flux Quantification—Application to a Methane Plume at Scanner Pockmark, Central North Sea: Journal of Geophysical Research: Oceans, **125**.

Li, J., Roche, B., Bull, J.M., White, P.R., Davis, J.W., Deponte, M., Gordini, E., Cotterle, D., 2020b. Passive acoustic monitoring of a natural CO2 seep site – Implications for carbon capture and storage. Int. J. Greenh. Gas Control 93, 102899. https://doi.org/10.1016/j.ijggc.2019.102899

Li, J., White, P.R., J.M. Bull, Leighton, T.G., Roche, B., and Davis, J.W., 2021a, Passive acoustic localisation of undersea gas seeps using beamforming: International Journal of Greenhouse Gas Control, 108, 103316.

Li, J., White, P.R., Roche, B., Bull, J. M., Leighton, T.G., Davis, J. W., and Fone, J.W., 2021b, Acoustic and optical determination of bubble size distributions – Quantification of seabed gas emissions: International Journal of Greenhouse Gas Control, 108, 103313.

Li, S., Bush, R.T., Santos, I.R., Zhang, Q., Song, K., Mao, R., Wen, Z., Lu, X.X., 2018. Large greenhouse gases emissions from China's lakes and reservoirs. Water Res. 147, 13–24. https://doi.org/10.1016/j.watres.2018.09.053

Liang, J.H., McWilliams, J.C., Sullivan, P.P., and Baschek, B., 2011, Modeling bubbles and dissolved gases in the ocean: Journal of Geophysical Research, **116**, C03015.

Linkhorst, A., Hiller, C., DelSontro, T., M. Azevedo, G., Barros, N., Mendonça, R. and Sobek, S. (2020), Comparing methane ebullition variability across space and time in a Brazilian reservoir. Limnol Oceanogr, 65: 1623-1634. https://doi.org/10.1002/lno.11410

Liu, L., Wilkinson, J., Koca, K., Buchmann, C., Lorke, A., 2016. The role of sediment structure in gas bubble storage and release. J. Geophys. Res. Biogeosciences 121, 1992–2005. https://doi.org/10.1002/2016JG003456

Loewen, M. R., Melville, W. K., 1994, An experimental investigation of the collective oscillations of bubble plumes entrained by breaking waves: The Journal of the Acoustical Society of America, 95, 1329–1343.

Longuet-Higgins, M. S., Kerman, B. R., and Lunde, K., 1991, The release of air bubbles from an underwater nozzle: Journal of Fluid Mechanics, **230**, 365–390.

Lu, N. Q., Prosperetti, A., and Yoon, S. W., 1990, Underwater noise emissions from bubble clouds: IEEE Journal of Oceanic Engineering, **15**, 275–281.

Lumley, D., 2019, The Role of Geophysics in Carbon Capture and Storage, *in* Geophysics and Geosequestration, Cambridge University Press, 11–53.

Ma, B. B., and Nystuen, J. A., 2007, Detection of Rainfall Events Using Underwater Passive Aquatic Sensors and Air–Sea Temperature Changes in the Tropical Pacific Ocean: Monthly Weather Review, **135**, 3599–3612.

Ma, B.B., Nystuen, J.A., 2005. Passive Acoustic Detection and Measurement of Rainfall at Sea. J. Atmos. Ocean. Technol. 22, 1225–1248. https://doi.org/10.1175/JTECH1773.1

Maeck, A., Hofmann, H., Lorke, A., 2014. Pumping methane out of aquatic sediments – ebullition forcing mechanisms in an impounded river. Biogeosciences 11, 2925–2938. https://doi.org/10.5194/bg-11-2925-2014

Makarov, M. M., Muyakshin, S. I., Kucher, K. M., Aslamov, I. A., and Granin, N. G., 2020, A study of the gas seep Istok in the Selenga shoal using active acoustic, passive acoustic and optical methods: Journal of Great Lakes Research, **46**, 95–101.

Maksimov, A. O., Burov, B. A., Salomatin, A. S., and Chernykh, D.v., 2016, Sounds of Undersea Gas Leaks, *in* Underwater Acoustics and Ocean Dynamics, Springer Singapore, 107–116.

Mamalakis, A., Randerson, J. T., Yu, J.Y., Pritchard, M.S., Magnusdottir, G., Smyth, P., Levine, P.A., Yu, S., and Foufoula-Georgiou, E., 2021, Zonally contrasting shifts of the tropical rain belt in response to climate change: Nature Climate Change, **11**, 143–151.

Manasseh, R., Babanin, A.v., Forbes, C., Rickards, K., Bobevski, I., Ooi, A., 2006, Passive Acoustic Determination of Wave-Breaking Events and Their Severity across the Spectrum: Journal of Atmospheric and Oceanic Technology, **23**, 599–618.

Marcon, L., Bleninger, T., Männich, M., Hilgert, S., 2019. High-frequency measurements of gas ebullition in a Brazilian subtropical reservoir—identification of relevant triggers and seasonal patterns. Environ. Monit. Assess. 191, 357. https://doi.org/10.1007/s10661-019-7498-9

Martin, T. E., and Mouton, J. C., 2020, Longer-lived tropical songbirds reduce breeding activity as they buffer impacts of drought: Nature Climate Change, **10**, 953–958.

Mattson, M.D., Likens, G.E., 1990. Air pressure and methane fluxes. Nature 347, 718–719. https://doi.org/10.1038/347718b0

McGinnis, D. F., Greinert, J., Artemov, Y., Beaubien, S.E., and Wüest, A., 2006, Fate of rising methane bubbles in stratified waters: How much methane reaches the atmosphere? Journal of Geophysical Research, **111**, C09007.

Medwin, H., and Beaky, M.M., 1989, Bubble sources of the Knudsen sea noise spectra: The Journal of the Acoustical Society of America, **86**, 1124–1130.

Medwin, H., Kurgan, A., and Nystuen, J. A., 1990, Impact and bubble sound from raindrops at normal and oblique incidence: The Journal of the Acoustical Society of America, **88**, 413–418.

Mikunda, T., Brunner, L., Skylogianni, E., Monteiro, J., Rycroft, L., and Kemper, J., 2021, Carbon capture and storage and the sustainable development goals: International Journal of Greenhouse Gas Control, **108**, 103318.

Minnaert, M., 1933. XVI. On musical air-bubbles and the sounds of running water. London, Edinburgh, Dublin Philos. Mag. J. Sci. 16, 235–248. https://doi.org/10.1080/14786443309462277

Moffette, F., Alix-Garcia, J., Shea, K., and Pickens, A.H., 2021, The impact of near-real-time deforestation alerts across the tropics: Nature Climate Change, **11**, 172–178.

Molari, M., Guilini, K., Lins, L., Ramette, A., Vanreusel, A., 2019, CO2 leakage can cause loss of benthic biodiversity in submarine sands: Marine Environmental Research, 144, 213–229.

Monahan, E. C., and Lu, M., 1990, Acoustically relevant bubble assemblages and their dependence on meteorological parameters: IEEE Journal of Oceanic Engineering, **15**, 340–349.

Monecke, T., Petersen, S., Hannington, M.D., Anzidei, M., Esposito, A., Giordano, G., Garbe-Schönberg, D., Augustin, N., Melchert, B., Hocking, M., 2012, Explosion craters associated with shallow submarine gas venting off Panarea island, Italy: Bulletin of Volcanology, 74, 1937–1944.

Muyakshin, S. I., and Sauter, E., 2010, The hydroacoustic method for the quantification of the gas flux from a submersed bubble plume: Oceanology, **50**, 995–1001.

NAO, 2017, Carbon Capture and Storage: the second competition for government support: National Audit Office (UK), **ISBN: 9781**.

Nicholls, R. J., Lincke, D., Hinkel, J., Brown, S., Vafeidis, A.T., Meyssignac, B., Hanson, S.E., Merkens, J.L., and Fang J., 2021, A global analysis of subsidence, relative sea-level change and coastal flood exposure: Nature Climate Change, **11**, 338–342.

NRC, 2003, Ocean Noise and Marine Mammals: National Research Council (U.S.) (Ed.).

Nystuen, J. A., 1986, Rainfall measurements using underwater ambient noise: The Journal of the Acoustical Society of America, **79**, 972–982.

Nystuen, J. A., 2001, Listening to Raindrops from Underwater: An Acoustic Disdrometer: Journal of Atmospheric and Oceanic Technology, **18**, 1640–1657.

Nystuen, J. A., and Selsor, H. D., 1997, Weather Classification Using Passive Acoustic Drifters: Journal of Atmospheric and Oceanic Technology, **14**, 656–666.

Nystuen, J.A., Amitai E., Anagnostou, E.N., and Anagnostou, M. N., 2008, Spatial averaging of oceanic rainfall variability using underwater sound: Ionian sea rainfall experiment 2004: The Journal of the Acoustical Society of America, **123**, 1952–1962.

Nystuen, J.A., Anagnostou, M.N., Anagnostou, E.N., and Papadopoulos, A., 2015, Monitoring Greek Seas Using Passive Underwater Acoustics: Journal of Atmospheric and Oceanic Technology, **32**, 334–349.

Nystuen, J.A., McPhaden, M.J., and Freitag, H.P., 2000, Surface Measurements of Precipitation from an Ocean Mooring: The Underwater Acoustic Log from the South China Sea*: Journal of Applied Meteorology, **39**, 2182–2197.

Oberheide, J., Hagan, M.E., Richmond, A.D., Forbes, J.M., 2015. DYNAMICAL METEOROLOGY | Atmospheric Tides, in: Encyclopedia of Atmospheric Sciences. Elsevier, pp. 287–297. https://doi.org/10.1016/B978-0-12-382225-3.00409-6

Oppo, D., de Siena, L., Kemp, D. B., 2020, A record of seafloor methane seepage across the last 150 million years: Scientific Reports, **10**, 2562.

Ortiz-Bobea, A., Ault, T. R., Carrillo, C.M., Chambers, R.G., and Lobell, D.B., 2021, Anthropogenic climate change has slowed global agricultural productivity growth: Nature Climate Change, **11**, 306–312.

Ostrovsky, I., McGinnis, D. F., Lapidus, L., Eckert, W., 2008, Quantifying gas ebullition with echosounder: the role of methane transport by bubbles in a medium-sized lake: Limnology and Oceanography: Methods, **6**, 105–118.

Pensieri, S., Bozzano, R., Nystuen, J.A., Anagnostou, E.N., Anagnostou, M.N., Bechini, R. 2015, Underwater Acoustic Measurements to Estimate Wind and Rainfall in the Mediterranean Sea: Advances in Meteorology, **2015**, 1–18.

Phelps, A. D., Ramble, D. G., and Leighton, T. G., 1997, The use of a combination frequency technique to measure the surf zone bubble population: The Journal of the Acoustical Society of America, **101**, 1981–1989.

Pumphrey, H. C., Crum, L., 1989, Sources of ambient noise in the ocean an experimental investigation. Physics

Pumphrey, H. C., Elmore, P. A., 1990, The entrainment of bubbles by drop impacts: Journal of Fluid Mechanics, **220**, 539–567.

Pumphrey, H. C., Ffowcs-Williams, J.E., 1990, Bubbles as sources of ambient noise: IEEE Journal of Oceanic Engineering, 15, 268–274.

Pumphrey, H. C., Walton, A. J., 1988, Experimental study of the sound emitted by water drops impacting on a water surface: European Journal of Physics, **9**, 225–231.

Pumphrey, H.C., Crum, L.A., 1990. Free oscillations of near-surface bubbles as a source of the underwater noise of rain. J. Acoust. Soc. Am. 87, 142–148. https://doi.org/10.1121/1.399306

Quale, S., Rohling, V. 2016, The European Carbon dioxide Capture and Storage Laboratory Infrastructure (ECCSEL): Green Energy & Environment, 1, 180–194.

Razaz, M., di Iorio, D., Wang, B., Daneshgar Asl, S., Thurnherr, A. M., 2020, Variability of a natural hydrocarbon seep and its connection to the ocean surface: Scientific Reports, **10**, 12654.

Razaz, M., di Iorio, D., Wang, B., Daneshgar Asl, S., Thurnherr, A. M., 2020, Variability of a natural hydrocarbon seep and its connection to the ocean surface: Scientific Reports, 10, 12654.

Rehder, G., Brewer, P.W., Peltzer, E.T., Friederich, G., 2002. Enhanced lifetime of methane bubble streams within the deep ocean. Geophys. Res. Lett. 29, 21-1-21–4. https://doi.org/10.1029/2001GL013966

Riddick, S.N., Mauzerall, D.L., Celia, M.A., Kang, M., Bandilla, K., 2020. Variability observed over time in methane emissions from abandoned oil and gas wells. Int. J. Greenh. Gas Control 100, 103116. https://doi.org/10.1016/j.ijggc.2020.103116

Riedel, M., Scherwath, M., Römer, M., Veloso, M., Heesemann, M., Spence, G. D., 2018, Distributed natural gas venting offshore along the Cascadia margin: Nature Communications, **9**, 3264.

Ringrose, P. S., 2018, The CCS hub in Norway: some insights from 22 years of saline aquifer storage: Energy Procedia, **146**, 166–172.

Ringrose, P.S., Meckel, T.A., 2019. Maturing global CO2 storage resources on offshore continental margins to achieve 2DS emissions reductions. Sci. Rep. 9, 17944. https://doi.org/10.1038/s41598-019-54363-z

Robinson, A. H., Callow, B., Böttner, C., Yilo, N., Provenzano, G., Falcon-Suarez, I. H., Marín-Moreno, H., Lichtschlag, A., Bayrakci, G., Gehrmann, R., Parkes, L., Roche, B., Saleem, U., Schramm, B., Waage, M., Lavayssière, A., Li, J., Jedari-Eyvazi, F., Sahoo, S., Deusner, C., Kossel, E., Minshull, T. A., Berndt, C., Bull, J. M., Dean, M., James, R. H., Chapman, M., Best, A. I., Bünz, S., Chen, B., Connelly, D. P., Elger, J., Haeckel, M., Henstock, T. J., Karstens, J., Macdonald, C., Matter J.M., North, L., and Reinardy, B., 2021, Multiscale characterisation of chimneys/pipes: Fluid escape structures within sedimentary basins: International Journal of Greenhouse Gas Control, **106**, 103245.

Roche, B., Bull, J.M., Marin-Moreno, H., Leighton, T.G., Falcon-Suarez, I.H., Tholen, M., White, P.R., Provenzano, G., Lichtschlag, A., Li, J., Faggetter, M., 2021. Time-lapse imaging of CO2 migration within near-surface sediments during a controlled sub-seabed release experiment. Int. J. Greenh. Gas Control 109, 103363. https://doi.org/10.1016/j.ijggc.2021.103363

Roche, B., Li, J., White, P., Bull, J.M., Davis, J.W., Deponte, M., Gordini, E., Cotterle, D., 2019. Validating passive acoustic methods for gas flux quantification, offshore Panarea, Mediterranean Sea. J. Acoust. Soc. Am. 146, 2965–2965. https://doi.org/10.1121/1.5137306

Römer, M., Riedel, M., Scherwath, M., Heesemann, M., Spence, G. D., 2016, Tidally controlled gas bubble emissions: A comprehensive study using long-term monitoring data from the NEPTUNE cabled observatory offshore Vancouver Island: Geochemistry, Geophysics, Geosystems, **17**, 3797–3814.

Ruppel, C.D., Kessler, J.D., 2017. The interaction of climate change and methane hydrates. Rev. Geophys. 55, 126–168. https://doi.org/10.1002/2016RG000534

Salmi, M. S., Johnson, H.P., Leifer, I., Keister, J.E., 2011, Behaviour of methane seep bubbles over a pockmark on the Cascadia continental margin: Geosphere, **7**, 1273–1283.

Scandella, B. P., Varadharajan, C., Hemond, H.F., Ruppel, C., Juanes, R., 2011, A conduit dilation model of methane venting from lake sediments: Geophysical Research Letters, **38**,

Scandella, B.P., Pillsbury, L., Weber, T., Ruppel, C., Hemond, H. F., Juanes, R., 2016, Ephemerality of discrete methane vents in lake sediments: Geophysical Research Letters, **43**, 4374–4381.

Schneider von Deimling, Linke, J.,P., Schmidt, M., and Rehder, G., 2015, Ongoing methane discharge at well site 22/4b (North Sea) and discovery of a spiral vortex bubble plume motion: Marine and Petroleum Geology, 68, 718–730.

Schroder, H.G., 1992. Sediment surface in eastern Lake Constance—Side Scan-investigations related with construction measures of the Alpine Rhine River, Berichte der Internationalen Gewasscherschutzkom-misision für den Bodensee, Report 43.

Scrimger, J.A., Evans, D.J., McBean, G.A., Farmer, D.M., Kerman, B.R., 1987, Underwater noise due to rain, hail, and snow: The Journal of the Acoustical Society of America, **81**, 79–86.

Seroussi, H., Nowicki, S., Payne, A.J., Goelzer, H., Lipscomb, W.H., Abe-Ouchi, A., Agosta, C., Albrecht T., Asay-Davis, X., Barthel, A., Calov, R., Cullather, R., Dumas, C., Galton-Fenzi, B.K., Gladstone, R., Golledge, N.R., Gregory, J.M., Greve, R., Hattermann, T., Hoffman, M.J.,

Humbert, A., Huybrechts, P., N. C. Jourdain, T. Kleiner, E. Larour, G. R. Leguy, D. P. Lowry, C. M. Little, M. Morlighem, F. Pattyn, T. Pelle, S. F. Price, A. Quiquet, R. Reese, N.-J. Schlegel, A. Shepherd, Simon, E., Smith, R. S., Straneo, F., Sun, S., Trusel, L. D., van Breedam, J., van de Wal, R.S.W., Winkelmann, R., Zhao, C., Zhang, T. and Zwinger/ T., 2020, ISMIP6 Antarctica: a multi-model ensemble of the Antarctic ice sheet evolution over the 21st century: The Cryosphere, **14**, 3033–3070.

Serra, Y. L., 2018, Precipitation measurements from the Tropical Moored Array: A review and look ahead: Quarterly Journal of the Royal Meteorological Society, **144**, 221–234.

Shell U.K Ltd., 2018. Goldeneye Pipeline Emerging Recommendation Report. Goldeneye Decommissioning Project, Shell Report Number GDP-PT-S-AA-7180-00002

Sirhan, S.T., Katsman, R., Lazar, M., 2019. Methane Bubble Ascent within Fine-Grained Cohesive Aquatic Sediments: Dynamics and Controlling Factors. Environ. Sci. Technol. 53, 6320–6329. https://doi.org/10.1021/acs.est.8b06848

Spiridonov, V., Ćurić, M., 2021. Fundamentals of Meteorology. Springer International Publishing, Cham. https://doi.org/10.1007/978-3-030-52655-9

Stoker M.S., Balson, P.S., Long, D., and Tappin, D.R., 2011. An overview of the lithostratigraphical framework for the Quaternary deposits on the United Kingdom continental shelf. Keyworth

Stoker, M.S., Long, D., Fyfe, J.A. 1985. A revised Quaternary stratigraphy for the central North Sea. London, HMSO.

Stolt, R.H., 1978. Migration by Fourior Transform. GEOPHYSICS 43, 23–48.

Strachan, N., Hoefnagels, R., Ramírez, A., van den Broek, M., Fidje, A., Espegren, K., Seljom, P., Blesl, M., Kober, T., Grohnheit, P.E., 2011. CCS in the North Sea region: A comparison on the cost-effectiveness of storing CO2 in the Utsira formation at regional and national scales. Int. J. Greenh. Gas Control 5, 1517–1532. https://doi.org/10.1016/j.ijggc.2011.08.009

Strasberg, M., 1953, The Pulsation Frequency of Nonspherical Gas Bubbles in Liquids: The Journal of the Acoustical Society of America, **25**, 536–537.

Suess, E., 2014, Marine cold seeps and their manifestations: geological control, biogeochemical criteria and environmental conditions: International Journal of Earth Sciences, **103**, 1889–1916.

Sultan, N., Plaza-Faverola, A., Vadakkepuliyambatta, S., Buenz, S., Knies, J., 2020, Impact of tides and sea-level on deep-sea Arctic methane emissions: Nature Communications, **11**, 5087.

Taner, M.T., Koehler, F., Sheriff, R.E., 1979. Complex seismic trace analysis. GEOPHYSICS 44, 1041–1063. https://doi.org/10.1190/1.1440994

Taylor, P., Stahl, H., Vardy, M.E., Bull, J.M., Akhurst, M., Hauton, C., James, R.H., Lichtschlag, A., Long, D., Aleynik, D., Toberman, M., Naylor, M., Connelly, D., Smith, D., Sayer, M.D.J., Widdicombe, S., Wright, I.C., Blackford, J., 2015. A novel sub-seabed CO 2 release experiment informing monitoring and impact assessment for geological carbon storage. Int. J. Greenh. Gas Control 38, 3–17. https://doi.org/10.1016/j.ijggc.2014.09.007

Taylor, W. O., Anagnostou, M. N., Cerrai, D., Anagnostou, E.N., 2020, Machine Learning Methods to Approximate Rainfall and Wind From Acoustic Underwater Measurements (February 2020): IEEE Transactions on Geoscience and Remote Sensing, 1–12.

Thorpe, S.A., 1982, On the Clouds of Bubbles Formed by Breaking Wind-Waves in Deep Water, and their Role in Air -- Sea Gas Transfer: Philosophical Transactions of the Royal Society of London. Series A, Mathematical and Physical Sciences, **304**, 155–210.

Tokida, T., Miyazaki, T., Mizoguchi, M., Nagata, O., Takakai, F., Kagemoto, A., Hatano, R., 2007. Falling atmospheric pressure as a trigger for methane ebullition from peatland. Global Biogeochem. Cycles 21, n/a-n/a. https://doi.org/10.1029/2006GB002790

Tsuchiya, K., Ohsaki, K., and Taguchi, K., 1996, Large and small bubble interaction patterns in a bubble column: International Journal of Multiphase Flow, 22, 121–132.

UNFCCC, 2015, United Nations / Framework Convention on Climate Change, Adoption of the Paris Agreement: United Nations.

United Nations, 2015. United Nations / Framework Convention on Climate Change, Adoption of the Paris Agreement. United Nations, Paris.

Vagle, S., Large, W. G., Farmer, D. M., 1990, An Evaluation of the WOTAN Technique of Inferring Oceanic Winds from Underwater Ambient Sound: Journal of Atmospheric and Oceanic Technology, **7**, 576–595.

Vagle, S., McNeil, C., Steiner, N., 2010, Upper ocean bubble measurements from the NE Pacific and estimates of their role in air-sea gas transfer of the weakly soluble gases nitrogen and oxygen: Journal of Geophysical Research, **115**, C12054.

Van der meer, L.G.H., 2013. The K12-B CO 2 injection project in the Netherlands, in: Geological Storage of Carbon Dioxide (CO2). Elsevier, pp. 301-332e. https://doi.org/10.1533/9780857097279.3.301

Vandeweijer, V., van der Meer, B., Hofstee, C., Mulders, F., D'Hoore, D. and Graven, H., 2011. Monitoring the CO2 injection site: K12-B. Energy Procedia 4, 5471–5478.

Varadharajan, C. and H. F. Hemond (2012). Time-series analysis of high-resolution ebullition fluxes from a stratified, freshwater lake. Journal of Geophysical Research 117(G2): G02004.

Vardy, M.E., Vanneste, M., Henstock, T.J., Clare, M.A., Forsberg, C.F., Provenzano, G., 2017. State-of-the-art remote characterization of shallow marine sediments: the road to a fully integrated solution. Near Surf. Geophys. 15, 387–402. https://doi.org/10.3997/1873-0604.2017024

Vazquez, A., Manasseh, R., Chicharro, R., 2015, Can acoustic emissions be used to size bubbles seeping from a sediment bed? Chemical Engineering Science, **131**, 187–196.

Vielstädte, L., Karstens, J., Haeckel, M., Schmidt, M., Linke, P., Reimann, S., Liebetrau, V., McGinnis, D. F., Wallmann K., 2015, Quantification of methane emissions at abandoned gas wells in the Central North Sea: Marine and Petroleum Geology, **68**, 848–860.

Walton, A. J., Gunn, M. G., Reynolds, G. T., 2005, The Quality Factor of Oscillating Bubbles as an Indication of Gas Content With Particular Reference to Methane: IEEE Journal of Oceanic Engineering, **30**, 924–926.

Wang, B., Socolofsky, S.A., 2015. A deep-sea, high-speed, stereoscopic imaging system for in situ measurement of natural seep bubble and droplet characteristics. Deep Sea Res. Part I Oceanogr. Res. Pap. 104, 134–148. https://doi.org/10.1016/j.dsr.2015.08.001

Wang, D. W., Wijesekera, H. W., Jarosz, E., Teague, W. J., and Pegau, W. S., 2016, Turbulent Diffusivity under High Winds from Acoustic Measurements of Bubbles: Journal of Physical Oceanography, **46**, 1593–1613.

Wangen, M., Halvorsen, G., 2020. A Three-Dimensional Analytical Solution for Reservoir Expansion, Surface Uplift and Caprock Stress Due to Pressurized Reservoirs. Math. Geosci. 52, 253–284. https://doi.org/10.1007/s11004-019-09821-9

Wenz, G. M., 1962, Acoustic Ambient Noise in the Ocean: Spectra and Sources: The Journal of the Acoustical Society of America, **34**, 1936–1956.

Werner, R., & Riffler, M. (2005). *Land-See-Wind am Bodensee*. 153–166.

Wessels, M., Bussmann, I., Schloemer, S., Schlüter, M., & Böder, V. (2010). Distribution, morphology, and formation of pockmarks in Lake Constance, Germany. *Limnology and Oceanography*, *55*(6), 2623–2633. https://doi.org/10.4319/lo.2010.55.6.2623

Wessels, M., Bussmann, I., Schloemer, S., Ter, M.S., Dere, V.B., 2010. Distribution, morphology, and formation of pockmarks in Lake Constance, Germany. Limnol. Oceanogr. 55, 2623–2633. https://doi.org/10.4319/lo.2010.55.6.2623

Westergaard, H.M., "Bearing Pressures and Cracks," Journal of Applied Mechanics, Vol. 6, pp. A49-53, 1939

Wiggins, S. M., Leifer, I., Linke, P., Hildebrand, J. A., 2015, Long-term acoustic monitoring at North Sea well site 22/4b: Marine and Petroleum Geology, **68**, 776–788.

Woolway, R. I., Maberly S. C., 2020, Climate velocity in inland standing waters: Nature Climate Change, **10**, 1124–1129.

World Economic Forum, 2020, The Global Risks Report 2020:

Wu, J., 1979, Oceanic Whitecaps and Sea State: Journal of Physical Oceanography, **9**, 1064–1068.

Yang, J., Riser, S., Nystuen J., Asher, W., Jessup, A., 2015, Regional Rainfall Measurements Using the Passive Aquatic Listener During the SPURS Field Campaign: Oceanography, **28**, 124–133.

Zhao, B., Qiao, F., Cavaleri, L., Wang, G., Bertotti, L., Liu L., 2017, Sensitivity of typhoon modeling to surface waves and rainfall: Journal of Geophysical Research: Oceans, **122**, 1702–1723.

Zhao, Z., D'Asaro, E. A., and Nystuen, J. A., 2014, The Sound of Tropical Cyclones: Journal of Physical Oceanography, **44**, 2763–2778.

Zhou, C., Zelinka, M. D., Dessler, A. E., Wang, M., 2021, Greater committed warming after accounting for the pattern effect: Nature Climate Change, **11**, 132–136.